The
University
Of
Sheffield.

3D EXPERIMENTAL STUDY OF THE MOTION OF SINGLE PARTICLES USING IMAGE-BASED TECHNIQUES

A thesis submitted in partial fulfilment of the
requirements for the degree of Doctor of Philosophy
(PhD) in the Faculty of Engineering at the University
of Sheffield

Francisco Javier Carranza Chavez

Mechanical Engineering Department

August 2016

CONTENTS

ACKNOWLEDGEMENTS

I would like to thank the National Council of Science and Technology (CONACYT, in Spanish), and the Centre of Engineering and Industrial Development (CIDESI, in Spanish), both from Mexico, for giving me the required economical support to do this work. Additionally, I say thanks to The University of Sheffield for all the help and training provided to my development as a PhD student.

I also would like to show my gratitude to my first supervisor Professor Yang Zhang for his good guidance and friendship throughout this PhD work, to my second supervisor Doctor Robert Woolley for his valuable advice and encouragement, and to my dear colleagues for their irreplaceable help and friendship.

I must give thanks as well to my beloved family in Mexico, to my treasured local Church community, to my highly appreciated friends that I met during my time in Sheffield, and above all to my Lord Jesus. Without them this work would have not been possible.

NOMENCLATURE

a	[m]	Particle longest dimension
a_P	[m/s^2]	Particle acceleration
a_N	[m/s^2]	Normal acceleration
a_T	[m/s^2]	Tangential acceleration
A	[m^2]	Arithmetic average of the particle surface area visible to the camera
A_{mmm}	[-]	Particle max-med-min area
A_P	[m^2]	Particle projected area
b	[m]	Particle intermediate dimension
$\boldsymbol{B}$	[-]	Binormal unit vector of the Frenet frame
c	[m]	Particle smallest dimension
C_D	[-]	Drag coefficient
C_L	[-]	Lift coefficient
D	[m]	Diameter
d_*	[-]	Dimensionless diameter
d_c	[m]	Diameter of the equal projected circular area
d_n	[m]	Nominal diameter
d_{off}	[m]	Distance between the centre of mass and the centre of pressure
f	[m]	Focal distance
F_D	[N]	Drag force
F_L	[N]	Lift force
g	[m/s^2]	Acceleration due to gravity
g_L	[m/s^2]	Gravity acceleration in the direction of lift
I	[kg·m^2]	Moment of inertia
K_1	[-]	Stokes' shape factor
K_2	[-]	Newton's shape factor
l	[m]	Distance
L	[m]	Length
m	[kg]	Mass of the particle
m_f	[kg]	Mass of the fluid displaced by the particle
M	[N·m]	Torque
N	[-]	Number of measurements
$\boldsymbol{N}$	[-]	Normal unit vector of the Frenet frame
P	[-]	Any measured variable for error analysis
r	[m]	Radius
Re_P	[-]	Particle Reynolds number
S	[m^2]	Particle surface area
S_V	[m^2]	Surface area of the same volume sphere
SF	[-]	Corey shape factor
t	[s]	Time
T	[C]	Temperature
$\boldsymbol{T}$	[-]	Tangential unit vector of the Frenet frame
u	[pixel]	Pixel horizontal axis
$\boldsymbol{u}$	[m/s]	Flow field velocity vector
U_*	[-]	Dimensionless velocity
U_T	[m/s]	Particle terminal velocity

v	[pixel]	Pixel vertical axis
V_P	[m/s]	Particle velocity
x, X	[m]	Horizontal coordinate axis
X'	[m]	Coordinate axis along the direction of the particle longest dimension
y, Y	[m]	Vertical coordinate axis
Y'	[m]	Coordinate axis normal to X'
z, Z	[m]	Depth coordinate axis
Z'	[m]	Coordinate axis normal to X' and Y'

SPECIAL CHARACTERS

α	[°]	Angle of incidence
Δ	[-]	Difference
ε	[°]	Angular deflection
ρ_f	[kg/m^3]	Fluid density
ρ_P	[kg/m^3]	Particle density
μ	[Pa·s]	Fluid dynamic viscosity
σ	[-]	Aspect ratio, standard deviation
η	[-]	Uncertainty
τ	[s]	Time constant
χ	[-]	Particle circularity
Ψ	[-]	Enhanced shape factor
ω	[rad/s]	Angular velocity
$\emptyset$	[-]	Degree of sphericity
$\emptyset_{\parallel}$	[-]	Lengthwise sphericity
$\emptyset_{\perp}$	[-]	Crosswise sphericity
$\forall$	[m^3]	Particle volume

SUBSCRIPTS

C	Centroid
f	Fluid
L	Lift
P	Particle
W	World reference frame

ABSTRACT

A new methodology to study the free-settling motion of single particles in a fluid at $Re_P \leq 5000$ within a three-dimensional reference frame is presented. After certain value of Re_P the descend of any non-spherical solid is characterised by secondary motions which alter the particle orientation, therefore, their influence on quantities such as the velocity and drag coefficient have to be investigated within a context that ensures the interaction between the solid and the fluid is preserved undisturbed. To meet this requirement, this work is entirely based on high-speed imaging techniques, such as stereo vision and Schlieren photography, combined with digital image processing, vector algebra, and differential geometry operations. For spherical particles, the evolution of the structures in the surrounding fluid and their impact on the settling trajectories was observed. Additionally, a strong similarity between the calculated values of the coefficient of drag and those from literature correlations was achieved, which validates the proposed methodology. For non-spherical solids, it was found that after $Re_P > 200$, secondary motions such as oscillation, gliding, and tumbling occurred and caused the formation of a turbulent wake structure in the fluid surrounding the particle. Their effect on the solids velocity and drag coefficient was also quantified, being more significant on disks than on cylinders, however a direct relation between the angular orientation changes and the drag coefficient could not be suggested. It was noticed too that for irregular particles the secondary motions were not evenly defined, and that the settling may be accompanied by continuous rotations, even at low Re_P, which further alter the trajectory, orientation, and surrounding fluid structure, thus complicating the quantification of the motion parameters and imposing restrictions on the visualisation systems employed here.

Chapter 1

INTRODUCTION

1.1 MOTIVATION

Due to the global trend of reducing the emissions of greenhouse gases, the utilisation of solid biomass as an alternative fuel for direct-firing power plants has been encouraged during the last decades. The main advantage of employing this type of fuel relies on the fact that it is carbon dioxide (CO_2) neutral, since the same amount of CO_2 consumed during its growing stage is released to the atmosphere when it is burned [1]. Moreover, it contributes to the overall reduction of the atmospheric levels of CO_2 and other gases generated as a product of disposing already existing solid waste biomass through different methods [2].

Any organic material derived from photosynthesis reactions in a relatively short period of time can technically be considered as biomass [3], however only woody products and agriculture residues can accomplish the large-scale energy requirements of power plants [4]. Furthermore, already built installations can still be used by firing these substances in the form of particles, and the necessity to construct new infrastructure is greatly diminished. In fact, the best cost-effective approach to solid biomass exploitation consists on burning it mixed with pulverised coal in a process known as cofiring [5, 6].

Because solid biomass is friable and fibrous, and its content of volatile matter is significantly high, it is neither economical nor necessary to mill it to a size similar to that of pulverised coal, which typically varies from 70 μm to 90 μm according to Osborne [7]. Actually, biomass particles usually found in cofiring applications have lengths which vary from 1 mm to 10 mm, or even larger as reported by Rosendahl et al. [8]. Besides the size discrepancy, a second issue posed by the biomass solids is that, contrary to coal, their shape does not resemble a sphere, and possess aspect ratios 3 to 7 times higher [9, 10].

Provided that most of the existing installations have been designed to handle coal particles, the differences in size, shape, and chemical composition of the biomass solids encompass a series of technical challenges that arise during their pneumatic transportation to the burners and their subsequent combustion. Their distinct aerodynamic, heating, and combustion characteristics alter the flow patterns in the pipes and furnaces, and cause non-isothermal particle heating which leads to the coexistence of different combustion stages at the same time, enlarging the burnout times in consequence [9, 11-13].

It is under these complex circumstances where the motivation for the present work origins because the detailed knowledge of the motion of one single particle immersed in a flow constitutes the basis for the correct design of the transportation and firing systems which handle solid biomass. As in these systems the particles are free to move, the straightest approach to investigate the aerodynamics of a single one is through free settling studies. Moreover, quantities determined in this type of analyses, such as the terminal velocity U_T and coefficient of drag C_D are essential for the design equations of such biomass-exploitation systems [14].

Most of the experimental work done on free-falling particles have been focused on the development of correlations to predict average values of C_D and U_T [15-24], nevertheless it has been reported that when a non-spherical solid settles in a fluid, it exhibits some kind of secondary motion which continually alters its angular orientation and the structure of the surrounding fluid [25-27]. The influence of these changes on the motion parameters has normally been skipped [28].

On the other hand, considerable numerical work in this field has been done [11, 12, 28-33]. Even drag correlations which include the influence of the angular change have been proposed [11, 28, 30, 33, 34]. Nonetheless, for most of the simulations, the motion equations were solved subjected to the condition of a fixed particle at different inclination angles with respect to the flow [28, 29, 32-34]. Therefore, the application of the obtained results in situations where the particle motion is not restrained must be taken with care, since the interaction between the particle and the fluid is different. For instance, a C_D variance of 15 % – 30 % between a free-moving sphere and a fixed one has been reported in the literature [35]. Another disadvantage of the numerical models is the fact that they are still not able to deal with a solid of irregular geometry.

Within this context, the aim of this research is to examine the settling behaviour of free-moving single particles, of regular and irregular shape, in a way which preserves the solid-fluid interaction undisturbed whilst still revealing the influence that secondary motions and continuous angular orientation changes have on the quantities relevant for the design and optimisation of transportation and combustion systems which deal with non-spherical, solid biomass particles. In order to so, this experimental study is entirely based on high-speed imaging techniques coupled with digital image processing operations.

1.2 OBJECTIVES

Because the motion of single particles in a fluid is fully described within a three-dimensional (3D) frame, the principle of stereo vision is employed in this thesis to generate 3D metric data on which the analysis can be further developed. In addition, the method of Schlieren photography is used to visualise the fluid surrounding the particles in some of the cases. More specifically, this work pursues the following objectives:

i. The development of a non-intrusive technique based on high-speed photography suitable to resolve quantitatively the instantaneous 3D displacement and orientation of spherical and non-spherical particles falling freely in a fluid.
ii. The application of high-speed Schlieren imaging to reveal the structure of the fluid surrounding the particles in as many cases as possible.
iii. The derivation of a mathematical procedure appropriate to estimate the instantaneous kinematics and dynamics of the solids out of their 3D trajectory-coordinates only.
iv. The investigation of the effect that the angular orientation of a regular, non-spherical particle has on C_D and other motion parameters.
v. The exploration of the behaviour of irregular, chip-like, particles immersed in fluids at rest and in motion.

1.3 THESIS STRUCTURE

The present thesis is divided in eight chapters, being Chapter 1 the Introduction and Chapter 8 the Conclusions and Future Work Recommendations. In Chapter 2 the literature regarding the motion experienced by a single spherical and non-spherical particle immersed in a fluid is reviewed. The first part of the chapter deals with some of the most popular methods to characterise the geometry of the solid. The second part provides a detailed description of the motion characteristics and the relevant equations. In the third part of the chapter the quantitative and qualitative image-based techniques which have been used previously to analyse the motion of particles are discussed.

Since the experimental technique applied in this work to obtain quantitative data is entirely based on stereo visualisation and 3D metric reconstruction, which also involves the process of camera calibration, the theory and methods to perform such tasks are covered in Chapter 3. The digital image processing operations required by the process of camera calibration are also reviewed. The chapter ends with a study of the accuracy of the 3D generated data.

In Chapter 4 the digital image processing calculations and the methodology followed to extract particle data from the stereo pictures to be the input of the stereo reconstruction algorithms are exposed in the first section of the chapter. Then, the procedure developed to track the kinematics, dynamics, and orientation of the moving solids from the 3D output data of the algorithms is portrayed.

Chapters 5 and 6 comprehend the experimental study of settling spheres, cylinders, and disks, employing both stereo vision and Schlieren photography. In Chapter 5, the geometrical characterisation of the particles, description of the installations, and results of the calibration of the stereo system are exposed first. Then, the experimental data obtained for the spheres is discussed, along with comparisons with correlations from the literature to compute U_T and C_D.

The results generated for the free-falling cylinders and disks are given in the first two sections of Chapter 6. Comparisons between the experimental average results of U_T and C_D and those predicted by published correlations are also provided. Because these solids do experience changes in their orientation, an analysis about the influence of the angle of incidence on the coefficient of resistance is done in the last part of the chapter.

Chapter 7 is formed by an exploratory study of the behaviour of irregular particles, which resemble a wood chip, as they move in stagnant liquids and inside a pipe-enclosed airflow. The challenges posed by the irregularity of the geometry on the motion are highlighted, and the advantages and limitations of the employed stereo technique to address them are discussed.

As mentioned before, Chapter 8 contains the conclusions and future work recommendations of this experimental thesis. First the conclusions corresponding to the applied image-based techniques are given, followed by those regarding the procedure used to measure the particle kinematics, dynamics, and orientation. Afterwards, the conclusions about the experimental works on spheres, disks, cylinders, and irregular particles are provided.

This thesis also includes seven appendices. The first five of them contain an explanation of the mathematical analyses and formulas required by the processes of camera calibration and 3D metric stereo reconstruction. In the sixth appendix, the calculation of the time derivatives, needed by the particle motion tracking methodology, through finite difference schemes is exemplified. Finally, in the seventh appendix the list of computer programs written in Matlab to execute all the mathematical operations posed by this investigation is given.

Chapter 2

LITERATURE REVIEW

Since the geometry of the particles is of paramount importance for the study of their motion, it has to be characterised in such a way that its effect on the motion can be preserved. Moreover, the characterising technique has to be able to deal with different shapes and produce parameters that allow the comparison between one shape and another. Therefore, this chapter begins with the revision of the most common methods of non-spherical particle characterisation for motion studies.

The chapter then continues with the revision of the already existing knowledge about the motion of single particles in a fluid. Detailed descriptions of the translational and rotational motions of spherical and non-spherical solids are given. Equations developed by both experimental and numerical approaches are illustrated, and empirical correlations to predict the coefficient of resistance and other parameters are also provided. In addition, the characteristics of the surrounding flow as well as the evolution of the secondary motions which have been reported in the literature are discussed.

Finally, the chapter ends with a review of the experimental techniques that have been employed by other researchers to study the motion of particles, both qualitatively and quantitatively. The application of stereo vision for 3D analyses, and the use of Schlieren photography to visualise the structures of the neighbouring fluid are also explicated. Additionally, a brief introduction to digital image processing is given as a basis for the more advanced topics of this field covered in Chapters 3 and 4.

2.1 GEOMETRICAL CHARACTERISATION OF A NON-SPHERICAL PARTICLE

From a geometrical point of view and according to their shape all particles can be broadly classified in two types: spherical and non-spherical, and in agreement with the ability of their geometry to be perfectly represented in mathematical form, non-spherical particles are further differentiated into regular and irregular. Thus, an irregular particle is defined as that solid whose exact geometry cannot be determined mathematically [36], [37].

The geometry of any particle, whether regular or irregular, is normally stated in terms of its size and shape; nevertheless, there is not a unique way to calculate both parameters since they can take different values depending on the characterising method employed. The size is usually expressed in function of certain diameter which can correspond to the one of an sphere or a circle that meets some physical or statistical requirements [38].

When measurements of the particle length on each of the three dimensions are available, then it is better to express its size in terms of an equivalent sphere, as shown in Figure 2.1. Care must be taken in selecting that sphere whose diameter definition is the most suitable one for the case under study. In contrast, when only two-dimensional representations (i.e. photographs) of the particle are available, the diameter of an equivalent circle or any other statistically predefined linear dimension can be chosen as the size descriptor, like the ones depicted in Figure 2.2.

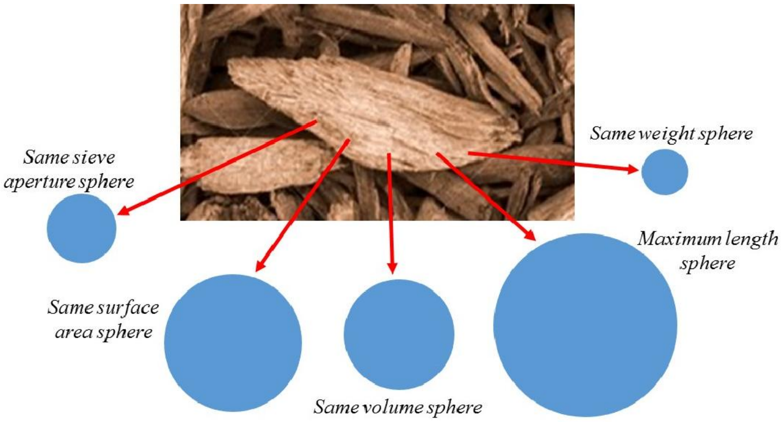

Figure 2.1 Different equivalent sphere definitions for a biomass irregular wood chip.

In Figure 2.2 the equivalent circle diameter refers to that circle whose area matches the area of the particle projected onto a planar surface. On the other hand, the Feret and Martin diameters do not result from a circle definition, but from a specific linear distance which is statistically measured. The first one corresponds to the distance between two parallel lines tangent to the particle on its extremes, and the second is the length of the bisecting line which splits the projected area into two other equal-area parts. These type of diameters are normally detected by optical microscopy.

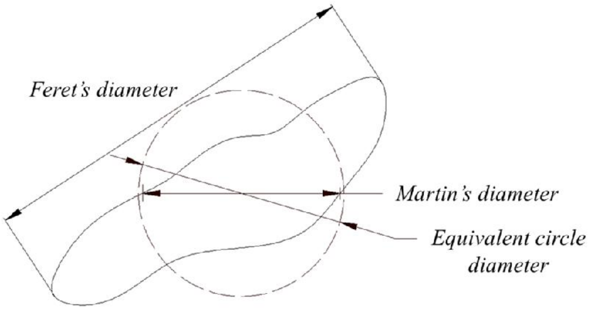

Figure 2.2 Equivalent circle definition and the statistical Feret and Martin diameters.

Wadell [39] was the first to use the same volume sphere concept to characterise irregularly shaped particles in aerodynamic studies. In his investigation about the coefficient of resistance and settling velocity of rock particles he suggested to approximate the volume ∀ of the solid as the product of its largest (*a*), intermediate (*b*), and smallest dimensions (*c*), all of them measured in mutually perpendicular directions (Figure 2.3). Thus, the equation he proposed to obtain the diameter of the equivalent same volume sphere is

$$d_n = \sqrt[3]{\frac{6\forall}{\pi}} \tag{2.1}$$

The quantity d_n is commonly known as the nominal diameter of the particle. Because the measurements to approximate the particle volume are relatively easy to do and if greater precision is required alternative ways to provide an accurate value of the particle volume, such as the Archimedes principle, are available, this diameter definition is the most used one in aerodynamics. Correspondingly, it is also chosen here to characterise the non-spherical particles employed in the work.

Whilst size provides the means to express dimension in one single number, shape constitutes the way to quantitatively describe the degree to which a non-spherical particle resembles a sphere. Its value can change from 0, for null similarity, to 1 for perfect matching. Based on the belief that any solid can be modelled as a sphere of the same volume but with deformed dimensions, Wadell [39] was again the first to provide a shape descriptor, the degree of sphericity $\emptyset$, defined as the ratio of the surface area S_V of a sphere having the same volume as the particle to the actual surface area S

$$\emptyset = \frac{S_V}{S} \tag{2.2}$$

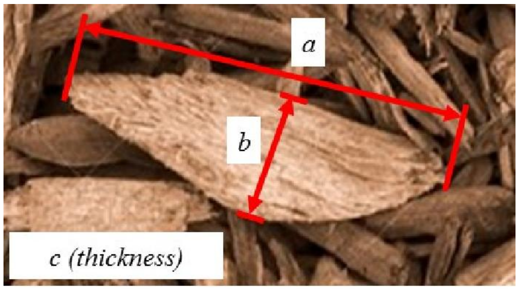

Figure 2.3 Largest, intermediate, and smallest particle dimensions.

The process of computing S accurately for an irregular particle constitutes a formidably complicated task, only achievable using three-dimensional imaging systems and extensive computing time. Lu et al. [40] developed a method to create a 3D model of an irregular sawdust particle by photographing it with three cameras to record the top, front, and side views of the solid. Once the model is finished, S and $\forall$ can be calculated. Bagheri et al. [41] also proposed the use of 3D laser scanning to generate a 3D representation of irregular particles larger than 5 mm, or scanning electron microscope micro-computed tomography (SEM micro-CT) for smaller sizes.

Despite its inherent limitations, however, two-dimensional analyses can still generate useful representations of the shape as long as the particle possess relatively small size [42]. For larger particles, a simple and faster estimation of $\emptyset$, according to Mandø et. al. [36], can be obtained from

$$\emptyset = \sqrt[3]{\frac{bc}{a^2}} \tag{2.3}$$

Another shape descriptor commonly found in the literature although less utilised in equations is the Corey shape factor [43], which is defined as the ratio of the smallest particle dimension to the square root of the medium and largest perpendicular dimensions

$$SF = \frac{c}{\sqrt{ab}} \tag{2.4}$$

By means of free-fall experiments it was later acknowledged that this parameter poorly correlates the fall velocity of the particle to that of a sphere for all sizes and shapes, therefore an improved form of the Corey shape factor which relates better with drag correlations was suggested by Loth [21]. It is known as the *max-med-min area,* A_{mmm}, and defined as

$$A_{mmm} = \frac{ab}{c^2} \tag{2.5}$$

Despite the disadvantages that the shape factor presents, it is still a considerably more convenient way to characterise an irregular particle because it does not involve complicated calculations or sophisticated three-dimensional visualisation arrangements. Furthermore, if the particles are relatively large to be observed by the human eye, the three dimensions *a, b* and *c* can be easily measured with a hand calibrator.

In order to extend the use of the shape factor, Dellino [44], and Dioguardi and Mele [23] proposed to improve it by recalculating it in a different way. They argued that an enhanced shape factor Ψ, suitable to describe irregular geometries, can be obtained through the division of the particle sphericity by its circularity χ, defined as the ratio between the true particle perimeter and the equivalent circle perimeter, thus

$$\Psi = \frac{\emptyset}{\chi} \tag{2.6}$$

In spite of the fact that Ψ seems to provide improved accuracy for calculations, the determination of χ can only be done through image processing methods. This further complicates the measurement process because a set of pictures of the particles, taken at different orientations, has to be digitally analysed in order to compute both perimeters.

A third particle geometry-describing parameter is the so-called *aspect ratio σ*. Even though it is the least employed one in the equations, it is extensively used as a classification tool given the simplicity of its calculation, which consists in dividing the major particle dimension by the minor one, as follows

$$\sigma = \frac{a}{c} \tag{2.7}$$

The shape descriptors explicated in this section are employed by most of the correlations to calculate the drag coefficient available in the literature, however, some equations require the definition of more complicated descriptors. The non-spherical particles used in this investigation were characterised through the nominal diameter, sphericity, and aspect ratio.

2.2 THEORY OF THE MOTION OF A SINGLE PARTICLE

2.2.1 TRANSLATION

Because the motion of a single particle in a fluid is dominated by the properties of both the solid and the fluid, then if the densities of both materials are different or if the particle size is larger than the smallest velocity gradient length scale of the fluid, the particle will alter the dynamics of the flow and become subject to different forces, such as drag, lift, inertia, and buoyancy [45]. In the situations where these characteristics are present, it is said that the particles are inertial [46].

The drag is simply defined as the resistance posed by the fluid to the movement of the particle. It results as consequence of the tangential force caused by the shear stress exerted over the whole particle surface and by the pressure difference between the front and rear sides of the particle. The drag force F_D is normally expressed by means of the drag coefficient through the next equation

$$C_D = \frac{F_D}{0.5 A_P \rho_f {V_P}^2} \tag{2.8}$$

where A_P is the area of the particle projected perpendicularly to the direction of F_D, ρ_f is the fluid density, and V_P is the velocity of the particle relative to the flow. Traditionally, it has been assumed that as the particle descends, there is a time when a balance between the forces of weight, buoyancy, and drag is attained, and the object no longer accelerates, but falls at constant terminal velocity. In such conditions, C_D can be determined from the force balance as follows

$$C_D = 2mg\left(1 - \frac{\rho_f}{\rho_p}\right) / \rho_f {U_T}^2 A_P \tag{2.9}$$

where m and ρ_p are the mass and density of the particle, respectively, and g is the acceleration due to gravity. Haider and Levenspiel [16] have published the following empirical correlation to predict the terminal velocity of a regular, symmetric, object in free-fall conditions

$$U_T = U_* \left[\frac{{\rho_f}^2}{g\mu(\rho_p - \rho_f)}\right]^{1/3} \tag{2.10}$$

with μ being the fluid dynamic viscosity. The quantity U_* corresponds to a dimensionless velocity which, for spheres, is defined as

$$U_* = \left[\left(\frac{18}{{d_*}^2}\right)^{0.824} + \left(\frac{0.321}{d_*}\right)^{0.412}\right]^{-1.214} \tag{2.11}$$

and for other geometries as

$$U_* = \left[\frac{18}{{d_*}^2} + \left(\frac{2.3348 - 1.7439\emptyset}{{d_*}^{0.5}}\right)\right]^{-1} \quad , \qquad 0.5 \le \emptyset \le 1 \tag{2.12}$$

The parameter d_* which appears in Equations (2.11) and (2.12) is a non-dimensional diameter, defined for both spherical and non-spherical objects as shown in the equation below

$$d_* = d_n \left[\frac{g\rho_f(\rho_p - \rho_f)}{\mu^2}\right]^{1/3} \tag{2.13}$$

So long as different terminal velocity conditions give rise to different particle Reynolds numbers Re_P, it is common practice to correlate the values of the drag coefficient with Re_P for the geometry under study, so that the so-called drag curve can be generated. Figure 2.4 shows the drag curve corresponding to a free-falling sphere, for which the particle Reynolds number is defined by the formula

$$Re_P = \frac{U_T d_n \rho_f}{\mu} \tag{2.14}$$

As it can be observed from Figure 2.4, different flow regimes may exist for the same geometry depending on what value the particle Reynolds number takes. In the figure, the narrow region to the left of the plot is known as the creeping flow regime and is governed by the law of Stokes, which for a sphere is written as

$$F_D = 3\pi d_n \mu V \tag{2.15}$$

The creeping flow criteria is valid for considerably low Reynolds numbers ($Re_P \ll 1$) and in this zone C_D and Re_P exhibit the inverse relation $C_D = 24/Re_P$, which is also true for non-spherical geometries [34]. From the same figure it can also be seen that the Stokes' law flow regime is correct until $Re_P \approx 0.3$ for spherical bodies. Similar drag curves can be found in the literature for cylinders, disks, cubes, spheroids, and other geometries, but not for entirely irregular particles.

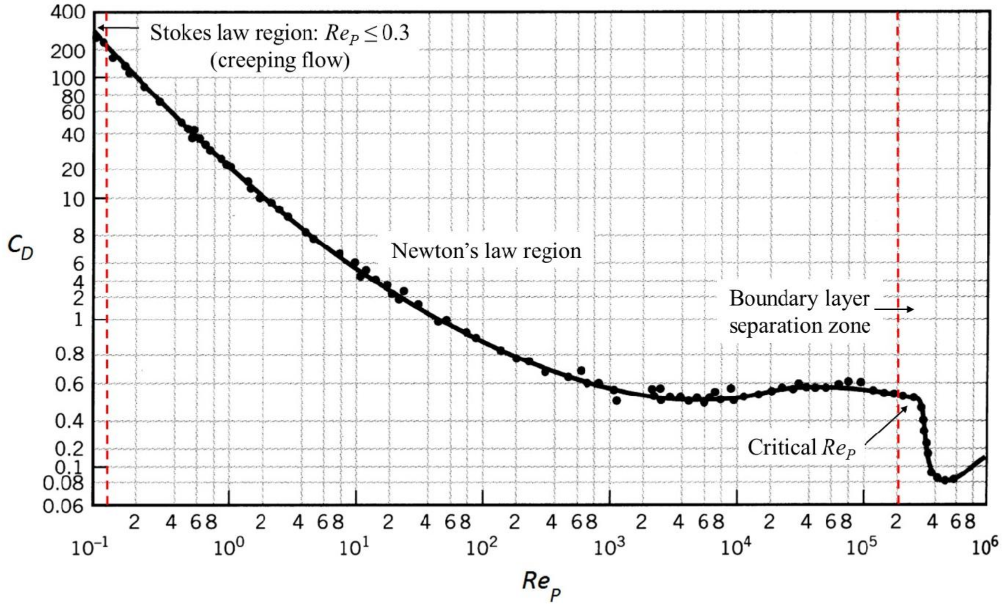

Figure 2.4 Standard drag curve for a sphere immersed in a moving fluid [47, 48].

Equation (2.9) was developed under steady-state conditions, where the most relevant forces are weight, buoyancy, and drag. Nonetheless, if different circumstances exist, another motion equation valid under any flow conditions has to be found. For the case of a relatively small and heavy sphere moving with velocity vector $\boldsymbol{V_P}$ in an arbitrary, incompressible flow field $\boldsymbol{u}$, at time t such general motion equation is

$$m\frac{d\boldsymbol{V_P}}{dt} = \left(m - m_f\right)\boldsymbol{g} + 3\pi D\mu(\boldsymbol{u} - \boldsymbol{V_P}) + m_f\frac{D\boldsymbol{u}}{Dt} + \frac{1}{2}m_f\frac{d}{dt}(\boldsymbol{u} - \boldsymbol{V_P})$$
$$-\frac{3}{2}\pi d^2\mu\int_0^t \frac{d(\boldsymbol{V_P} - \boldsymbol{u})/d\tau}{\left(\pi\mu(t-\tau)/\rho_f\right)^{1/2}}d\tau \qquad (2.16)$$

where m_f is the mass of fluid displaced by the particle, and τ is a time constant [49]. The left hand side of Equation (2.16) denotes the particle inertia, and the right hand side accounts for buoyancy, Stokes drag, pressure gradient, virtual mass acceleration, and the augmented viscous drag from the Basset history term. The derivative d/dt denotes the time derivative following the moving sphere whilst D/Dt expresses the time derivative following a fluid element, therefore the fluid acceleration for each notation system is

$$\begin{aligned}\frac{du_i}{dt} &= \frac{\partial u_i}{\partial t} + V_j\frac{\partial u_i}{\partial x_j}\\ \frac{Du_i}{Dt} &= \frac{\partial u_i}{\partial t} + u_j\frac{\partial u_i}{\partial x_j}\end{aligned} \qquad (2.17)$$

In Equation (2.16) it is assumed that neither chemical reactions nor electric or magnetic effects are present. In addition, not all of the terms involved have the same relevance since some might play a more important role than others. For the only purpose of aerodynamic studies, Lazaro and Lasheras [50] made a comparison of the orders of magnitude of each term by analysing the dispersion of water droplets in a turbulent free shear air flow and concluded that as long as the spherical particles remain small, it can be considered that the motion is mostly governed by drag.

Even though Equation (2.16) was developed for spheres, non-spherical particles with aspect ratios smaller than 1.70 can still be modelled using this equation, however for higher aspect ratios the particles must be analysed preserving their original shape or, at least according to the regular geometry they resemble the most [36]. Using Equation (2.16) as basis Yin et al. [12], and Mandø and Rosendahl [30] proposed the following equation to simulate the translational motion of large and regularly-shaped, non-spherical biomass particles in a Lagrangian framework

$$m\frac{d\boldsymbol{V_P}}{dt} = (m - m_f)\boldsymbol{g} + \boldsymbol{F_D} + m_f\frac{D\boldsymbol{u}}{Dt} + \frac{1}{2}m_f\frac{d}{dt}(\boldsymbol{u} - \boldsymbol{V_P}) + \boldsymbol{F_L} \tag{2.18}$$

where the left-hand side again expresses the particle inertia whilst the right-hand side contains, in order, the buoyancy, drag, pressure gradient, and virtual mass acceleration forces, respectively, plus an extra term, the aerodynamic lift $\boldsymbol{F_L}$. The drag force term was rewritten by the authors to account for the entire Reynolds number

$$\boldsymbol{F_D} = 0.5C_DA_P\rho_f|\boldsymbol{u} - \boldsymbol{V_P}|(\boldsymbol{u} - \boldsymbol{V_P}) \tag{2.19}$$

The lift arises as a result of the changes in the orientation of the particle during its trajectory and due to flow separation caused by both the non-sphericity and the velocity. Similar to the drag, the lift force is also defined in terms of another variable, the lift coefficient $\boldsymbol{C_L}$, through the following expression

$$C_L = \frac{F_L}{0.5A_{P,L}\rho_fV^2} \tag{2.20}$$

where $A_{P,L}$ is the particle projected area in the direction perpendicular to the lift force. From a close analysis to Equations (2.8) and (2.20) it can be observed that the values of the drag and lift coefficients can be modified by changes in the forces, orientation, and velocity, which in turn are entirely dependent on the geometry, the flow conditions, and the solid-fluid interaction. Therefore, it is recommended to study the motion keeping the original particle geometry, so its entire influence on the flow can be conserved. In fact, for values of σ larger than 1.70 the equivalent sphere assumption is not valid for non-spherical geometries [51].

2.2.2 DRAG AND LIFT CORRELATIONS

Because spheres can be geometrically described using only one dimension and since they always have a constant projected area, the coefficient of resistance can be solely expressed in terms of the particle Reynolds number

$$C_D = f(Re_P) \tag{2.21}$$

Nonetheless, for all the other shapes at least two parameters are needed for their geometrical description. Moreover, since those objects do not always project the same area in the direction of motion, therefore the dependence of the drag coefficient is normally written as

$$C_D = f(Re_P, shape\ descriptor\ ) \tag{2.22}$$

Different researchers have published empirical correlations obtained from both experimental and numerical analyses to calculate the drag coefficient as dictated by Equations (2.21) and (2.22) for spherical and non-spherical geometries, respectively. The most common equations are listed in Tables 2.1 and 2.2, correspondingly.

Table 2.1 Correlations to calculate the drag coefficient for spheres.

Year	Author	Equation	
1970	Clift and Gauvin [15]	$C_D = \frac{24}{Re_P}\left(1 + 0.15{Re_P}^{0.687}\right) + \frac{0.42}{1 + 4.25 \times 10^4 {Re_P}^{-1.16}}$ $Re_P < 10^5$	(2.23a)
1989	Haider and Levenspiel [16]	$C_D = \frac{24}{Re_P}\left(1 + 0.1806{Re_P}^{0.6459}\right) + \frac{0.4251}{1 + \frac{6880.95}{Re_P}}$ $Re_P < 2.6 \times 10^5$	(2.23b)
2005	Yow et al. [52]	$C_D = 0.3 + \frac{23.5}{Re_P} + \frac{4.6}{\sqrt{Re_P}}$ $Re_P < 2 \times 10^4$	(2.23c)
2013	Terfous et al. [35]	$C_D = 2.689 + \frac{21.683}{Re_P} + \frac{0.131}{{Re_P}^2} - \frac{10.616}{{Re_P}^{0.1}} + \frac{12.216}{{Re_P}^{0.2}}$ $0.1 < Re_P < 5 \times 10^4$	(2.23d)

From the inspection of the correlations of Table 2.2 it can be noticed that traditionally any non-spherical body is virtually converted into an equivalent sphere to compute its drag coefficient, and in some cases that transformation involves the calculation of complex parameters such as those required in Equation (2.24e). The utilisation of all those geometry-dependent factors also constitutes an effort to include the effect that the orientation of the body has on the drag force.

Table 2.2 Correlations to calculate the drag coefficient for non-spherical geometries.

Year	**Author**	**Equation**	
1989	Haider and Levenspiel [16]	$C_D = \frac{24}{Re_P}\left\{1 + \left[8.1716e^{-4.0655\emptyset}\right]{Re_P}^{0.0964+0.5565\emptyset}\right\} + \frac{73.69Re_P\left(e^{-5.0748\emptyset}\right)}{Re_P + 5.378e^{6.2122\emptyset}}$ Isometric particles, $Re_P < 2.5 \times 10^4$, $\emptyset \geq 0.67$	(2.24a)
1991	Swamee and Ojha [17]	$C_D = \left\{\frac{48.5}{\left[1 + 4.5(SF)^{0.35}\right]^{0.8}{Re_P}^{0.64}} + \left[\frac{Re_P}{Re_P + 100 + 1000(SF)}\right]^{0.32}\frac{1}{(SF)^{18} + 1.05(SF)^{0.8}}\right\}^{1.25}$ Irregular particles, $Re_P < 1 \times 10^4$, $0.3 \leq SF \leq 1$	(2.24b)
1993	Ganser [18, 20]	$C_D = \left\{\frac{24}{Re_PK_1K_2}\left[1 + 0.1118(Re_PK_1K_2)^{0.6567}\right] + \frac{0.4305}{1 + \frac{3305}{Re_PK_1K_2}}\right\}K_2$ $K_1K_2Re_P < 10^5$ K_1 is known as the *Stokes' shape factor* and K_2 as the *Newton's shape factor*. For isometric shapes K_1 is calculated as $K_1 = \left(\frac{1}{3} + \frac{2}{3\sqrt{\emptyset}}\right)^{-1}$ and for non-isometrics like $K_1 = \left(\frac{d_c}{3d_n} + \frac{2}{3\sqrt{\emptyset}}\right)^{-1}$ where d_c is the diameter of the corresponding *equal projected circular area*. On the other hand, K_2 has the same equation for both isometric and non-isometric bodies $K_2 = 10^{1.8148\chi}$ where $\chi = (-log\emptyset)^{0.5743}$	(2.24c)
1994	Chien [53]	$C_D = \frac{30}{Re_P} + 67.289e^{-5.03\emptyset}$ $Re_P < 5000$, $0.2 \leq \emptyset \leq 1$	(2.24d)

Table 2.2 cont. Correlations to calculate the drag coefficient for non-spherical geometries.

Year	Author	Equation	
2008	Hölzer and Sommer-feld [34]	$$C_D = \frac{8}{Re_P\sqrt{\emptyset_\parallel}} + \frac{16}{Re_P\sqrt{\emptyset}} + \frac{3}{\sqrt{Re_P}\emptyset^{3/4}} + \frac{0.4210^{0.4(-log\emptyset)^{0.2}}}{\emptyset_\perp}$$ $Re_P < 10^7$ where $\emptyset_\perp$, called the *crosswise sphericity*, is obtained by diving the projected area of the same volume sphere by the true projected area. Likewise, $\emptyset_\parallel$, named the lengthwise sphericity, is equivalent to the division of the projected area of the same volume sphere by the difference between half the true surface area and the mean longitudinally projected true projected area.	(2.24e)
2011	Chow and Adams [27]	$$C_D = \frac{1}{2}\left(1 + cos\sqrt{\frac{\rho_s/\rho_f}{\sigma}}\right) \qquad \sqrt{\frac{\rho_s/\rho_f}{\sigma}} < 1.5$$ $$C_D = \frac{\pi}{2} \qquad \sqrt{\frac{\rho_s/\rho_f}{\sigma}} > 1.5$$ Cylinder, $200 < Re_P < 6000$, σ is the aspect ratio	(2.24f)

In his modelling of the motion of particles by means of a master shape, called the super-ellipsoid, from which all other regular shapes can be derived, Rosendahl [11] incorporated the angular orientation of the solid in the estimation of C_D and suggested that it would vary according to the following relation.

$$C_D = C_{D,sel}(sin\alpha)^3 \tag{2.25}$$

where α is the angle of incidence of the particle, defined as the angle between the particle major axis and the undisturbed fluid velocity vector, which for free-falling cases can be approximated as the particle velocity vector (Figure 2.5), and $C_{D,sel}$ is the value of the drag coefficient when $\alpha = 90°$.

Although it is a direct approach to integrate the angular variation of non-spherical solids into the analysis, Equation (2.25) has not been validated experimentally. Aiming for an improved result, later, Mandø and Rosendahl [30] recommended the substitution of $(sin\alpha)^3$ in Equation (2.25) for just $sin\alpha$, thus

$$C_D = C_{D,sel}sin\alpha \tag{2.26}$$

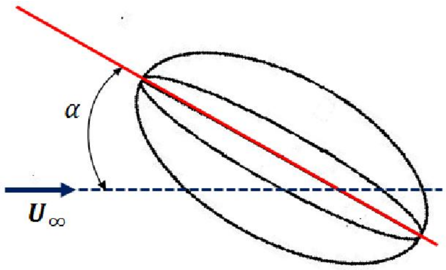

Figure 2.5 Angle of incidence of a non-spherical particle. The red line denotes the particle longest axis. $\boldsymbol{U}_\infty$ is the free-stream velocity vector.

Through a different approach to combine the already published empirical drag correlations (Table 2.2) with the effects of angular variation, in their simulation of cylindrical particle motion Yin et al. [12] assumed a constant value of C_D, computed with Equation (2.24c), and introduced the influence of α into the calculation of the projected area as shown

$$A_P = \pi r^2 \sqrt{(cos\alpha)^2 + (4\sigma/\pi)^2 (sin\alpha)^2} \tag{2.27}$$

where r is the radius of the cylinder and σ is the aspect ratio. Making use of an alternative framework, Zastawny et al. [28] simulated the motion of ellipsoids, disks, and cylindrical fibres held at different orientations with respect to the free-stream velocity, and obtained another trigonometric variation for the drag coefficient of the form

$$C_D = C_{D,\alpha=0} + \left(C_{D,\alpha=90} - C_{D,\alpha=0}\right) sin^{2.12}\alpha \tag{2.28}$$

where

$$\begin{aligned} C_{D,\alpha=0} &= \frac{a_1}{{Re_P}^{a_2}} + \frac{a_3}{{Re_P}^{a_4}} \\ C_{D,\alpha=90} &= \frac{a_5}{{Re_P}^{a_6}} + \frac{a_7}{{Re_P}^{a_8}} \end{aligned} \tag{2.29}$$

The values of the constants a_0 to a_8 can be found in the corresponding reference. Equation (2.28) is valid for $Re_P < 300$. Equations (2.25), (2.26) and (2.28) are the most obvious attempts to introduce the influence of α on C_D that can be found in the literature, nevertheless, they have the disadvantage of keeping the particles fixed, restricting therefore the free interaction between the solid and the fluid.

As for the drag, the lift force also needs to be determined. Yet, because it often is smaller than the drag by one or more orders of magnitude, its calculation is commonly omitted, hence few works with correlations to compute the lift coefficient are available in the literature. By neglecting any lift contributor other than the aerodynamic lift product of the particle orientation changes, Rosendahl [11] and Yin et al. [12] made use of the crossflow principle of Hoerner [54], valid in the interval $0 < Re_P < 1000$, to suggest the following relation to estimate the lift force in their numerical models

$$\boldsymbol{F_L} = (sin\alpha)^2 cos\alpha \boldsymbol{F_D} \tag{2.30}$$

In an effort to enhance the simulation results Mandø and Rosendahl [30] proposed a similar expression including as well some dependence of the lift coefficient on the particle Reynolds number in the interval $30 < Re_P < 1500$

$$C_L = \frac{(sin\alpha)^2 cos\alpha}{0.65 + 40{Re_P}^{0.72}} C_D \tag{2.31}$$

The crossflow principle of Hoerner was originally developed for cylinders positioned at some oblique angle to the direction of a uniform and steady flow [55]. Therefore, the application of Equations (2.30) and (2.31) to non-cylindrical geometries or unsteady flow conditions has to be done with care. Zastawny et al. [28] also published an alternative equation to determine the lift coefficient, written as follows

$$C_L = \left(\frac{b_1}{{Re_P}^{b_2}} + \frac{b_3}{{Re_P}^{b_4}}\right)(sin\alpha)^{b_5 + b_6 {Re_P}^{b_7}} (cos\alpha)^{b_8 + b_9 {Re_P}^{b_{10}}} \tag{2.32}$$

where the terms enclosed within the first parenthesis provide the magnitude of C_L whilst the trigonometric functions only describe its dependence on the angle of attack. The values of the constants $b_0, \ldots, b_8$ can be found in the cited reference for each of the geometries they studied. It is claimed that Equation (2.32) provides good results for all the investigated particle shapes at any value of Re_P and α, respectively, though it has not been contrasted with experimental investigations. Similar to Equation (2.28), the validity of Equation (2.32) extends to $Re_P < 300$.

A radically different method which avoids the use of α in the prediction of the lift coefficient was proposed by Krueger et al. [56]. In their experimental study of the motion of free falling regular and irregular solids with the assistance of stereo vision, they treated the vector difference of the velocity at two successive positions as the outcome of the lifting effect and advised the use of the next formula to compute the lift coefficient

$$C_L = \frac{2m\left(\frac{\Delta V_L}{\Delta t} + g_L\right)}{\rho_f A V} \tag{2.33}$$

where ΔV_L is the magnitude of such vector difference, g_L is the gravity acceleration component in the direction of the lift, Δt is the period of time taken by the particle to move from position 1 to position 2, and A is the arithmetic average of the particle surface areas visible to the cameras. Since the visible surface area varies due to the changes in orientation, it could be said that the effect of α is already included in A.

Although Equation (2.33) constitutes one of the few recent experimental approaches to lift calculation, its output was not compared against the results from other works. Furthermore, the particle velocity change between two consecutive points may be due to other reasons rather than lift, thus the employment of ΔV_L is not be properly justified.

2.2.3 ROTATION

Up till now the discussion has been centred on the aerodynamic forces of drag and lift, however any rotation of the particle will also induce torques which cannot be included in Equation (2.18) since it applies exclusively for translational motion. Based on the free-body diagram of Figure 2.6, a set of equations to describe the particle rotational motion around the three axes $X'Y'Z'$ can be formed. Notice that X' is always along the direction of the largest particle dimension. Then, if $\omega_{X'}$, $\omega_{Y'}$, $\omega_{Z'}$ are the angular velocities, and $M_{X'}$, $M_{Y'}$, $M_{Z'}$ denote the torques with respect to each axis, it can be written

$$M_{X'} = I_{X'}\frac{d\omega_{X'}}{dt} - \omega_{Y'}\omega_{Z'}(I_{Y'} - I_{Z'}) \tag{2.34}$$

$$M_{Y'} = I_{Y'}\frac{d\omega_{Y'}}{dt} - \omega_{Z'}\omega_{X'}(I_{Z'} - I_{X'}) \tag{2.35}$$

$$M_{Z'} = I_{Z'}\frac{d\omega_{Z'}}{dt} - \omega_{X'}\omega_{Y'}(I_{X'} - I_{Y'}) \tag{2.36}$$

where $I_{X'}$, $I_{Y'}$, and $I_{Z'}$ are the moments of inertia of the solid [12]. Thus, Equation (2.18) define the translational motion in the fixed world reference frame $X_W Y_W Z_W$ whilst Equations (2.34 – 2.36) describe the rotational motion, expressed in the particle frame $X'Y'Z'$. Since this latter frame changes every time there is a change in the angular orientation, a mathematical relation between both frames is required.

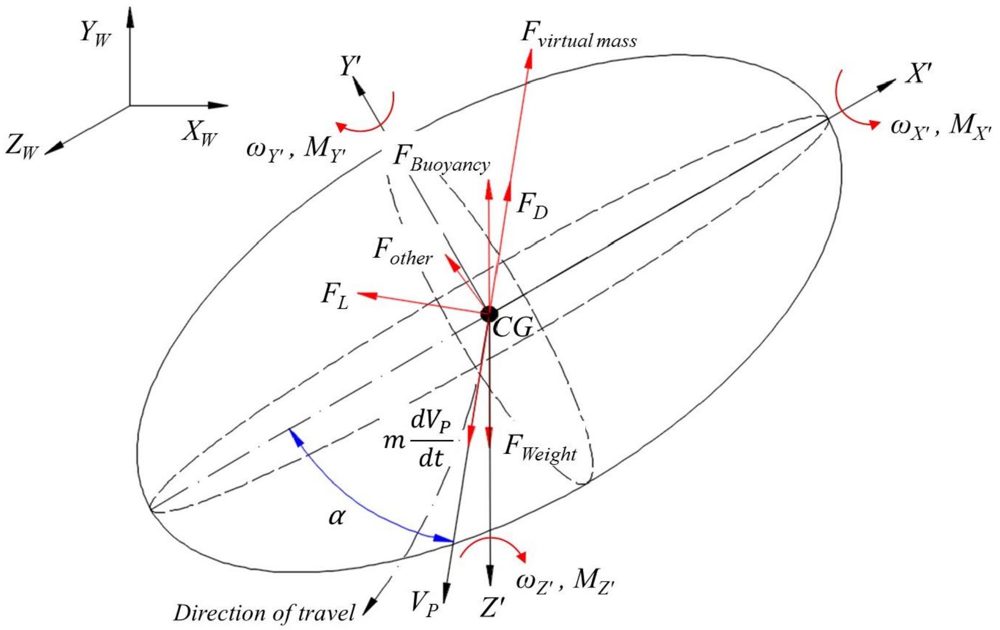

Figure 2.6 Forces and moments acting on a non-spherical particle. *CG* = centre of mass.

The moment of inertia of a solid represents its resistance to angular acceleration around the axis of rotation, and is defined as the sum of the moments of inertia of each differential mass component of the solid, where in turn, each of them is calculated as the product of the mass component times the distance from the respective axis squared. For every particle geometry and every axis of rotation there exists a moment of inertia, which can be accurately calculated as long as the shape of the body is regular. The calculation formulas can be found in any dynamics textbook. For instance, the moments of inertial of the ellipsoid of Figure 2.6 are

$$I_{X'} = \frac{m}{5}(b^2 + c^2)\ ;\ I_{Y'} = \frac{m}{5}(a^2 + c^2)\ ;\ I_{Z'} = \frac{m}{5}(a^2 + b^2)$$

where a, b, and c denote the lengths of the semi-axes along the X', Y', and Z' directions, respectively. The computation of the moment of inertia of an irregular geometry is more complicated and can only be approximated through integral calculus expressions.

2.2.4 SECONDARY MOTION

The relevant parameters characterising the motion of a single particle within a fluid have already been described, nonetheless the patterns of the flow around the solid have not been addressed yet. In general, they cannot be expressed in terms of quantitative data, thus they have to be analysed qualitatively through visualisation methods.

In the case of spheres, the flow around them show different behaviours depending on the value of the Reynolds number. According to Magarvey and Bishop [57], and Magarvey and MacLatchy [58], for a free falling sphere, the streamlines remain symmetrical and attached to the body up to $Re_P = 10$, to form then a stable, symmetrical circulation zone at the rear part of the sphere which lasts up to $Re_P = 210$, as illustrated in Figure 2.7. It should be remarked that for the case of a rigidly held sphere exposed to crossflow the starting point of flow separation occurs approximately at $Re_P = 24$ [32, 59, 60].

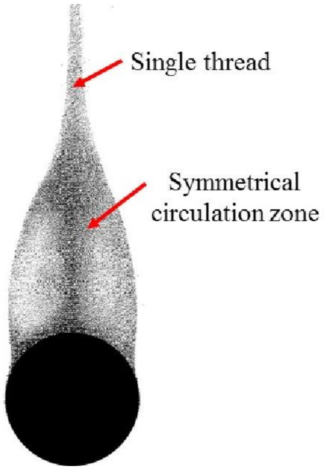

Figure 2.7 Symmetrical wake behind a liquid droplet at $Re_P = 170$ [57].

The stability and symmetry of the circulation zone decreases as Re_P augments, causing the sphere deviate from a vertical settling path. The asymmetry causes a sidewise force which can be understand as lift. In addition, at $Re_P = 210$ the single thread disappears and two parallel threads appear, as shown in Figure. 2.8. Furthermore, at $Re_P = 270$ and up to $Re_P = 290$, regularly spaced wavy patterns form in the trail left by the sphere (Figure 2.9).

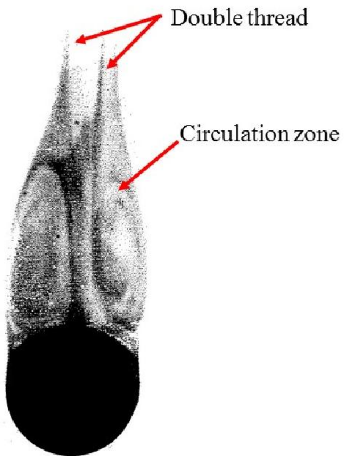

Figure 2.8 Wake behind a liquid droplet at $Re_P = 220$ [57].

At $Re_P > 290$ there is no more symmetry in the circulation zone and the process of vortex shedding appears. It has been reported that for a rigidly held sphere the vortex shedding appears at $Re_P = 270$. The vorticity is transferred to the fluid stream in the form of two periodic, parallel vortex trails (Figure 2.10), also known as hairpins. The regularity of the hairpin vortex shedding remains up to $Re_P = 700$, and approximately at $Re_P = 1000$ the wake behind the sphere becomes totally turbulent, as shown in Figure 2.11.

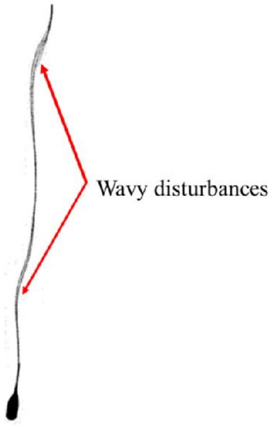

Figure 2.9 Wavy trail left by a free-falling liquid sphere at $270 < Re_P < 290$ [57].

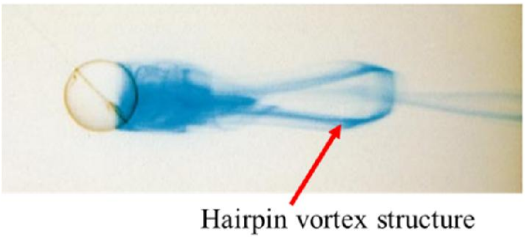

Figure 2.10 Dye visualisation of the structure of a hairpin vortex shedding from a fixed sphere at $Re_P = 300$ [59].

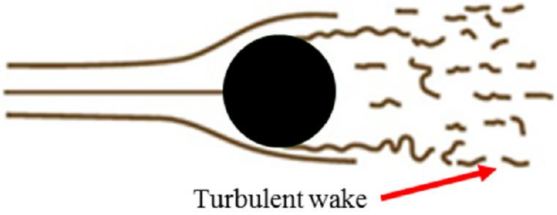

Figure 2.11 Turbulent wake behind a fixed sphere at $Re_P = 1000$ [61].

Experimental visualisations of the neighbouring flow around free falling objects of non-spherical shape are scarce in the literature, however it is assumed that, likewise for spheres, at considerably small values of Re_P there is no flow separation. Then, as Re_P increases, the phenomena of flow separation, recirculation, and vortex shedding appear, with regular characteristics in the beginning, to gradually evolve into turbulent irregular configurations. In all the cases, there is a strong relation between the vortex shedding pattern and the pressure distribution in the wake, and it is believed that this radically affects the orientation of the particle and the form of its trajectory [26, 27].

Marchildon et al. [25] reported that a free-settling cylinder falls with fixed orientation, projecting its maximum area perpendicularly to the main motion direction, so long as $Re_P < 80$. Once this value is exceeded, some regular oscillation may accompany the fall-path; nonetheless, they said that oscillation was always present for $Re_P > 300$, and undoubtedly proposed that the vortex shedding configuration was responsible for this secondary motion. Figure 2.12 displays the observed oscillation pattern. They also affirmed that any free-moving particle will always achieve the same corresponding type of terminal flow, suggesting that any effect derived from the particle dropping method can be neglected.

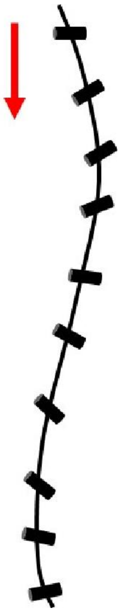

Figure 2.12 Regular oscillation in a free-falling cylinder at $Re_P > 300$ [25].

Chow and Adams [27] also found the same oscillation type described in the previous paragraph, and attributed the causes to the bending provoked on the cylinder orientation every time a vortex is released. They suggested that such an orientation change modifies the pressure distribution along the body, which in consequence gives rise to a resultant torque that tends to return the particle to its horizontal position, as depicted in Figure 2.13. They also reported that when $\sqrt{\rho_P D/\rho_f L} > 1.5$, besides oscillation the secondary motion will also include some tumble, and for $\sqrt{\rho_P D/\rho_f L} \sim 2$ tumbling dominates the secondary motion. The equations they recommended to calculate the torque and projected area are

$$M = 0.35(\rho_P - \rho_f) g D^2 L \times d_{off} \tag{2.37}$$

$$A_P = LDcos\alpha \tag{2.38}$$

where d_{off} is the distance between the centroid and the centre of pressure, and is calculated within 10% of precision in the range $0° < \alpha < 90°$ through the following equation

$$d_{off} = 0.75 sin\alpha (4 + \pi cos\alpha) L \approx 0.12 \alpha L \tag{2.39}$$

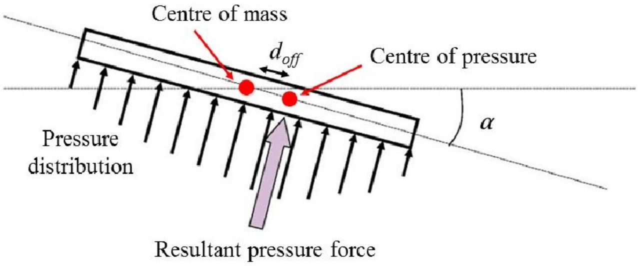

Figure 2.13 Schematic of the effect of angular deflection on a falling cylinder [27].

Stringham et al. [26] investigated the behaviour of the drag coefficient for relatively large aluminium and lead disks into quiescent mixtures of water and glycerine, and noticed that for $Re_P > 300$ the influence of shape on the pressure distribution gave origin to different patterns of fall (Figure 2.14 and Table 2.3), which they classified as follows:

i. Steady regime, described by a steady-flat fall of the disk with the maximum projected area perpendicular to the motion direction (Figure 2.14a),

ii. Transition regime, in which the disk can fall with regular oscillation (Figure 2.14b) or with a combination of oscillation, gliding, and tumbling (Figures 2.14c and 2.14d),

iii. Tumble regime, characterised by a uniform tumble and nearly constant angular rotation (Figure 2.14e).

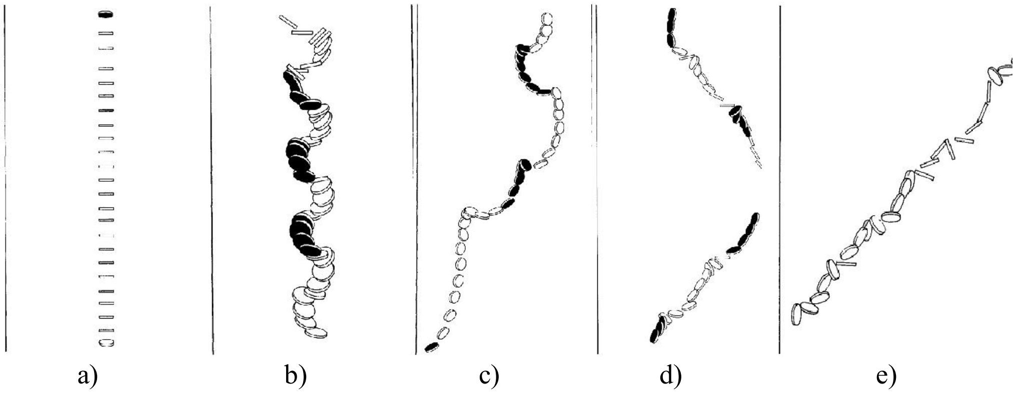

Figure 2.14 The four fall patterns for free falling disks: a) Steady-flat; b) Regular oscillation perpendicular to the fall direction; c) Just entering the oscillation, gliding, and tumbling; d) Just leaving the oscillation, gliding, and tumbling; e) Tumble, almost 360° rotation at nearly constant angular velocity [26].

Table 2.3 Path parameters of each of the disk-fall patterns shown in Figure 2.14 [26].

Fall pattern	**Material**	d_P **(cm)**	V **(m/s)**	Re_P	C_D
Steady-flat (a)	Lead	2.54	0.420	38	2.0
Regular oscillation (b)	Aluminium	3.81	0.471	1092	0.46
Just entering oscillation, gliding and tumbling (c)	Aluminium	2.54	0.585	17900	0.26
Just leaving oscillation, gliding and tumbling (d)	Lead	3.81	0.951	300	0.60
Tumble (e)	Lead	2.54	0.668	16800	1.02

The results of the coefficient of resistance they calculated were reported graphically and are shown in the $C_D - Re_P$ diagram of Figure 2.15, where it can be distinguished that after certain value of Re_P, the density ratio ρ_P/ρ_f between the solid and the fluid exerts an important influence on C_D, causing a subdivision in the $C_D - Re_P$ curve. They said that the upper branch corresponds to disks with high density ratios, whilst the lower branch is for low ones [26]. Nonetheless, they did not provide a quantity of reference on which a disk can be classified as with high or low density ratio.

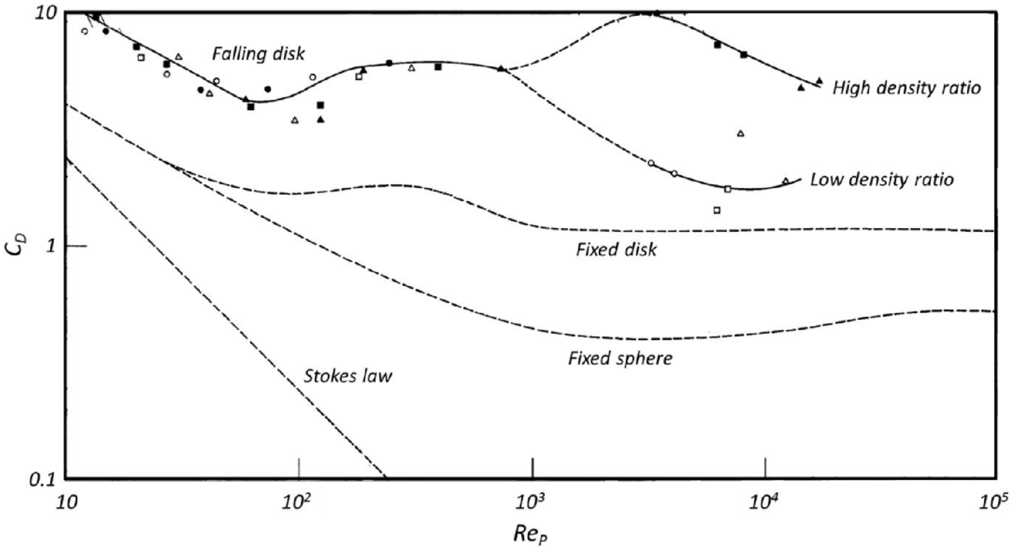

Figure 2.15 $C_D - Re_P$ relationship for a free falling disk. Stokes equation and drag curves for a fixed sphere and disk are also included for comparison [26].

Chow and Adams [27], and Bagheri and Bonadonna [24] have also emphasised that the secondary motions have a direct effect on the magnitude of the drag coefficient of a settling particle of regular shape. Moreover, based on this fact, it is believed that irregular particles will exhibit a similar behaviour as long as secondary motions are present, however, it cannot be affirmed that such motions will be as well-defined as for a regular solid because of the nature of their shapes.

2.3 EXPERIMENTAL TECHNIQUES FOR SINGLE PARTICLE MOTION RESEARCH

2.3.1 2D AND 3D QUANTITATIVE TECHNIQUES

As it was previously stated, in the study of the motion of particles immersed in a fluid it is vital to give them the chance to move freely so that the interaction between the solid and the fluid is not obstructed. The only possible way to meet this requirement is by using non-intrusive measuring techniques. Experimental alternatives to this method comprise keeping the solid fixed to some structure which in turn can either move through the fluid at certain velocity or remain static whilst the fluid travels at the desired speed. However, these alternatives may lead to an invalid estimation of the motion parameters since they disturb the free particle-fluid interaction [35].

So long as in this thesis, the interest is placed exclusively on the motion of single particles, techniques such as Particle Image Velocimetry (PIV), and cross correlation using electrostatic, capacitive, or optical sensors, were discarded because they are designed to operate with multi-particle environments, despite the ability to track the velocity of the solids they have shown in previous studies [62-66]. The algorithms and methods of analysis of these techniques work only if there is a relatively large number of particles involved in the motion. They cannot track the velocity if there is only one. On the other hand, Laser Doppler Velocimetry (LDV) has been successfully applied by Lu et al. [67] to determine the velocity of individual glass beads in a pneumatic conveying installation operating at dilute phase, nonetheless due to its high cost it was not considered here.

Because of its versatility and lower price, the direct imaging with a high-speed camera constitutes the simplest and most used approach for particle motion research. In the last decade, Yin et al. [12] and Chow and Adams [27], with the assistance of only one camera, analysed the oscillatory motion of a cylinder in free fall within a 2D context. In addition, following a similar route, Terfous et al. [35], and Dioguardi and Mele [23] investigated the drag exerted on smooth and rough, spherical and non-spherical particles as they settled in a liquid column. The installation they used is depicted in Figure 2.16.

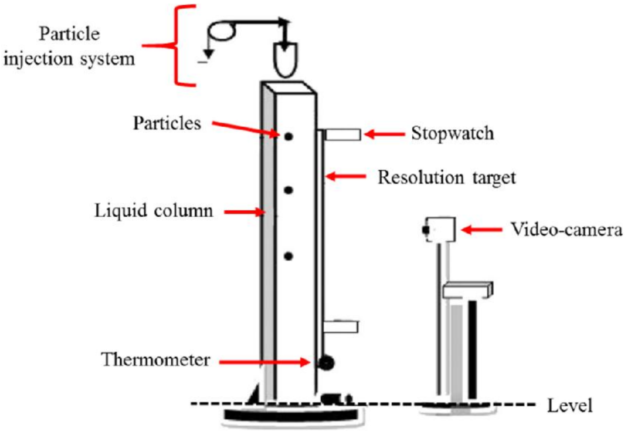

Figure 2.16 Experimental installation used by Terfous et al. [35].

In an effort to study the phenomenon in three dimensions, other researchers have employed a second camera positioned at right angle with respect to the first one in order to record as well the motion in a perpendicular plane. Stringham et al. [26] applied this configuration in their study of the settling of relatively large particles. The experimental rig they employed is depicted in Figure 2.17. Although this approach offers a straightforward and comparatively easy way to meet the 3D condition, it requires a remarkably precise alignment of the cameras so that the precise tracking of the particle coordinates can be achieved.

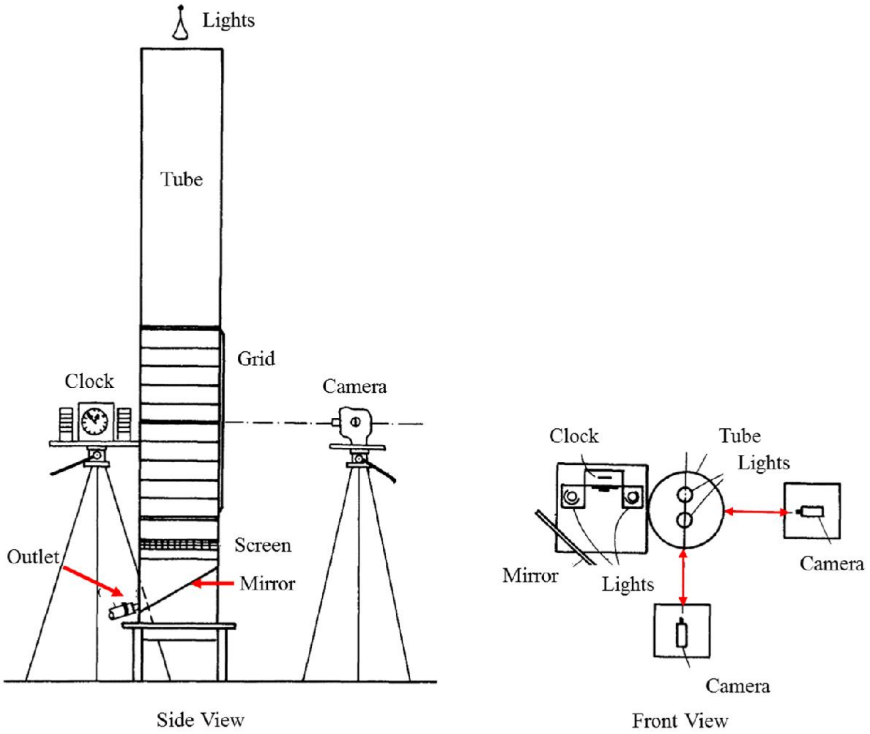

Figure 2.17 Experimental rig used by Stringham et al. [26].

The 3D configuration mentioned in the previous paragraph can still be accomplished with only one camera, if, instead of photographing the particle directly, the camera records the images of both the front and normal motion planes collected by a group of mirrors carefully situated, such as the one illustrated in Figure 2.18, which was employed by Veldhuis et al. [68-70] to study the motion of freely rising and falling spheres. Marchildon et al. [25] also used the same principle to analyse the secondary motion of a settling cylinder.

An alternate route for three-dimensional analysis is offered by applying the principle of two-camera stereo vision, which consists on obtaining the 3D information of a scene given two views of it taken from slightly different points of view. This principle has been recently used by Krueger et al. [56] to measure the drag coefficient of irregular shape, waste-derived fuel solid particles, as displayed in Figure 2.19. A disadvantage of stereo vision is that every camera employed in the study has to be calibrated with respect to a frame of reference.

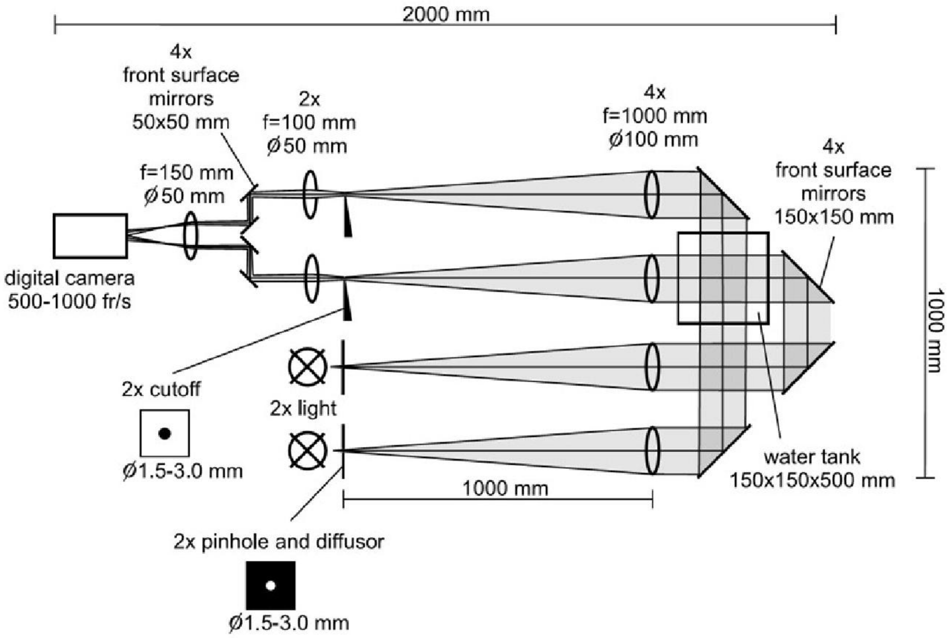

Figure 2.18 Experimental setup employed by Veldhuis et al. [68-70].

Stereo vision is the process by which human beings are able to see objects in three-dimensions, as depicted in Figure 2.20, where it can be perceived that due to their proximity to each other, every eye gets an image of the same object from at slightly different angle of view. The then brain processes those two pictures to produce a view in 3D, adding the perception of depth. Computer stereo vision can be understood in a similar way by replacing each eye with a digital camera and the brain with a computer program.

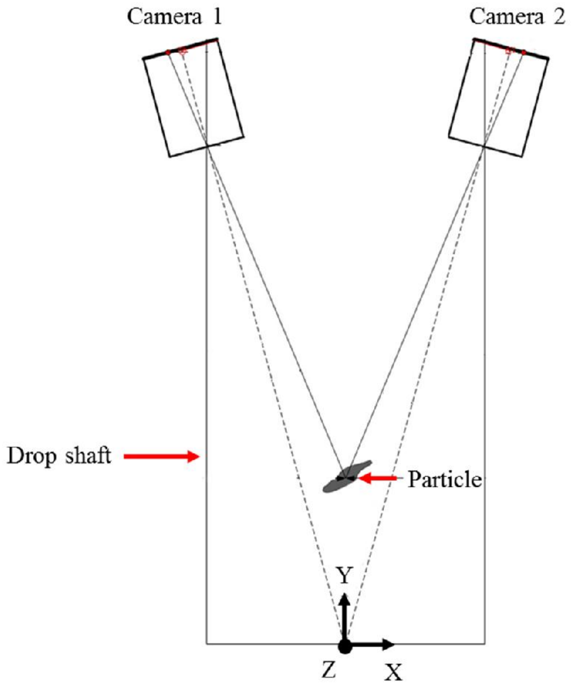

Figure 2.19 Experimental installation used by Krueger et al. [56].

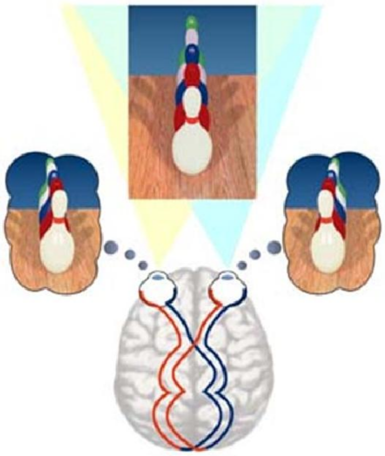

Figure 2.20 Human stereo vision.

The creation of stereo vision can be greatly simplified by employing only one camera coupled to a stereo adapter, which is a compact arrangement of four mirrors that can easily be attached to the camera lens, as shown in Figure 2.21. Through this configuration, the problems of misalignment are minimized, though at the expense of a reduced field of view [71]. Nevertheless, due to simplicity reasons and because of its great versatility, this is the approach chosen for the 3D particle motion studies of this thesis, and is revised in-deep in Chapter 3.

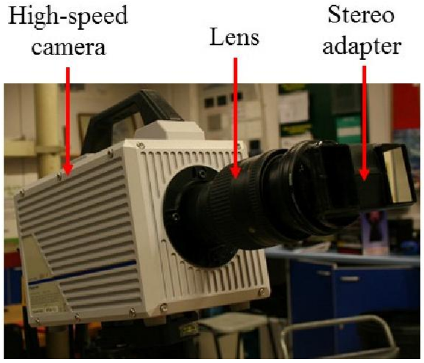

Figure 2.21 Camera attached to a stereo adapter.

Binocular stereo vision has been actively used since the last decade as a 3D measuring tool for different physical magnitudes such as linear distances, size of objects, instantaneous velocities, as well as for computing 3D particle and bubble trajectories [56, 68-70, 72-75]. It has also been successfully applied to the investigation of the structure of combustion flames [76-78] and the dynamics of a bursting bubble [79]. For the present work, it is employed to track the instantaneous 3D position and angular orientation of the particles as they travel through the fluid.

Up to this point all of the experimental installations have consisted on columns or tanks where the solid settles freely, however, according to Bagheri et al. [24, 80] the aerodynamic behaviour of single particles can also be investigated in vertical wind tunnels, such as the one they proposed in Figure 2.22. Moreover, this type of setup allows the study of the motion at significantly high particle-fluid density ratios without the necessity of employing considerably tall dropping columns. Nonetheless, since the secondary motions determine the orientation changes of a settling non-spherical object, and given the fact that the authors did not report the existence of any secondary motion in the wind tunnel experiments, it is not clear whether the angular variation exhibited by a non-spherical solid falling freely in a tank is the same as if it were suspended in the wind tunnel.

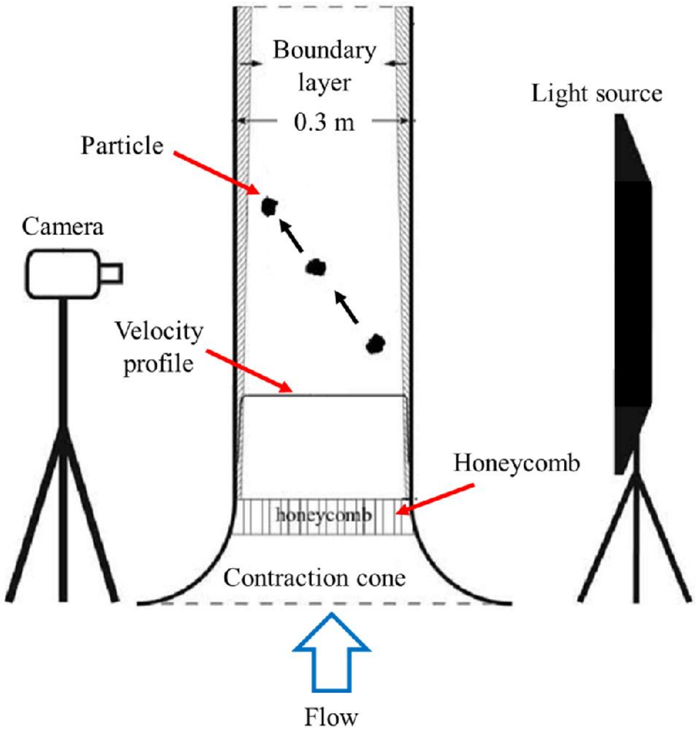

Figure 2.22 Wind tunnel for single particle motion studies [80].

2.3.2 DIGITAL IMAGE PROCESSING

Independently of the measuring technique employed, as long as the data is in the form of digital images, they need to be enhanced before any further analysis is attempted. Enhancement is done to improve the quality of the images by removing noise and any other undesired effect they may contain. The most common method to accomplish this task is through digital image processing, which treats each picture as a matrix of real numbers where the rows and columns represent the spatial coordinates, and the value of each element denotes the level of light intensity at each location [81], as illustrated in Figure 2.23.

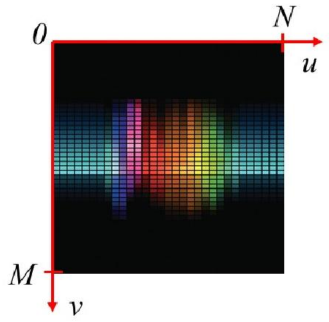

$$f(u,v) = \begin{bmatrix} f(0,0) & f(0,1) & \cdots & f(0,N-1) \\ f(1,0) & f(1,1) & \cdots & f(1,N-1) \\ \vdots & \vdots & \cdots & \vdots \\ f(M-1,0) & f(M-1,1) & \cdots & f(M-1,N-1) \end{bmatrix}$$

Figure 2.23 Digital image and its matrix representation. *M* and *N* denote the size.

In the field of particle motion, digital image processing has already been extensively used to determine the size and shape of both static and moving particles, as well as to calculate parameters such as the velocity or mass flow rate [74, 82-87]. Therefore, in the present research not only it was applied to improve the quality of the recorded stereo pictures but also to get quantitative information about the position and orientation of the solids at every instant.

The main advantage of using digital image analysis relies on the fact that it offers the possibility to highly automate the work when a large number of particle pictures have to be processed. Moreover, thanks to the enhancement operations, the instantaneous locations of the particles can be obtained with improved resolution and precision. The image processing tasks employed here for the purpose of particle motion are explicated in Chapter 4. Additionally, in this thesis, digital image processing was also used to assist on the calibration of the cameras, and the operations involved in such a task are described in Chapter 3.

2.3.3 SCHLIEREN VISUALISATION

Whenever there are variations in the density of a compressible fluid due to temperature changes, the value of the refractive index suffers alterations too, therefore any light ray that passes through the fluid is deflected. Furthermore, if the deflected rays are captured on a recording plane, as indicated in Figure 2.24, and contrasted with an undisturbed ray, some information about the flow can be obtained from the geometrical differences between both rays.

In Figure 2.24, ΔX and ΔY are the horizontal and vertical components, respectively, of the linear displacement Δ from point P to P'. Likewise, ε_X and ε_Y are the components of the angular deflection ε. Because of Δ the light intensity at P is null whilst that at P' is double, thus P is a dark point and P' a bright point. Moreover, the collection of all the dark points form an image of the fluid regions with density gradients, and through the dark and bright patterns the flow motion can be illustrated. This flow visualisation technique is named shadowgraph.

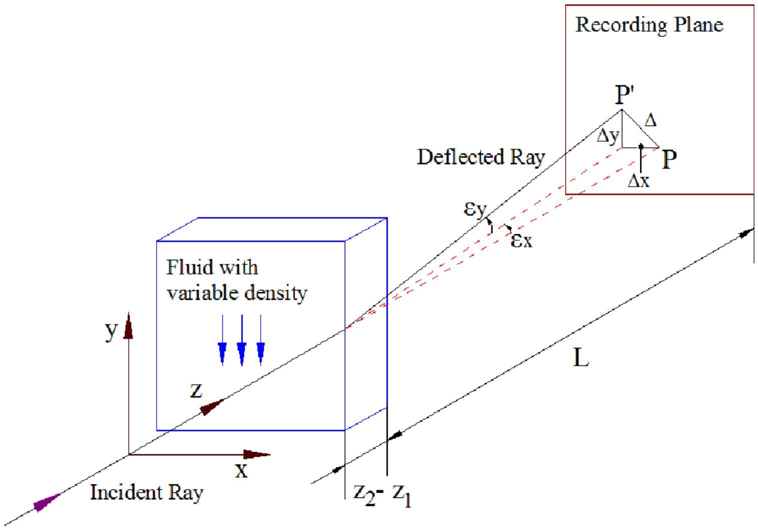

Figure 2.24 Deflection of a light ray due to changes in the fluid density [88].

In the field of particle motion, Shahi and Kuru [89, 90] have employed shadowgraphs to determine the size, shape, and velocity of irregular grains of sand as they settle in a fluid. However, because density gradients did not exist in their work, visualisations of the motion were not captured. In Figure 2.25, the shadowgraph of one of the sand particles they used is illustrated. It can be noticed, that no revelation of the surrounding fluid structure was achieved.

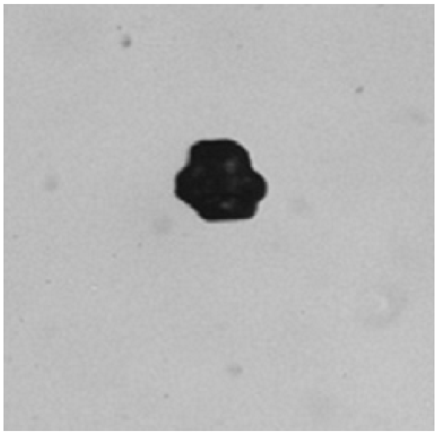

Figure 2.25 Shadowgraph of an irregular grain of sand in free fall [89].

The typical installation employed to take shadowgraph pictures is schematized in Figure 2.26, where the first spherical lens collimates the rays coming from the light source and the second one collects them for the camera imaging lens. It is recommended that the light source should be as small as possible and of high intensity.

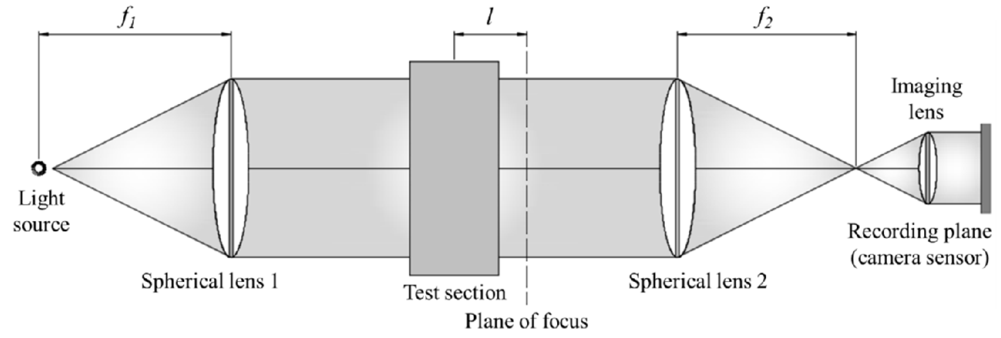

Figure 2.26 Setup for shadowgraph photography.

Now, if an obstruction, traditionally called knife edge, is set at the focal point of the second spherical lens, as depicted in Figure 2.27, to stop the deflected light rays from reaching the recording plane, a uniform reduction in the brightness of the whole picture is generated. This is the known as the Schlieren effect. Hence, it can be said that whilst shadowgraph is sensitive to Δ, Schlieren is sensitive to ε.

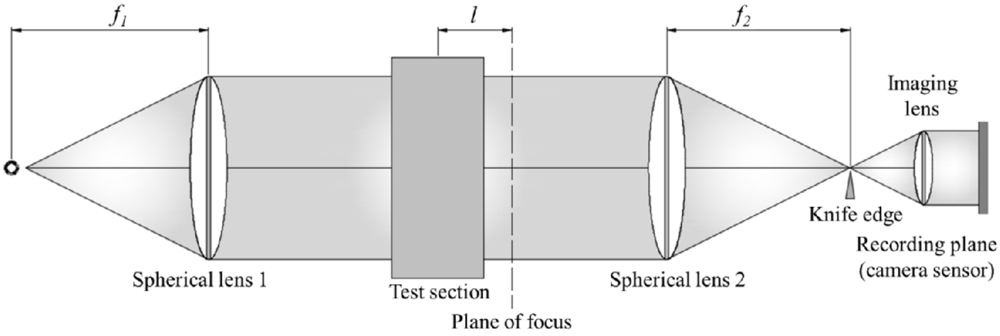

Figure 2.27 Conventional setup for Schlieren photography.

An alternative configuration to capture Schlieren images is by means of the so-called Z-type Schlieren setup, illustrated in Figure 2.28. This configuration was employed in this thesis to visualise the structures of the flow surrounding the falling particles. However, some modifications, explained in Section 5.2, were done to improve the magnification of the system.

In spite of the fact that Schlieren photography as diagnostic technique has been commonly used for compressible flows only, its application can be extended to studies in water provided that a regular small temperature gradient exists in the test section [68, 91, 92]. In fact, according to Fiedler and Nottmeyer [91] a temperature difference as low as $\Delta T \sim 0.6$ C° can be enough. In Figure 2.29, it is shown the Schlieren image they reported for a hemisphere falling in pre-heated water with that ΔT. The temperature gradient was accomplished by heating the surface of the water contained in the dropping tank. Veldhuis et al. [68] have also employed a similar approach to visualise the flow around rising and falling spherical objects in water.

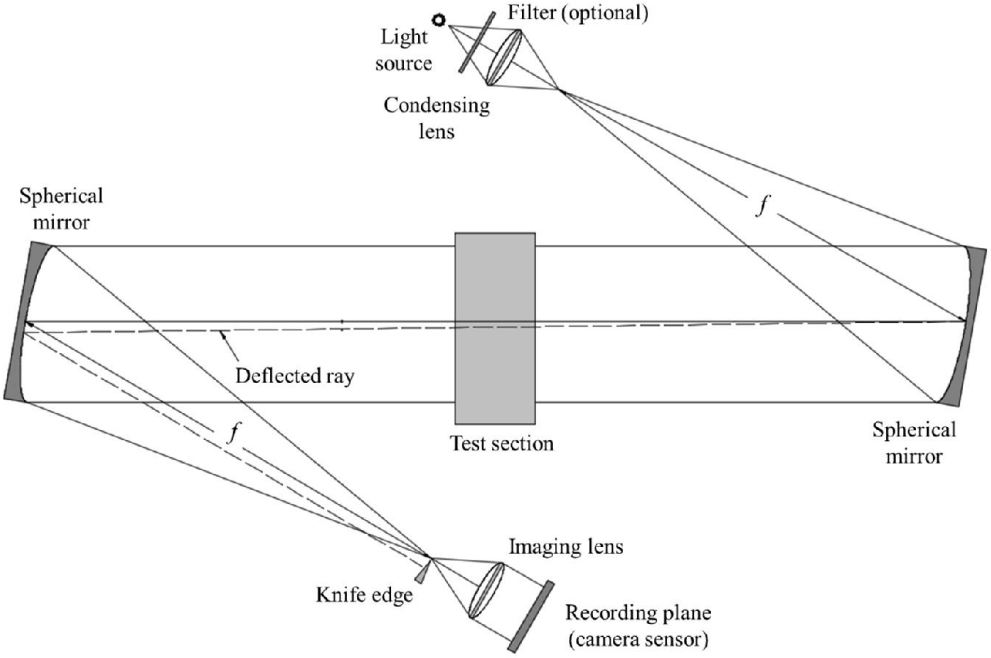

Figure 2.28 Conventional Z-type Schlieren setup.

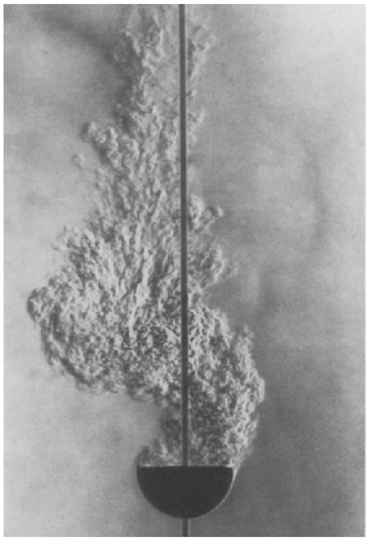

Figure 2.29 Falling of a hemispherical object in pre-heated water [91].

Fiedler and Nottmeyer [91] suggested that Schlieren visualisation in water at rest and heated from the top is possible because the broadly spaced isothermal surfaces are dragged together by the falling object, giving rise to the formation of relatively large local temperature gradients which permit to see the motion patterns of the neighbouring flow.

With the assistance of binocular, high-speed stereo vision to obtain 3D quantitative information about the position and orientation of the particles, and with the application of the Schlieren visualisation technique explained above to visualise the structures of the surrounding fluid, also at high speed, detailed knowledge about the behaviour of a single solid settling in a fluid can be acquired, as it will be shown later in this thesis.

Chapter 3

STEREO VISION AND CAMERA CALIBRATION

In the previous chapter it was explicated that the most suitable experimental methods to study the motion of freely moving particles are image-based because they do not constraint the solid/fluid interaction. In addition, it was mentioned that due to the inherent simplicity of its setup and relatively good cost-effectiveness, stereo vision achieved with only one camera and a stereo adapter was chosen in this research as the experimental technique to get 3D metric information from the moving particles. The full description of such single-camera technique constitutes the topic of the first section of this chapter.

In order to generate the quantitative information, the camera had to be calibrated before the motion of the solids started. Therefore, the mathematical procedures as well as the background theory required for camera calibration was reviewed too, and it is presented in the second section of the chapter. In the third one, the methodology employed to make such quantitative data in the form of Cartesian *X*, *Y*, and *Z* coordinates is discussed. The chapter then ends with an evaluation of the accuracy of the single-camera stereo vision technique used here.

Because this chapter is entirely focused on camera and stereo concepts, and since no mention of any particle motion parameter or concept is made, the nomenclature of this chapter is exclusive. Nevertheless, there may be a re-use of terms and symbols in other parts of the thesis, though with a different meaning. Therefore, with the aim of avoiding confusion, all of the variables of this chapter were omitted from the Nomenclature list of the thesis, however, they are clearly defined as early as they appear in the chapter.

3.1 SINGLE-CAMERA STEREO VISION SYSTEM

Stereo vision can be defined as the process of obtaining the three-dimensional structure of a real world scene given two or more two-dimensional (2D) images of it taken simultaneously from slightly different points of view. The simplest approach to this process is depicted in Figure 3.1. Named as conventional or binocular stereo vision, it requires the use of only two cameras whose image planes are relatively closed to each other [93].

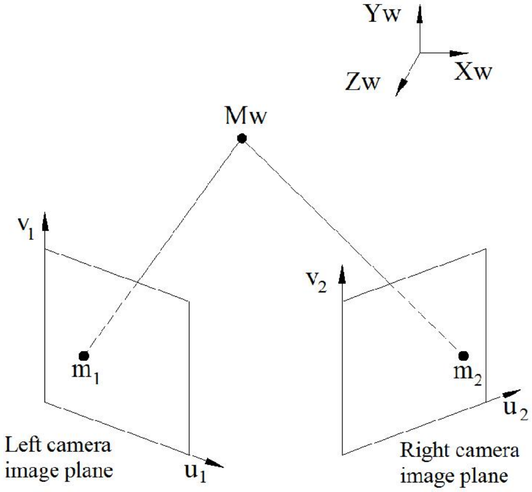

Figure 3.1 Conventional stereo system.

From Figure 3.1 it can be seen that any 3D point M_W whose coordinates are determined with respect to the world reference frame $O_WX_WY_WZ_W$ has two corresponding image points m_1 and m_2 with pixel coordinates (u_1, v_1) and (u_2, v_2), respectively, on each image plane. With no more information than the images themselves, the task of computational stereo vision, is to find the corresponding point m_2 on the right side for each point m_1 on the left.

The solution of the correspondence problem mentioned in the previous paragraph has been characterised as the most difficult job of computational stereo vision [93], [94], because technically any point on the right can be a candidate for m_1, therefore, certain constraints must be applied. The most widely used one is based on the epipolar geometry imposed by the stereo system configuration.

Once the two corresponding points m_1 and m_2 have been located, the scene depth information is obtained from the geometric difference, or *disparity*, between their respective positions. The disparity can be increased by the position, orientation, and physical characteristics of the cameras and lenses [93], therefore the use of a stereo system which keeps it as low as possible is always preferred. This is the main advantage of the stereo systems which employ only one camera, even though they possess a reduced field of view and lower spatial resolution.

As mentioned in Section 2.3.1, a single-camera stereo vision system can be created by attaching a stereo adapter to the lens. The adapter used in this investigation can be seen in Figure 3.2. It was manufactured by Ashai Pentax, and consists mainly on an arrangement of four mirrors. The detailed geometry is shown in Figure 3.3. Its main advantages are its simplicity, versatility, cost-effectiveness, and that it does not accentuate the disparity.

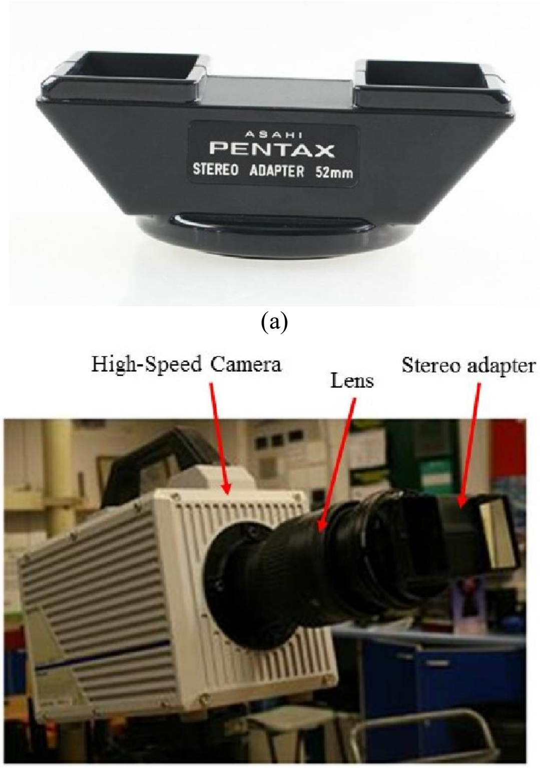

(a)

(b)

Figure 3.2 Four-mirror stereo adapter (a), high-speed camera with the stereo adapter attached to the lens (b).

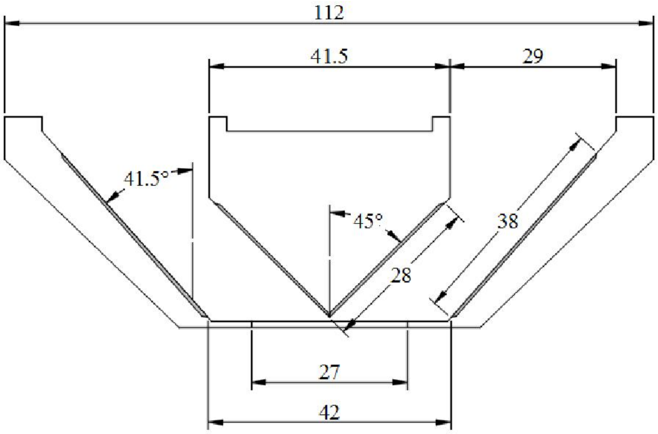

Figure 3.3 Geometry of the stereo adapter used in this investigation. Not to scale, units are expressed in mm [71].

The effect of the stereo adapter can be explicated as a virtual splitting of the physical high-speed camera into two other imaginary ones, as illustrated in Figure 3.4, where the optical centres C_l and C_r of the virtual cameras are separated by the baseline distance h. The coloured region among the lines $l_{1,0}$, $l_{2,0}$, $l_{1,i}$ and $l_{2,i}$ is the common field of view whilst the region enclosed by the inner mirrors and lines $l_{1,i}$ and $l_{2,i}$ is a blind area. The distance m between the outer mirrors corners is fixed and equal to 42 mm (Figure 3.3).

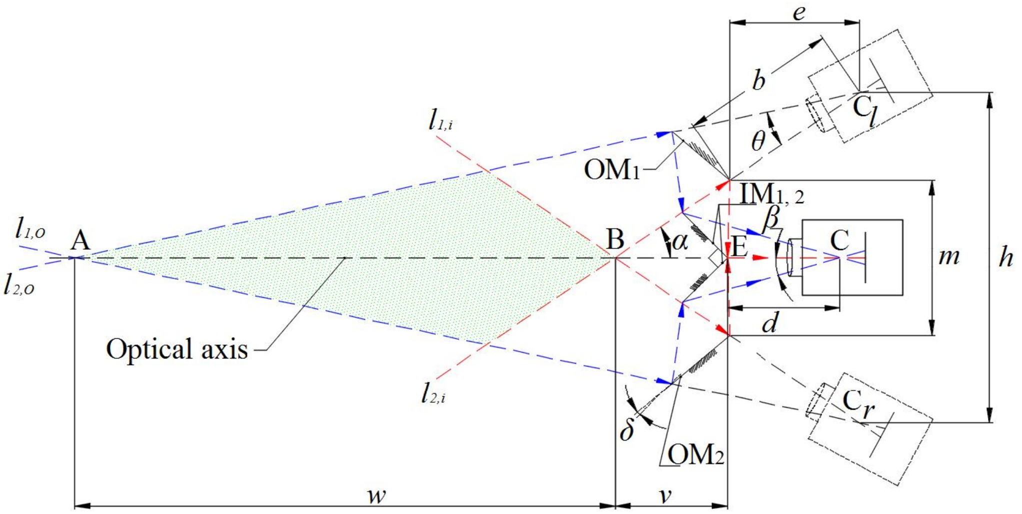

Figure 3.4 Conventional single-camera stereo vision system [95].

The difference in the inclination angles of the external and internal mirrors is known as the angular discrepancy δ. For the Asahi stereo adapter $\delta = 3.5^\circ$. In addition, the variation angle θ is equal to 2δ, or 7°. The angle α is equal to 45° whilst angle β and distance d depend on the focal distance and location of the camera centre, respectively. If needed, they both can be determined after the calibration of the camera. The equations to calculate the rest of the parameters are [71, 73, 95]

$$b = \frac{m}{2} + d \tag{3.1}$$

$$h = 2(b sin\theta + d) \tag{3.2}$$

$$e = d cos\theta + \frac{m}{2} sin2(\alpha - \delta) \tag{3.3}$$

$$v = \frac{\frac{m}{2} cos(\alpha - \delta) cos(\alpha + \delta)}{sin\delta cos\delta} \tag{3.4}$$

$$w = \frac{sin\beta(e + v)}{cos\theta sin(45 - \beta)} \tag{3.5}$$

3.2 CAMERA CALIBRATION

3.2.1 EXTRINSIC AND INTRINSIC PARAMETERS

In order to obtain the three-dimensional coordinates of point M_W given the points m_1 and m_2 (Figure 3.1) it is essential to find the position and orientation of each virtual camera relative to the world reference frame plus their relations with the corresponding pixel image planes. Such information is provided by the extrinsic and intrinsic parameters obtained from the calibration of the cameras.

Due to convenience in Figure 3.5, point M_W of Figure 3.1 is denoted as M and vector $\boldsymbol{M_W}$ is used to express its coordinates in the world frame whilst vector $\boldsymbol{M_C}$ accomplishes the same task but in the camera frame. The relation between both vectors involves a rigid transformation from the world to the camera frames, which in Euclidean coordinates is represented as

$$\boldsymbol{M_C} = R\boldsymbol{M_W} - \boldsymbol{C} \tag{3.6}$$

where R is a 3×3 rotation matrix whose elements constitute the orientation among the axes of both frames and vector $\boldsymbol{C}$ is a translation vector representing the displacement between O_W and O_C. Using homogeneous coordinates, Equation (3.6) can be rewritten as follows

$$\boldsymbol{M_C} = \begin{bmatrix} R & -R\boldsymbol{C} \\ 0 & 1 \end{bmatrix} \boldsymbol{M_W} \tag{3.7}$$

where vectors $\boldsymbol{M_W} = [X_W\ Y_W\ Z_W\ 1]^T$ and $\boldsymbol{M_C} = [X_C\ Y_C\ Z_C\ 1]^T$ are expressed in homogeneous coordinates [96]. It is common practice to keep the camera centre implicit by means of a second translation vector, defined as $\boldsymbol{t} \equiv -R\boldsymbol{C}$. The rotation matrix and the translation vector comprise the extrinsic parameters because they are external to the camera construction and describe the position and orientation of the camera frame with respect to the world reference frame.

The relation between the 3D camera frame coordinates (X_C, Y_C, Z_C) and the 2D coordinates (x, y) of the camera sensor or physical image plane are interpreted as a perspective projection effectuated by the so-called pin-hole camera model. Assuming that both planes $X_C Y_C$ and xy are parallel to each other, and being f the focal distance of the camera lens, the perspective equations of the model then are

$$
\begin{aligned}
x &= f\frac{X_C}{Z_C} \\
y &= f\frac{Y_C}{Z_C}
\end{aligned}
\tag{3.8}
$$

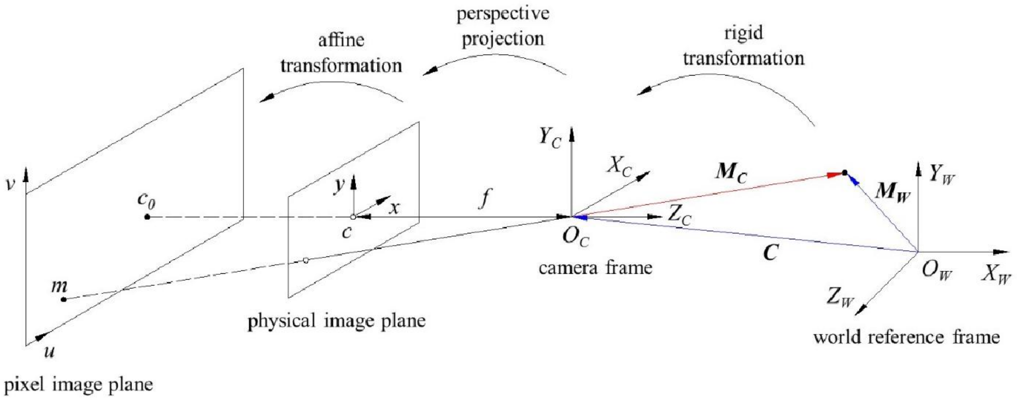

Figure 3.5 Camera projection.

With the assistance of homogeneous coordinates and Equation (3.7), after the perspective projection the next matrix can be written

$$
\boldsymbol{m} = \frac{1}{Z_C}\begin{bmatrix} f & 0 & 0 & 0 \\ 0 & f & 0 & 0 \\ 0 & 0 & 1 & 0 \end{bmatrix}[R \quad \boldsymbol{t}]\boldsymbol{M_W} \tag{3.9}
$$

where $\boldsymbol{m} = [x\ y\ 1]^T$. Point c in Figure 3.5 corresponds to the intersection of the camera principal axis (Z_C in the figure) with the physical image plane and is known as the principal point. In Equation (3.9) the image coordinates are still Euclidean. The conversion from these coordinates into pixel image coordinates is done through an affine transformation, hence the pixel coordinates (u, v) of point m are

$$
\begin{aligned}
u &= kf\frac{X_C}{Z_C} + u_0 \\
v &= lf\frac{Y_C}{Z_C} + v_0
\end{aligned}
\tag{3.10}
$$

where the ratios $X_C/Z_C \equiv \hat{x}$ and $Y_C/Z_C \equiv \hat{y}$ define normalized dimensionless coordinates and the products $kf \equiv \alpha$ and $lf \equiv \beta$ signify the pixel focal lengths on the horizontal and vertical directions, respectively [96], [97]. In addition, the pair (u_0, v_0) represents the location of the principal point in the pixel image plane. As each term of the right hand side of Equation (3.10) is expressed in pixel coordinates, so are u and v accordingly.

Up till now it has been considered that the axes x and y are perpendicular to each other, nonetheless in real camera sensors there is some skewedness (denoted by angle Θ in Figure 3.6) whose effect is included by rewriting Equations (3.10) as follows

$$\begin{aligned} u &= \alpha\hat{x} + \alpha cot\theta\hat{y} + u_0 \\ v &= \frac{\beta}{sin\theta}\hat{y} + v_0 \end{aligned} \tag{3.11}$$

By doing $\boldsymbol{m} = [u\ v\ 1]^T$, $\widehat{\boldsymbol{m}} = [\hat{x}\ \hat{y}\ 1]^T$, $\alpha_u = \alpha$, $\alpha_v = \beta/sin\Theta$, and $\gamma = \alpha cot\Theta$ [97], the matrix form of the affine transformation in homogeneous coordinates becomes

$$\boldsymbol{m} = \begin{bmatrix} \alpha_u & \gamma & u_0 \\ 0 & \alpha_v & v_0 \\ 0 & 0 & 1 \end{bmatrix} \begin{bmatrix} \hat{x} \\ \hat{y} \\ 1 \end{bmatrix} = A\widehat{\boldsymbol{m}} \tag{3.12}$$

where the intrinsic matrix A contains the five internal parameters of the camera: α, β, Θ, u_0 and v_0. The combination of Equations (3.10) and (3.12) establishes the camera projection in mathematical form as

$$s\boldsymbol{m} = P\boldsymbol{M_W} \tag{3.13}$$

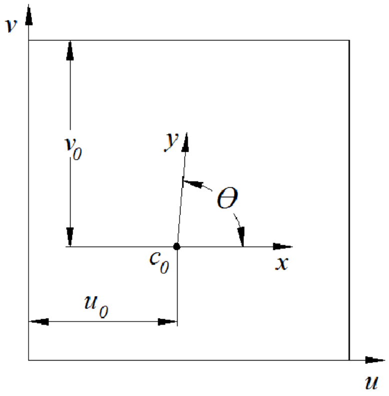

Figure 3.6 Skewedness angle Θ.

where $P = A[R \quad \boldsymbol{t}]$ is called the projective matrix. Equation (3.13) can be understood as the projective transformation, up to a scale factor s, from a real world 3D scene in the Euclidean space $\mathbb{R}^3$ into the 2D projective space $\mathbb{P}^2$. Such a transformation corresponds to a planar homography defined by a 3×3 matrix H in which eight of its nine elements are independent [98], [96]. Thus, if H is also defined up to a scale factor, Equation (3.13) becomes

$$\boldsymbol{m} = H\boldsymbol{M_W} \tag{3.14}$$

A series of known point correspondences is required for the estimation of H in Equation (3.14). Moreover, from its solution the intrinsic and extrinsic parameters can be determined, concluding therefore the calibration of the camera. One homography has to be obtained for each of the virtual cameras of the stereo system.

For the calculation of any homography a total of four point correspondences are enough in theory, provided that each point in the projective space $\mathbb{P}^2$ has two degrees of freedom; nonetheless, the effect of noise makes the extraction of the pixel image point coordinates inexact creating the necessity of having more than four correspondences. As consequence, the solution comes to be over-determined and incompatible with any real homography, and the task turns into the search of the best transformation H which diminishes some cost function based on the minimization of an algebraic, geometric or statistical error [77].

3.2.2 CAMERA CALIBRATION METHODOLOGY

The technique employed in this thesis to calibrate the virtual cameras was developed by Zhengyou [99]. It was chosen due to its ease of implementation. It uses the calibration model shown in Figure 3.7, which is formed by a set of black squares arranged in a known pattern where the corner points of each black square constitute the 3D world coordinates. For this technique to work, the model has to be positioned at different orientations with respect to the camera, therefore the same number of homographies such as the one of Equation (3.14) have to be computed.

In order to estimate the calibration homographies the pixel coordinates of the same corner points needed to be determined (Figure 3.8), so that there could be a full 3D to 2D point-correspondence set for each homography computation. The extraction of those pixel coordinates can be done either manually or automatically. In this work the second approach was followed through the application of digital image processing techniques, mainly for edge detection.

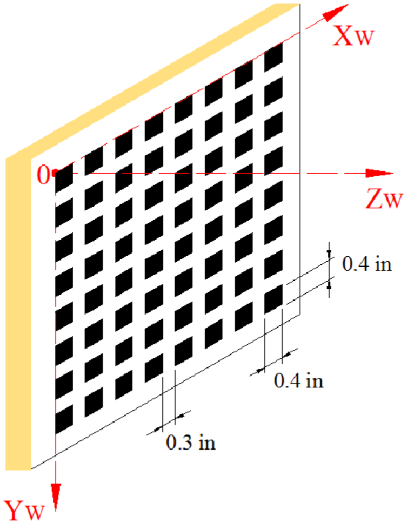

Figure 3.7 Camera calibration model and origin of the world reference frame.

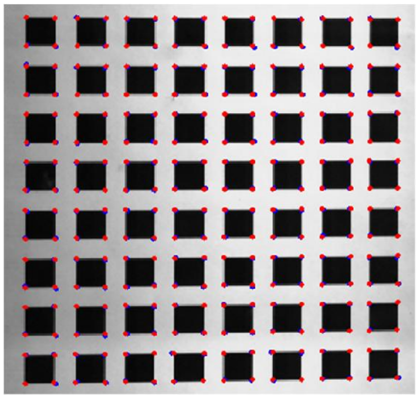

Figure 3.8 Pixel corner points of the squares of the calibration model found by digital image processing.

Given the fact that an edge in an image is that border of a region where there exists a sudden change in intensity, all of the candidates to be edge points must exhibit some local maximum intensity, therefore the ideal mathematical tool for searching such points is the vector gradient ∇f, which for a two-dimensional function $f(x,y)$ is defined as follows

$$\boldsymbol{\nabla f} \equiv \begin{bmatrix} \dfrac{\partial f}{\partial x} \\ \dfrac{\partial f}{\partial y} \end{bmatrix} \tag{3.15}$$

and its magnitude and directional angle are

$$\nabla f = \sqrt{\left(\frac{\partial f}{\partial x}\right)^2 + \left(\frac{\partial f}{\partial y}\right)^2} \tag{3.16}$$

$$\alpha = tan^{-1}\left(\frac{\partial f}{\partial y} \Big/ \frac{\partial f}{\partial x}\right) \tag{3.17}$$

The procedure employed in this work to detect the square edges is the one proposed by Canny [100]. It starts with the computation of the gradient magnitude and angle for each image point after some proper noise reduction. Then the points with local maximums are compared against two user-given values T_1 and T_2, and the edge is formed by all of those strong points whose intensity is larger than T_2 or at least larger than T_1 provided that their eight neighbouring pixels are classified as strong.

Afterwards, the edge selections were further refined through the use of Hough transform [101], which starts by writing a straight line equation of the form $x_i cos\theta + y_j sin\theta = \rho$ for each candidate point (x_i, y_i). Then by plotting all of the sinusoidal lines in the $\rho\theta$-plane, known as Hough space, some intersections are formed (Figure 3.9), where each of them denotes the pair of parameters (ρ', θ') of the line in the *xy*-plane linking as many points as sinusoids intersect at that pair. Finally, only those line-segments representing the four edges of each black calibration square are preserved, and the corner coordinates can be obtained.

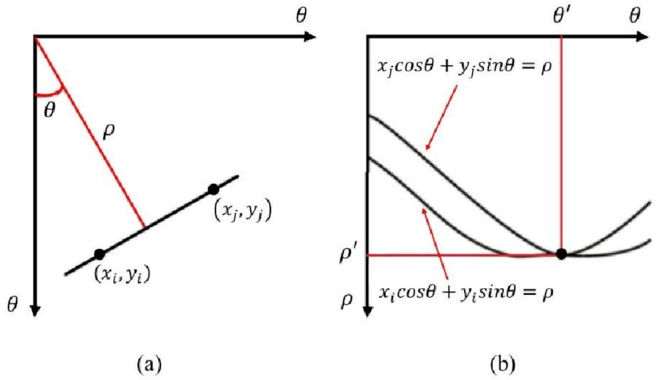

Figure 3.9 (a) Straight line linking two points (x_i, y_i) and (x_j, y_j) in the *xy*-plane. (b) Sinusoidal curves for each point in the Hough space [79].

As mentioned in the beginning of the section, in order to generate the three or more groups of 3D-2D point correspondences needed by the calibration technique, the model was placed at the same number of different orientations relative to the camera, as illustrated in Figure 3.10 where five orientations are represented. The motion between one position and the next one does not have to be known.

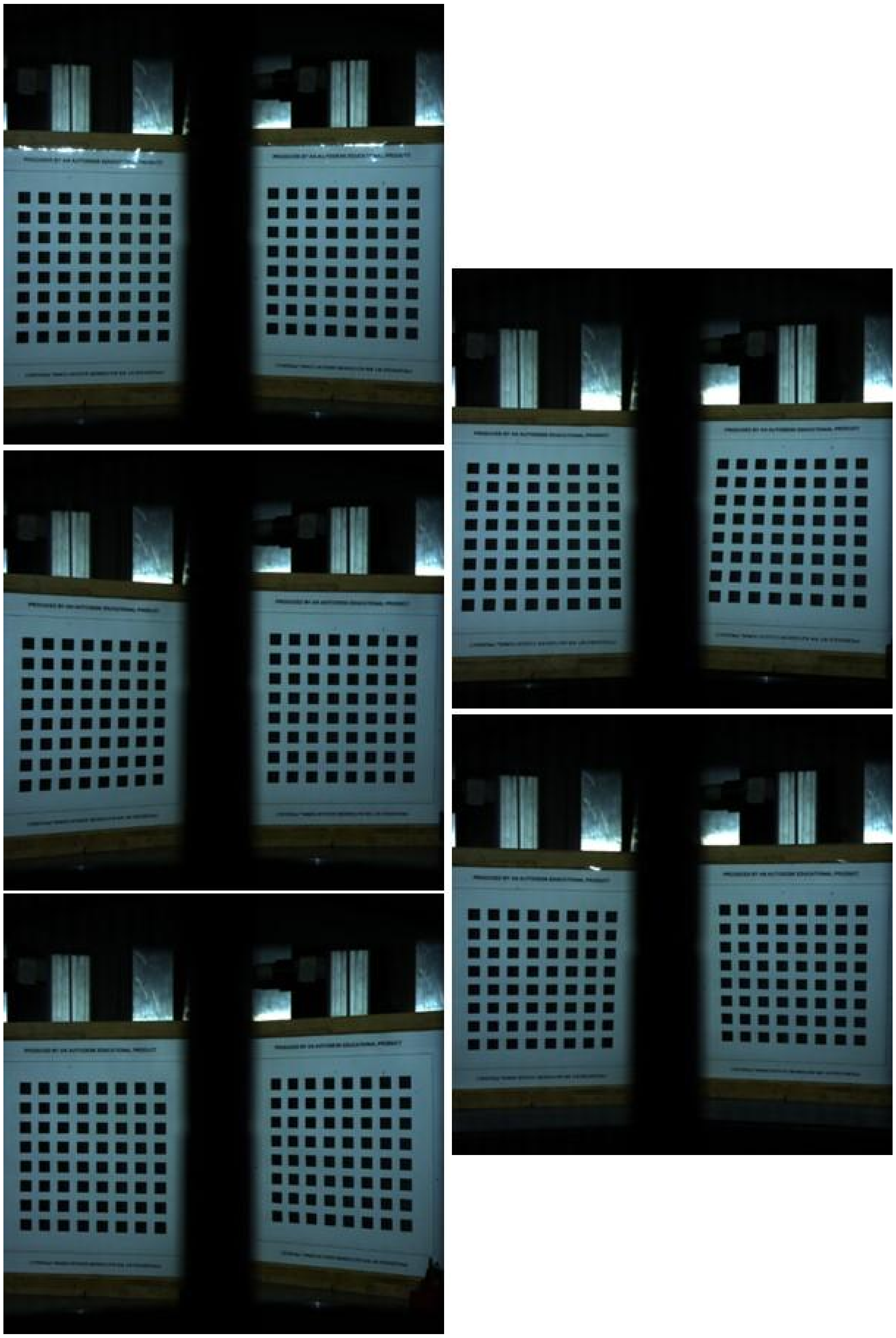

Figure 3.10 Five stereo pictures of the calibration model at different orientations with respect to the camera.

Although the parameters of the camera employed in the stereo-vision system used in this research are given in Section 3.4, it is convenient to highlight that each single picture captured by the system included both left and right images, as seen in Figure 3.10. The size of each stereo picture was $M \times N$ = 1024 × 1024 pixels, where M denotes the number of rows, or the size in the vertical pixel axis v, whilst N represents the number of columns, or the size in the horizontal pixel axis u, provided that a digital image is understood as a matrix of real numbers.

If it is assumed that the origin of the world frame is rigidly attached to the calibration model, it can be stated that the black squares plane is always located at $Z_W = 0$ despite the variations in orientation, and Equation (3.13) can be reduced to

$$s\boldsymbol{m} = A[\boldsymbol{r_1} \quad \boldsymbol{r_2} \quad \boldsymbol{t}]\boldsymbol{M_W} \tag{3.18}$$

where $\boldsymbol{r_1}$, $\boldsymbol{r_2}$ are the first two column vectors of matrix R. The column vectors of the rotation matrix represent the basis vectors of the camera frame axes in the world frame and are orthonormal. In addition, by expressing matrix H in the form of column vectors, Equation (3.14) can be rewritten as follows

$$[\boldsymbol{h_1} \quad \boldsymbol{h_2} \quad \boldsymbol{h_3}] = \lambda A[\boldsymbol{r_1} \quad \boldsymbol{r_2} \quad \boldsymbol{t}]\boldsymbol{M_W} \tag{3.19}$$

where λ is an arbitrary scalar accounting for the scale factor s and $\boldsymbol{h}_{j=1,2,3}$ are the column vectors of H. The solution of Equation (3.19) for each of the virtual cameras of the stereo vision system provides the way to compute their intrinsic and extrinsic parameters. The steps recommended by Zhang [99] for the solution of Equation (3.19) are shown in Figure 3.11 in the form of a flow chart.

The execution of every step of the methodology of Figure 3.11 involves different mathematical procedures, which were not included in this chapter but are carefully explained in Appendices A, B, C, and E. To execute all of the operations, a large number of computer programs, which are listed by name in Appendix G, were written and run in Matlab.

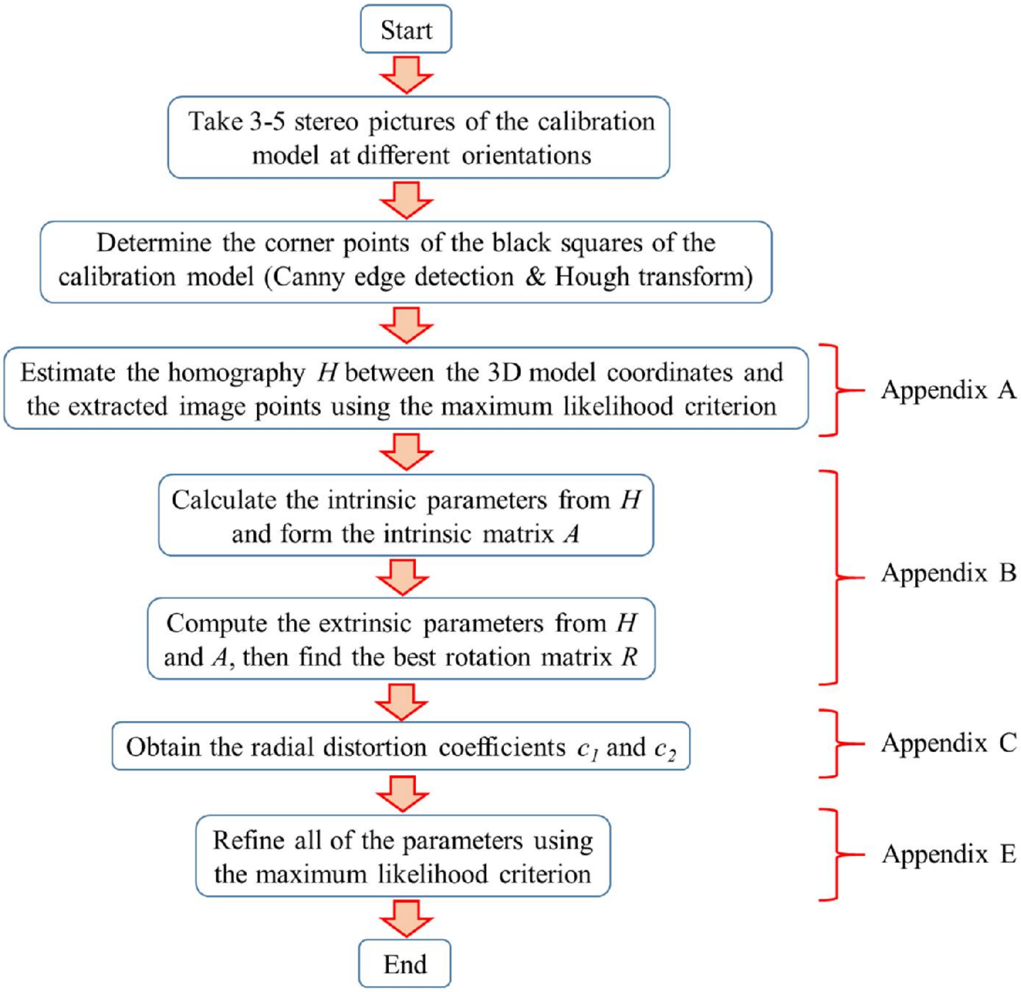

Figure 3.11 Flow chart of the camera calibration methodology of Zhengyou [99].

3.3 THREE-DIMENSIONAL STEREO RECONSTRUCTION

3.3.1 EPIPOLAR GEOMETRY OF THE TWO-CAMERA STEREO SYSTEM

As said in Section 3.1, the epipolar geometry restriction imposed by the stereo system was the criteria followed in this work to find the matching points between the left and right images. The mathematical derivation of the epipolar constraint starts with the application of Equation (3.13) to image points m_1 and m_2 (Figure 3.1), respectively, assuming that both cameras have already been calibrated. Thus, after placing the intrinsic matrix on the left-hand side of the equation the next expressions are formed

$$s_1 {A_1}^{-1} \boldsymbol{m_1} = [R \quad \boldsymbol{t}]_1 \boldsymbol{M_W} \tag{3.20}$$

$$s_2 {A_2}^{-1} \boldsymbol{m_2} = [R \quad \boldsymbol{t}]_2 \boldsymbol{M_W}$$

where it can be easily acknowledged that the right hand side of both equations correspond to the representations of M_W on the left and right camera reference frames: $M_{C,l}$ and $M_{C,r}$, respectively. Furthermore, if the coordinate frame of the right camera is related to its homologous one on the left by a rigid transformation with rotation matrix R and translation vector $\boldsymbol{t}$, Equation (3.20) becomes

$$\begin{aligned} s_1 \boldsymbol{\widehat{m}_1} &= [I \quad \boldsymbol{0}] \boldsymbol{M}_{C,l} \\ s_2 \boldsymbol{\widehat{m}_2} &= [R \quad \boldsymbol{t}] \boldsymbol{M}_{C,l} \end{aligned} \tag{3.21}$$

where $\widehat{\boldsymbol{m_1}} = {A_1}^{-1} \boldsymbol{m_1}$ and $\widehat{\boldsymbol{m_2}} = {A_2}^{-1} \boldsymbol{m_2}$. After the elimination of $\boldsymbol{M}_{C,l}$, s_1 and s_2, and some rearrangement, from Equation (3.21) the next fundamental relation is obtained

$$\widehat{\boldsymbol{m_2}}^T \mathcal{E} \widehat{\boldsymbol{m_1}} = 0 \tag{3.22}$$

where

$$\mathcal{E} \equiv [\mathbf{t}_\times] R \tag{3.23}$$

is called the essential matrix [102]. $[\mathbf{t}_\times]$ is a skew-symmetric matrix defined by $\boldsymbol{t}$ in such a way that $[\mathbf{t}_\times]\boldsymbol{q} = \boldsymbol{t} \times \boldsymbol{q}$ for any 3D vector $\boldsymbol{q}$ [103]. Matrix $\mathcal{E}$ is singular (i.e. $det\, \mathcal{E} = 0$) and has two equal non-zero singular values [97]. Equation (3.22) can also be written as

$$\boldsymbol{m_2}^T \left({A_2}^{-1}\right)^T \mathcal{E} {A_1}^{-1} \boldsymbol{m_1} = 0 \tag{3.24}$$

from which the so-called fundamental matrix is defined as

$$\mathcal{F} \equiv \left({A_2}^{-1}\right)^T \mathcal{E} {A_1}^{-1} \tag{3.25}$$

$\mathcal{F}$ constitutes the algebraic representation of the epipolar geometry. It is a rank-2 matrix, also singular (i.e. $det\mathcal{F} = 0$), and defined in such a way that if $\mathcal{F}$ corresponds to the arrangement where the left camera is the leading one, $\mathcal{F}^T$ is the fundamental matrix corresponding to the opposite arrangement [96].

Figure 3.12 shows the physical illustration of the epipolar geometry, where M_W represents a real world point with image points m_1 and m_2. In addition, the image planes of both cameras are π_1 and π_2, and the camera centres C_1 and C_2. The epipolar plane is the one defined by the rays C_1M and C_2M and contains the baseline h.

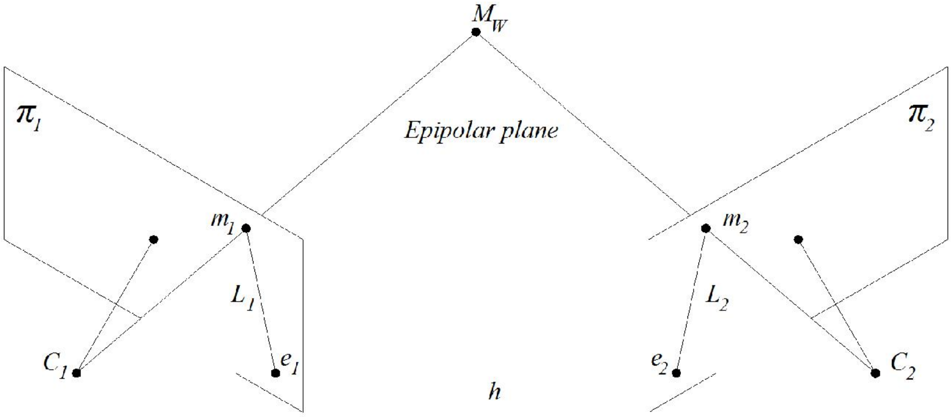

Figure 3.12 The epipolar geometry between two images captured with a stereo system [97].

Continuing with Figure 3.12, the point e_1 where the baseline pierces plane π_1 is called the epipole of the first camera and indicates the projection of C_2 in this image plane. Similarly, e_2, being the epipole of the second camera, denotes the projection of C_1 in π_2. The epipolar lines are formed by the intersections of the epipolar plane with the image planes π_1 and π_2. The epipolar line L_2, defined by points e_2 and m_2, is related to m_1 because it depicts the projection of the semi-line C_1m_1 on the second image. Likewise, specified by points e_1 and m_1, L_1 is the epipolar line associated to m_2 representing the projection of the semi-line C_2m_2 on the first image.

The physical explanation of the epipolar geometry restriction consists on the fact that being m_1 and m_2 images of the same point M, then m_2 must lie on the epipolar line L_2 associated with m_1. This means that, if both cameras are calibrated and their centers are known, the coordinates of m_1 fully determine line C_1m_1, the epipolar plane C_1C_2M, and epipolar line L_2 in consequence. Then, the possible matches of m_1 in π_2 are only searched along this line instead of in the whole image. Indeed, for any point $\boldsymbol{m_i}$ lying on L_2, Equation (3.24) can be generalized as

$$\boldsymbol{m_2}^T\mathcal{F}\boldsymbol{m_1} = 0 \tag{3.26}$$

from which

$$\begin{aligned} \boldsymbol{L_2} &= \mathcal{F}\boldsymbol{m_1} \\ \boldsymbol{L_1} &= \mathcal{F}^T\boldsymbol{m_2} \end{aligned} \tag{3.27}$$

where $\boldsymbol{L_1}$ and $\boldsymbol{L_2}$ are the coordinate-vectors of both epipolar lines L_1 and L_2. The coordinates of the epipoles are determined using the following relations

$$\begin{aligned} \mathcal{F}\boldsymbol{e_1} &= \boldsymbol{0} \\ \mathcal{F}^T\boldsymbol{e_2} &= \boldsymbol{0} \end{aligned} \tag{3.28}$$

where $\boldsymbol{e_2}$ is the is the left null-vector and $\boldsymbol{e_1}$ is its right null-vector of $\mathcal{F}$ [96]. Although there are alternative ways for the analysis, in this research it was preferred to estimate first the fundamental matrix with Equation (3.26), then to compute the essential matrix using Equation (3.25), and to calculate the motion parameters R and $\boldsymbol{t}$ from it through Equation (3.23), as suggested by Zhang [102]. The mathematical procedure involved is explicated in Appendix D.

3.3.2 THE LINEAR TRIANGULATION METHOD

Once the motion parameters between both cameras are determined, the unknown 3D coordinates of every stereo corresponding pair (m_1, m_2) can be computed through a reconstruction method called linear triangulation. The procedure applied here to derive the equations of this method was taken from Hartley, Gupta and Chang [104] and Hartley and Sturm [105]. First if the homogeneous coordinates of both image points are $\boldsymbol{m_1} = [u_1, v_1, 1]^T$ and $\boldsymbol{m_2} = [u_2, v_2, 1]^T$ and the 3D homogeneous coordinates of M are $\boldsymbol{M} = [X, Y, Z, 1]^T$, then, in the left camera frame Equation (3.13) gives

$$s_1 \begin{bmatrix} u_1 \\ v_1 \\ 1 \end{bmatrix} = \begin{bmatrix} p_{11} & p_{12} & p_{13} & p_{14} \\ p_{21} & p_{22} & p_{23} & p_{24} \\ p_{31} & p_{32} & p_{33} & p_{34} \end{bmatrix} \begin{bmatrix} X \\ Y \\ Z \\ 1 \end{bmatrix} \tag{3.29}$$

from which the following system of three equations arise

$$s_1 u_1 = [p_{11} \quad p_{12} \quad p_{13} \quad p_{14}] \begin{bmatrix} X \\ Y \\ Z \\ 1 \end{bmatrix} = {P_{1,l}}^T \boldsymbol{M} \tag{3.30a}$$

$$s_1 v_1 = {P_{2,l}}^T \boldsymbol{M} \tag{3.30b}$$

$$s_1 = {P_{3,l}}^T \boldsymbol{M} \tag{3.30c}$$

As long as P is determined up to a scale factor and through the substitution of Equation (3.30c) into the other two it is obtained

$$\begin{aligned} \left(u_1 {P_{3,l}}^T - {P_{1,l}}^T\right)\boldsymbol{M} &= 0 \\ \left(v_1 {P_{3,l}}^T - {P_{2,l}}^T\right)\boldsymbol{M} &= 0 \end{aligned} \tag{3.31}$$

The same procedure applied to the right camera produces

$$\begin{aligned} \left(u_2 {P_{3,r}}^T - {P_{1,r}}^T\right)\boldsymbol{M} &= 0 \\ \left(v_2 {P_{3,r}}^T - {P_{2,r}}^T\right)\boldsymbol{M} &= 0 \end{aligned} \tag{3.32}$$

Finally, by stacking Equations (3.31) and (3.32), the next system of linear equations is generated

$$\begin{bmatrix} u_1 {P_{3,l}}^T - {P_{1,l}}^T \\ v_1 {P_{3,l}}^T - {P_{2,l}}^T \\ u_2 {P_{3,r}}^T - {P_{1,r}}^T \\ v_2 {P_{3,r}}^T - {P_{2,r}}^T \end{bmatrix} \boldsymbol{M} = \boldsymbol{0} \tag{3.33}$$

or

$$W\boldsymbol{M} = \boldsymbol{0} \tag{3.34}$$

The solution of Equation (3.34) can be accomplished through the singular value decomposition of matrix W, thus it is obtained

$$W = USV^T \tag{3.35}$$

where U is a unitary, square matrix whose columns are the orthonormal singular values of matrix WW^T, S is a diagonal matrix of the same size as W whose non-zero elements correspond to the singular values of W, and V is also a unitary, square matrix whose columns are the orthonormal singular values of matrix W^TW. The solution vector $\boldsymbol{M}$ corresponds to the last (4th) column of matrix V. It is common practice to further optimise the results obtained with Equation (3.35) by some appropriate criteria. Here, the method of maximum likelihood criterion was employed.

The methodology recommended by Zhang [102] for the estimation of the epipolar geometry of the stereo vision system, and the three-dimensional reconstruction of the matching pairs of points was applied in this investigation. It is summarised in the flow chart of Figure 3.13, and likewise for the camera calibration operations (Section 3.2.2), a series of Matlab programs were written to do all the required calculations. They are listed in Appendix G.

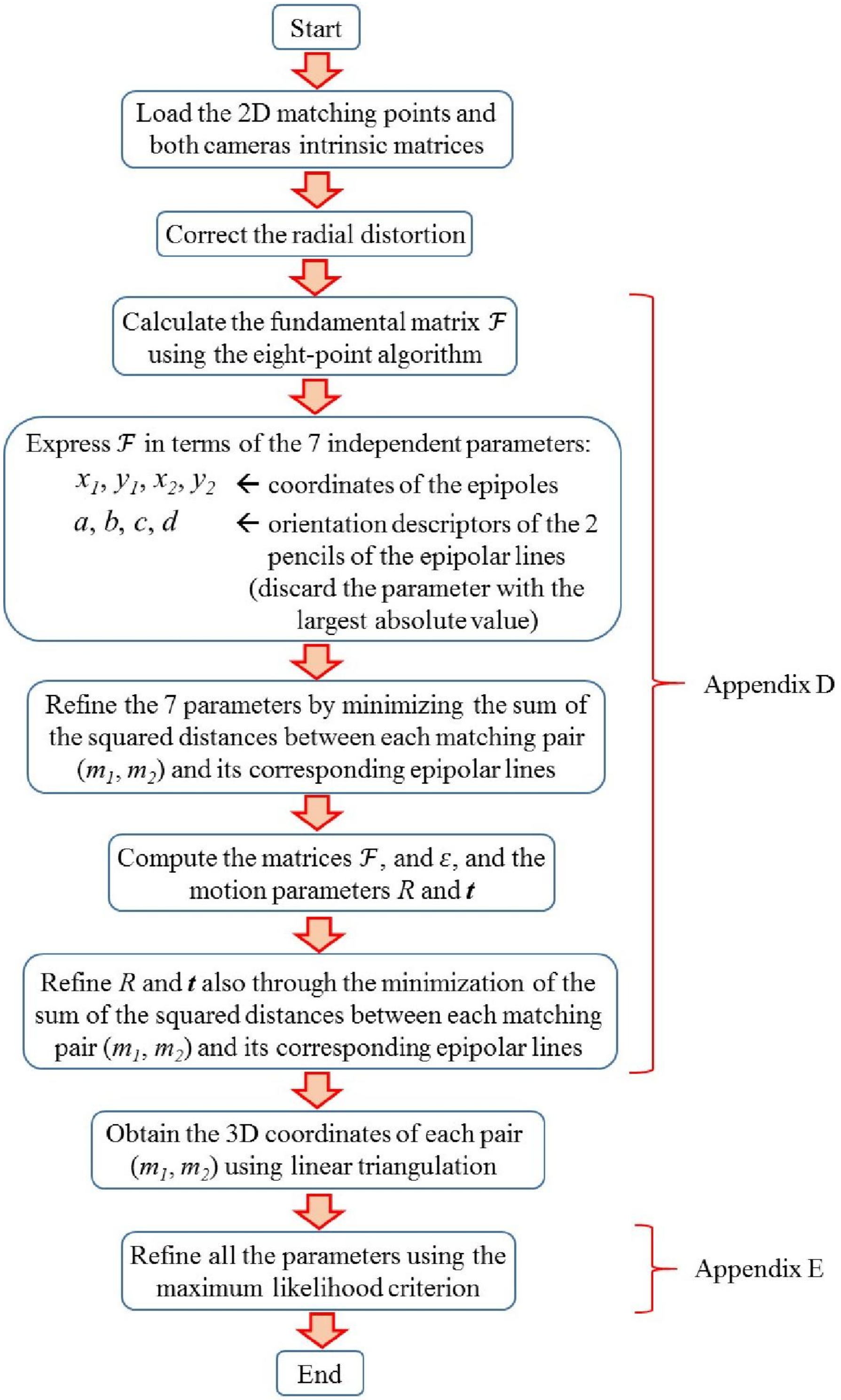

Figure 3.13 Stereo geometry estimation and 3D reconstruction flow-chart according to Zhang [102, 106].

3.4 ACCURACY

In order to test the accuracy of the of the methods used in this thesis, a series of three-dimensional point-sets generated by moving the calibration board forwards and backwards along the axis Z_W were reconstructed. The motion was executed by means of a high-precision traverse system on which the board was kept fixed. Pictures were taken at 34 different positions within the interval [-100 mm, 100 mm], being $Z_W = 0$ the plane of calibration. The relation between each position number and its corresponding Z_W-coordinate is given in Table 3.1.

Table 3.1 Corresponding Z_W-coordinates for the positions along Z_W.

Position	**Z_W *(mm)***	**Position**	**Z_W *(mm)***
0 (Calib. plane)	0.0	17	100.0
		18	-2.5
1	2.5	19	-5.0
2	5.0	20	-7.5
3	7.5	21	-10.0
4	10.0	22	-15.0
5	15.0	23	-20.0
6	20.0	24	-25.0
7	25.0	25	-30.0
8	30.0	26	-35.0
9	35.0	27	-40.0
10	40.0	28	-45.0
11	45.0	29	-50.0
12	50.0	30	-60.0
13	60.0	31	-70.0
14	70.0	32	-80.0
15	80.0	33	-90.0
16	90.0	34	-100.0

The camera and lens employed to do this study were the same ones used for all of the experiments done in this thesis. The FASTCAM SA4 high-speed, colour camera, developed by Photron, was utilized. Its picture is shown in Figure 3.14. The camera is equipped with a CMOS sensor of dimensions 20.48 × 20.48 mm, giving a maximum resolution of 1024 × 1024 pixels (50 mm per pixel). At this resolution, the system is capable of taking up to 3600 frames per second, however for the present accuracy study the pictures were taken at 500 frames per second, because this the rate used to track the motion of the particles investigated in Chapters 5 and 6.

Figure 3.14 Photron FASTCAM SA4 high-speed camera.

The lens attached to the camera was the SIGMA 24-70 mm 1:2.8 EX DG MACRO lens illustrated in Figure 3.15. It is suitable for manual control of the aperture, zoom, and focus. Because its filter diameter is 82 mm, the stereo adapter was fitted to the camera by a series of rings going from 52 to 82 mm. For the given camera sensor dimensions, the angle of view of the lens ranges from 23.4 to 62.2 degrees at the minimum and maximum focal distances, respectively.

Figure 3.15 SIGMA 24-70 mm 1:2.8 EX DG MACRO lens.

The minimum focusing distance of the lens corresponds to 0.40 m over the complete zoom range. The effect of stereo vision was achieved through the attachment of the Ashai Pentax stereo adapter described in Section 3.1. For the illumination of the scene, the LED-light source displayed in Figure 3.16 was employed. It produces a continuous flux of 12700 lm, with a white light colour temperature of 6200 K. This means that the appearance of the light is similar to that of normal daylight. This light appearance is recommended for research purposes. In Figure 3.17, a schematic of the experimental installation is portrayed. Once the setup was ready, five stereo pictures (similar to the ones shown in Figure 3.10) were taken to calibrate both the left and right virtual cameras.

Figure 3.16 LED illumination source.

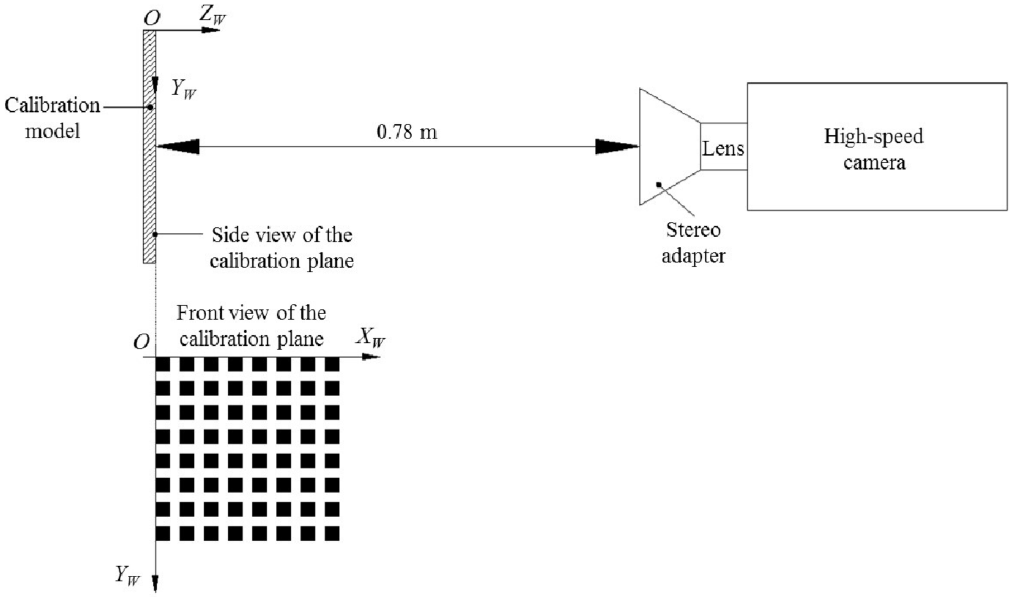

Figure 3.17 Position and orientation of the stereo system relative to the calibration plane.

The calibration of each of the virtual cameras was done as dictated by the methodology explained in Figure 3.11. The results are summarised in Table 3.2. Because the left camera frame was taken as the leading coordinate system, only the information obtained for this camera is discussed. There is not a particular reason to elect the left camera as the leading one, it was done by simply convention.

From the examination of the intrinsic matrix of the left camera together with the sensor resolution and dimensions, a skewedness angle and a pixel aspect ratio of 89.79° and 1.0, respectively, were obtained. This means that the sensor horizontal and vertical axes are practically perpendicular to each other, and the pixels are square. In addition, from the same data, the horizontal and vertical focal lengths attained were 39.89 mm and 39.73 mm, respectively. These values are considerably well located within the zoom interval of the lens. Moreover, the coordinates of the principal point offset were (u_0, v_0) = (9.44, 10.49) mm, remarkably near the geometrical centre of the camera sensor.

From the extrinsic parameters, the world coordinates of the left camera centre, vector $\boldsymbol{C}$ in Equation (3.6), were computed: $\boldsymbol{C}$ = (27.67, 110.03, 888.54) mm, which was in excellent agreement with the setup shown in Fig. 3.17 considering the longitude of the stereo adapter and the lens. Likewise, from the calibration results, the estimated radial distortion coefficients were $c_1 = 0.0045$ and $c_2 = 0.1169$.

After the calibration was completed, the three-dimensional coordinates of all of the corners of the black squares were determined in the left camera coordinate system according to the procedure described in Figure 3.13, and then projected back to the world reference frame by using the next equation

$$\boldsymbol{M_{W.R}} = \begin{bmatrix} R^T & R^T\boldsymbol{C} \\ \boldsymbol{0} & 1 \end{bmatrix} \boldsymbol{M_{C,l}} \tag{3.32}$$

where $\boldsymbol{M_{W.R}}$ represents each reconstructed, back-projected 3D point. So long as there were 256 corner points per plane, the arithmetic mean was taken as the representative value. The maximum standard deviations of the mean registered for X_W, Y_W, and Z_W were 0.02 mm, 0.03 mm, and 0.1 mm, respectively.

Table 3.2 Both virtual cameras intrinsic and extrinsic parameters.

Left Camera		
Intrinsic matrix *A*	Rotation matrix *R*	Translation vector ***t***
$\begin{bmatrix} 1994.55 & -7.41 & 472.24 \\ 0 & 1986.35 & 524.43 \\ 0 & 0 & 1 \end{bmatrix}$	$\begin{bmatrix} -0.9855 & 0.0017 & -0.1695 \\ -0.0073 & -0.9994 & 0.0324 \\ -0.1693 & 0.0332 & 0.9850 \end{bmatrix}$	$\begin{bmatrix} 6.9950 \\ 3.2030 \\ 34.4165 \end{bmatrix}$
Right Camera		
Intrinsic matrix *A*	Rotation matrix *R*	Translation vector ***t***
$\begin{bmatrix} 1992.66 & -5.00 & 538.48 \\ 0 & 1987.08 & 526.86 \\ 0 & 0 & 1 \end{bmatrix}$	$\begin{bmatrix} -0.9875 & 0.0051 & 0.1576 \\ -0.0016 & -0.9997 & 0.0225 \\ 0.1577 & 0.0219 & 0.9872 \end{bmatrix}$	$\begin{bmatrix} -1.5880 \\ 3.5117 \\ 35.3455 \end{bmatrix}$

In Figure 3.18 the Z_W-coordinates of both the true ($Z_{W,true}$) and the estimated ($Z_{W,rec}$) points are shown graphically for the 34 positions, where a relatively strong agreement between each pair of points can be noticed. Additionally, in Figure 3.19 the plot of the absolute error of the reconstructed coordinates $X_{W,rec}$, $Y_{W,rec}$, and $Z_{W,rec}$ within the interval $-100 \text{ mm} \leq Z_W \leq 100 \text{ mm}$ is portrayed.

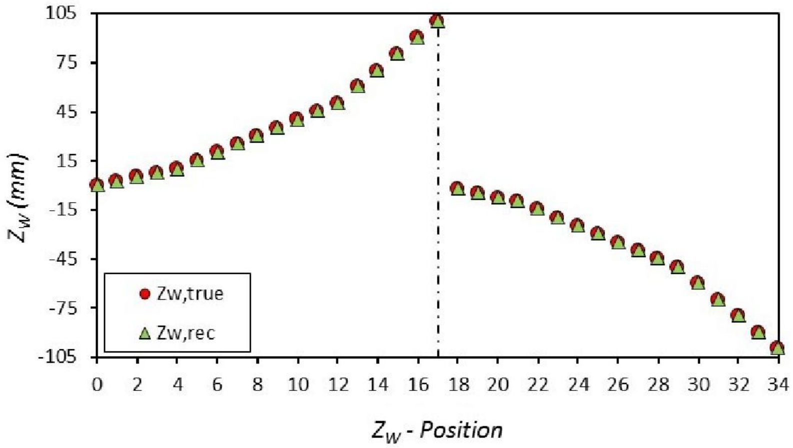

Figure 3.18 True and reconstructed, back-projected points on the Z_W-axis.

From the plot in Figure 3.19 it can be observed that the absolute error in the X_W and Y_W directions was nearly constant for the whole interval, with the error in X_W being slightly higher than that in Y_W, nonetheless neither of them ever surpassed 0.2 mm. On the other hand, the absolute error in Z_W behaved in a different way. Although it took random values within the interval studied, it was always noticeably smaller when the analysed plane became closer to the camera compared to that when it became further. However, its highest value was below 1.0 mm.

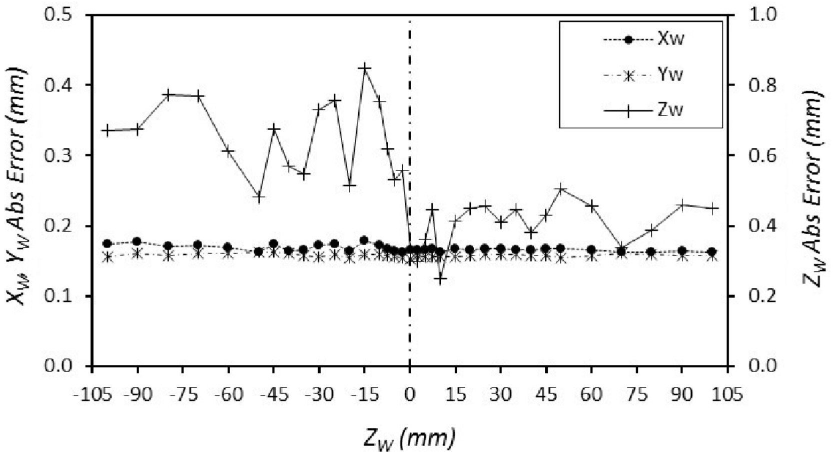

Figure 3.19 Absolute error of the reconstructed coordinates in the X_W, Y_W, Z_W axes.

A three-dimensional comparison between the true and the reconstructed 34 positions of the calibration model is represented in Figure 3.20, where a relatively good agreement can be perceived, even though some minor variations can also be appreciated, mainly in the negative side of the Z_W axis, thus confirming the results shown in the plot of Figure 3.19.

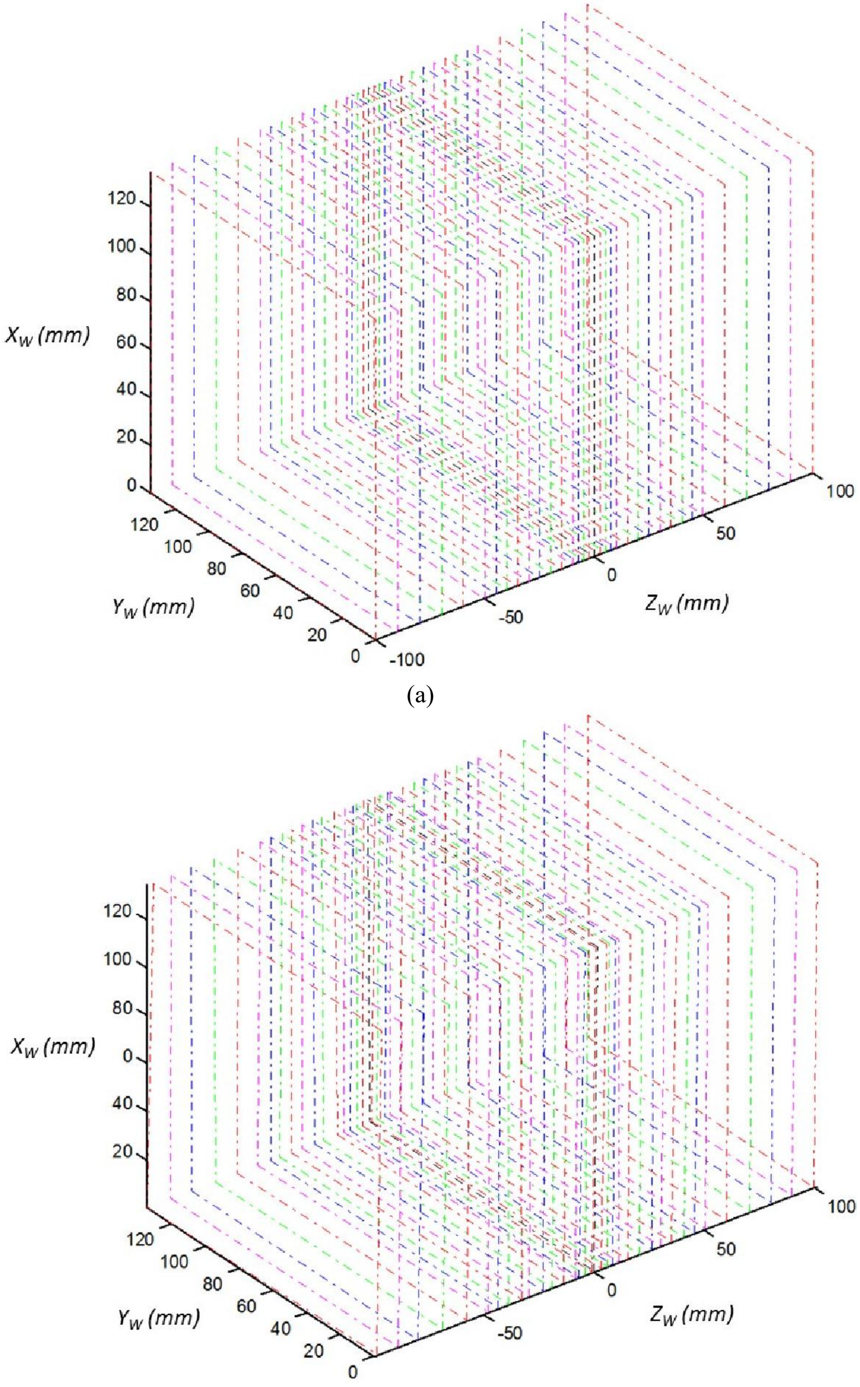

(a)

(b)

Figure 3.20 3D comparison between the original (a) and the reconstructed (b) 34 positions of the calibration model along the Z_W-axis.

In general, from this study it was observed that the error is mostly dominated by the uncertainties in Z_W, at least in the interval -100 mm $\leq Z_W \leq$ 100 mm. This was expected given the fact that in stereo vision Z_W is obtained from the knowledge of X_W and Y_W, then it contains the uncertainties of both. Moreover, the error is further augmented by the numerical operations performed by the stereo algorithms. Nevertheless, the error can be kept low provided that the calibration of the stereo system is done carefully. Therefore, it can be concluded that the single-camera technique chosen for this thesis experimental work is suitable to track the three-dimensional required positions of moving particles as long as their size exceeds 1.0 mm. In this way, the size will always be larger than the interval of absolute error in Z_W.

Chapter 4

APPLICATION OF STEREO VISION AND DIGITAL IMAGE PROCESSING TO THE MOTION OF SINGLE PARTICLES

In Chapter 3 it was explained the way to obtain 3D metric information of any photographed scene out of a set of 2D corresponding features by means of stereo vision, provided that the cameras were previously calibrated. Therefore, the process of stereo vision can be used to obtain quantitative 3D information of the motion of single particles without disturbing the physical phenomena. However, in order to obtain the 2D matching features, which are normally expressed in terms of pixel coordinates, certain digital image processing operations needed to be applied to the stereo images. The description of such operations are the topic of the first section of this chapter.

Through image processing procedures the quality of the stereo pictures was first improved, then the pixel coordinates of representative particle points, whose knowledge is vital for the motion analysis, were extracted. The selection of the image processing operations employed in this research was entirely based on trial and error. Different operations were applied to the stereo pictures, but only those whose result was considered superior were kept in the analysis exposed in Section 4.1. Also, since a large number of the terms used in the section may be re-used in other parts of the thesis though with different meaning, and provided that they belong exclusively to this section, they were not included in the Nomenclature list of the thesis to avoid confusion. However, each term is clearly explicated as soon as it appears in the text.

Once the digital image processing operations were concluded and the three-dimensional particle-feature metric coordinates were found using the algorithms exposed in Section 3.3, the displacement, velocity, and angle of attack in the world reference frame were computed. Furthermore, through the introduction of a Frenet reference frame moving along the particle trajectory, the forces exerted on the solid were also estimated, from which the drag force was subsequently computed. The methods to determine such kinematic and dynamic quantities are explicated in Sections 4.2 and 4.3.

4.1 DIGITAL IMAGE PROCESSING OPERATIONS FOR THE MOTION OF A SINGLE PARTICLE

4.1.1 IMAGE ENHANCEMENT

So long as the stereo images acquired in the experiments were not suitable for the direct extraction of the corresponding particle features which were going to be reconstructed in three-dimensions, they needed to be properly enhanced before, by means of digital image processing operations. Figure 4.1 shows the stereo picture of a woody cylindrical particle falling freely in quiescent air as taken by the camera, without any modification. It is clear that in order to obtain useful quantitative information from the picture, digital image processing was a mandatory step.

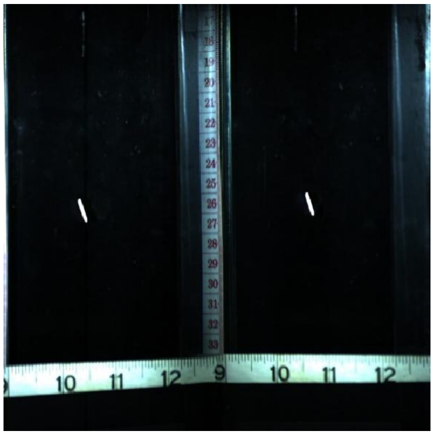

Figure 4.1 Stereo image of a cylindrical particle in free fall in quiescent air.

The first operation towards the improvement of the stereo pictures, consisted on the isolation of all of the pixels representing the image of the cylinder from the rest of the pixels in the frame. This task is known as background removal, and the most straightforward way to do it is by applying the following equation

$$h = c(f - g) \tag{4.1}$$

where f corresponds to the stereo picture with both particle and background (Figure 4.1), g is the stereo picture of the background only (Figure 4.2a), and h is a new stereo image containing only those pixels that represent the cylinder (Figure 4.2b). Multiplication by scalar c is optional, its only purpose is to produce an increase in brightness. For Equation (4.1) to work, f and g must be both images of the same size and type.

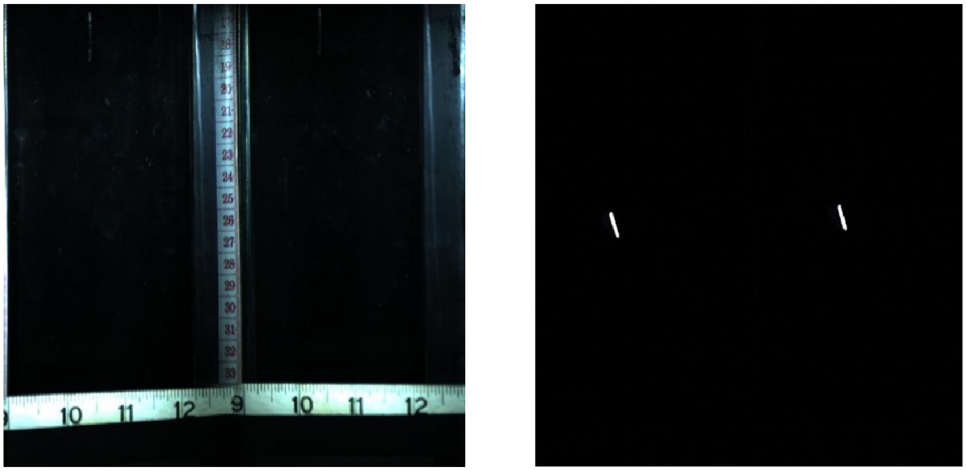
a) b)

Figure 4.2 Stereo images of the background (a), and of the isolated particle pixels (b) of Figure 4.1.

In many cases, removing the background was not sufficient to extract the necessary pixel coordinates correctly, therefore subsequent enhancement was required. In their work about calculating the size distribution of coal particles using image segmentation techniques, Z. Zhang et al. [83] started their analysis by converting the given colour coal pictures into grey-scale intensity images employing the next equation

$$h_g = 0.2989R + 0.5870G + 0.1140B \tag{4.2}$$

where R, G, and B are the amounts of red, green, and blue colours as obtained from the imaging device, and h_g is an 8-bit, monochrome image whose brightness ranges from 0 (black) to 255 (white). The coefficients multiplying R, G, and B are the standard values used by Matlab, according to the recommendations given by the National Television System Committee (NTSC) for luminance. Since the pictures collected from the experiments in this research were also expressed in the RGB colour system, the same conversion equation was applied.

Assuming that the brightness of the particle pixels is higher than that of the background, a common separation method relies on the application of a suitable threshold to the image. This means that all of those pixels whose grey-intensity values are equal or smaller than certain cutting parameter T, will be eliminated. However, in order to ensure a successful thresholding, Gonzalez et al. [81] recommended to smooth the image first by reducing noise effects through spatial filtering.

The concept of filtering refers to the implementation of a set of linear or non-linear operations directly on the image space for the purpose of enhancement. Because any pixel in the image can be treated as a point, both terms pixel and point are used here to mean the same. The filter, also called mask, is normally an odd size $m \times n$ matrix whose centre is consecutively placed onto each point $P(u,v)$ of the picture in such a way that the matrix coefficients can multiply the $mn-1$ neighbouring pixels. The sum of the multiplication results is considered the response of the filter at that point. When the filter mask is placed on a pixel, only two mathematical operations are possible: a correlation, expressed as

$$\mathcal{M}(u,v) \star h_g(u,v) = \sum_{s=-a}^{a} \sum_{t=-b}^{b} \mathcal{M}(s,t) h_g(u+s, v+t) \tag{4.3}$$

or a convolution, written in the form

$$\mathcal{M}(u,v) \bigstar h_g(u,v) = \sum_{s=-a}^{a} \sum_{t=-b}^{b} \mathcal{M}(s,t) h_g(u-s, v-t) \tag{4.4}$$

where $\mathcal{M}$ is the $m \times n$ filter mask, and a and b are two non-negative integers which relate to m and n as follows: $m = 2a+1$ and $n = 2b+1$. The process of convolution means to rotate the mask 180° before placing it over the pixel. The filtering operation utilized in this experimental work to smooth the particle stereo images was a correlation with a circular averaging mask of radius $r = 5$, defined within a square of size $2r+1$.

Once the spatial filtering step has been completed, the thresholding operations can be executed to separate the particle pixels from the background. A thresholded image h_T is a black and white binary image defined as follows

$$h_T(u,v) \equiv \begin{cases} 1 \;\; if \; h_g(u,v) > T \\ 0 \;\; if \; h_g(u,v) \leq T \end{cases} \tag{4.5}$$

Thus, for every pixel if the condition is met, it becomes white, otherwise it turns black. The value of T can be chosen manually by trial and error from the plot of the image grey-level intensity values in the form of a histogram (Figure 4.3), nevertheless, since in this work multiple particle motion pictures required to be processed, it was preferred to employ an automatic thresholding algorithm capable to select the best value for T only from data of the image itself.

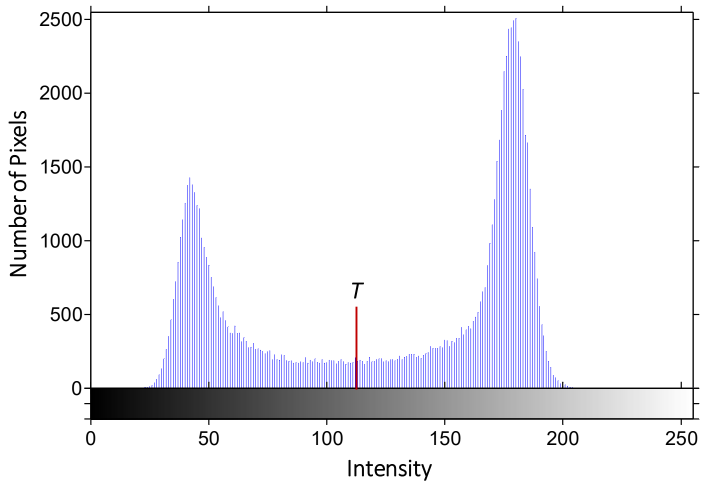

Figure 4.3 Sample of a grey-intensity level histogram with a clear valley between two maximums.

So long as any possible thresholding value *k* separates the image pixels into two classes, C_0 for those with grey-levels [*1,2,…,k*], and C_1 for the other ones with levels [*k+1,…,L*], the histogram of Figure 4.3 can be normalized and treated like a probability distribution, as recommended by Otsu [107]. The normalizing equation is

$$p_i = \frac{n_i}{N}, \qquad i = 1,2,\dots,L, \qquad p_i \geq 0, \qquad \sum_{i=1}^{L} p_i = 1 \tag{4.6}$$

where *N* is the total number of pixels, n_i is the number of pixels with intensity level *i*, and *L* is the total number of possible levels. The equations for the probability of each class to occur and for the mean of each class intensity levels are

$$\omega_0 = Pr(C_0) = \sum_{i=1}^{k} p_i = \omega(k) \tag{4.7}$$

$$\omega_1 = Pr(C_1) = \sum_{i=k+1}^{L} p_i = 1 - \omega(k) \tag{4.8}$$

and

$$\mu_0 = \sum_{i=1}^{k} iPr(i|C_0) = \sum_{i=1}^{k} ip_i/\omega_0 = \mu(k)/\omega(k) \tag{4.9}$$

$$\mu_1 = \sum_{i=k+1}^{L} iPr(i|C_1) = \sum_{i=k+1}^{L} ip_i/\omega_1 = \frac{\mu_T - \mu(k)}{1 - \omega(k)} \tag{4.10}$$

where

$$\mu(k) = \sum_{i=1}^{k} i p_i \tag{4.11}$$

$$\mu_T = \mu(L) = \sum_{i=1}^{L} i p_i \tag{4.12}$$

The variables $\mu(k)$ and μ_T are the mean intensity up to level k, and the mean intensity of the whole image. Otsu [107] suggested that the best value of k to be T should be the one which maximizes the between-class variance ${\sigma_B}^2(k)$, defined as

$${\sigma_B}^2(k) = \omega_0 \omega_1 (\mu_1 - \mu_0)^2 \tag{4.13}$$

Figure 4.4a shows the stereo image of an irregular PTFE particle in free fall in quiescent water where some background pixels were not successfully removed with Equation (4.1), and Figure 4.4b shows the same stereo image after being spatially filtered and thresholded using the method proposed by Otsu [107].

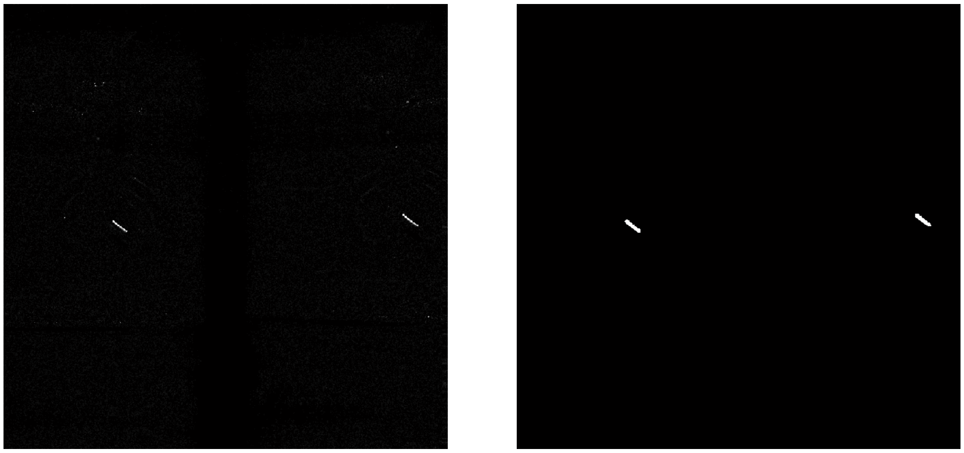

a) b)

Figure 4.4 a) Unsuccessful background removal with Equation (4.1), b) background fully removed through spatial filtering and thresholding.

After a successful thresholding, the stereo pictures were enhanced even further by means of morphological image processing. Moreover, if the image still contained background pixels which survived the thresholding, or if there were pixels within the particle perimeter which were turned black by the threshold, then morphological processing was a mandatory stage. Not only mathematical morphology does improve the images visual quality, but also it can be regarded as a tool to extract particle characteristics such as boundaries and other shape descriptors.

By definition mathematical morphology works only on binary images, since it considers each image as a *set* of 1-valued pixels whose intensity equals one. The two most common morphological applications are dilation and erosion which through the assistance of matrices formed by 0's and 1's, denominated structuring elements, and set theory operations can make components in the image thicker or thinner. The morphological tasks employed in this research were close, clean, and fill.

The close operation encompasses a dilation followed by an erosion which results in the smoothing of the particle contour, the fusion of narrow breaks, and the filling of any hole smaller than the structuring element. The clean operation has the effect of removing any single foreground pixel which endured the thresholding, whilst the last operation fills any single zero-value pixel surrounded by one-pixels. After the morphological processing, the only bright pixels remaining were those which corresponded to the particle image, as illustrated in Figure 4.5.

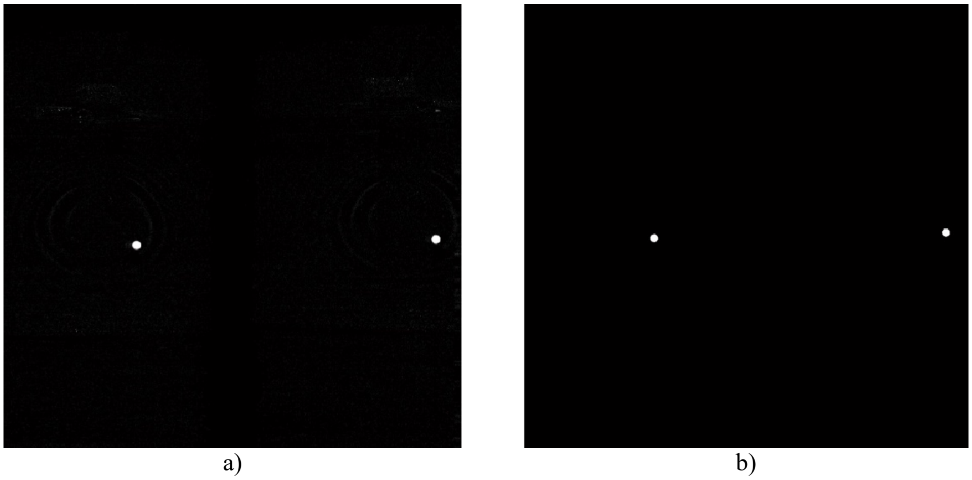

a) b)

Figure 4.5 Stereo image of a PTFE spherical particle before (a) and after (b) full enhancement.

Once the enhancement step was finished, every improved stereo picture was visually examined, and if approved, it was then selected for the next stage of digital image processing operations, which were focused on detecting the centroid, boundaries, and longest axis of the particle, which in turn were used for later analyses. The boundaries were not identified for size measurements because the representation of the longest axis can be done as a vector, therefore independently from the size of the particle. All the particle dimensions essential for the investigation were determined manually with a Vernier calliper.

4.1.2 PARTICLE CENTROID, PERIMETER, AND LONGEST AXIS RECOGNITION

The computation of the centroid was necessary because the particle kinematics and dynamics are linked to it. Provided that the particles are of uniform density, the method employed in this work to calculate the centroid pixel coordinates is based on weighting the grey-scale intensity values of each pixel, as follows

$$X_C = \frac{\sum u * h_{g,2}(u,v)}{\sum h_{g,2}(u,v)}$$
$$Y_C = \frac{\sum v * h_{g,2}(u,v)}{\sum h_{g,2}(u,v)} \tag{4.14}$$

where *u* and *v* represent the horizontal and vertical coordinates of each pixel, $h_{g,2}(u,v)$ is the stereo image after full enhancement and converted back from binary class to grey-scale intensity, and X_C and Y_C are the centroid pixel coordinates. In Figure 4.6 the detected centroids of three solids with different shape are displayed.

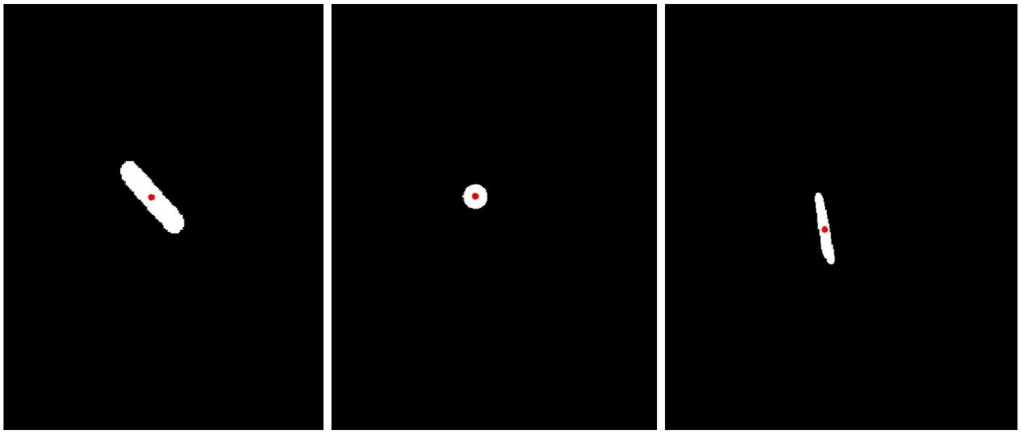
a) b) c)

Figure 4.6 Detected centroids for a cylinder, a sphere, and an irregular particle.

For the cases when the solid was not spherical, the orientation it had with respect to the motion direction needed to be tracked too. The procedure followed here to estimate the orientation required the knowledge of the particle perimeter and longest axis. To identify the perimeter the algorithm recommended by Nishino et al. [74], which is based on the maximum-gradient point principle, was implemented. The algorithm requires first to complete a rough recognition of all the tentative peripheral points (P_t in Figure 4.7), which can be obtained by finding the coordinates of all those image pixels which have background pixels in their neighbourhood [81]. This task was accomplished employing the binary image of the particle after full enhancement.

Then, every point P_t is joined with the centroid by a radial line which extends some random distance further out of the boundary up to point P_a (Figure 4.7). Finally, in agreement with Nishino et al. [74], if the intensity values along this line are determined and plotted (Figure 4.8), the true perimeter point corresponds to the one where the gradient is the highest. Therefore, by approximating the intensity curve as a 3rd order polynomial between its maximum and minimum values, the true boundary point can be taken as the inflection point P_i (Figure 4.9). To avoid any intrusion from the image enhancement operations, the maximum-gradient point quest was executed on the original picture just after background removal and grey-scale conversion.

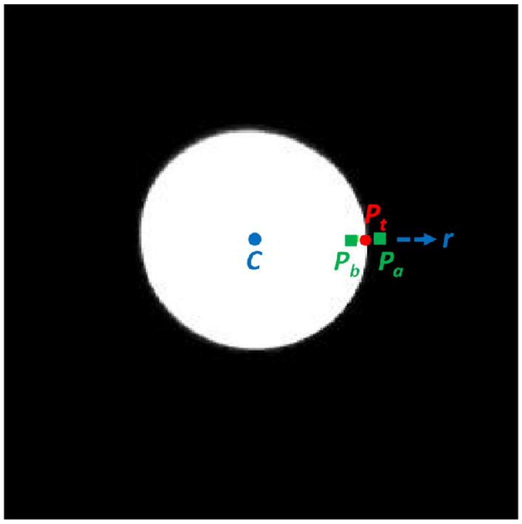

Figure 4.7 Image of a nylon sphere in free fall with one tentative perimeter point P_t determined.

Figures 4.10a and 4.10b shows the tentative and true perimeters of the nylon sphere of Figure 4.7, respectively, whilst Figures 4.10c and 4.10d depicts the same perimeters for the cylindrical biomass particle of Figure 4.1. Both particles were descending in quiescent air. The refinement, characterised by a smoothing of the boundary, gained through application of the maximum-gradient point principle is clearly evident for both solids.

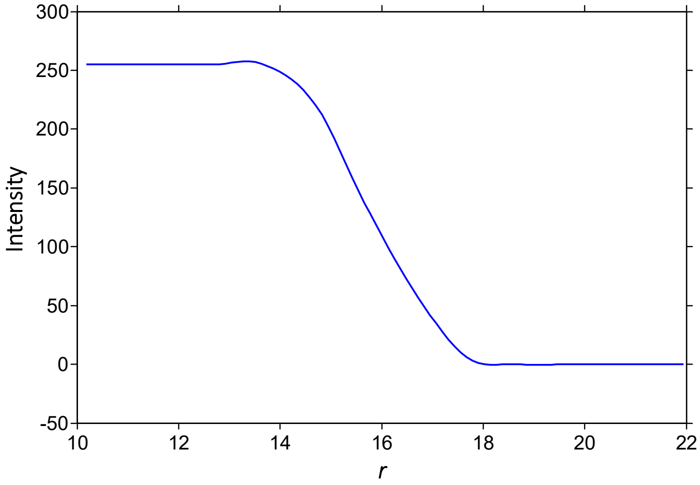

Figure 4.8 Intensity profile between the random points P_a and P_b.

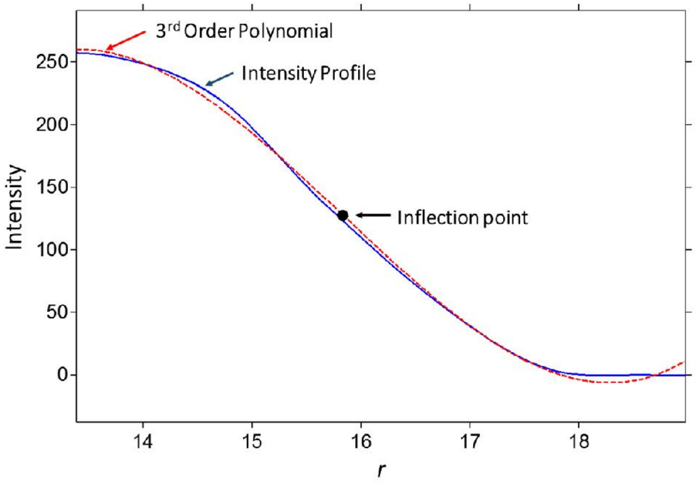

Figure 4.9 Approximation of the intensity curve as a 3rd order polynomial and inflection point.

After the set of perimeter pixels was successfully detected, the next step became the identification of the particle longest axis, which was done by finding the two peripheral points P_1 (u_1, v_1) and P_2 (u_2, v_2) whose distance between each other was the largest, compared to the rest of the boundary points.

In Figure 4.11 the three key points C, P_1, and P_2, relevant to determine the particle motion and orientation, are marked on both the left and right sides of the stereo image of a falling cylinder. The set of pixel coordinates formed by these corresponding points in every stereo picture constituted the input data for the reconstruction methodology described in Figure 3.13. The output was then the 3D metric coordinates of such points at each time increment.

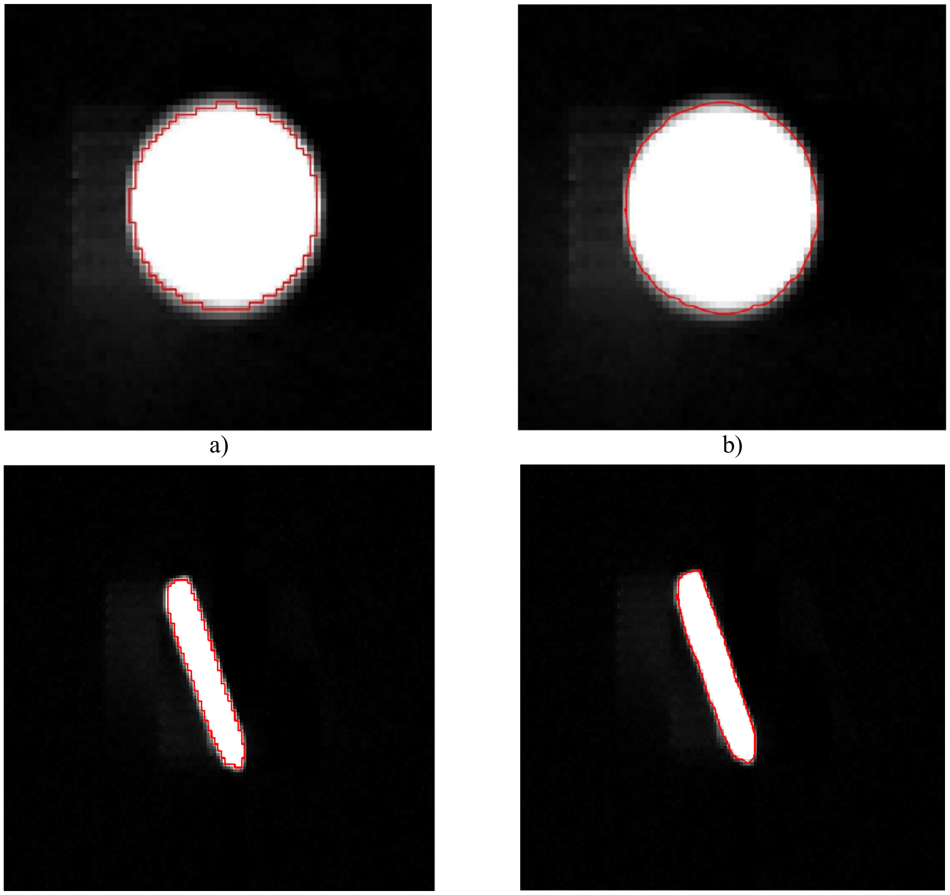
a) b)
c) d)

Figure 4.10 Tentative and true perimeters of the nylon sphere of Figure 4.7 (a, b), and of a cylindrical biomass particle (c, d). Both solids are moving in free fall conditions.

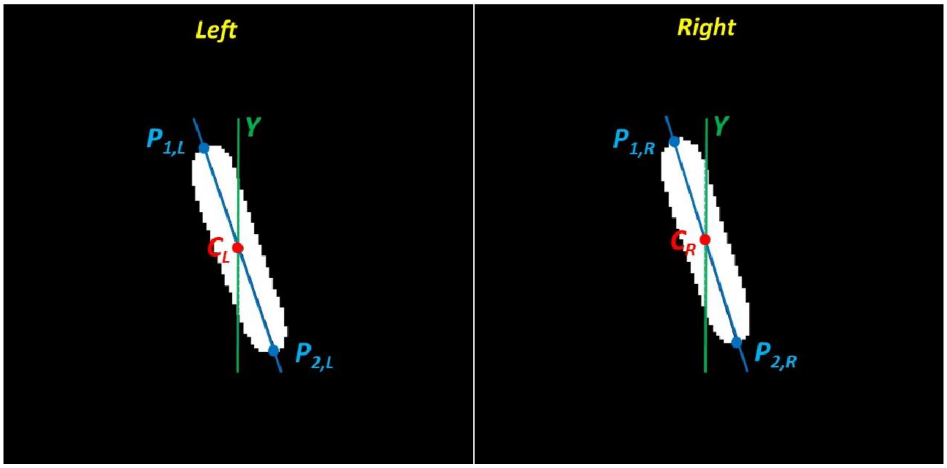

Figure 4.11 Centroid C and points P_1 and P_2 on both left and right sides of the stereo image corresponding to a cylindrical particle.

The complete list of digital image processing operations exposed in this section is summarised in the flowchart of Figure 4.12. For the execution of every operation in an automated way, various computer programs were written and run in Matlab. They are listed in Appendix G, at the end of the thesis.

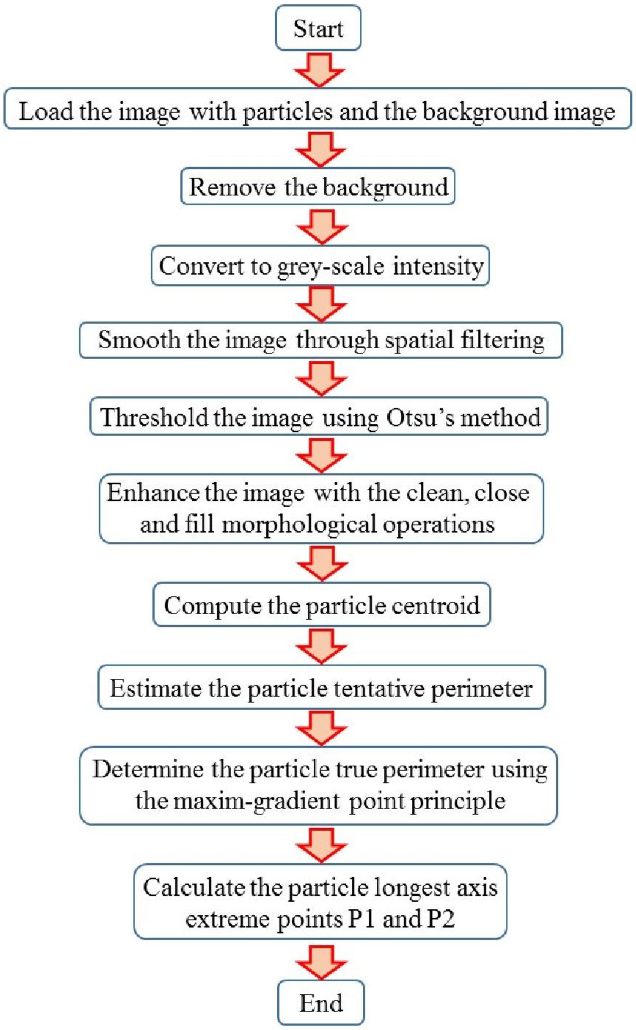

Figure 4.12 Flowchart of the digital image processing operations used in this research.

4.2 3D PARTICLE MOTION IN THE WORLD REFERENCE FRAME

Once the three-dimensional coordinates of points C, P_1, and P_2 were reconstructed, they were projected from the left camera frame to the world reference frame using Equation (3.32), so that all the analysis can be effectuated within this frame. Assuming that at time t_1 the position of the particle centroid was C_1 (x_1, y_1, z_1), and at time t_2 it was C_2 (x_2, y_2, z_2), respectively, then the displacement vector $\boldsymbol{D}$ between the two consecutive times was obtained as follows

$$\boldsymbol{D} = (x_2 - x_1)\boldsymbol{i} + (y_2 - y_1)\boldsymbol{j} + (z_2 - z_1)\boldsymbol{k} \tag{4.15}$$

The magnitude of vector $\boldsymbol{D}$ is defined as the travelled distance between those two positions. Provided that the time increment $\Delta t = t_2 - t_1$ is equal to the inverse of the frame rate at which the stereo pictures were taken, the corresponding particle velocity vector $\boldsymbol{V_P}$ was computed with the next equation

$$\boldsymbol{V_P} = \frac{\boldsymbol{D}}{\Delta t} \tag{4.16}$$

The magnitude of vector $\boldsymbol{V_P}$ is called the particle speed v_p. Analogous accelerations of the body could also be computed in a similar way by working with the velocity vector, nevertheless, the analysis can acquire a more significant meaning if the accelerations are derived within a Frenet reference frame moving with the particle, as exposed Section 4.3.

In Figure 4.13a the motion of a 6.4-mm nylon sphere falling freely in quiescent air is displayed through some selected stereo images after full enhancement and centroid detection. The fall 3D trajectory within the world reference frame is exhibited in Figure 4.13b, and the respective velocity plot is shown in Figure 4.13c, where it can be observed that the speed kept increasing continuously, proving that terminal velocity conditions were not achieved. When the sphere left the field of view, it had a velocity equal to 3.45 m/s, equivalent to $Re_P = 1465$.

In the case of non-spherical particles, the 3D reconstructed points P_1 (x_{11}, y_{11}, z_{11}) and P_2 (x_{22}, y_{22}, z_{22}) were utilized to determine the longest axis in the world reference frame as indicated with the next equation

$$\boldsymbol{P_1P_2} = (x_{22} - x_{11})\boldsymbol{i} + (y_{22} - y_{11})\boldsymbol{j} + (z_{22} - z_{11})\boldsymbol{k} \tag{4.17}$$

where $\boldsymbol{P_1P_2}$ represent the longest axis vector. Provided that the free-stream fluid velocity vector $\boldsymbol{U_\infty}$ marked in Figure 2.5 (Section 2.2.2) could be approximated by the particle velocity vector $\boldsymbol{V_P}$ for free-fall conditions, the angle of incidence α was calculated as follows

$$\alpha = acos\left(\frac{\boldsymbol{P_1P_2}\cdot\boldsymbol{V_P}}{|\boldsymbol{P_1P_2}||\boldsymbol{V_P}|}\right) \tag{4.18}$$

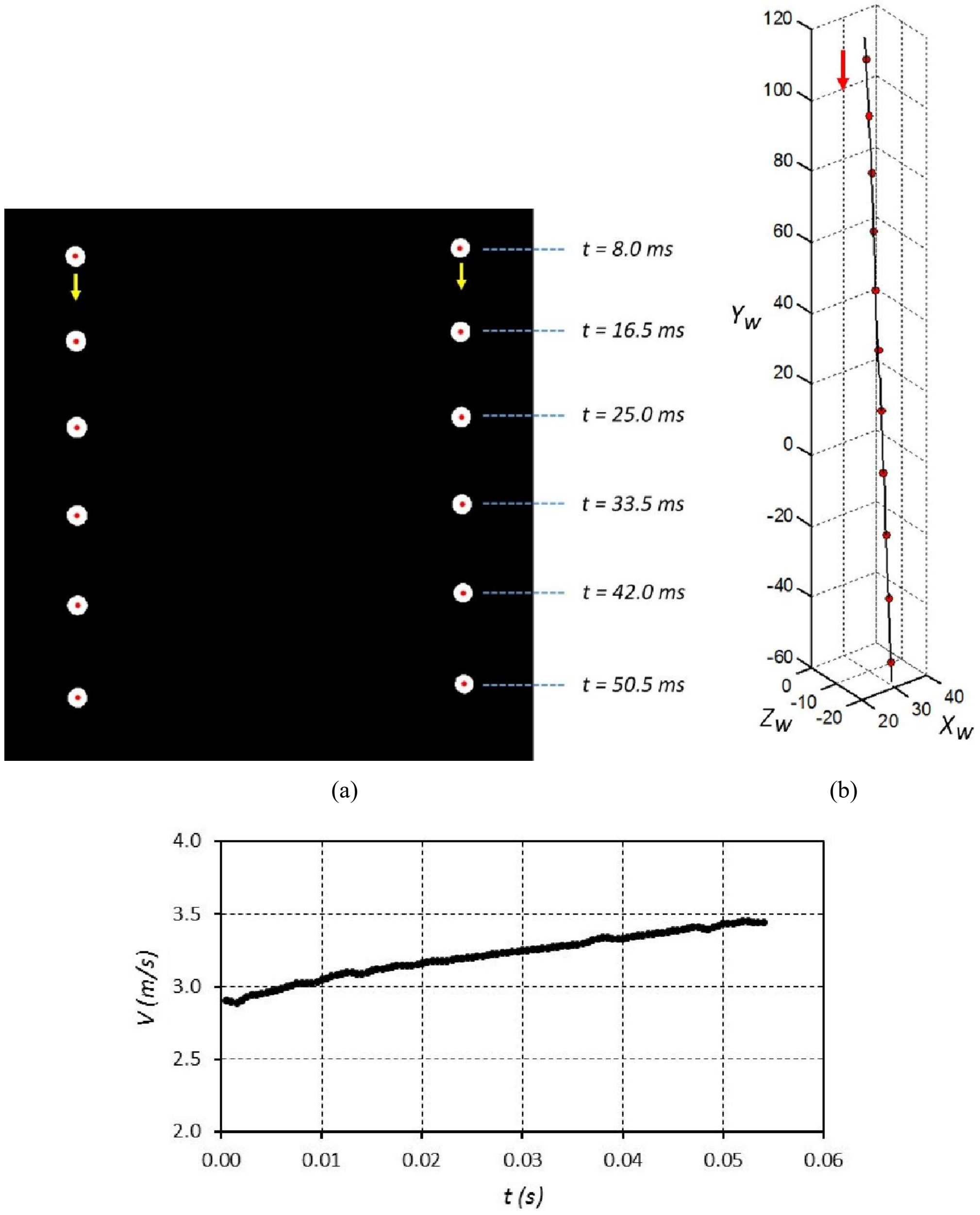

(a)

(b)

(c)

Figure 4.13 Selected stereo images of a 6.35-mm nylon sphere falling freely in quiescent air after enhancement and centroid detection (a), corresponding fall path reconstructed in 3D in the world reference frame (b), and time-velocity plot (c). Re_P = 1465. The dimensions in the 3D plot are expressed in mm.

Figure 4.14a portrays a stereo visualisation of the free-fall of a wood cylinder, with dimensions 1.9 mm × 10.5 mm, in quiescent air. The cylinder was originally dropped in vertical position, however it can be appreciated that it did not keep that orientation throughout the fall. The 3D path described by the cylinder centroid is plotted in Figure 4.14b, where the longest axis at some randomly chosen positions was highlighted with blue lines. From the plot of velocity in Figure 4.14c, it can be seen that a steady, terminal velocity value was not reached. Its velocity at the exit of the field of view was 3.32 m/s, equivalent to $Re_P = 861$. The nominal diameter was 3.9 mm.

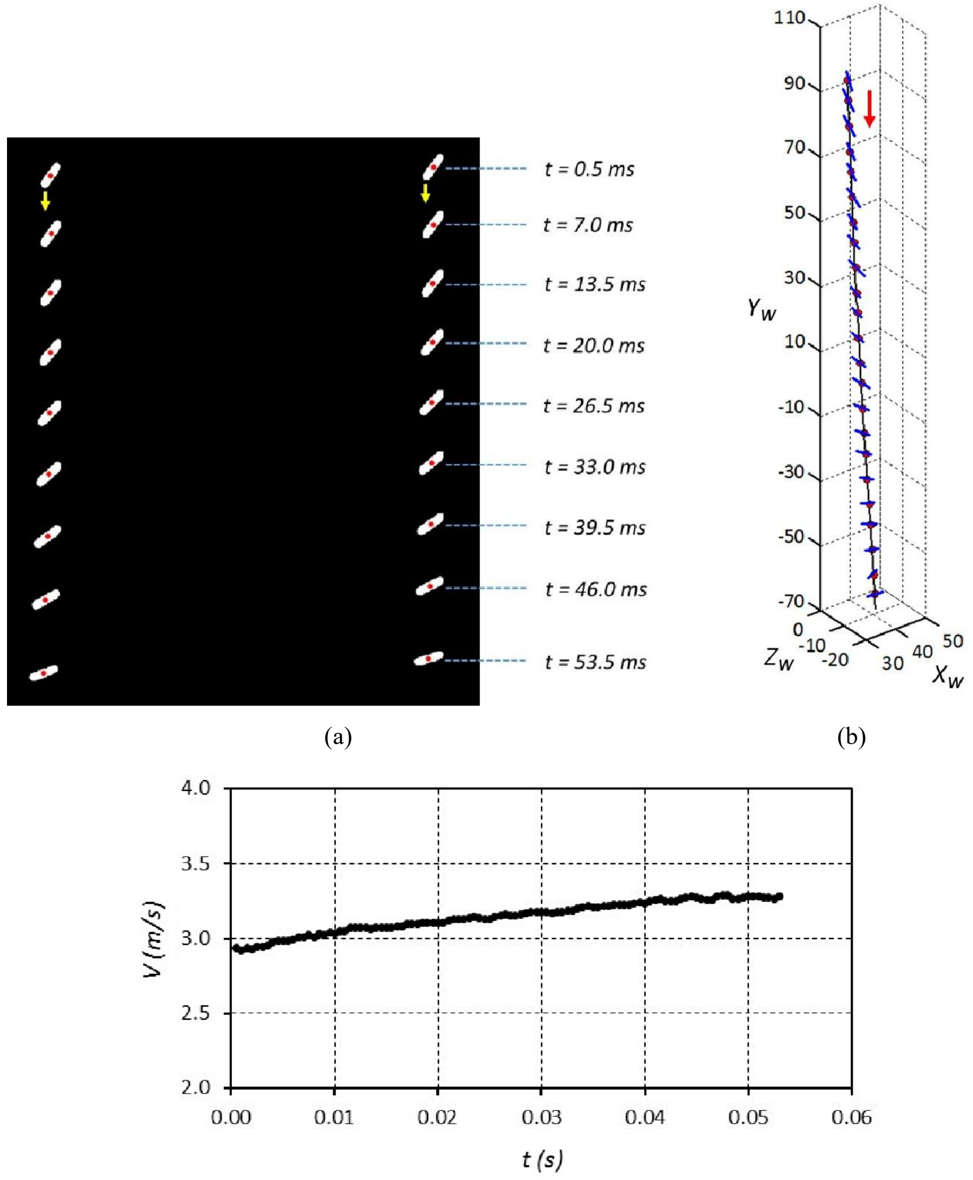

(a) (b)

(c)

Figure 4.14 Selected stereo pictures of a 1.9 mm x 10.5 mm wood cylinder during its fall in quiescent air (a), 3D trajectory in the world frame (b), and velocity plot (c). The blue lines denote the cylinder longest axis orientation. Dimensions in mm. $Re_P = 861$.

Through the application of Equation (4.18) the magnitude of the cylinder angular orientation was computed at each time instant. The corresponding plot is shown in Figure 4.15, where it can be noticed that a change of 25° occurred within the field of view. If the values of the angle of incidence and the dimensions of the particle are both known, the true projected area can be obtained straightforward.

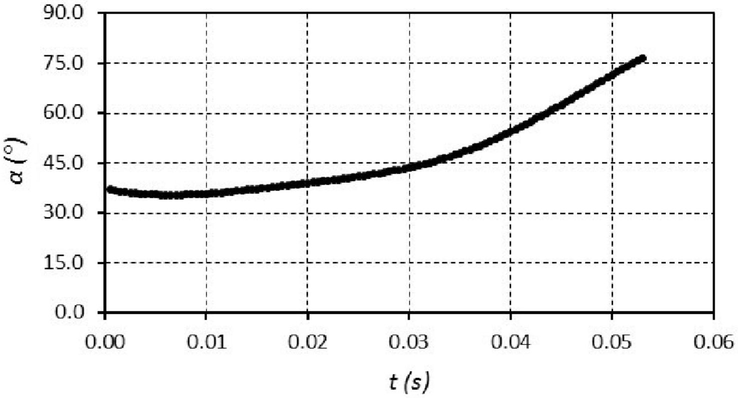

Figure 4.15 Variation of the angle of incidence in the fall of cylinder of Figure 4.14.

4.3 3D PARTICLE MOTION IN A FRENET REFERENCE FRAME

In order to determine the drag force exerted on the moving solid, a Frenet reference frame with origin on the centroid and orientation dependent on the path curve was employed, as displayed in Figure 4.16, following an approach similar to that of Veldhuis et al. [70]. So long as the time is the parameter in common for the three world coordinate frame axes X_W, Y_W, and Z_W, the curve can be parameterized as follows

$$\sigma(t) \equiv \langle X_W(t), Y_W(t), Z_W(t) \rangle \tag{4.19}$$

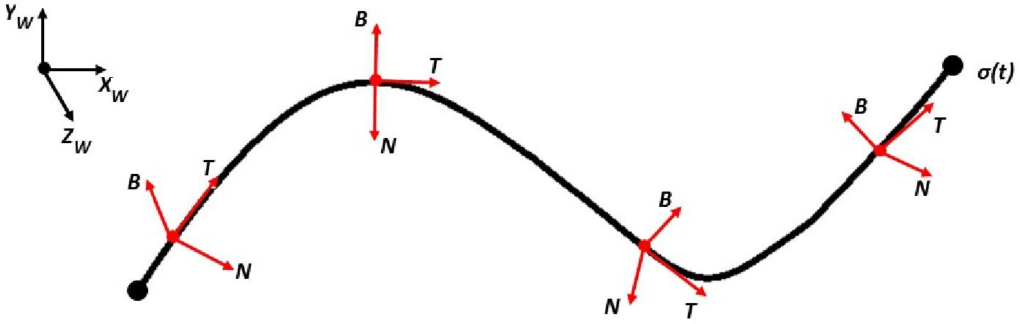

Figure 4.16 World reference frame (black), and moving Frenet reference frame (red) on a 3D curve $\sigma(t)$.

Assuming that $\sigma(t)$ is smooth in $\mathbb{R}^3$ for all $t \in (a,b)$, then $\dot{\sigma}(t) \equiv d\sigma/dt \neq 0$, and the curve can be re-parameterized in terms of the arc-length s, resulting in $\sigma = \sigma(s)$. The arc-length can be understood as the distance the particle travels from an initial time $t_0 \in (a,b)$ to a final time t also included in the same interval. Consequently, it can be defined as

$$s(t) \equiv \int_{t_0}^{t} \|\dot{\sigma}(t)\|\, dt \tag{4.20}$$

where $\|\dot{\sigma}(t)\|$ is the speed v of the particle. Once $\sigma(s)$ is known, the triplet formed by the tangent $\boldsymbol{T}$, normal $\boldsymbol{N}$, and binormal $\boldsymbol{B}$ unit vectors which constitute the Frenet frame (Figure 4.16) can be determined using the next equations

$$\boldsymbol{T}(s) \equiv \frac{d\sigma}{ds} \tag{4.21}$$

$$\boldsymbol{N}(s) \equiv \frac{d\boldsymbol{T}}{ds}/K(s) \tag{4.22}$$

$$\boldsymbol{B}(s) \equiv \boldsymbol{T} \times \boldsymbol{N} \tag{4.23}$$

where

$$K(s) \equiv \left\|\frac{d\boldsymbol{T}}{ds}\right\| \tag{4.24}$$

is a positive scalar known as the curvature, and represents the extent to which the path deviates from a straight line. The inverse of the curvature is called the radius of curvature $\zeta = 1/K$. Another important parameter is the torsion τ, which measures the amount by which the curve is twisted. It is computed from

$$\tau(s) \equiv -\left(\frac{d\boldsymbol{B}}{ds}\right)\frac{1}{\boldsymbol{N}} \tag{4.25}$$

Contrary to K, τ can be either positive or negative. Some propositions derived from the Frenet theory are: 1) any curve with $\tau = 0$ is planar, 2) the curvature of a straight line is 0, and 3) only planar circles can have a non-zero constant value of ζ. Most of the times the arc-length re-parameterization of the path is either too complicated or impossible, in consequence, provided that $K(s) \neq 0$ for all $s \in (a,b)$, re-parameterizing can be skipped and $\{\boldsymbol{T}, \boldsymbol{N}, \boldsymbol{B}, K, \tau\}$ are directly computed with the following equations

$$\boldsymbol{T}(t) = \frac{\dot{\sigma}}{\|\dot{\sigma}\|} \tag{4.26}$$

$$\boldsymbol{B}(t) = \frac{\dot{\sigma} \times \ddot{\sigma}}{\|\dot{\sigma} \times \ddot{\sigma}\|} \tag{4.27}$$

$$\boldsymbol{N}(t) = \boldsymbol{B} \times \boldsymbol{T} \tag{4.28}$$

$$K(t) = \frac{\|\dot{\sigma} \times \ddot{\sigma}\|}{\|\dot{\sigma}\|^3} \tag{4.29}$$

$$\tau(t) = \frac{(\dot{\sigma} \times \ddot{\sigma}) \cdot \dddot{\sigma}}{\|\dot{\sigma} \times \ddot{\sigma}\|^2} \tag{4.30}$$

In the context of the Frenet reference frame, the kinematics of the particle can be fully determined, provided that the vectors corresponding to the tangential velocity $\boldsymbol{V_T}$ and acceleration $\boldsymbol{a_P}$ can be expressed as follows

$$\boldsymbol{V_T} = \dot{\sigma} = \nu \boldsymbol{T} \tag{4.31}$$

$$\boldsymbol{a_P} = \frac{d\nu}{dt}\boldsymbol{T} + \frac{\nu^2}{\zeta}\boldsymbol{N} \tag{4.32}$$

where the first term in the right-hand side of Equation (4.34) denotes the tangential acceleration $\boldsymbol{a_T}$, which is the rate of change of the magnitude of the velocity vector in the tangential direction, whilst the second term connotes the normal acceleration $\boldsymbol{a_N}$, which indicates the rate of change of the direction of the velocity vector in an orthogonal direction.

The mathematical development from Equation (4.19) to Equation (4.32) assumes that X_W, Y_W, and Z_W are expressed as smooth and regular functions of time, which was not the case for this investigation, nevertheless, since X_W, Y_W, and Z_W were equally spaced in time, it was possible to approximate their derivatives using finite difference equations. For such a task, the forward, backward, and centred finite difference schemes were used, depending on which points were known. The equations involved in the three schemes are listed in Appendix F.

For the computation of the forces involved in the motion of the single particle, the form of the linear momentum equation, Equation (2.18), proposed by Mandø and

Rosendahl [30] to simulate the motion of a cylindrical biomass particle in a given flow field $\boldsymbol{u}$ was applied in this research. At free-fall conditions, and considering that the fluid is at rest ($\boldsymbol{u} = \boldsymbol{0}$), this equation can be rewritten as

$$m\frac{d\boldsymbol{V_P}}{dt} = \left(m - m_f\right)\boldsymbol{g} - \frac{1}{2}m_f\frac{d\boldsymbol{V_P}}{dt} + \boldsymbol{F} \tag{4.33}$$

where any non-inertial or buoyancy force is comprised into one single force term $\boldsymbol{F}$, which is the outcome of the presence of vorticity in the flow according to Mougin and Magnaudet [108]. Acknowledging that $d\boldsymbol{V_P}/dt$ corresponds to the particle acceleration vector $\boldsymbol{a_P}$ and that the mass of the fluid displaced due to translation and rotation of the solid is $m_f = \rho_f \forall$, Equation (4.35) can be further re-stated as follows

$$\left(1 + \frac{\rho_f}{2\rho_P}\right)m\boldsymbol{a_P} - \left(1 - \frac{\rho_f}{\rho_P}\right)m\boldsymbol{g} = \boldsymbol{F} \tag{4.34}$$

From Equation (4.34) it is explicit that the particle accelerates as if its total mass were that of its own plus half of that which the fluid displaces. Since the motion kinematics are fully resolved in the Frenet reference frame, it seems natural to continue the analysis within it. Consequently, the decomposition of Equation (4.34) into its tangential, normal, and binormal components results in

$$\left(1 + \frac{\rho_f}{2\rho_P}\right)ma_T - \left(1 - \frac{\rho_f}{\rho_P}\right)mg_T = F_T \tag{4.35}$$

$$\left(1 + \frac{\rho_f}{2\rho_P}\right)ma_N - \left(1 - \frac{\rho_f}{\rho_P}\right)mg_N = F_N \tag{4.36}$$

$$-\left(1 - \frac{\rho_f}{\rho_P}\right)mg_B = F_B \tag{4.37}$$

which are the same equations employed by Veldhuis et al. [70] to approximate the variation of the virtual momentum of freely rising spheres in a fluid at rest. The quantities F_T, F_N, and F_B are the instantaneous tangential, normal, and binormal Frenet forces, respectively. Once the Frenet forces are determined, the authors suggested that the drag force vector could then be predicted with the next equation

$$\boldsymbol{F_D} = F_T\boldsymbol{T} \tag{4.38}$$

In Equations (4.35) to (4.37), g_T, g_N ,and g_B are the tangential and normal components of the gravity acceleration vector. In the world reference frame, this vector is expressed as $\boldsymbol{g} = -9.81\boldsymbol{i}\ \ (m/s^2)$. In this work, such components were calculated by projecting $\boldsymbol{g}$ onto the directions of $\boldsymbol{T}$, $\boldsymbol{N}$, and $\boldsymbol{B}$. In summary, the procedure applied in the current investigation for the computation of the drag force is portrayed in the flow chart of Figure 4.17.

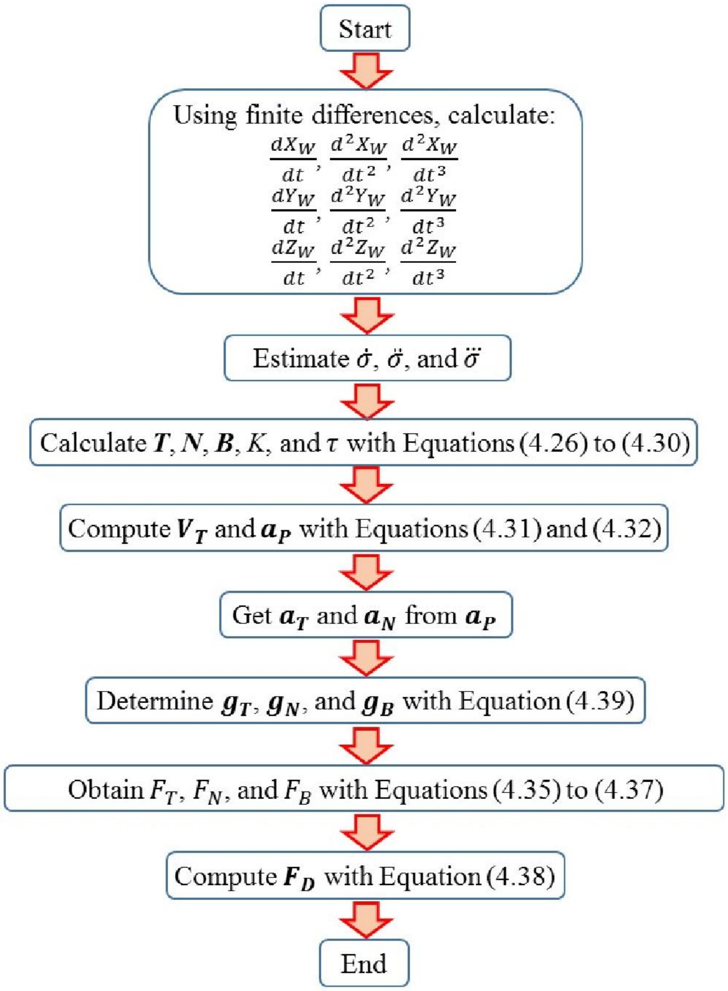

Figure 4.17 Flowchart of the methodology used for the computation of the drag force.

For the completion of each step of the methodology of Figure 4.17 different computer programs were written and executed in Matlab. They are listed in Appendix G, at the end of the thesis. With this last figure, the review of the procedure followed to determine the particle orientation, velocity, and drag force in a non-intrusive way is completed. Also, by using these data, the calculation of the drag coefficient can be achieved easily, as demonstrated in the next chapters.

Chapter 5

INVESTIGATION OF THE MOTION OF REGULAR PARTICLES IN FREE FALL USING STEREO VISION AND SCHLIEREN – PART 1

In the previous chapters the necessity of doing a comprehensive study on the influence of angular orientation on the main parameters of the free motion of a single particle in a fluid was highlighted. Moreover, it was also revised how such study can be accomplished in three dimensions through the use of single-camera stereo vision and digital image processing. Furthermore, the generation of additional qualitative information by photographing the flow with a Z-type Schlieren arrangement was explained too. Hence, the goal of this chapter as well as of the next one is the application of such techniques and methods to the case of regular particles (spheres, cylinders, and disks) settling in quiescent viscous fluids, as an effort to meet the necessity previously mentioned.

The study is divided in two parts, each of them making one chapter. The first part is reviewed in this chapter and includes the geometrical characterisation of all of the particles studied, the description of the experimental installation and methodology, the discussion of the camera calibration results, and the examination of the data obtained for the case of spherical particles only. The second part of the study corresponds to the analysis of the other two shapes (cylinders and disks) and constitutes Chapter 6. Along both chapters, visualizations of the flow around the objects from both Schlieren and direct photography are illustrated for some cases.

Given the fact that a sphere does not have an angular orientation, only the kinematics and dynamics of its centroid are considered relevant for the purpose of this investigation. Therefore, only the velocity, drag force, and coefficient of resistance are computed. At the end of the chapter, the experimental results of the drag coefficient are compared in a $\log(Re_P) - \log(C_D)$ plot against those predicted with the literature correlations listed in Section 2.2 for spherical shapes. In this way, the generated graph can be used as a validation tool for the techniques and methodologies described in this investigation to determine the motion parameters of particles settling freely in liquids at rest.

5.1 CHARACTERISATION OF THE PARTICLES

The regular particles used to do this study on free-motion are made of three geometrical shapes: sphere, cylinder, and disk. Images of them are provided in Figure 5.1. All of the particles were made of one of the next materials: nylon, polytetrafluoroethylene (PTFE), aluminium, and brass. The density of each material is listed in Table 5.1. Because all the geometric quantities relevant for this study can be expressed in terms of the diameter only, the characterisation of the spherical particles was relatively easy and straightforward. The results are shown in Table 5.2.

Table 5.1 Density of the materials employed to make the particles.

Material	ρ_P **(kg/m³)**
Nylon	1136
PTFE	2160
Aluminium	2690
Brass	8400

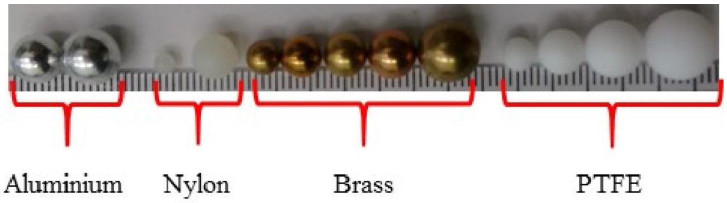

Figure 1 Spherical particles.

Table 5.2 Geometrical characterisation of the spheres.

d **(mm)**	**Material**	***S*** **(mm²)**	**∀ (mm³)**	**Name**
3.0	Nylon	28.3	14.1	S1
4.8	PTFE	71.2	56.5	S2
5.0	Brass	78.5	65.4	S3
6.0	Brass	113.1	113.1	S4
6.4	Nylon	126.7	134.1	S5
6.4	PTFE	126.7	134.1	S6
6.4	Brass	126.7	134.1	S7
7.0	Aluminium	153.9	179.6	S8
7.9	PTFE	198.1	262.1	S9
9.0	Brass	254.5	381.7	S10
9.5	PTFE	285.3	453.2	S11

Contrary to the spheres, the geometrical description of the cylinders and disks depends on two variables: the diameter, and the length or thickness. Additionally, besides the calculation of the area and volume, it requires too the computation of the nominal diameter, sphericity, and aspect ratio, which was effectuated through Equations (2.1), (2.2), and (2.7), respectively. The results are summarised in Tables 5.3 and 5.4, and images of the particles are displayed in Figures 5.2 and 5.3, respectively.

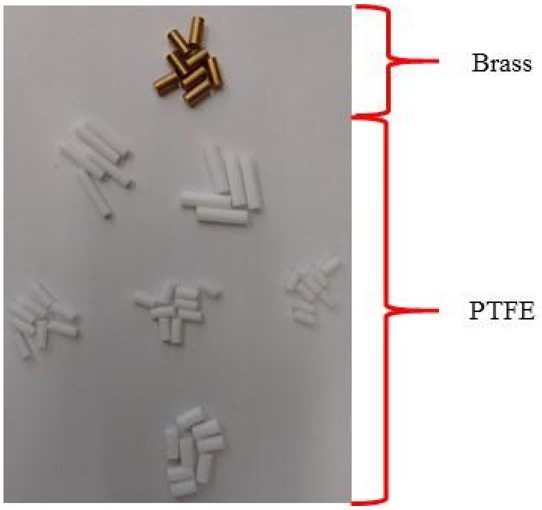

Figure 5.2 Cylindrical particles.

Table 5.3 Geometrical characterisation of the cylinders.

d (mm)	L (mm)	Material	S (mm^2)	$\forall$ (mm^3)	d_n (mm)	$\varnothing$	σ	Name
5.0	10.2	Brass	199.6	200.5	7.3	0.8	2.0	C1
4.0	8.3	PTFE	129.9	104.8	5.8	0.8	2.1	C2
4.0	9.2	PTFE	140.1	115.0	6.0	0.8	2.3	C3
4.0	10.4	PTFE	156.3	131.2	6.3	0.8	2.6	C4
4.0	20.2	PTFE	279.5	254.3	7.9	0.7	5.1	C5
5.0	10.4	PTFE	203.3	205.0	7.3	0.8	2.1	C6
5.0	20.3	PTFE	357.8	398.2	9.1	0.7	4.1	C7

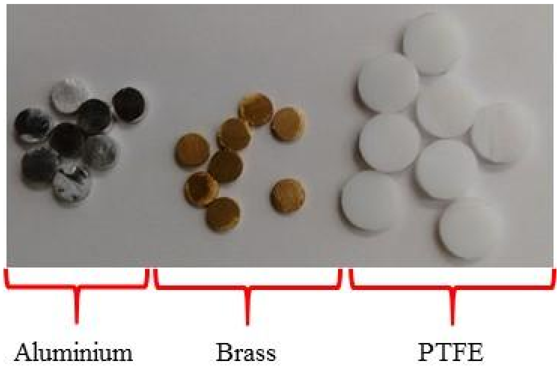

Figure 5.3 Disk-shaped particles.

Table 5.4 Geometrical characterisation of the disks.

d (mm)	L (mm)	Material	S (mm^2)	$\forall$ (mm^3)	d_n (mm)	$\varnothing$	σ	Name
6.0	1.6	Brass	86.0	44.1	4.4	0.7	0.3	D1
6.4	2.5	Aluminium	113.6	79.8	5.3	0.8	0.4	D2
10.0	2.9	PTFE	248.2	227.8	7.6	0.7	0.3	D3

From Tables 5.3 and 5.4 it can be seen that the nominal diameter ranged from 4.4 mm to 9.1 mm, and the sphericity fluctuated considerably less between 0.7 and 0.8. In addition, whilst the aspect ratio for the cylinders varied from 2.0 to 5.1, for the disks it stayed below 1.0. Only these three shape descriptors were determined since they are the most used ones in the drag correlations, however other parameters could also be calculated.

5.2 EXPERIMENTAL INSTALLATION AND METHODOLOGY

In Figure 5.4 the schematic of the installation employed for the stereo vision studies is illustrated. The camera, lens, stereo adapter, and illumination source shown are the same ones used during the accuracy test of the stereo system. Their specifications are detailed in Section 3.4. The tank was made of 6-mm thick glass, and had the following dimensions: 0.2 m × 0.2 m × 0.4 m. It was placed 1.1 m away from the stereo adapter. The ordinary, plastic funnel was big enough for the particles to pass through freely.

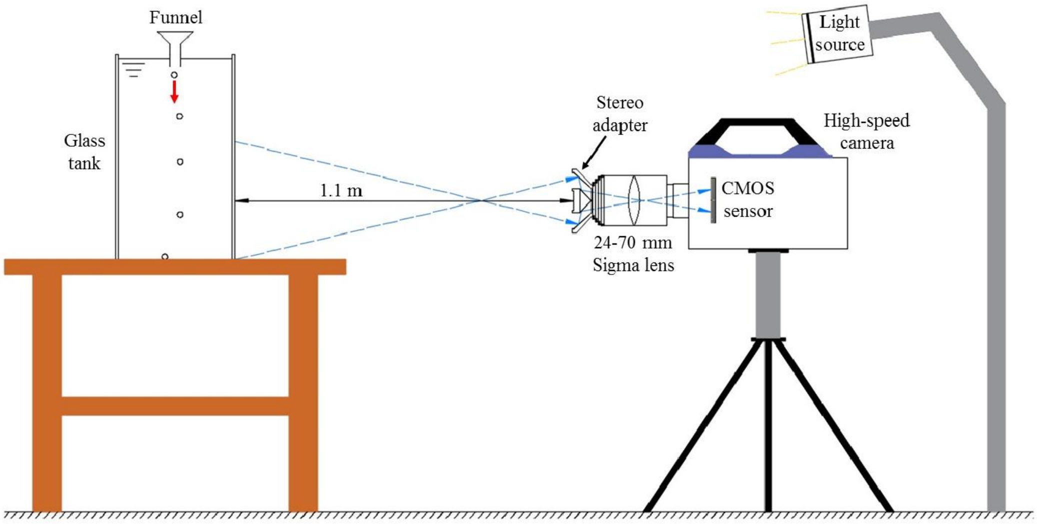

Figure 5.4 Schematic of the experimental installation for the stereo vision studies.

The Schlieren pictures of the surrounding flow structures were recorded with the setup portrayed in Figure 5.5. In order to generate the required density gradients, the recommendations given by Fiedler and Nottmeyer [91] were applied, therefore the fluid was heated from the top with the assistance of an incandescent lamp. Before each particle was dropped, the temperature of the liquid was measured at the top, centre, and bottom levels of the tank, and the average was used in the calculations. The measuring instrument was the Testo 905-T1 digital, immersion thermometer shown in Figure 5.6. Its equipped with a type–K thermocouple sensor, able to measure the temperature in the range: -50 °C to 350 °C, with a resolution of 0.1 °C and accuracy of ±1 °C. The camera used for the Schlieren recordings was the same one employed for the stereo vision studies.

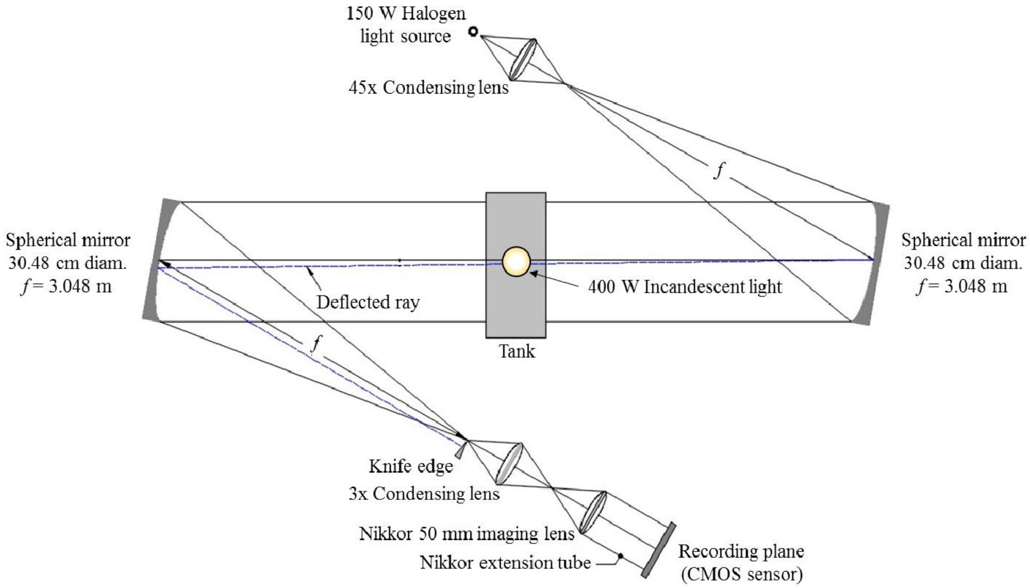

Figure 5.5 Diagram of the Schlieren setup used in the investigation.

Figure 5.6 Testo 905-T1 digital, immersion thermometer.

As mentioned in Section 2.2.2, Marchildon et al. [25] argued that any object in free fall will always exhibit the same pattern of terminal flow. In consequence the method of release is practically irrelevant, thus in this investigation the particles were dropped manually in all the cases. The pictures for both stereo and Schlieren were recorded at 500 frames per second with a resolution of 1024 × 1024 pixels. To reduce the risk of bubble formation and splash, the lower end of the funnel was carefully located just underneath the fluid level.

Besides using different materials and sizes for the particles, pure water, pure glycerine, and three mixtures of water and glycerine were also employed as working fluids to ensure that a wide range of particle Reynolds numbers could be achieved. In Table 5.5 the properties of the fluids at the average temperature are provided. The percentages were expressed by weight. The glycerine and water-glycerine mixtures were not suitable fluids for Schlieren visualisation because they did not allow an appropriate transmission of the light, consequently Schlieren visualisation was done only for the cases where pure water was utilized.

Table 5.5 Working fluids and their properties at the average temperature registered in the tank. The properties were taken from the Glycerine Producers Association [109].

Mixture Name	% wt. Glycerine	% wt. Water	$T_{f,avg}$ (°C)	ρ_f (kg/m^3)	μ (Pa·s)
100/0	100	0	20	1261.1	1.400
80/20	80	20	25	1205.5	0.047
65/35	65	35	30	1162.0	0.010
50/50	50	50	30	1121.1	0.004
0/100	0	100	20	998.2	0.001

Not all of the particles were dropped in each fluid mixture, instead, every experiment was done according to a number of previously targeted Reynolds numbers within the interval $0.1 < Re_P < 5000$. The corresponding list is presented in Table 5.6. Each drop was repeated 3 times to ensure consistency in the analysis; however, in a later experiment, the fall of sphere S1 in mixture 100/0 was repeated 9 times in order to estimate the uncertainty of the results. Before every particle was released, the temperature of the mixture was measured. In addition, between two consecutive droppings some time was allowed to pass in order to let the fluid stabilise.

Table 5.6 Matrix of experiments.

Mixture Name	Particles Dropped
100/0	S3, S4, C1
80/20	S2, S3, S8, S9, S11, C2, C4, C6, D1 – D3
65/35	S3, S4, S6 – S8, C4 – C7, D1 – D3
50/50	S6, C2, C3, C6, D3
0/100	S1, S5, S11, C4, D3

5.3 CALIBRATION OF THE STEREO VISION SYSTEM

Before pouring any liquid into the tank, the pair of virtual cameras of the stereo vision system were calibrated using the methodology explained in Figure 3.11 of Section 3.2.2. The results of the calibration are summarised in Table 5.7. Recalling that the dimensions of the CMOS sensor are 20.48 mm × 20.48 mm, and considering the intrinsic matrix of the left camera, the values of the skewedness angle and the pixel aspect ratio were 1.0 and 89.8°, respectively, demonstrating that the horizontal and vertical edges of the sensor are practically perpendicular to each other and that the pixels are square. Moreover, the determined horizontal and vertical focal lengths were equal to 46.1 mm and 45.6 mm, respectively, and the principal point offset (u_0, v_0) was (10.1, 10.5) mm, nearly located at the centre of the sensor. The coordinates of the left camera centre vector ***C*** were (0.06, 0.15, 1.10) m, denoting a noticeably agreement with the setup shown in Figure 5.4. Also, the estimated radial distortion coefficients were c_1 = -0.093 and c_2 = 0.450.

Table 5.7 Calibration results of both virtual cameras.

Left Camera		
Intrinsic matrix *A*	Rotation matrix *R*	Translation vector ***t***
$\begin{bmatrix} 2305.85 & -9.86 & 505.32 \\ 0 & 2278.39 & 527.16 \\ 0 & 0 & 1 \end{bmatrix}$	$\begin{bmatrix} -0.99 & 0.01 & -0.15 \\ -0.02 & -1.00 & 0.08 \\ -0.15 & 0.08 & 0.99 \end{bmatrix}$	$\begin{bmatrix} 8.70 \\ 2.88 \\ 42.23 \end{bmatrix}$
Right Camera		
Intrinsic matrix *A*	Rotation matrix *R*	Translation vector ***t***
$\begin{bmatrix} 2272.84 & -4.29 & 523.33 \\ 0 & 2245.97 & 549.14 \\ 0 & 0 & 1 \end{bmatrix}$	$\begin{bmatrix} 0.98 & -0.03 & 0.21 \\ 0.02 & 1.00 & 0.06 \\ -0.21 & -0.05 & 0.98 \end{bmatrix}$	$\begin{bmatrix} 3.38 \\ -3.52 \\ -43.12 \end{bmatrix}$

Once all of the experiments were finished and all of the particle stereo pictures were digitally processed to extract the 2D pixel coordinates of points *C*, P_1, and P_2 of both the left and right images, in agreement with the procedure discussed in Figure 4.12 of Section 4.1, the methodology explained in Figure 3.13 of Section 3.3.2 and Equation (3.32) were applied to find the 3D coordinates of such points in the world reference frame, so that the subsequence kinematic and dynamic analysis described in Sections 4.2 and 4.3 could be executed.

5.4 KINEMATICS AND DYNAMICS OF SPHERICAL PARTICLES AT DIFFERENT REYNOLDS NUMBERS

The smallest value of the particle Reynolds number found in the study for the spheres only was Re_P = 0.3, whilst the largest one was Re_P = 4939, therefore covering the targeted interval. The results equivalent to $Re_P = 0.3$, which also is the upper limit of Stokes' law, were those of the brass sphere S3 falling in pure glycerine. In this case, the travel path was practically vertical throughout the whole field of view, as portrayed in Figure 5.7 in three dimensions. It is believed that this behaviour was produced by the dominance of the viscous forces at such low values of Re_P, which kept the flow streamlines symmetrically attached to the object causing no appreciable disturbances, as suggested by Magarvey and Bishop [57], and Moradian et al. [60].

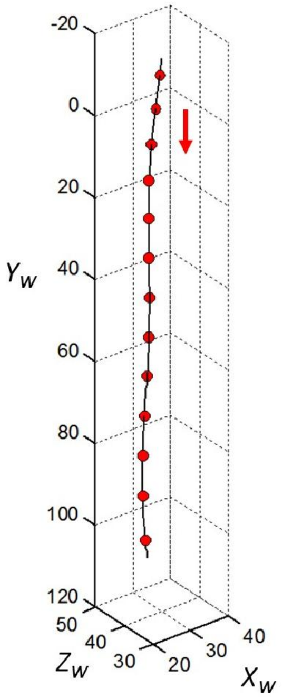

Figure 5.7 3D fall path of sphere S3 in pure glycerine ($Re_P = 0.3$). Scale in mm.

In Figure 5.8 the variation of the velocity of the particle, computed with Equation (4.18), is plotted as a function of time. The theoretical value of U_T, estimated with Equation (2.10), is also drawn with a red, dotted line. At $t = 0.7$ s, approximately, terminal conditions were reached. Moreover, both the experimental and predicted magnitudes of U_T agreed at 0.06 m/s after the marked time limit. The particle Reynolds number at this velocity, calculated with Equation (2.14), was $Re_P = 0.3$.

By following the methodology of Figure 4.17 in Section 4.3 the motion of the sphere was analysed within the moving Frenet frame of reference in order to estimate the drag force experienced by the particle. In Figure 5.9 the values of F_D are plotted with respect to time. It can be observed that a relatively constant magnitude of 4.5 mN remained at terminal velocity conditions. The slight drop after t = 2.0 s could be a consequence of the proximity to the bottom of the tank. The drag force predicted by the law of Stokes (Equation 2.15) was 4.0 mN, 11 % below the experimental result.

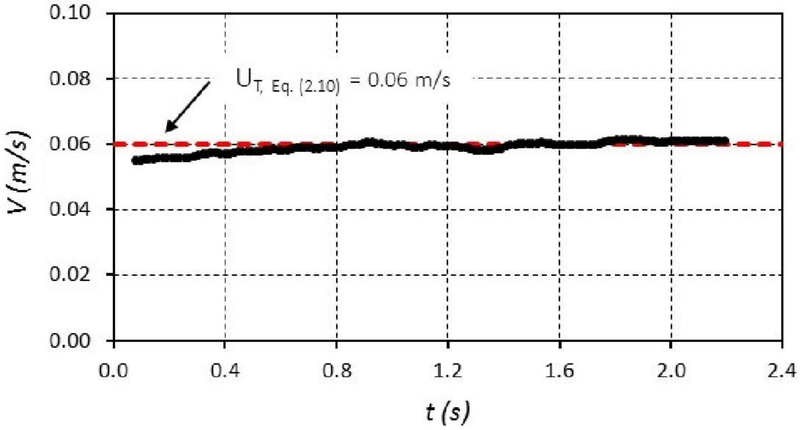

Figure 5.8 Velocity plot of sphere S3 falling in pure glycerine at $Re_P = 0.3$.

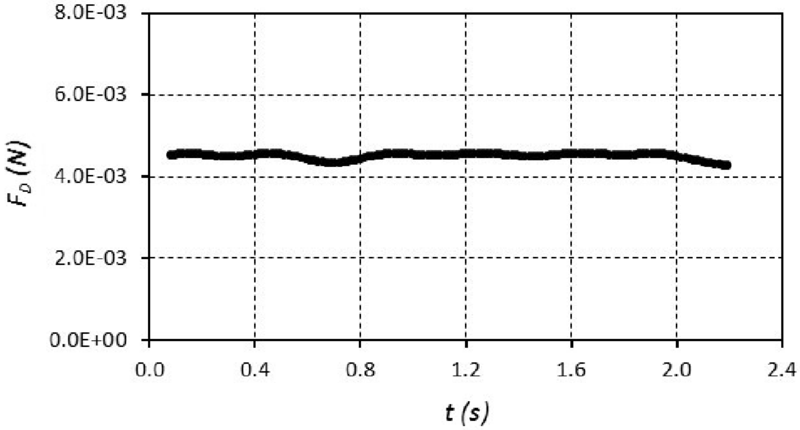

Figure 5.9 Graph of the drag force exerted on sphere S3 whilst settling in pure glycerine at $Re_P = 0.3$.

Since the projected area of a sphere is always that of a circle with the same radius, it was possible to compute the drag coefficient at each instant with Equation (2.8) and to plot it against time, as depicted in Figure 5.10. For comparison, the coefficient predicted by Equation (2.23b) of Haider and Levenspiel [16] was also included in the graph. At final velocity conditions an average value of C_D equal to 101.0 was found, given the fact that fluctuations were registered. Nevertheless, the difference with respect to the correlation results was just 5 %.

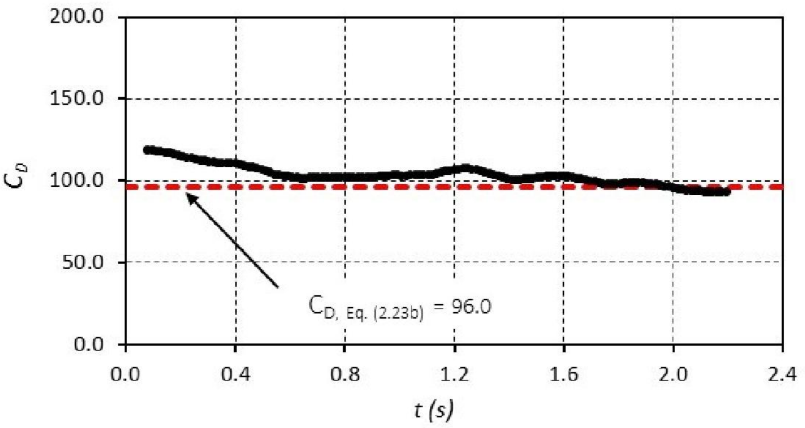

Figure 5.10 Plot of the coefficient of resistance obtained for the fall of sphere S3 in pure glycerine at $Re_P = 0.3$.

Still inside the interval $Re_P < 1.0$, the settling of 6-mm sphere S4 in pure glycerine exhibited a similar behaviour to S3 at terminal velocity conditions. The results achieved are listed in Table 5.8, where the theoretical values are also contained for the purpose of comparison. The proximity between both was evident for U_T and Re_P, but not for F_D, suggesting that the motion did not obey the law of Stokes anymore. Additionally, the values of C_D were also marginally different.

Table 5.8 Experimental and theoretical results at terminal velocity conditions for the 6-mm, brass sphere S4 falling in pure glycerine.

Parameter	Experimental Result	Theoretical Value	% Difference
U_T	0.09 m/s	0.08 m/s (Eq. 2.10)	13.0
Re_P	0.5	0.5	0.0
F_D	7.9 mN	6.3 mN (Eq. 2.15)	20.0
C_D	56.9	58.9 (Eq. 2.23b)	3.0

As explicated in Section 2.2.4, further increments of Re_P make the streamlines separate from the object creating a zone of fluid recirculation at the rear, highly symmetrical and balanced in the beginning, but unstable at larger values of the Reynolds number, thus deviating the particles from a vertical trajectory [57, 68]. These characteristics can be observed in Figure 5.11, which corresponds to PTFE sphere S9 sinking freely in mixture 80/20 at $Re_P = 43.4$. Additionally, the path deviation can be seen clearly by comparing the 3D trajectories of spheres S2 and S3 falling in the same mixture, which are plotted in Figure 5.12.

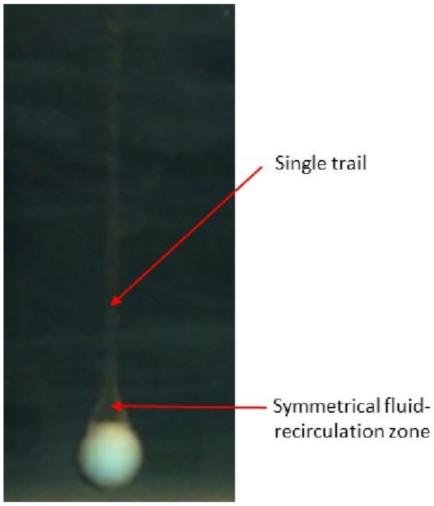

Figure 5.11 Visualisation of the trail and fluid recirculation zone found for PTFE sphere S9 falling in mixture 80/20 at $Re_P = 43.4$.

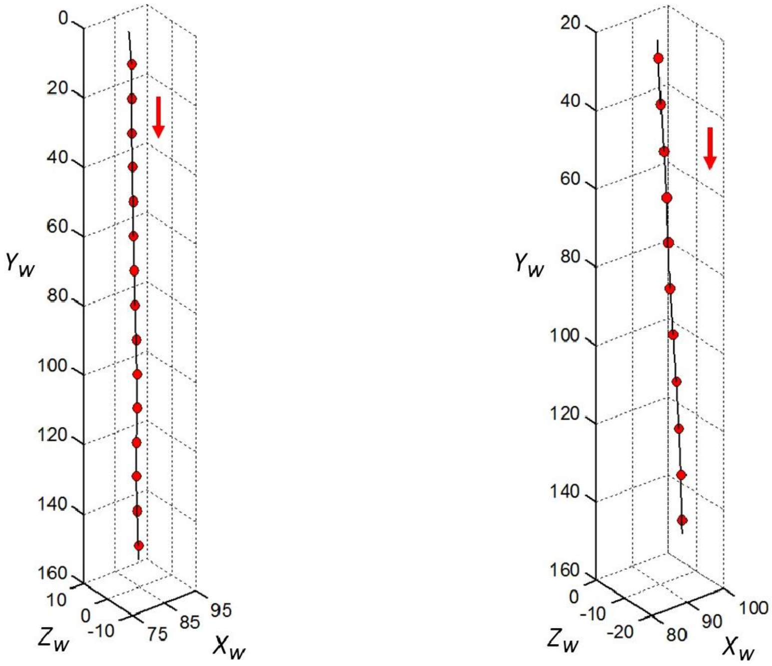

(a)

(b)

Figure 5.12 3D fall paths of spheres S2 (a) and S3 (b) in mixture 80/20 at $Re_P = 15.1$ and 73.7, respectively. Scale in mm.

The change of the centroid velocity with time is plotted in Figure 5.13 for both spheres S2 and S3. The theoretical values of U_T calculated with Equation (2.10) are also marked with red-dotted lines. As it can be noticed, when S2 entered the field of view it already was in the final velocity regime with $U_T = 0.12$ m/s, thus disagreeing with Equation (2.10) for 8 %. Contrary to S2, sphere S3 achieved steady velocity conditions at $t = 0.05$ s, approximately, in remarkable accordance with Equation (2.10). The discrepancy was only 2 %, however after $t = 0.15$ s it presented a fluctuation between

0.57 m/s and 0.59 m/s. Nonetheless, Re_P was calculated with the average magnitude $U_T = 0.58$ m/s.

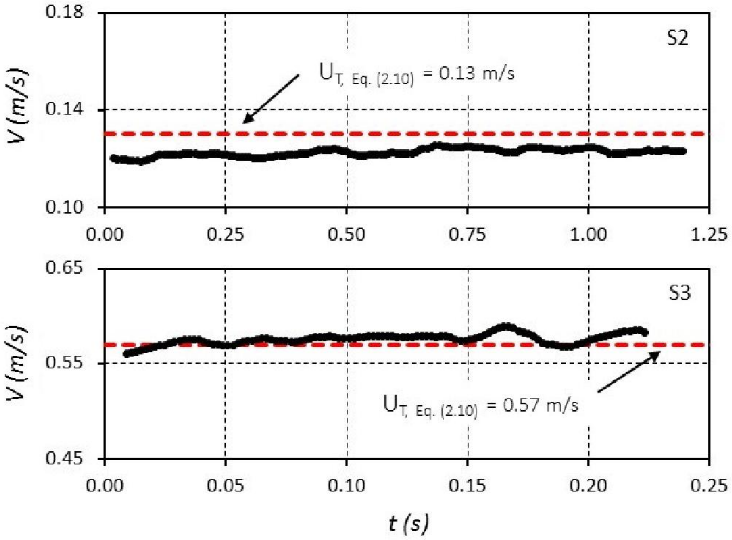

Figure 5.13 Velocity plots of spheres S2 and S3 settling in a mixture with 80% (by wt.) of glycerine at $Re_P = 15.1$ and 73.7, respectively.

From the drag force graphs of particles S2 and S3 showed in Figure 5.14, it can be seen that S2 exhibited the mostly constant value $F_D = 0.5$ mN, whilst S3 was subject to drag fluctuations once terminal velocity conditions were achieved. Nevertheless, the average $F_D = 4.6$ mN could be assumed given the fact that the greatest difference among the registered data was 0.1 mN.

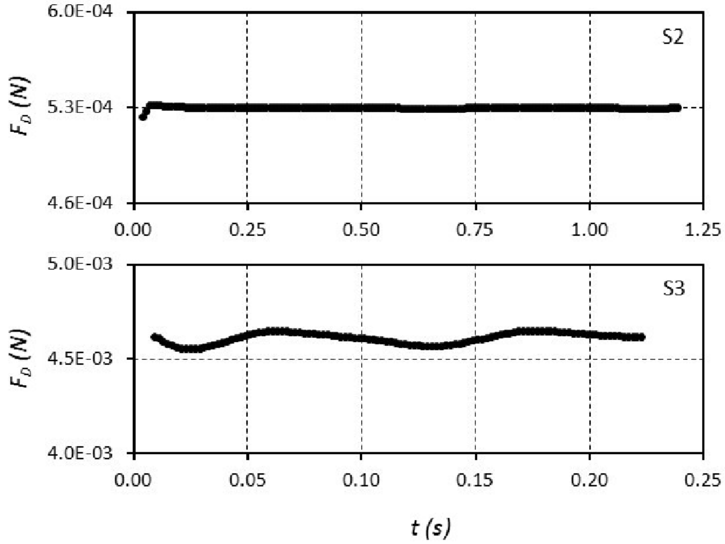

Figure 5.14 Drag force graphs determined for spheres S2 and S3 settling in mixture 80/20 at $Re_P = 15.1$ and 73.7, respectively.

The plots of the coefficient of resistance portrayed in Figure 5.15, for both solids, showed a marked agreement with Equation (2.23b) for sphere S2 despite the fluctuations. Nevertheless, for S3 the discrepancies were higher. A relatively smaller value of C_D = 1.2, away from the correlation prediction by 8 % was obtained. Moreover, due to the smaller order of magnitude of F_D, the oscillation of V caused C_D to fluctuate slightly after t = 0.16 s, however with an almost negligible amplitude.

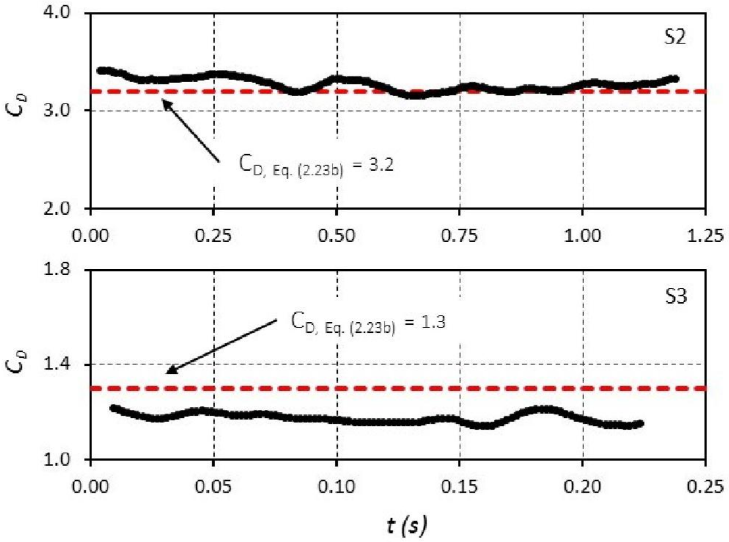

Figure 5.15 Variation of the coefficient of resistance of spheres S2 and S3 falling in mixture 80/20 at Re_P = 15.1 and 73.7, respectively.

According to the literature reviewed in Section 2.2.4, it has been reported that when the sphere Reynolds number exceeds 210, the downstream single trail becomes double, and may exhibit some waviness in the interval 270 < Re_P < 290 [57, 68, 69]. Such behaviour was also found in this research during the fall of particles S6 in mixture 65/35 (Re_P = 235.5) and S1 in pure water (Re_P = 277.1), respectively. The wavy, double-trail exhibited by the latter one was visualized with Schlieren photography and is depicted in Figure 5.16.

Because the double trail is not entirely symmetrical, the particle does not follow a straight line during its falling motion. Additionally, the deviation can be accentuated by the effects producing the wavy pattern in the trail. This further increment can be easily verified by comparing the 3D generated trajectories of the centroids of both spheres, S6 and S1, displayed in Figure 5.17.

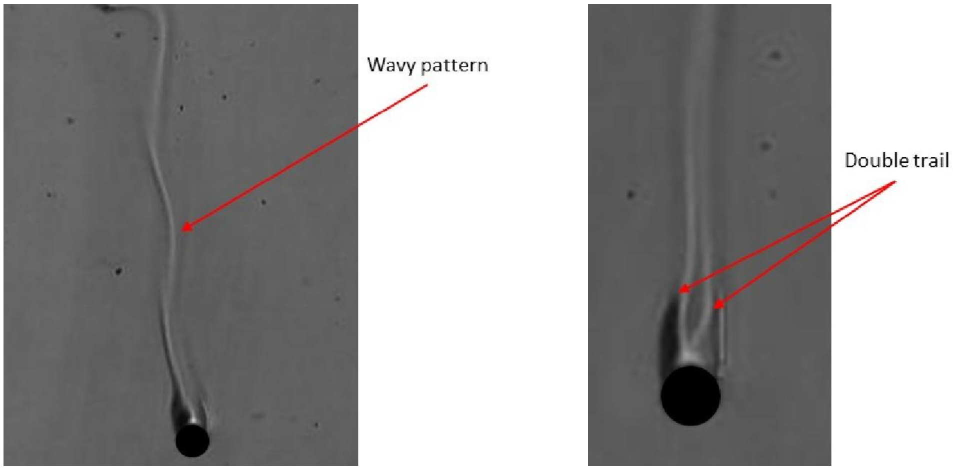

(a) (b)

Figure 5.16 Schlieren visualisation of the wavy pattern (a) and the double trail (b) left downstream by sphere S1 falling in pure water at $Re_P = 277.1$.

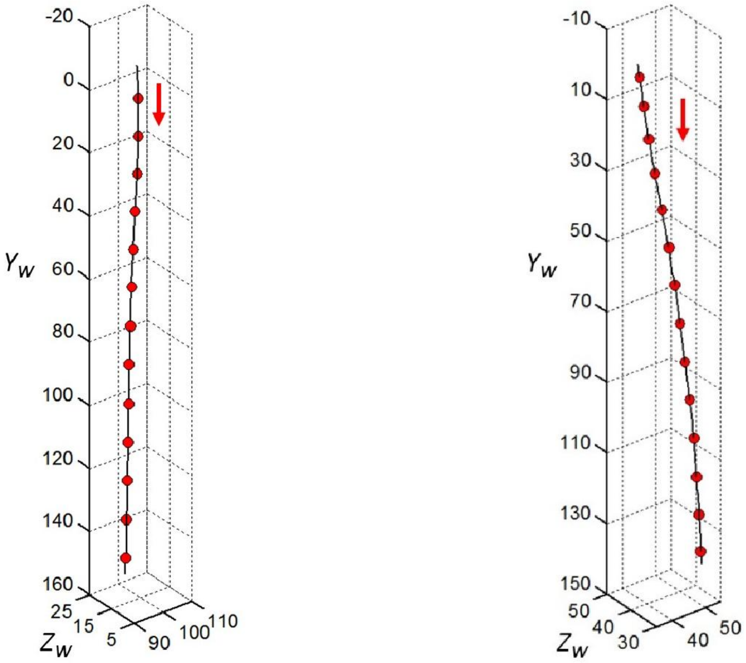

(a) (b)

Figure 5.17 3D paths of sphere S6 falling in mixture 65/35 at $Re_P = 235.5$ (a), and of sphere S1 settling in pure water at $Re_P = 277.1$ (b). Scale in mm.

In Figure 5.18 it is plotted the speed time variation of spheres S6 and S1 during their fall. It can be noticed that both reached the state of terminal velocity. Whilst it happened at $t = 0.3$ s for S6, it occurred at $t = 0.75$ s for S1. Furthermore, the agreement with the theoretical values predicted by Equation (2.10) was noticeably close. The discrepancies did not exceed 6 %, even considering the slight oscillation exhibited by particle S6 at $t = 0.51$ s.

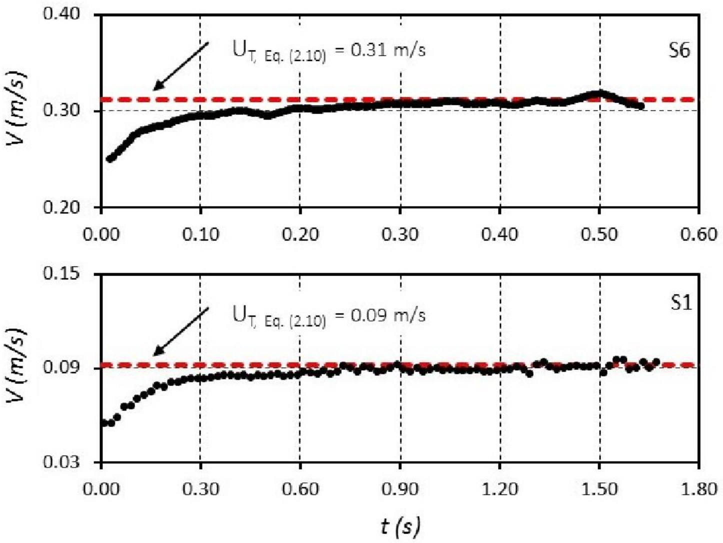

Figure 5.18 Variation of the velocity of sphere S6 falling in mixture 65/35 at $Re_P = 235.5$, and of sphere S1 settling in pure water at $Re_P = 277.1$.

The drag forces acting on particles S6 and S1 are plotted in Figure 5.19, where it was observed that within the terminal velocity conditions interval sphere S6 was under the action of a nearly constant drag equal to 1.3 mN. On the other hand, the force exerted over particle S1 registered an abrupt increment up to the onset of final conditions, to then continue to augment gradually from 18 μN to 19 μN. Nonetheless, it is believed that such a change can be considered negligible.

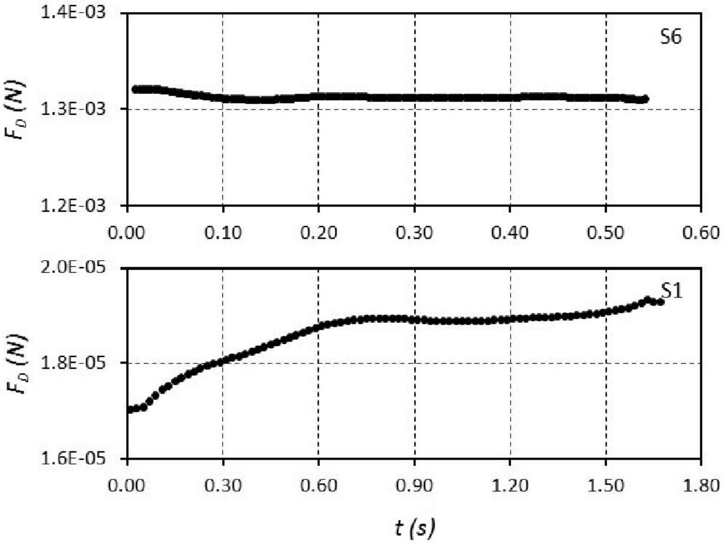

Figure 5.19 Graphs of the drag force magnitude experienced by spheres S6 falling in mixture 65/35 at $Re_P = 235.5$, and S1 settling in pure water at $Re_P = 277.1$.

In the plots of the coefficient of resistance of spheres S6 and S1 given in Figure 5.20 it can be appreciated that both of them showed a nearly constant coefficient once the conditions of final velocity were met. In addition, the similitude with the values estimated by Equation (2.23b) was remarkable. Whilst the difference in the first case was practically null, in the second one did not surpass 10 %.

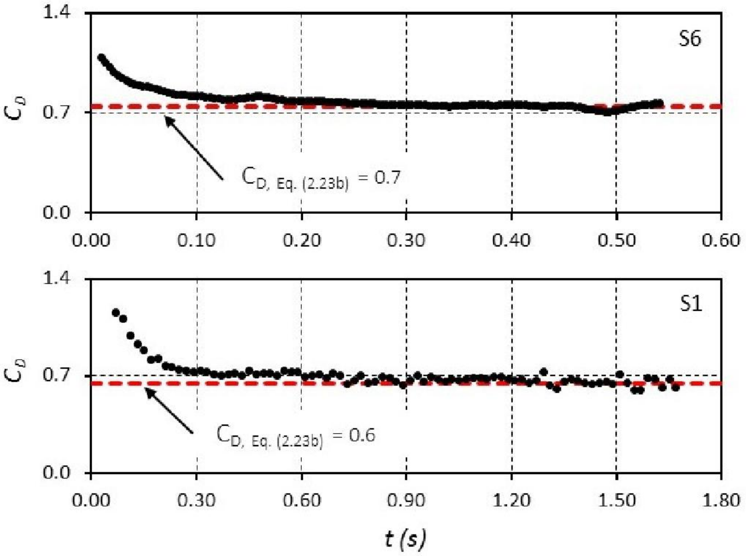

Figure 5.20 Drag coefficient plots of spheres S6 falling in mixture 65/35 at $Re_P = 235.5$, and of S1 settling in pure water $Re_P = 277.1$.

Once the value of the particle Reynolds number is larger than 290, the settling motion of the sphere is accompanied by the alternating process of vortex separation and shedding in the form of the so-called hairpin structures, represented in Figure 5.21, obtained using Schlieren photography to visualize the fall of sphere S5 in pure water. Initial time $t = 0$ s was placed on the first picture that showed the entire sphere within the camera field of view. Opposite to the findings of Magarvey and Bishop [57] who informed that the hairpin vortex patterns end at $Re_P = 700$, in this study it was established that they can still be present up to $Re_P \sim 900$.

From Figure 5.21 it can be inferred that the separation and shedding of the vortices alter the direction of the particle trajectory, deviating it even farther from resembling a straight path. This was observed too in the three-dimensional plot of the reconstructed centroid trajectory of sphere S4 sinking in mixture 65/35 at $Re_P = 656.3$, which is illustrated in Figure 5.22.

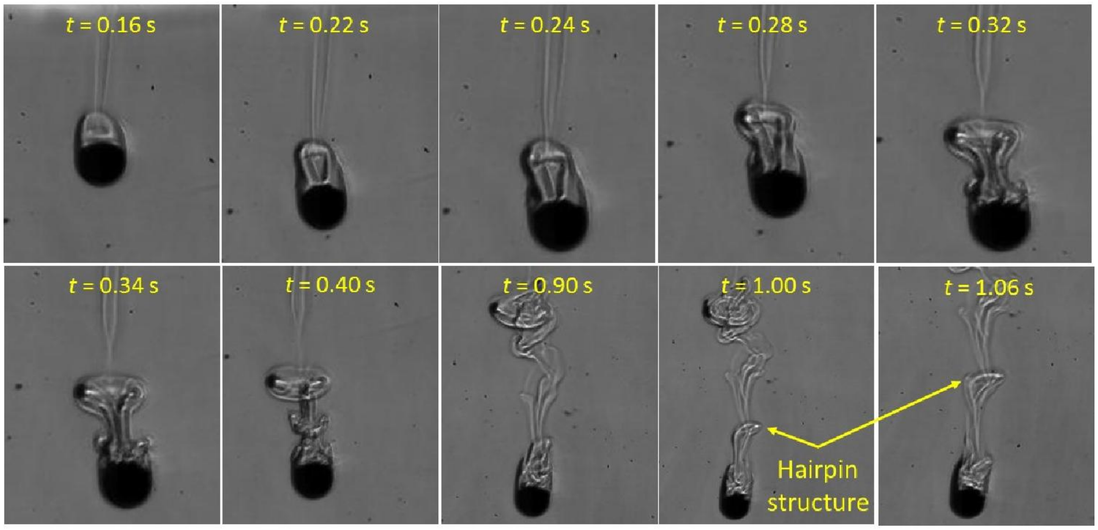

Figure 5.21 Schlieren pictures of the formation and evolution of a hairpin structure described by sphere S5 falling in pure water ($Re_P = 901.9$).

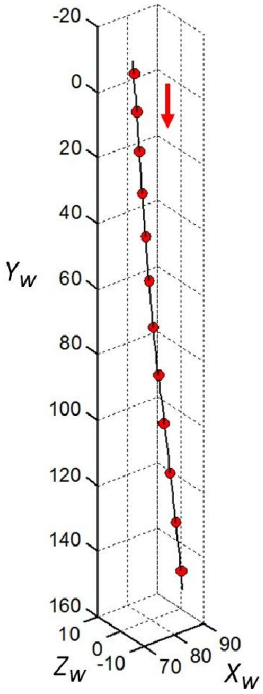

Figure 5.22 3D reconstructed path of sphere S4 falling in mixture 65/35 at $Re_P = 656.3$. Scale in mm.

In Figures 5.23 and 5.24, respectively, the time change of the fall-velocity and drag force exhibited by sphere S4 are portrayed. Final velocity conditions were reached at $t = 0.16$ s, approximately, with negligible disagreement with respect to the correlation result. In addition, from Figure 5.24, it was found that the force of drag incremented continuously before and during the interval of terminal conditions, achieving a maximum of F_D = 8.2 mN by the time it left the field of view.

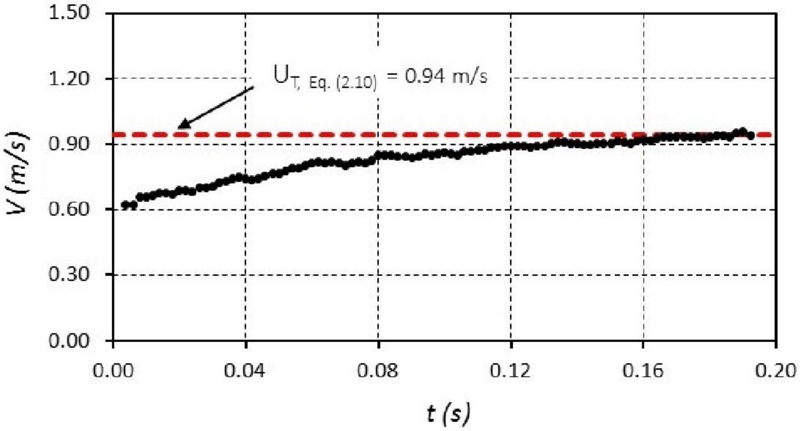

Figure 5.23 Plot of the velocity change of sphere S4 falling in mixture 65/35 at Re_P = 656.3.

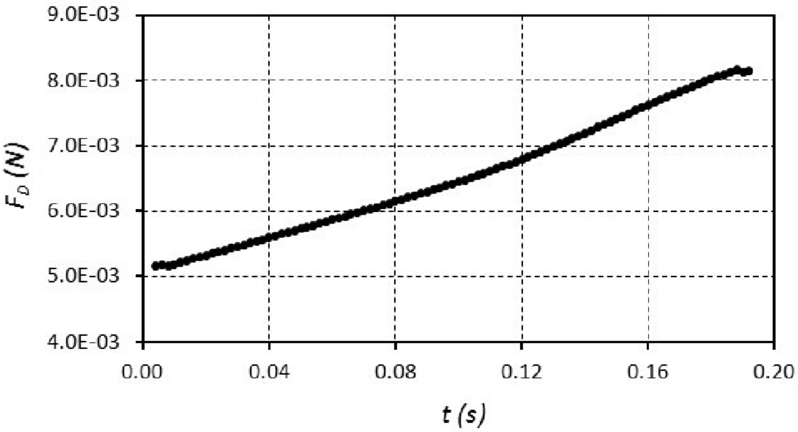

Figure 5.24 Variation of the drag force experienced by sphere S4 falling in mixture 65/35 at Re_P = 656.3.

The plot of the drag coefficient of sphere S4 is displayed in Figure 5.25, where it can be observed that between t = 0.08 s and t = 0.14 s, a nearly constant coefficient equal to 0.5 was registered, close to the magnitude predicted by Equation (2.23b). Nevertheless, in the following times the coefficient increased almost linearly up to a maximum of C_D = 0.6 when it left the camera field of view. This increment was due to the continuous augment of the force in the period when the terminal velocity did not change anymore. However, if an average is taken, the difference with respect to the theoretical magnitude of C_D was not greater than 10 %.

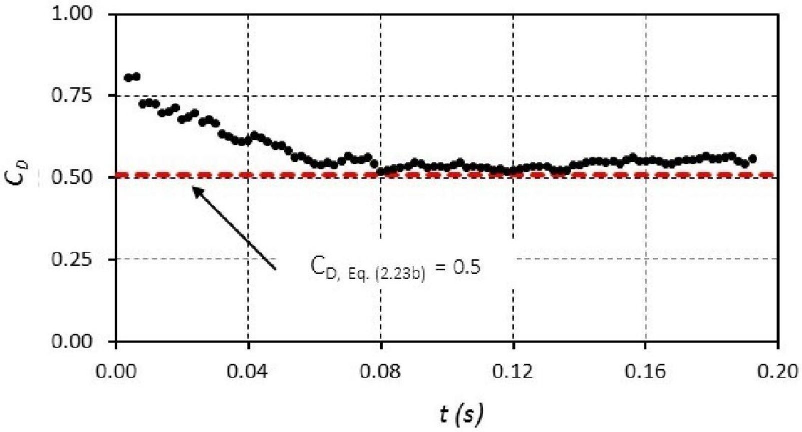

Figure 5.25 Plot of the coefficient of resistance determined for sphere S4 falling in mixture 65/35 at Re_P = 656.3.

As the particle Reynolds number becomes larger than 1000, the wake at the rear of a spherical object is completely turbulent, causing the extinction of the hairpin structures, as illustrated in the Schlieren visualization portrayed in Figure 5.26, which belongs to sphere S11 falling in pure water at Re_P = 4939. Furthermore, because of the irregular behaviour of the turbulence, the settling trajectory at this regime is significantly deviated from a straight line, as it can be noticed from the 3D plot of the fall path of the same sphere shown in Figure 5.27.

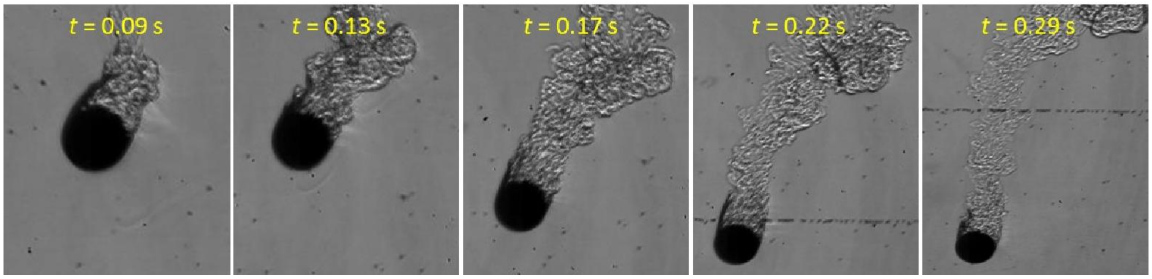

Figure 5.26 Schlieren visualisation of the wake behind sphere S11 falling in pure water at Re_P = 4939.

The time change of the fall-velocity of sphere S11 is plotted in Figure 5.28 and the drag force in Figure 5.29. It can be noticed that at t = 0.35 s, approximately, the measured velocity was 0.52 m/s and it did not change noticeably afterwards, suggesting that terminal conditions were reached. In this case, Equation (2.10) over predicted U_T for 9 %, approximately. Additionally, from Figure 5.29, it was observed that the drag force did not show a steady value at the same time period, on the other hand, it displayed an uninterrupted increment followed by a fluctuation at the end, with an amplitude of 0.5 mN.

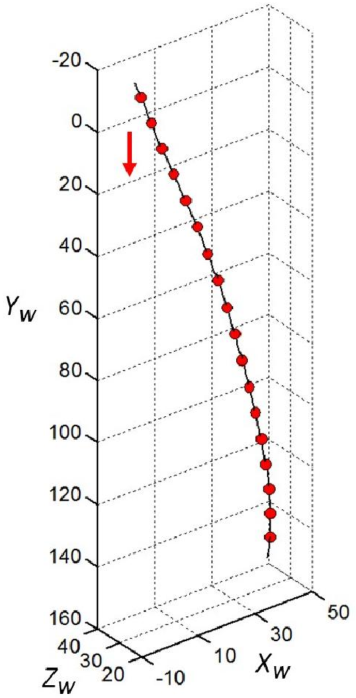

Figure 5.27 3D fall-path of sphere S11 falling in pure water at Re_P = 4939. Scale in mm.

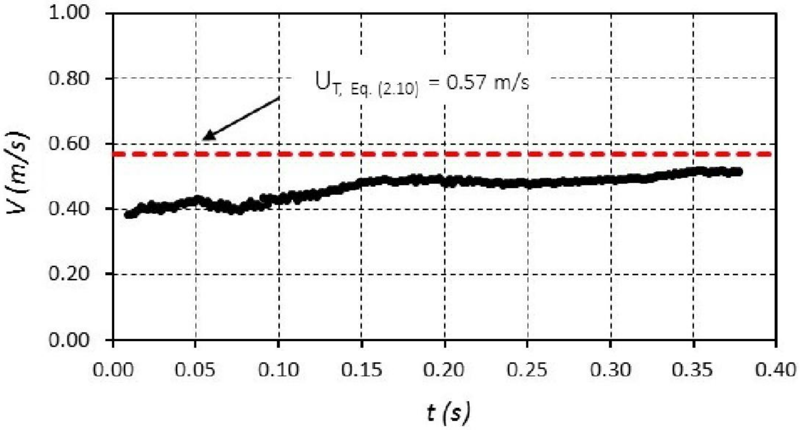

Figure 5.28 Time variation of the velocity of sphere S11 falling in pure water at Re_P = 4939.

The variation of the drag coefficient with time for sphere S11 is plotted in Figure 5.30, where a minimum of C_D = 0.5 was seen at t = 0.15 s, approximately, to then increase gradually up to C_D = 0.6 at t = 0.36 s, which was coincident with the greatest value of the drag force. If the average magnitude of C_D is considered, the discrepancy with Equation (2.23b) was equal to 38 %.

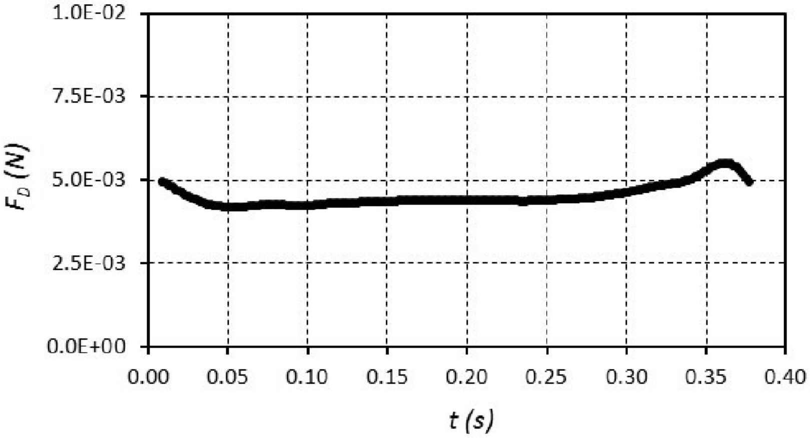

Figure 5.29 Graph of the drag force experienced by sphere S11 whilst sinking in pure water at $Re_P = 4939$.

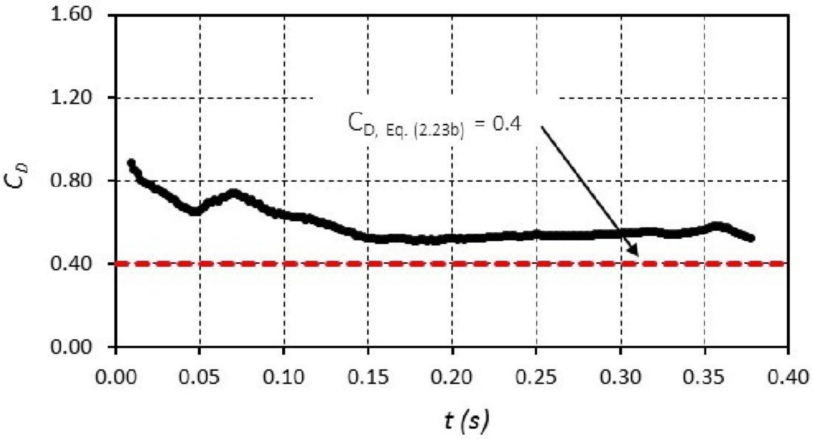

Figure 5.30 Variation of the coefficient of resistance determined for sphere S11 settling in pure water at $Re_P = 4939$.

A summary of the measured terminal velocities is provided in Figure 5.31. The theoretical values computed using the correlation published by Haider and Levenspiel (Equation 2.10) are also included in the graph. Instead of plotting directly as a function of Re_P, it is plotted in terms of N, the number of Re_P analysed, because this delivered greater clarity, however a relation between N and Re_P is provided in Table 5.8. Because for each value of N there is more than one test, the U_T magnitudes plotted correspond to the arithmetic mean.

As it can be seen in Figure 5.31, the agreement between the averaged experimental results of terminal velocity and their theoretical counterparts estimated with Equation (2.10) was noteworthy throughout the whole Reynolds number interval. The largest difference that it was found corresponded to 13 %.

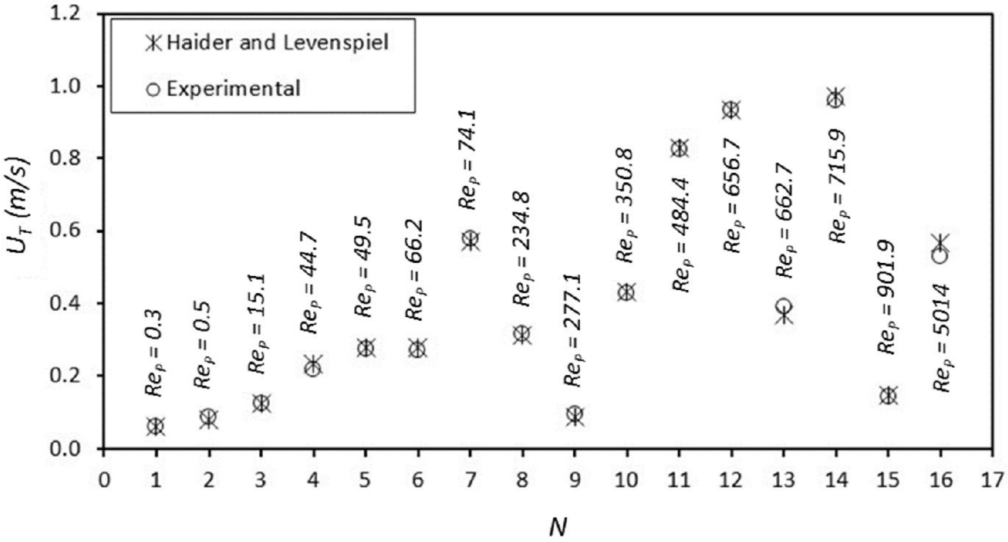

Figure 5.31 Comparison of the terminal velocity achieved by the spherical particles.

Table 5.8 Relation between *N* and Re_P of Figure 5.31.

N	Re_P	***N***	Re_P
1	0.3	9	277.1
2	0.5	10	350.8
3	15.1	11	484.4
4	44.7	12	656.7
5	49.5	13	662.7
6	66.2	14	715.9
7	74.1	15	901.9
8	234.8	16	5014.0

In the same way, the summary of all of the values of the coefficient of resistance obtained experimentally for each *N* is displayed in Table 5.9 and in Figure 5.32, now as a function of the particle Reynolds number. The values of C_D predicted by Equations (2.23a – 2.23d) are also incorporated for the purpose of comparison. Re_P was calculated using the values of U_T illustrated in Figure 5.31.

Table 5.9 Relation between Re_P and C_D.

N	Re_P	C_D	***N***	Re_P	C_D
1	0.3	99.9	9	277.1	0.6
2	0.5	58.2	10	350.8	0.7
3	15.1	3.2	11	484.4	0.6
4	44.7	1.7	12	656.7	0.5
5	49.5	1.5	13	662.7	0.5
6	66.2	1.3	14	715.9	0.5
7	74.1	1.2	15	901.9	0.4
8	234.8	0.7	16	5014.0	0.5

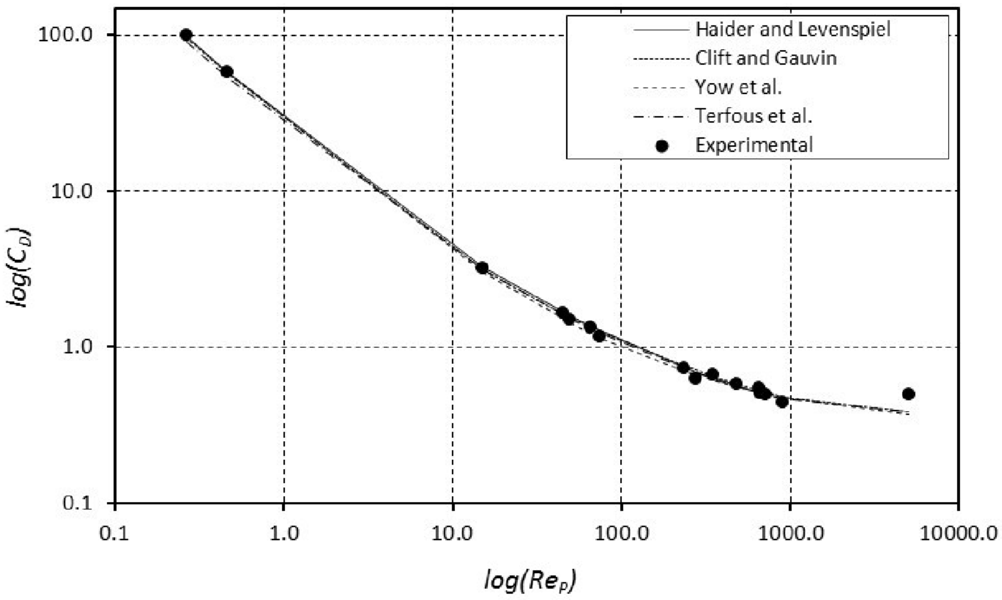

Figure 5.32 Comparison of the experimental and theoretical values of the drag coefficient of the spheres.

As observed in Figure 5.32, the agreement between the experimental results and those from the literature correlations was remarkable so long as $Re_P < 1000$. In fact, the discrepancies never surpassed 12 % in this range. On the other hand, for the unique case investigated at $Re_P > 1000$ the difference was 38 %, with the experimental magnitude of C_D being superior to all of the correlation-predicted values.

In order to estimate the uncertainty in the calculations of the U_T and C_D, the free-fall of sphere S1 in pure water at $T_f = 15$ °C ($\rho_f = 999.1$ kg/m^3, $\mu = 1.2\times10^{-3}$ Pa·s) was repeated and analysed 9 times. The obtained results are listed in Table 5.10. For this error analysis, the procedure suggested by Taylor [110] was applied. He said that the best estimation of the measured variable, P_{best}, corresponds to the arithmetic mean of all of the individual readings P_i, and that the uncertainty η associated to the measurement can be approximated as the standard deviation of the mean, therefore

$$P_{best} = \frac{\sum P_i}{N} \tag{5.1}$$

$$\sigma = \sqrt{\frac{\sum (P_i - P_{best})^2}{N-1}} \tag{5.2}$$

$$\eta = \frac{\sigma}{\sqrt{N}} \tag{5.3}$$

where σ is the standard deviation of the sample of readings. Then, for the present study the best results were: $U_T = 0.08$ m/s $\pm$ 1 % and $C_D = 0.8 \pm 1$ %, respectively. In regard to Equations (2.10) and (2.23b), they had discrepancies of 2 % and 3 %, respectively.

Table 5.10 U_T and C_D values obtained in the repeatability study of sphere S1 falling freely in pure water at $Re_P = 220$.

N	U_T (m/s)	C_D	N	U_T (m/s)	C_D	N	U_T (m/s)	C_D
1	0.084	0.78	4	0.084	0.77	7	0.084	0.77
2	0.081	0.80	5	0.081	0.81	8	0.082	0.81
3	0.084	0.77	6	0.083	0.79	9	0.083	0.79

Based on the strong agreements illustrated through the plots of Figures 5.31 and 5.32, and on the significantly low uncertainty obtained from the repeatability test done for sphere S1, it can be affirmed that the methodology proposed in this thesis to estimate the kinematics and dynamics of a moving particle using only the 3D stereo-reconstructed coordinates of the trajectory of its centroid can be considered valid.

Chapter 6

INVESTIGATION OF THE MOTION OF REGULAR PARTICLES IN FREE FALL USING STEREO VISION AND SCHLIEREN – PART 2

This chapter constitutes the second part of the study of settling particles in viscous fluids started in chapter 5. The results analysed here are those corresponding to the cylindrical and disk shapes, tested as shown in Table 5.6 of Section 5.2. Additionally, the physical and dimensional characterisation of each of these solids was also shown in Section 5.1, being the results listed in Tables 5.3 and 5.4, respectively. The chapter is structured in such a way that the data obtained for the cylinders is analysed first, then the analysis of the disks goes second. Finally, because these two shapes possess certain orientation as they move, the chapter ends with a section dealing with the influence of such angular orientation onto the coefficient of resistance.

As it was done for the spheres in Chapter 5, the motion of each of the particles employed here was analysed following the same procedure, with the exception that the orientation was investigated too, according to the methodologies exposed in Sections 4.1 and 4.2 of Chapter 4. This is the first time that the motion of non-spherical particles is studied within the context of a moving Frenet reference frame to estimate the magnitudes of the drag force given the 3D path coordinates only. As for the spheres, for each geometry studied in this chapter, the experimental values of terminal velocity and coefficient of drag are also compared against those predicted by equations from the literature. In addition, for some selected cases, either direct or Schlieren visualisations of the flow structures around the moving particles are displayed.

6.1 KINEMATICS AND DYNAMICS OF CYLINDRICAL PARTICLES AT DIFFERENT REYNOLDS NUMBERS

The experimental results obtained for the cylindrical solids covered the following particle Reynolds number: $0.7 < Re_P < 1975$, calculated using the nominal diameter as the characteristic length. The data corresponding to $Re_P = 0.7$ was extracted from the settling of brass cylinder C1 in pure glycerine (mixture 100/0 according to Table 5.5). The 3D path described by its centroid is portrayed in Figure 6.1, where the blue lines represent the longest axis. The red points denote the centroid, and the green ones the extreme points P_1 and P_2, respectively.

From Figure 6.1 it can be seen that the cylinder trajectory exhibited some curvature whilst its orientation apparently remained unchanged. However, from the plot of the time-variation of the angle of incidence showed in Figure 6.2, it was found that before t = 0.6 s there was some angular change. This was a consequence of the dropping method since the solid had to be released in vertical position in order to go through the funnel. Nevertheless, at this time final velocity conditions were also reached (Figure 6.3) and the particle orientation remained unaltered, as said by Marchildon et al. [25].

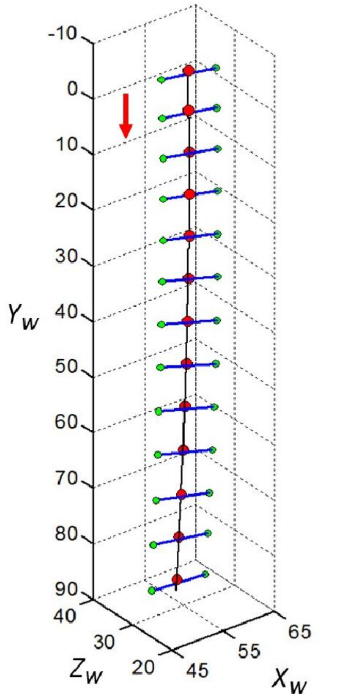

Figure 6.1 3D path of cylinder C1 settling in pure glycerine (Re_P = 0.7). Dimensions in mm.

In the graph of Figure 6.2 the particle projected area, calculated as $A_P = dLsin\alpha$, was also included. As it can be noted A_P exhibited the same behaviour as α. Its value at steady conditions was A_P = 0.5 μm^2. This behaviour occurred too for all the other cylinders analysed, regardless of the magnitude of their particle Reynolds number. In addition, from the velocity plot of Figure 6.3, the obtained terminal velocity for the currently discussed case was U_T = 0.10 m/s, approximately.

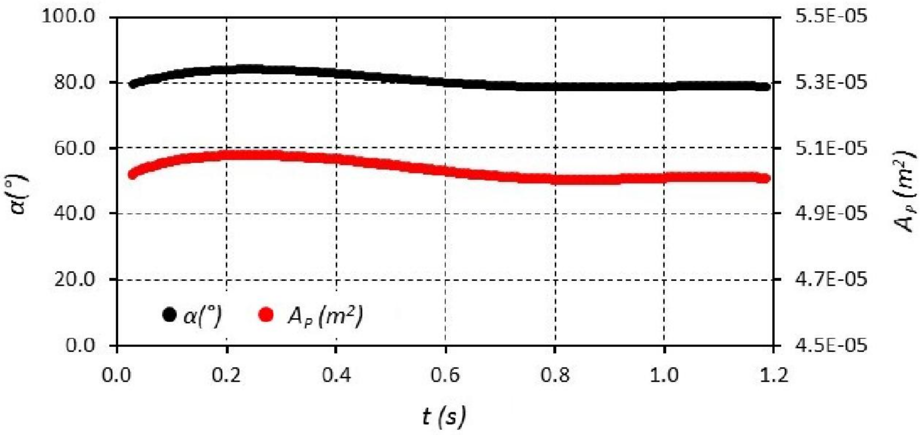

Figure 6.2 Time change of the angle of incidence and projected area of cylinder C1 settling in pure glycerine ($Re_P = 0.7$).

In Figure 6.3 the magnitude of the terminal velocity foretold by Equation (2.10) was also represented with a red, dotted line, showing a clear disagreement with the experimental data. Indeed, the U_T obtained from the experiment was 17 % lower than that of the correlation. It should be highlighted that in this research the value of Re_P shown in every plot or table has been computed using the value of U_T determined experimentally.

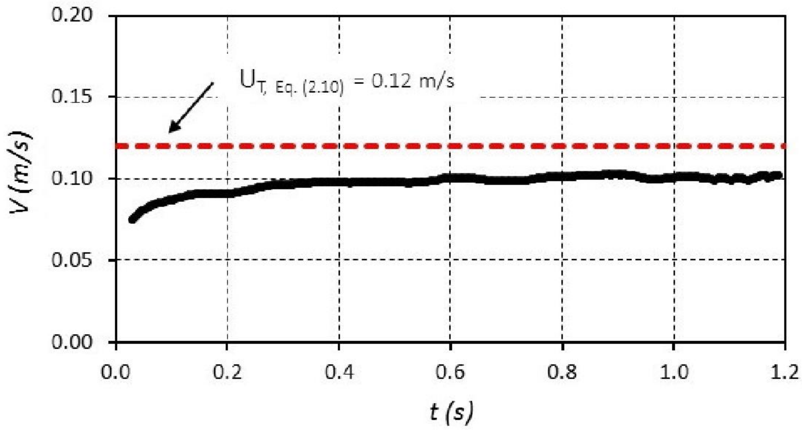

Figure 6.3 Velocity plot of cylinder C1 settling in pure glycerine ($Re_P = 0.7$).

The drag force acting on the cylinder as it settled in the glycerine was estimated with the methodology described in Section 4.3, and it is plotted in Figure 6.4, where a notorious decrement was detected during the same period of time when the angular change happened, nonetheless, from $t = 0.4$ s and onwards the force remained constant at $F_D = 14.0$ mN, approximately.

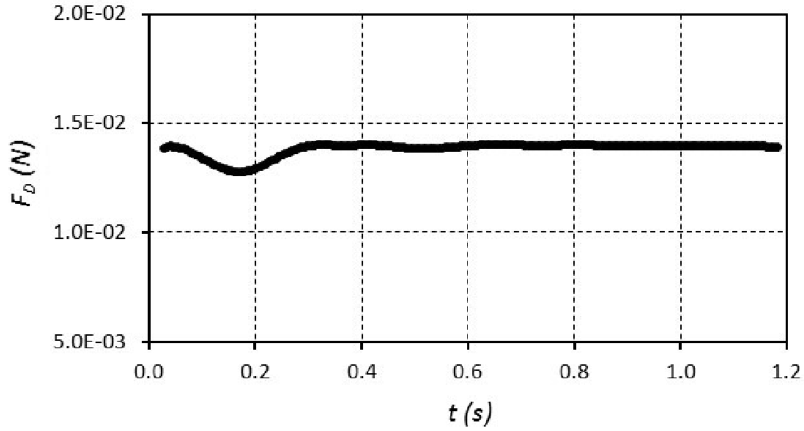

Figure 6.4 Plot of the drag force exerted over cylinder C1 while settling in pure glycerine ($Re_P = 0.7$).

Figure 6.5 shows the graph of the coefficient of resistance computed at each time step together with the theoretical value predicted by Equation (2.24a), calculated using the magnitude of U_T given by Equation (2.10), marked again with a red, dotted line. At terminal velocity conditions ($t > 0.6$ s) an average value of $C_D = 43.6$ was found, however it was accompanied by fluctuations between $C_D = 42.0$ and $C_D = 45.0$. The difference between the averaged C_D and that of the correlation was 14 %.

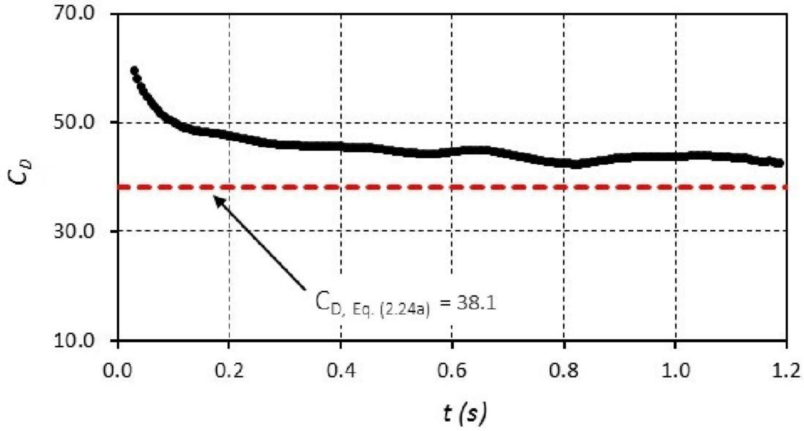

Figure 6.5 Time variation of the drag coefficient of cylinder C1 falling in pure glycerine ($Re_P = 0.7$).

In Figure 6.6 the settling of PTFE cylinder C4 in mixtures 80/20 (Figure 6.6a) and 65/35 (Figure 6.6b) as seen by the camera is displayed. The particle Reynolds numbers corresponding for each case were $Re_P = 21.3$ and 169.3, respectively. As it can be observed from the images, in both situations the solid left the camera field of view at a horizontal, fixed position regardless the initial orientation fluctuations caused by the dropping technique. The three-dimensional reconstructed paths for both cases are shown in Figure 6.7.

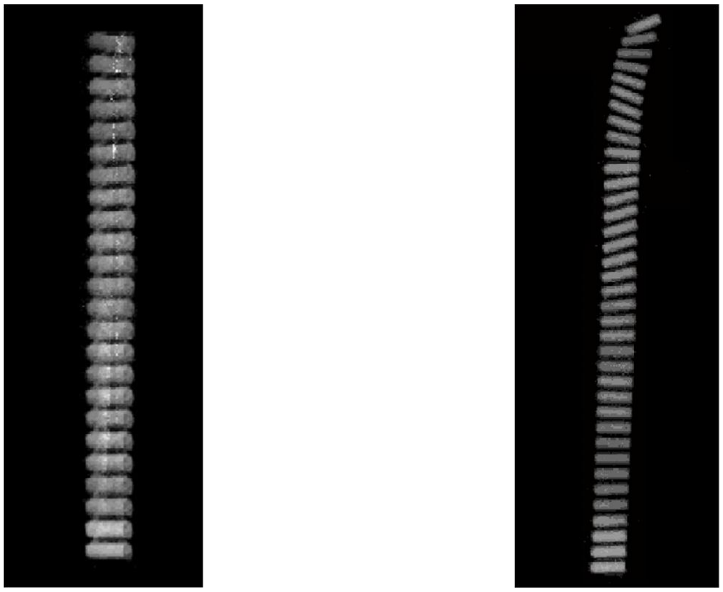
(a) (b)

Figure 6.6 2D visualization of the fall of cylinder C4 in mixtures 80/20 (a) and 65/35 (b). The corresponding particle Reynolds numbers were $Re_P = 21.3$ and 169.3.

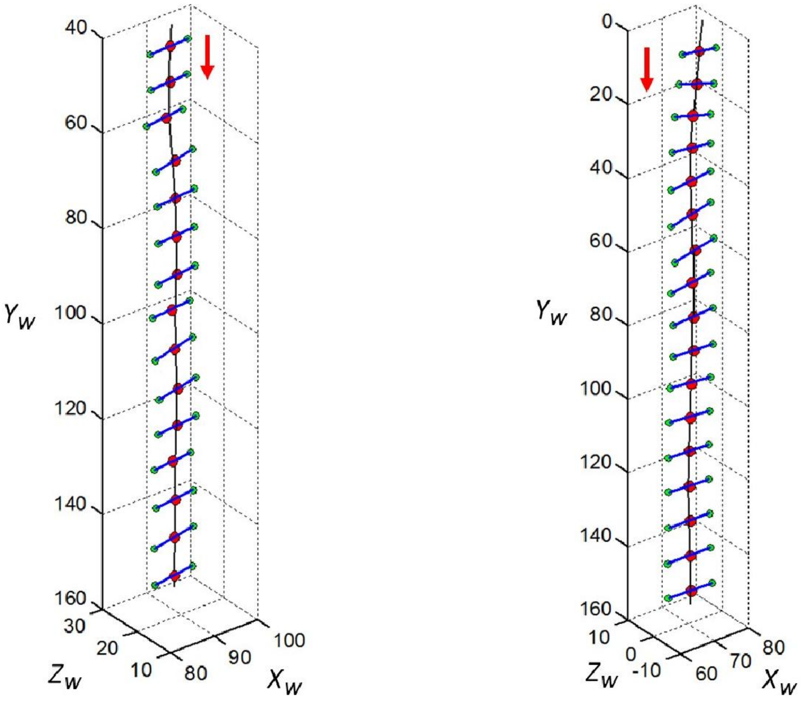

(a) (b)

Figure 6.7 3D fall paths of cylinder C4 in mixtures 80/20 (a), and 65/35 (b) at $Re_P = 21.3$ and 169.3, respectively. Dimensions in mm.

Figures 6.6a and 6.6b are the result of adding the images of the cylinder every 10 ms so that the pattern could be seen clearly. On the other hand, the number of blue lines representing the solid longest axis in Figures 6.7a and 6.7b was chosen randomly but with the same purpose. Therefore, a disagreement between the number of 2D cylinder images in Figure 6.6 and that of blue lines in Figure 6.7 may exist.

In both plots of Figure 6.7 it can be seen that once the dropping instabilities were surpassed the cylinder described a relatively smooth trajectory with minimum deviations from a straight path. Moreover, given the fact that the angular orientation remained unchanged, the projected area was practically constant and equal to 0.4 μm^2 for both cases. The reason for such behaviour was that at low values of the Reynolds number the secondary flow around the body and the trail are stable and symmetrical, as illustrated in Figure 6.8, which provides a direct visualization of such secondary flow for the settling in mixture 80/20.

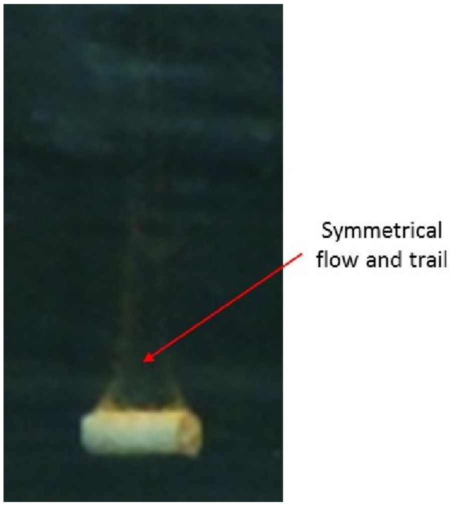

Figure 6.8 Direct visualization of the stable and symmetrical secondary flow and trail around cylinder C4 falling in mixture 80/20 at $Re_P = 21.3$.

The velocity of the centroid of the cylinder for both cases is illustrated in the plots of Figure 6.9, where, for mixture 80/20 it was observed that when the body entered the camera field of view it already was in the terminal flow conditions regime, however for mixture 65/35 such conditions were not reached until $t = 0.2$ s, approximately. The magnitudes of U_T for both cases were 0.13 m/s and 0.23 m/s, respectively. From the comparison with the theoretical values given by Equation (2.10) it can be noticed that whilst an over estimation of 15 % was found for the first case, the difference for the second one was only 5 %. This suggests that the predictions of Equation (2.10) improve as *Re_P* augments.

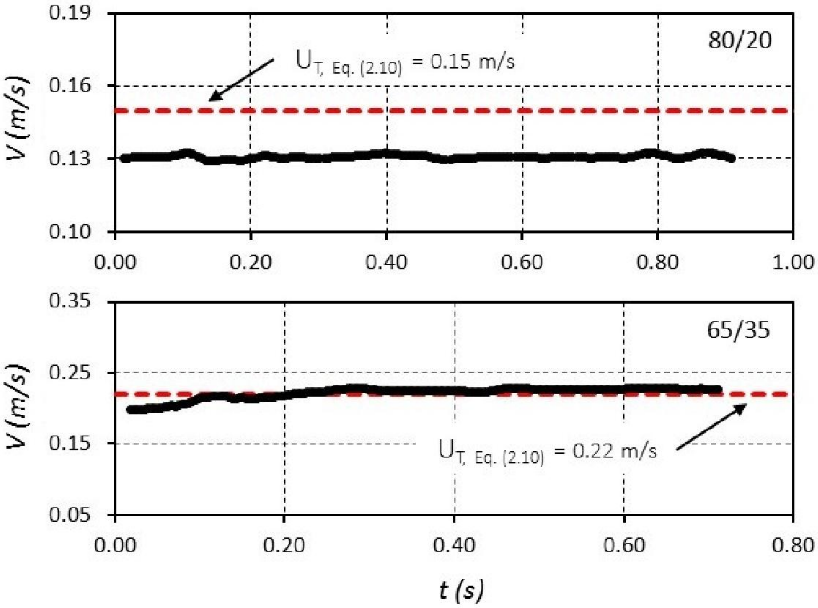

Figure 6.9 Time variation of the velocity of cylinder C4 falling in mixtures 80/20 and 65/35 at Re_P = 21.3 and 169.3, respectively.

In Figure 6.10 the force of drag exerted over the cylinder when falling in both liquid mixtures is plotted versus time, showing that a nearly constant magnitude was achieved for each case. For the first one, F_D was equal to 1.2 mN in average, whilst for the second it was 1.3 mN approximately. The values of the coefficient of resistance created by these force magnitudes are graphed in Figure 6.11, where a strong agreement with the theoretical results of Equation (2.24a) at steady state conditions can be noticed. The differences were 1 % and 9 %, respectively.

As it was mentioned in Section 2.2.4, Marchildon et al. [25] reported that the orientation of a cylindrical solid falling freely in a liquid will be characterised by regular oscillations once the particle Reynolds number exceeds 300. However, in this research such oscillations initiated at a lower value of Re_P, as it can be seen in Figure 6.12 which portrays a qualitative visualization in two-dimensions of the settling of PTFE cylinder C6 in the liquid mixtures 65/35 and 50/50 at Re_P = 240.2 and 614.6, respectively.

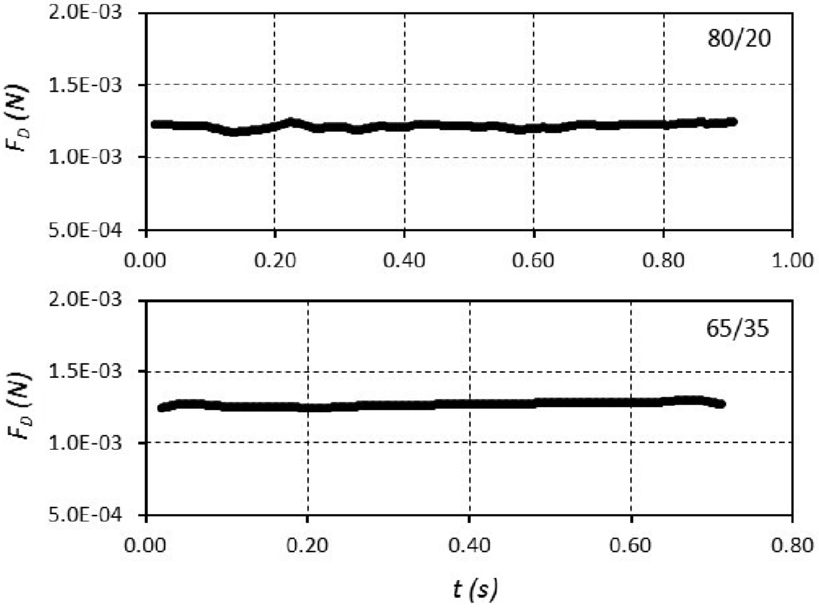

Figure 6.10 Graphs of the drag force acting on cylinder C4 as it settled in mixtures 80/20 and 65/35 at $Re_P = 21.3$ and 169.3, respectively.

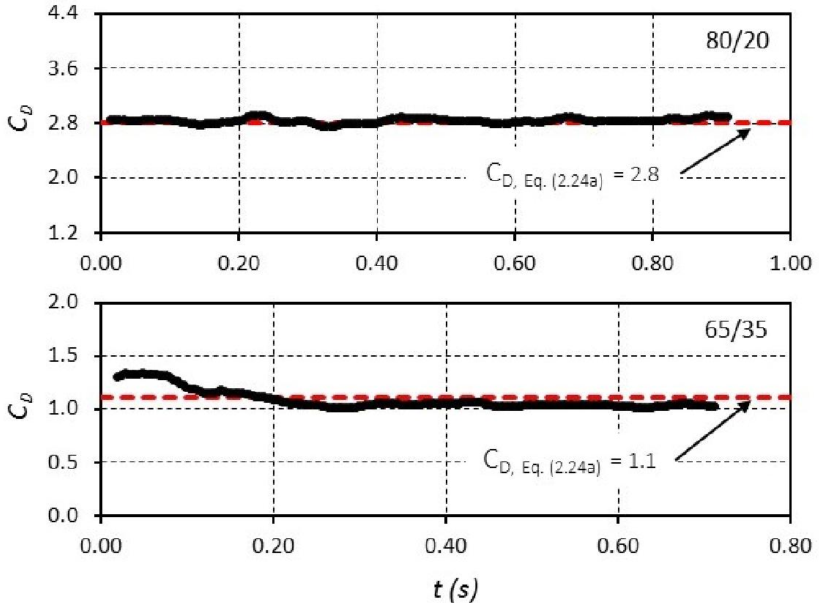

Figure 6.11 Plots of the coefficient of resistance found for cylinder C4 falling in mixtures 80/20 and 65/35 at $Re_P = 21.3$ and 169.3, respectively.

From Figure 6.12 it can be observed that the path exhibited a regular sinusoidal pattern, as suggested by Marchildon [25], and Chow and Adams [27], and that the starting and ending positions of the particle centroid were different. In addition, the orientation of the cylinder along the trajectory changed consistently. The three-dimensional reconstructed path of both cases is provided in Figure 6.13, where the trajectory deviations were more evident.

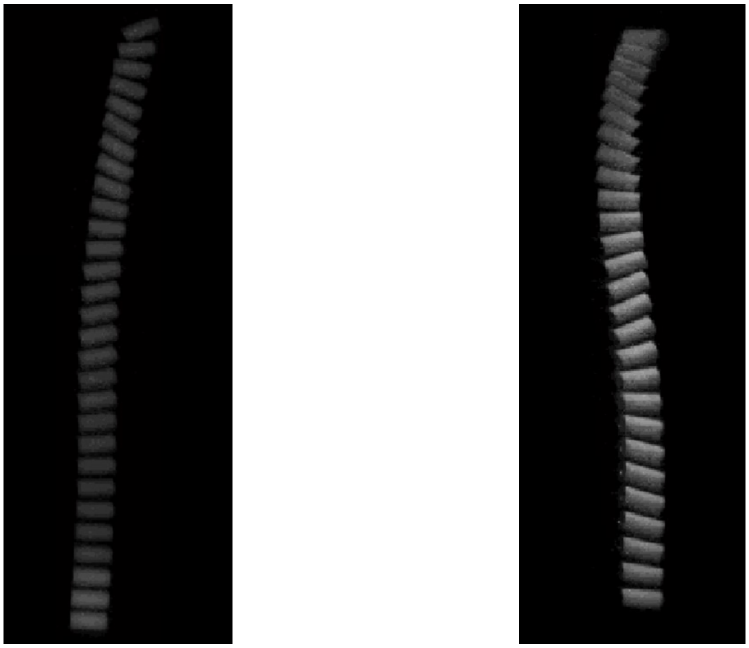

(a) (b)

Figure 6.12 Qualitative visualization of cylinder C6 settling in mixtures 65/35 (a) and 50/50 (b) at Re_P = 240.2 and 614.6, respectively.

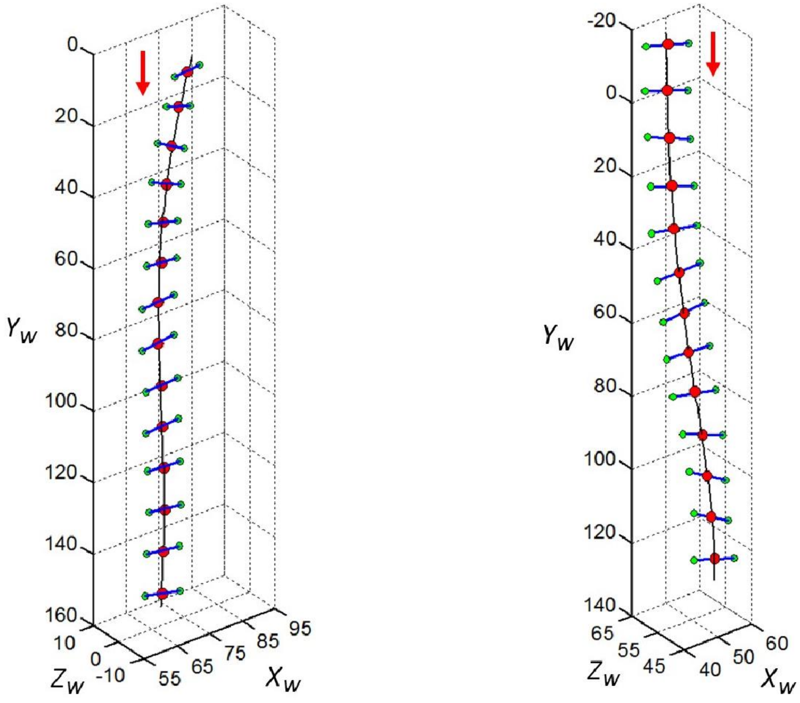

(a) (b)

Figure 6.13 3D paths depicted by cylinder C6 as it fell freely in mixtures 65/35 (a), and 50/50 (b) with Re_P = 240.2 and 614.6, respectively. Dimensions in mm.

The variations of the angle of incidence of the cylinder along the trajectories are exposed quantitatively in the plots of Figure 6.14, where it can be seen that for mixture 65/35 a full oscillation between α = 69° – 90° occurred before t = 0.25 s; after this value the pattern was only marked by a gradual decrease from 90°. On the other hand, for mixture 50/50 the angular behaviour was nearly symmetrical once $t > 0.05$ s, with peaks and valleys within the interval α = 66° – 89°.

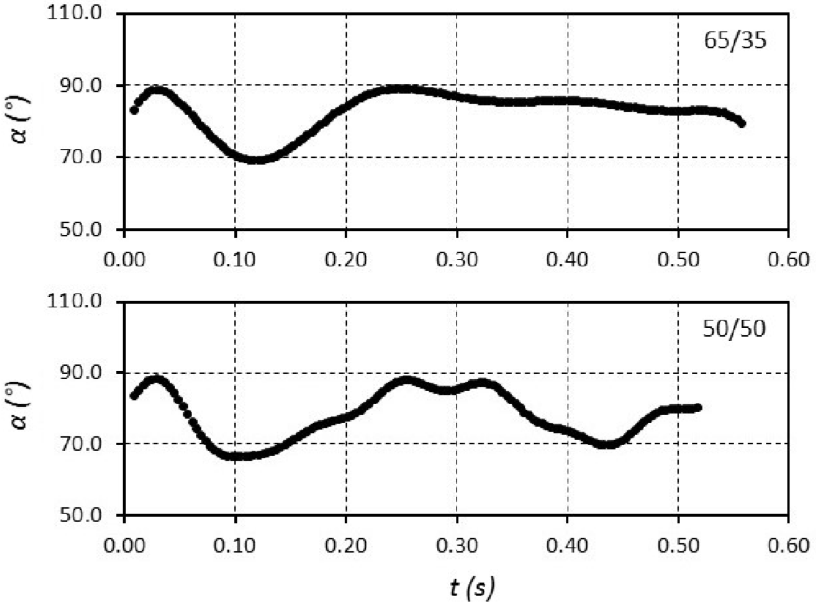

Figure 6.14 Variation of the orientation angle of cylinder C6 along the settling trajectories drawn in mixtures 65/35 and 50/50 at Re_P = 240.2 and 614.6, respectively.

In Figures 6.15 and 6.16 the plots of the fall velocity and drag force as function of time are portrayed for both cases. As it can be observed from the first figure, U_T achieved a magnitude equal to 0.28 m/s at t = 0.25 s for mixture 65/35 whilst for the second mixture the value of U_T reached was 0.32 m/s at t = 0.37 s. In both situations, Equation (2.10) failed on the prediction of the terminal velocity too, nonetheless this time with an under estimation of 12 % and 14 %, respectively. From Figure 6.16 it can also be said that contrary to the previous cases, the drag force did not achieve any fixed value but kept increasing throughout the whole time interval, with magnitudes up to 2.0 mN and 2.1 mN, respectively.

In Figure 6.17 the plots of the estimated coefficient of resistance versus time for cylinder C6 in both liquid combinations are displayed, revealing that a nearly stable value of C_D was accomplished for each situation at U_T conditions. For mixture 65/35, C_D was equal to 0.8 with a slight increment to 0.9 at the end of the interval, whilst for mixture 50/50 it remained at 0.7. Here too, the estimation of C_D done by Equation (2.24a) disagreed with the experimental data, but this time for 20 % and 22 %, respectively.

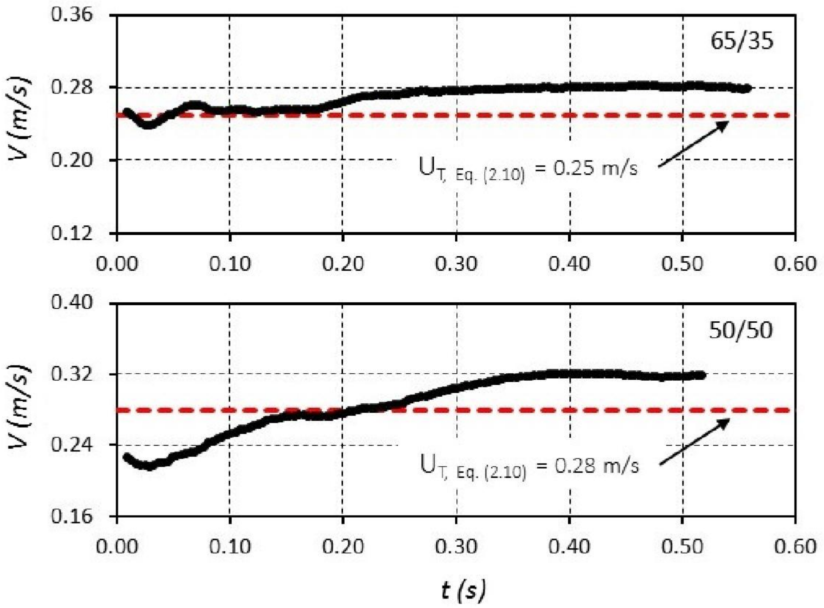

Figure 6.15 Plots of the fall velocities of cylinder C6 in mixtures 65/35 and 50/50. The corresponding particle Reynolds numbers were $Re_P = 240.2$ and 614.6, respectively.

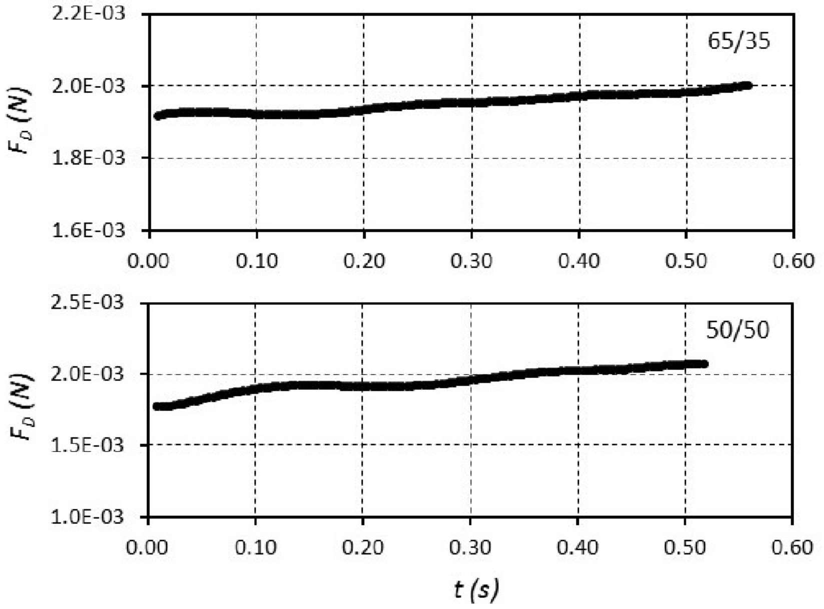

Figure 6.16 Graphs of the drag force exerted on cylinder C6 as it settled in mixtures 65/35 and 50/50 at $Re_P = 240.2$ and 614.6, respectively.

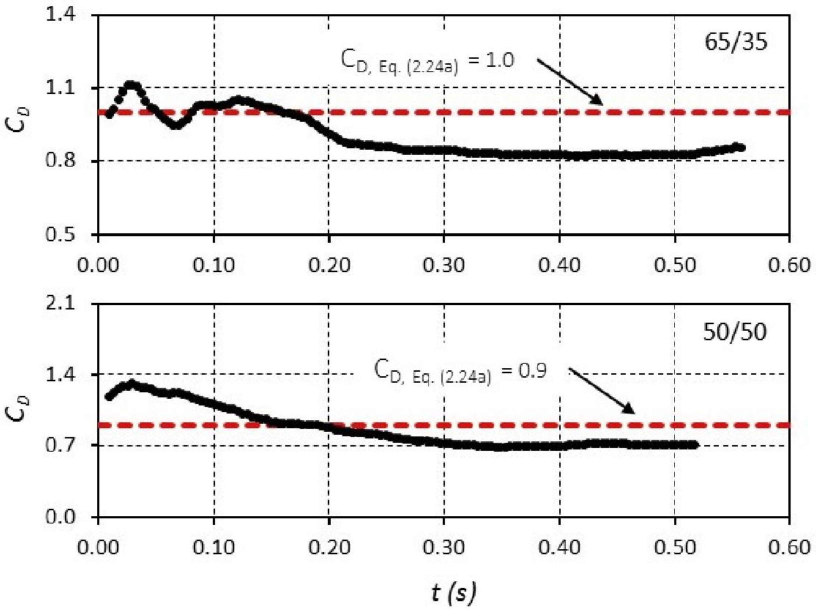

Figure 6.17 Variation of the coefficient of resistance estimated for cylinder C6 during its motion in mixtures 65/35 and 50/50 at Re_P = 240.2 and 614.6, respectively.

The sinusoid-like 2D trajectory as well as the changes in orientation of PTFE cylinder C2 as it fell in pure water (Re_P = 1661) can be observed in Figure 6.18a as recorded by the stereo camera, whilst in Figure 6.18b an augmented visualization through Schlieren photography of the flow around the cylinder as well as its trail downstream is provided. As it can be seen, the fluid downstream the particle is characterised by high turbulence and asymmetry.

In Figure 6.19 a series of Schlieren images of the cylinder C2 is portrayed in such a way that a whole angular oscillation cycle can be appreciated. It is believed that the manner in which the vorticity is released into the neighbouring liquid is responsible for the modifications of the pressure on the surface of the solid which in turn generate the torques that originate and sustain the oscillating motion, as proposed by Chow and Adams [27].

The largest particle Reynolds number investigated for the cylindrical solids of this work was Re_P = 1975, registered for the motion of PTFE cylinder C4 in pure water. A qualitative view of the fall path as seen by the camera is depicted in Figure 6.20a whilst in Figure 6.20b it is shown quantitatively in three dimensions. As with the previous cases, the trajectory continued to exhibit a regular sinusoidal pattern though with a larger period. Moreover, the orientation of the particle also kept the zig-zag, unceasing changes.

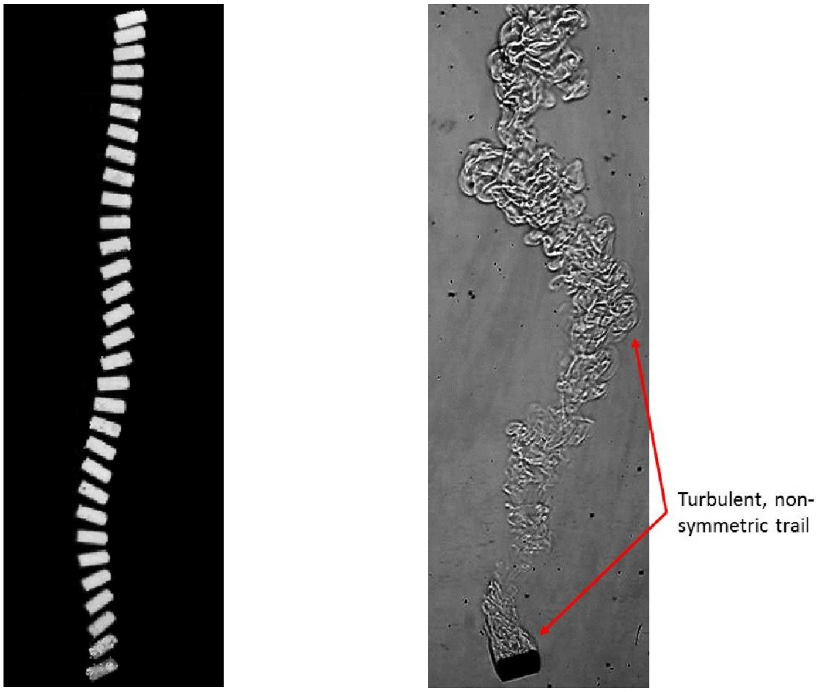

(a) (b)

Figure 6.18 Direct (a) and Schlieren (b) visualization of the secondary motion around cylinder C2 as it fell in pure water ($Re_P = 1661$).

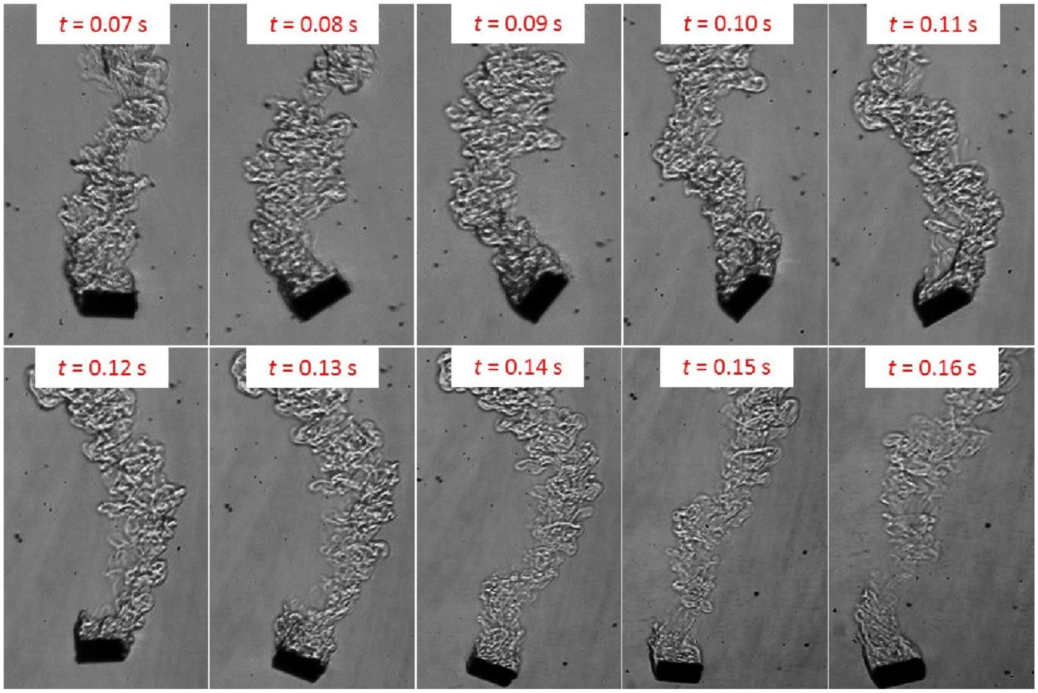

Figure 6.19 Time-series of the Schlieren visualization of Figure 6.18b illustrating a whole angular orientation cycle of cylinder C2 falling in pure water ($Re_P = 1661$).

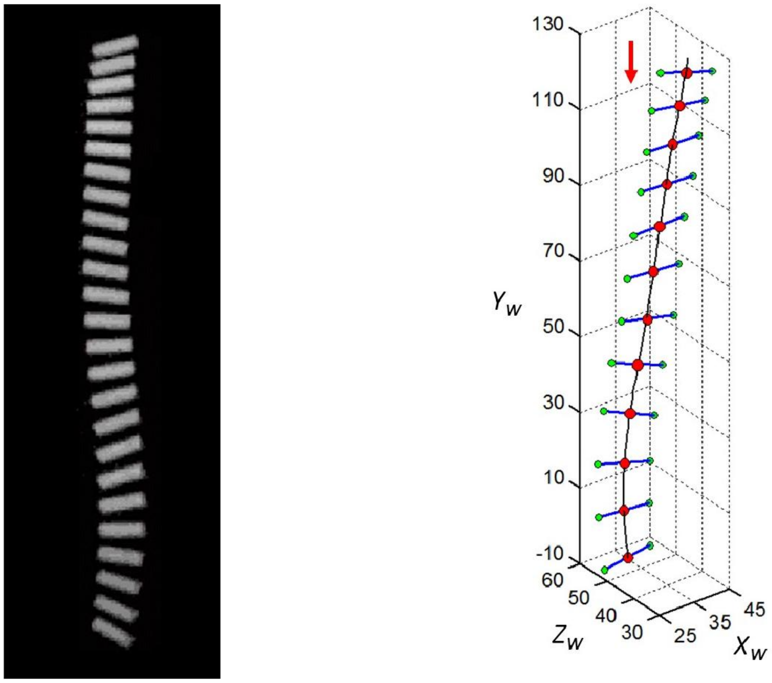

(a) (b)

Figure 6.20 2D visualization (a) and 3D plot (b) of the trajectory of cylinder C4 settling in pure water at $Re_P = 1975$. Dimensions in mm.

The plot of the different values of the angle of incidence is given in Figure 6.21, where it was observed that starting at $t = 0.2$ s, approximately, the behaviour was alike to that obtained for particle C6 at $Re_P = 614.6$ after 0.1 s. In fact, the magnitude of the angle also stayed within a similar interval: $\alpha = 70° – 88°$. Furthermore, considering that U_T conditions also were nearly achieved at $t = 0.2$ s, as illustrated in Figure 6.22, it can be said that the sinusoid-like pattern plus regular oscillations of α still dominate the settling motion of cylinders at $Re_P > 10^3$.

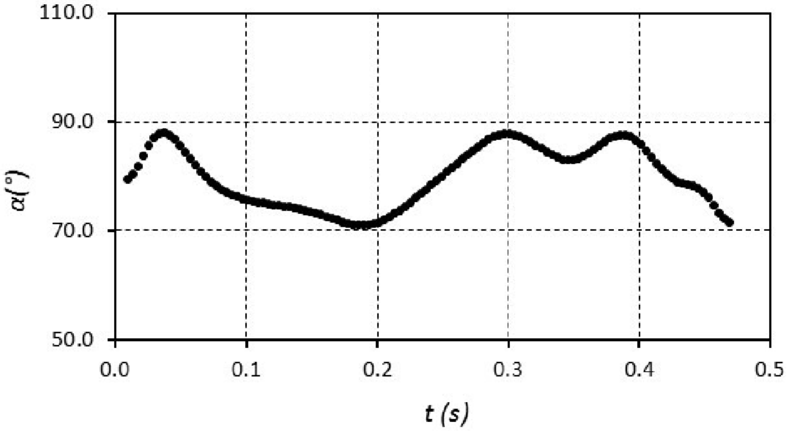

Figure 6.21 Variation of the angle of incidence of cylinder C4 along its fall-trajectory in pure water ($Re_P = 1975$).

The time variation of the velocity determined for cylinder C4 falling in pure water is exposed in Figure 6.22 along with the predicted value from Equation (2.10). As noted from the graph, at $t = 0.25$ s, the magnitude of U_T was 0.30 m/s, then it increased up to 0.33 m/s at $t = 0.34$ s, to later decrease again to 0.30 m/s. In consequence, 0.30 m/s was taken as the representative value of U_T, which also was approximately 7 % differed higher that the predicted magnitude.

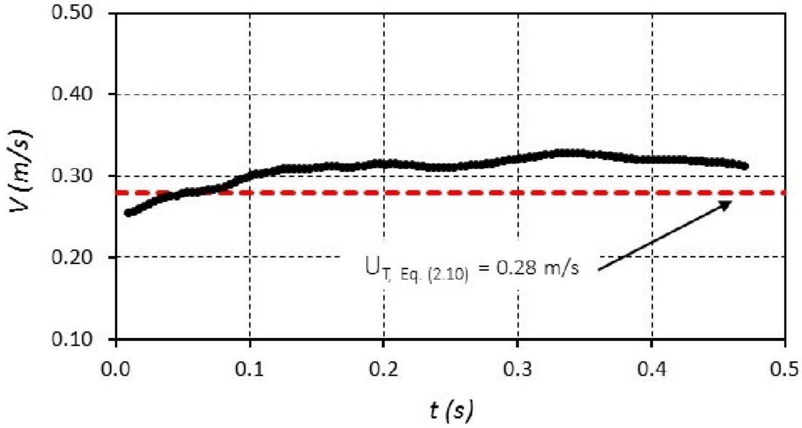

Figure 6.22 Velocity variation of cylinder C4 falling in pure water ($Re_P = 1975$).

The plots of the drag force exerted on particle C4 and the corresponding coefficients of resistance are given in Figures 6.23 and 6.24, respectively. In the same way as for the previous cylinders with oscillatory motion, F_D did not achieve a fixed value but kept increasing gradually from 1.3 mN to 1.5 mN. Additionally, at U_T conditions the magnitudes of the coefficient varied between $C_D = 0.7$ to $C_D = 0.8$, numbers which are 42 % and 33 % lower than the estimations given by Equation (2.24a). It is suggested that such variation was due to the presence of the secondary oscillating-motion.

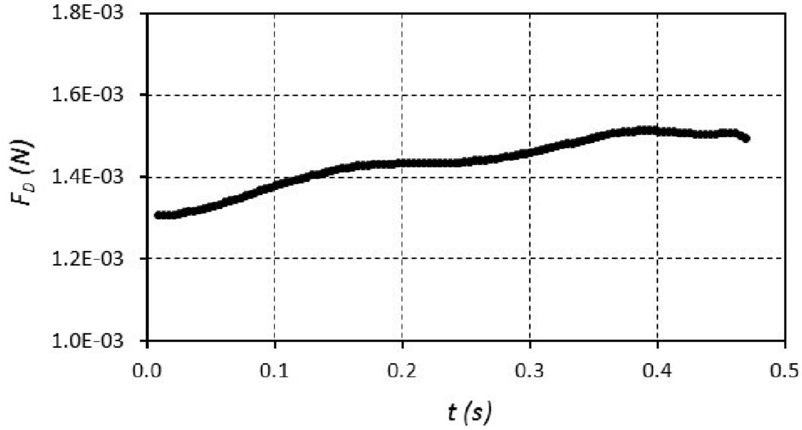

Figure 6.23 Plot of the drag force acting on cylinder C4 as it freely descended in pure water at $Re_P = 1975$.

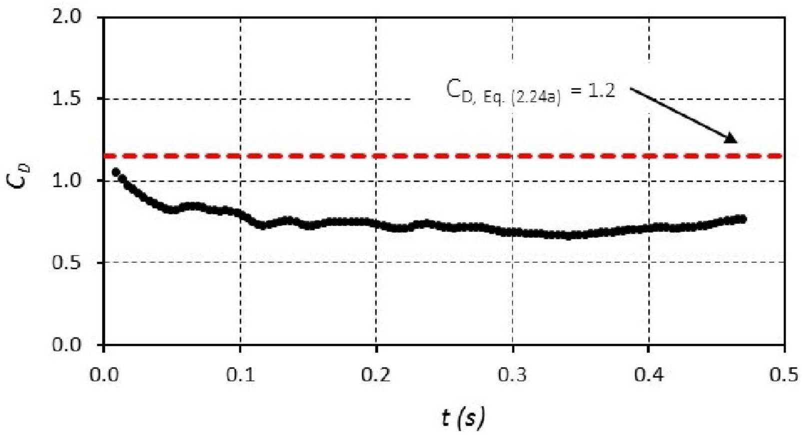

Figure 6.24 Drag coefficient estimated for cylinder C4 moving in pure water (Re_P = 1975).

In Figure 6.25 there is a graphical summary of the terminal velocities obtained for all the experiments with cylindrical particles. The corresponding values given by the correlation of Haider and Levenspiel (Equation 2.10) are also indicated for the purpose of comparison. As it was done for the spheres, Re_P was omitted from the horizontal axis and replaced by N, the number of different Re_P studied. The relation between Re_P and N is provided in Table 6.1. Since more than one test was done for every N, the magnitudes of U_T plotted correspond to the arithmetic mean for each case.

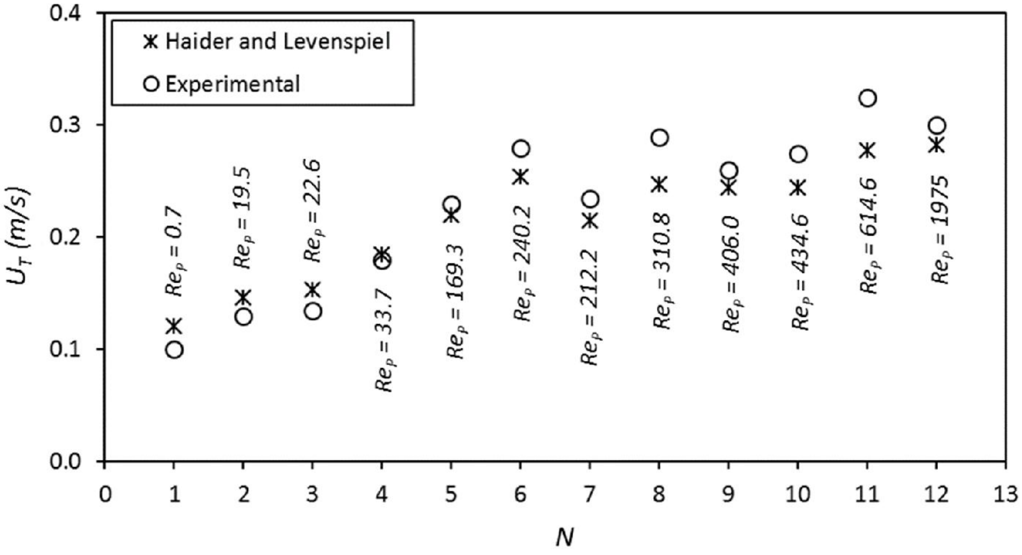

Figure 6.25 Comparison between the experimental and the predicted the terminal velocities obtained for the cylindrical particles.

As it is depicted in Figure 6.25, before Re_P ~ 30 the magnitude of the particle terminal velocity obtained experimentally was smaller than that predicted by Equation (2.10).

Then, in the interval $30 < Re_P < 240$ the agreement between both results was remarkable. Finally, for $Re_P > 240$ the correlation under-estimated the true value of U_T. In summary, throughout the whole Reynolds number range, the differences varied between 2 % to 17 %.

Table 6.1 Relation between Re_P and N of Figure 6.25.

N	Re_P	N	Re_P
1	0.7	7	212.2
2	19.5	8	310.8
3	22.6	9	406.0
4	33.7	10	434.6
5	169.3	11	614.6
6	240.2	12	1975.0

The corresponding values of the coefficient of resistance for all the experiments done are also summarised and presented in Table 6.2 and Figure 6.26 in function of Re_P. The magnitudes of C_D predicted by Equations (2.24a, 2.24c, 2.24d, 2.24f) for all the cases are included in the graph too. The values of Re_P employed in the correlations were calculated using the magnitudes of U_T determined experimentally, and not the theoretical results given by Equation (2.10). Also, like in Figure 6.25, the values of C_D plotted correspond to the averages of all the tests done for every N.

Table 6.2 Relation between Re_P and C_D.

N	Re_P	C_D	$\emptyset$	N	Re_P	C_D	$\emptyset$
1	0.7	43.6	0.8	7	212.2	1.0	0.7
2	19.5	3.1	0.8	8	310.8	0.8	0.7
3	22.6	2.7	0.8	9	406.0	0.9	0.8
4	33.7	1.9	0.8	10	434.6	0.8	0.8
5	169.3	1.0	0.8	11	614.6	0.7	0.8
6	240.2	0.8	0.8	12	1975.0	0.8	0.8

As observed in Figure 6.26, for cylinders with $\emptyset = 0.8$ ($L < 10.5$ mm), at $Re_P < 1.0$, the difference between the experimental result and those from the correlations was practically negligible, indeed the maximum discrepancy found was 3 %. However, in the interval $1.0 < Re_P < 169$, the disagreement fluctuated between 2 % and 28 %, and for $200 < Re_P < 1000$, the presence of secondary motions elevated it up to the range 14 % – 32 %, with respect to the correlations proposed by Haider and Levenspiel [16], Ganser [18], and Chien [53]. Finally, at $Re_P > 1000$, the discrepancy, still relative to the same three correlations, increased even further, to 36 % – 39 %. For cylinders with Ø = 0.7 (L > 20.0 mm), only evaluated in the interval 200 < Re_P < 350, the obtained differences were higher, fluctuating between 40 % – 55 % with respect to the same three authors.

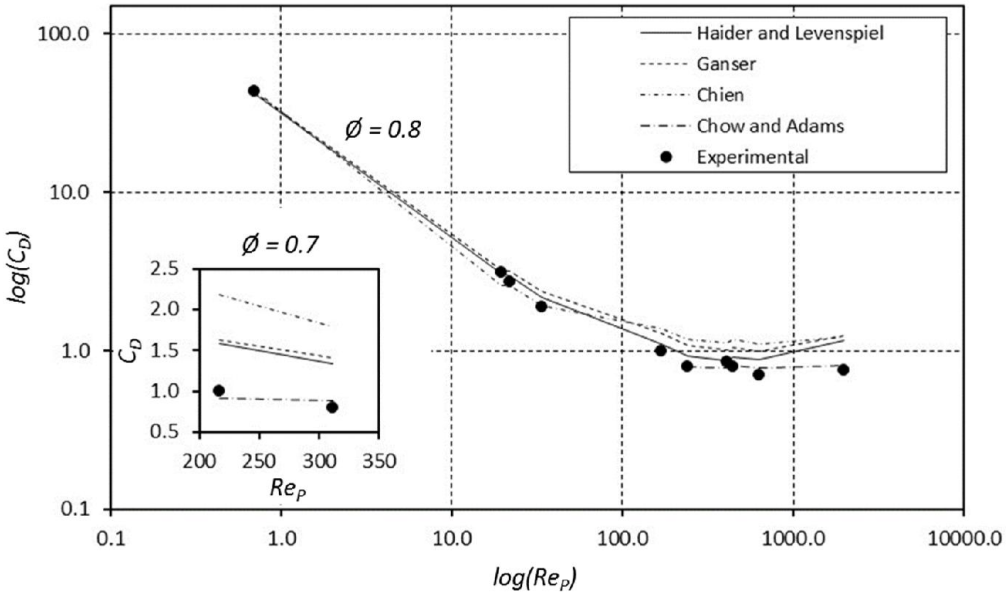

Figure 6.26 Comparison between the experimental and the correlation-predicted values of C_D found for the cylindrical particles.

From the three equations discussed in the previous paragraph, the one published by Haider and Levenspiel [16] had, in general, the lowest differences with respect to the experimental data obtained here, throughout the whole Re_P interval, nevertheless the correlation suggested by Chow and Adams [27] was not discussed yet because its validity begins at Re_P = 200. It was found that for all the particle Reynolds numbers larger than 200, the difference between their equation and the experimental data shown here did not surpass 11 %, regardless the magnitude of Ø. It is believed that this happened because in their correlation, they considered the influence of the secondary motions.

Chow and Adams [27] used the aspect ratio instead of the sphericity and nominal diameter to characterise the cylinders, and based on the experimental results given here, it seemed that such approach tends to be more accurate for Re_P > 200. Moreover, they also said that as long as $\sqrt{\frac{\rho_P/\rho_f}{\sigma}} > 0.5$, the oscillatory motion will always appear, nevertheless, in this work it was found that such condition applies only if $Re_P > 240$.

6.2 KINEMATICS AND DYNAMICS OF DISK-SHAPED PARTICLES AT DIFFERENT REYNOLDS NUMBERS

In Section 2.2.4 of Chapter 2 it was mentioned that for the case of a disk settling in a liquid at rest Stringham et al. [26] reported three different patterns of motion: steady, transition, and tumble. Whilst the first one normally appears at relatively small values of Re_P, the border between the other two is not clear. In this research, however, the lowest Reynolds number studied is $Re_P = 19.7$ and it was obtained for the settling of disk D2 in mixture 80/20. As illustrated in Figure 6.27a, the motion was totally steady with the maximum projected area perpendicular to the direction of fall. The corresponding 3D reconstructed trajectory is plotted in Figure 6.27b, where the disk centroid is coloured in red, the extreme points P_1 and P_2 in green, and the longest axis in blue.

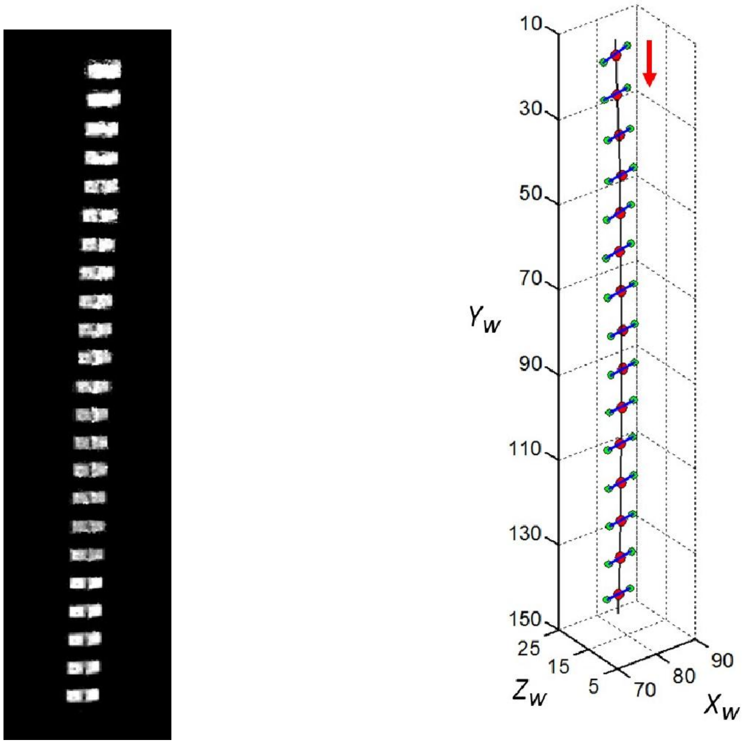

(a) (b)

Figure 6.27 2D (a) and 3D (b) visualizations of the free fall of disk D2 in mixture 80/20 at Re_P =19.7. Dimensions in mm.

From Figure 6.27 it can be noticed that despite describing a steady fall, the disk exhibited a slight horizontal deviation. Nevertheless, the orientation remained unchanged because, as represented in Figure 6.28, the secondary flow around the particle and the trail left downstream were highly symmetrical. In the plots of Figure 6.29, it can also be appreciated that the angle of incidence stayed fixed at α = 84.3° and the particle projected area, calculated as $A_P = 0.25\pi d^2 sin\alpha$, at A_P = 31.5 μm^2 during the whole time interval.

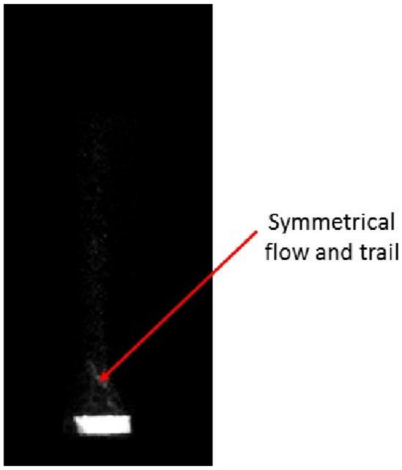

Figure 6.28 Augmented view of the secondary flow and trail left by disk D2 settling in mixture 80/20 at Re_P =19.7.

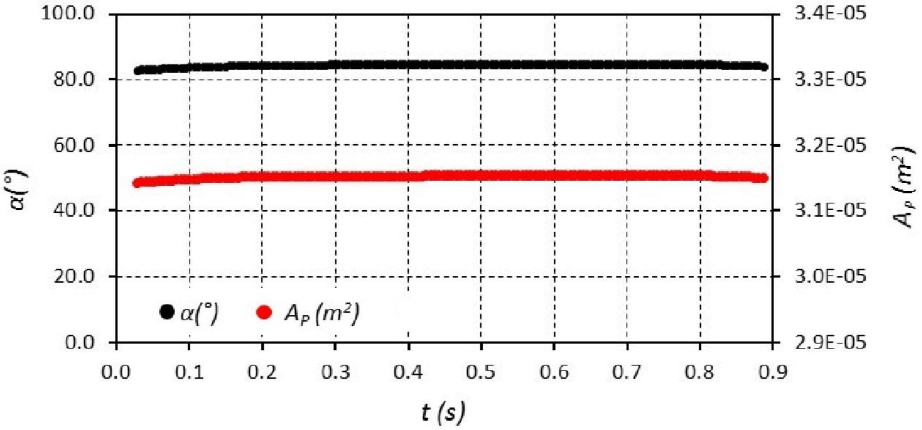

Figure 6.29 Angle and projected area variation of disk D2 sinking freely in mixture 80/20 at Re_P =19.7.

In Figure 6.30 the graph of the time variation of the velocity experienced by disk D2 is displayed, where it can be seen that after t = 0.15 s the particle achieved a terminal velocity which started at U_T = 0.15 m/s and progressively decreased to U_T = 0.14 m/s. The magnitude of U_T predicted by Equation (2.10) was 0.17 m/s, equivalent to 15 % of discrepancy with the experimental data.

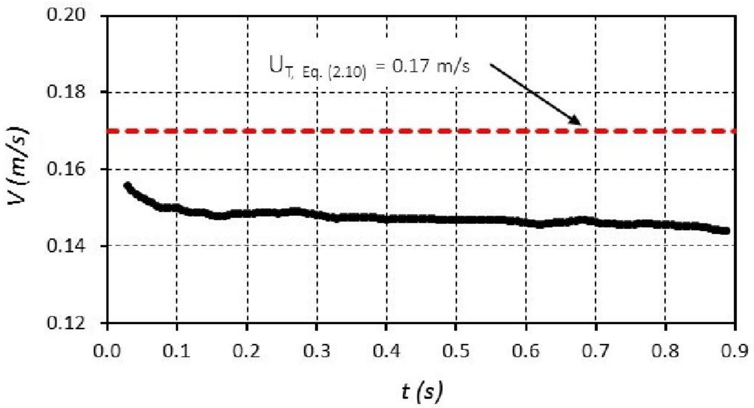

Figure 6.30 Velocity variation obtained for the fall of disk D2 in mixture 80/20 (*Re_P* =19.7).

The drag force acting on disk D2 as well as the corresponding coefficient of resistance are plotted in Figures 6.31 and 6.32, respectively, where it can be seen observed that *F_D* remained unchanged at 1.2 mN throughout the whole time interval, whilst the coefficient augmented steadily to reach *C_D* = 2.9, the same value estimated by Equation (2.24a), at *t* = 0.55 s, approximately.

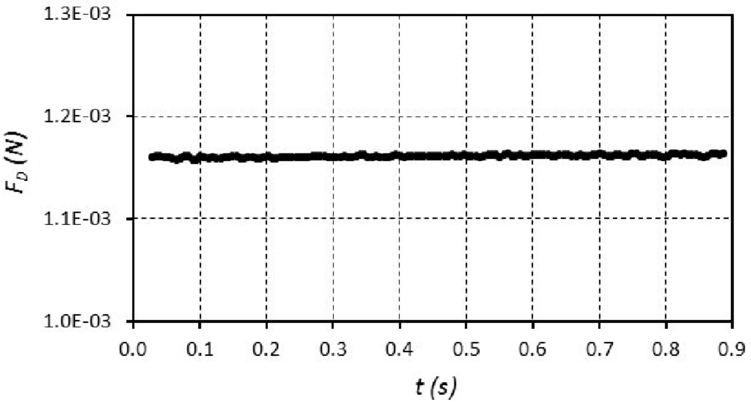

Figure 6.31 Plot of the drag force acting on disk D2 during its settling in mixture 80/20 at *Re_P* =19.7.

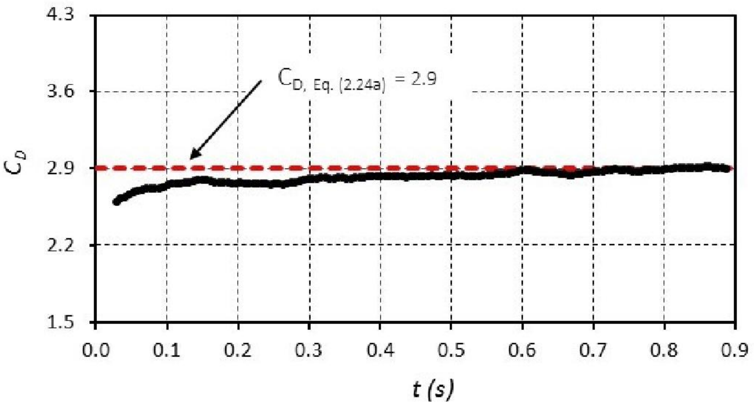

Figure 6.32 Drag coefficient estimated for disk D2 moving in mixture 80/20 (*Re_P* = 19.7).

The motion of disks at higher Reynolds numbers is represented in two dimensions in Figure 6.33, where the settling of disks D2 and D3 in mixture 65/35 at Re_P = 163.0 and 186.8, respectively, is imaged. As shown, the fall continued to be flat and steady for the first case, whilst few disk oscillations appeared in the second one, although by the time the solid left the camera field of view, its orientation was horizontally flat. The analogous three-dimensionally regenerated paths for both cases are portrayed in Figure 6.34. Here too, some slight fluctuations in the trajectory can be appreciated, mainly for the second disk.

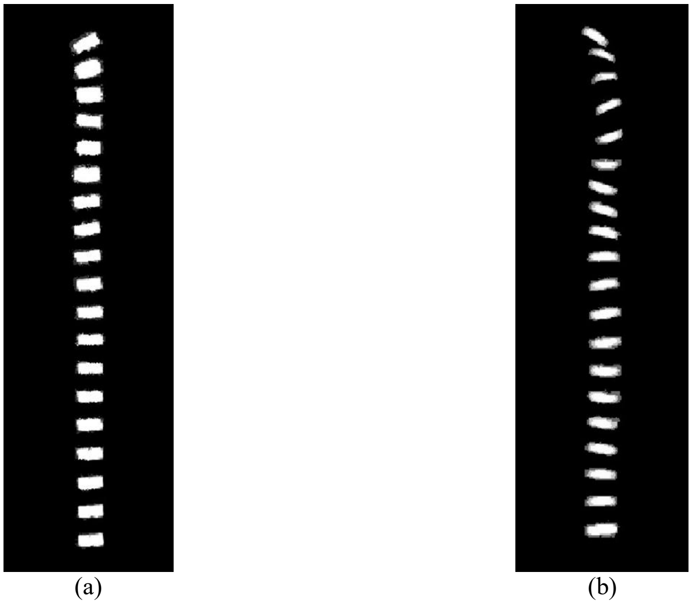
(a) (b)

Figure 6.33 2D visualizations of the paths of disks D2 (a) and D3 (b) falling in mixture 65/35 at Re_P = 163.0 and 186.8, respectively.

The change of the angle of incidence for both disks is graphed in Figure 6.35, where it can be said that after t = 0.37 s, approximately, both particles reached stable values, which in average were α = 83.7° for D2 and α = 87.7° for D3. In addition, this time also corresponded to the onset of terminal velocity conditions, as it can be proved from the velocity plots of Figure 6.36.

In Figure 6.35 the plots of the disk projected area where not included because it described exactly the same distribution as the angle of incidence. This situation occurred for all the disks, therefore in the coming graphs A_P was also omitted. As it is shown in Figure 6.36 the variation of U_T between the disks was different. Whilst D2 assumed a steady value equal to 0.26 m/s at t = 0.37 s, for D3 an oscillating behaviour in the range U_T = 0.19 m/s – 0.22 m/s was discovered. Nevertheless, for the purpose of comparison an averaged valued equal to 0.21 m/s was also calculated. In both cases, the discrepancies between the experimental results and the predictions of Equation (2.10) did not exceed 4 %.

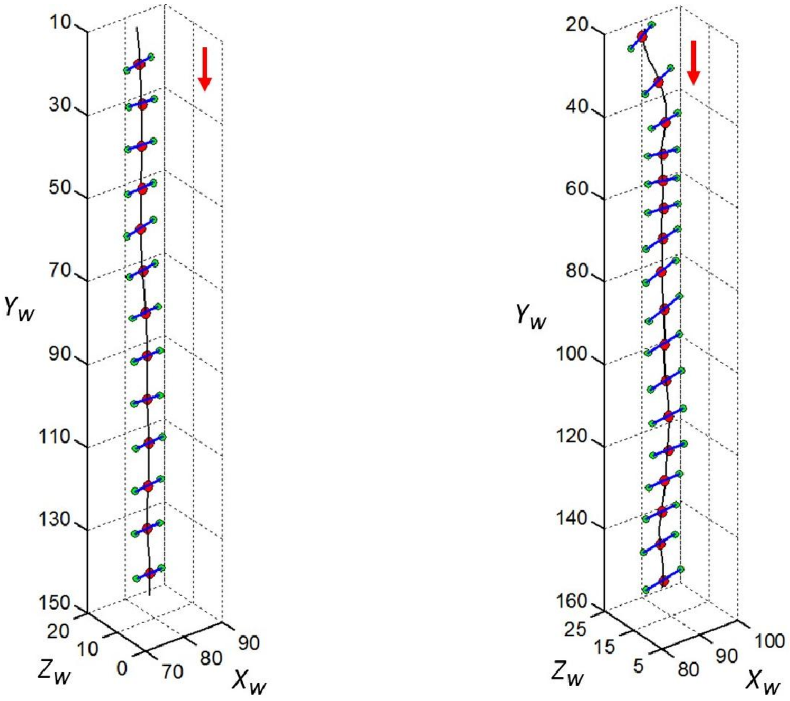

(a) (b)

Figure 6.34 3D reconstructed trajectories of disks D2 (a) and D3 (b) settling in mixture 65/35 with Re_P = 163.0 and 186.8, respectively.

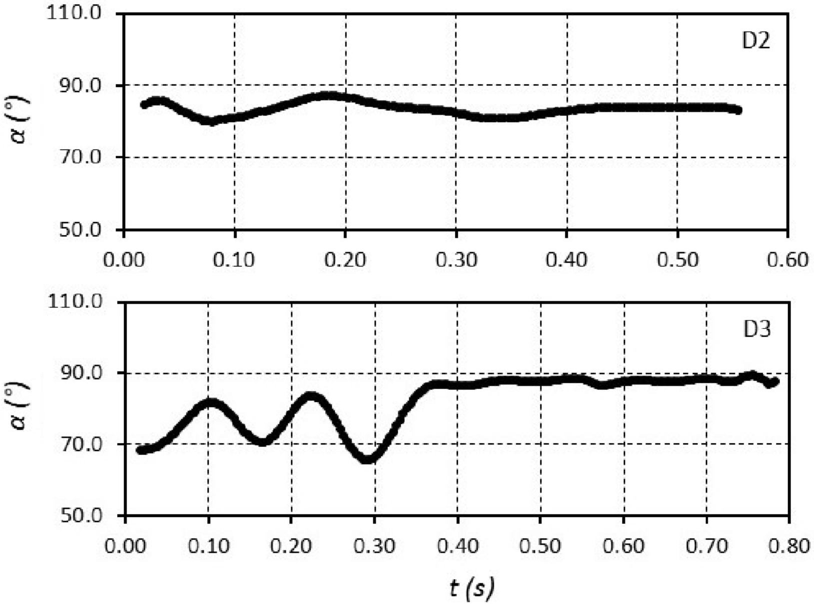

Figure 6.35 Orientation angle detected for disks D2 and D3 whilst descending in mixture 65/35 at Re_P = 163.0 and 186.8, respectively.

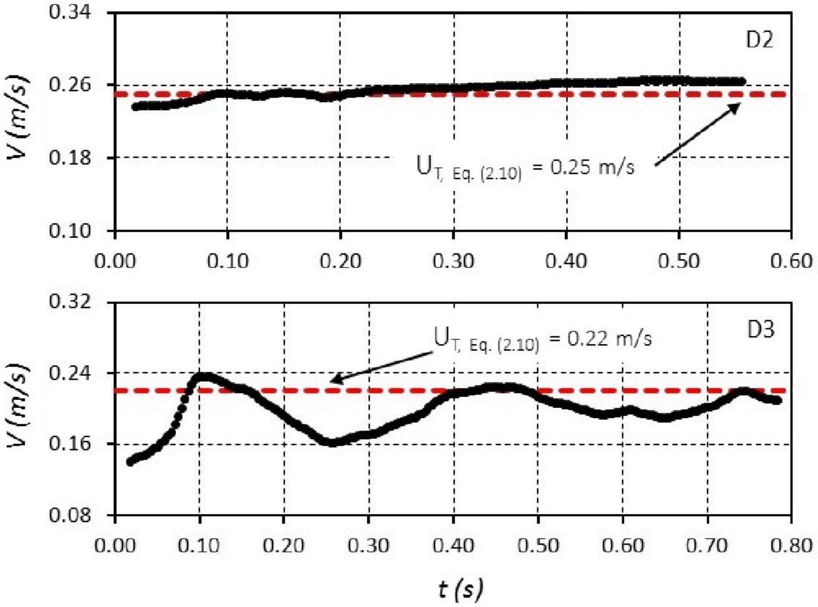

Figure 6.36 Velocity variation for disks D2 and D3 falling in mixture 65/35 at Re_P = 163.0 and 186.8, respectively.

Figures 6.37 and 6.38 display the time change of the drag force and the corresponding coefficient of resistance for both particles moving in mixture 65/35. As it can be observed in the first figure, for the solid D2 the magnitude of F_D was practically constant at 1.2 mN throughout the whole field of view. On the other hand, relatively large fluctuations were calculated for disk D3 before t = 0.20 s, however, since these were well before U_T was reached they were discarded. At U_T conditions, the force varied between F_D = 2.1 mN and 2.5 mN with fluctuations considerably reduced.

From Figure 6.38 it can be seen that at conditions of terminal velocity the coefficient of resistance determined for D2 was located in the interval C_D = 0.9 – 1.0, in average 21 % below from the value estimated using Equation (2.24a). In contrast, the range of variation of C_D found for disk D3 was considerably larger: C_D = 1.0 – 1.4. It is believed that this was the consequence of the oscillating behaviour of U_T because the plot of C_D followed a similar trend. Additionally, in this case the theoretical outcome of Equation (2.24a) was situated at the top of the interval, corresponding to an overestimation of 14 % with respect to the mean of the experimental data.

Although patterns of oscillation, gliding, and tumbling normally arise at considerably large numbers of Re_P, it was illustrated in Figure 2.14 and Table 2.3 of Chapter 2 that according to Stringham et al. [26] such behaviours can also be found for disks settling at values of Re_P as low as 300. This agreed with the results obtained in this research for the free-fall of particle D1 in mixture 65/35 where pure tumbling was visualized at $Re_P = 226.2$, as portrayed in Figure 6.39 in both two and three dimensions. The change in the corresponding values of the angle of incidence is also graphically displayed in Figure 6.40.

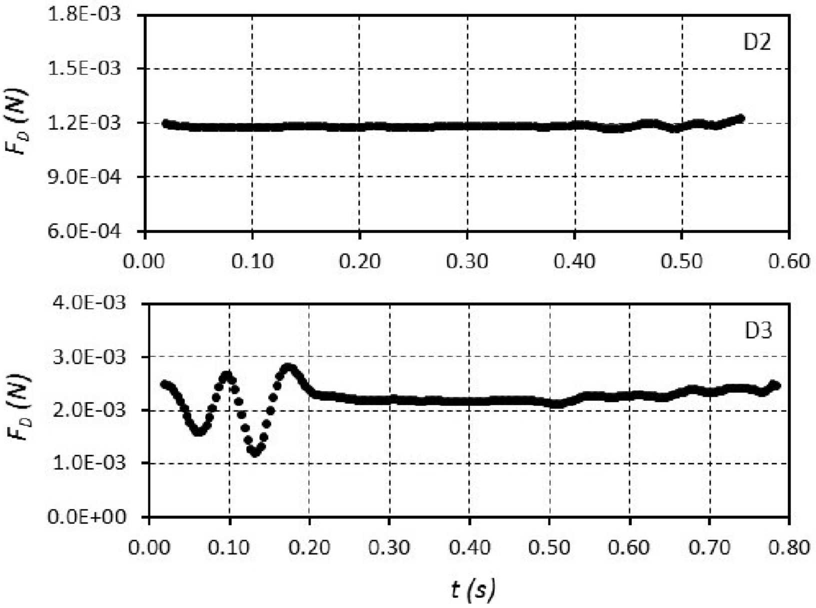

Figure 6.37 Drag force plots for disks D2 and D3 falling in mixture 65/35 at $Re_P = 163.0$ and 186.8, respectively.

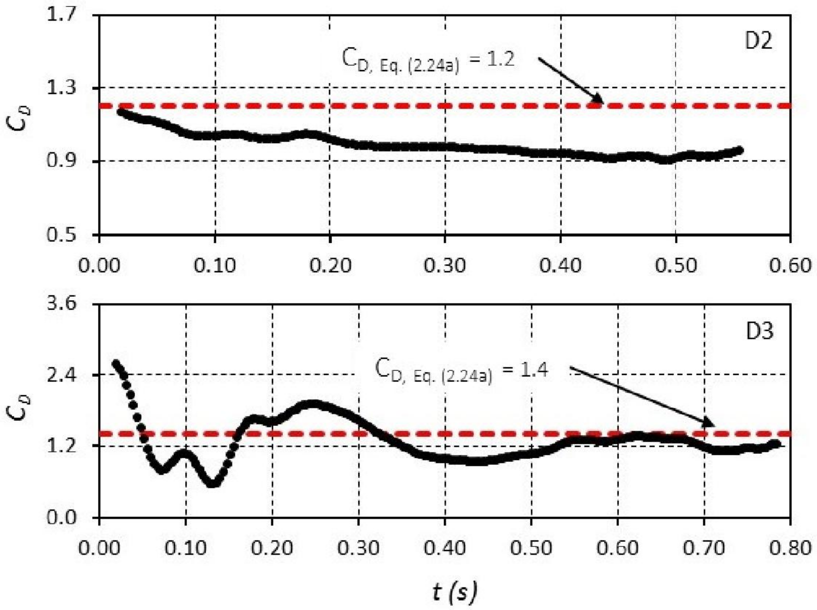

Figure 6.38 Time-change of the coefficient of drag found for disks D2 and D3 moving in mixture 65/35 at $Re_P = 163.0$ and 186.8, respectively.

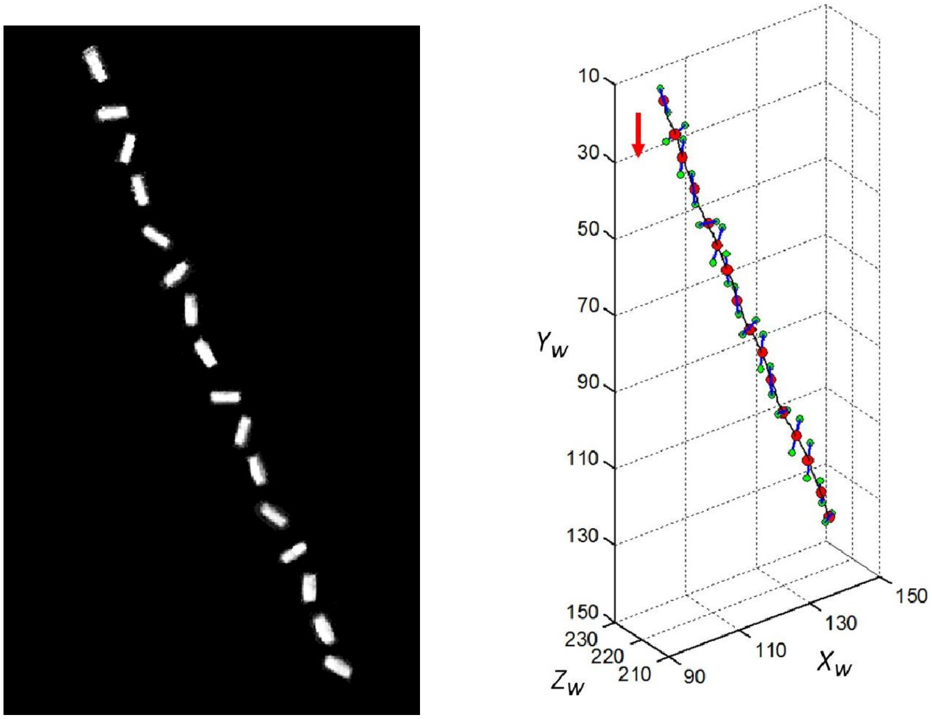

(a) (b)

Figure 6.39 2D path (a) and 3D path (b) of disk D1 falling in mixture 65/35 at $Re_P = 226.2$. Dimensions in mm.

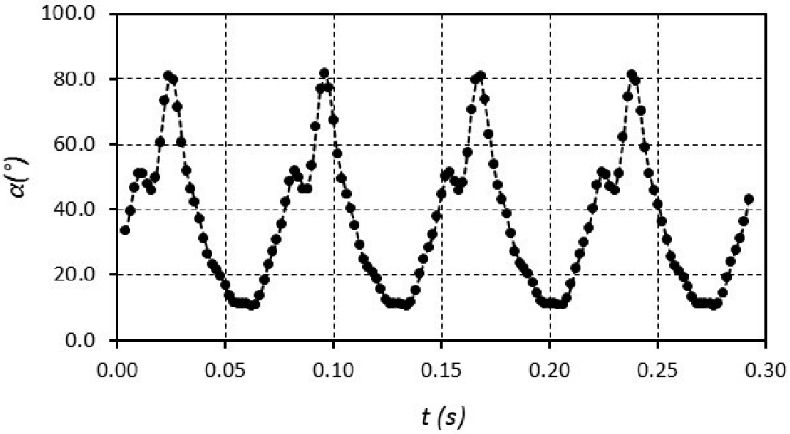

Figure 6.40 Angular variation shown by disk D1 falling in mixture 65/35 at $Re_P = 226.2$.

As observed in Figure 6.40, α described a regular sinusoidal pattern with 71.2° of amplitude and 0.07 s of period during the whole visualization. The minimum value of α was 10.5°, and the maximum was 81.7°. It was assumed that when the disk entered the field of view of the stereo camera it was already at final velocity conditions, since the plot of the velocity provided in Figure 6.41 also exhibited a similar tendency, with

U_T = 0.30 m/s and U_T = 0.58 m/s as the largest and lowest determined magnitudes. The average U_T = 0.44 m/s corresponded exactly to the prediction of Equation (2.10).

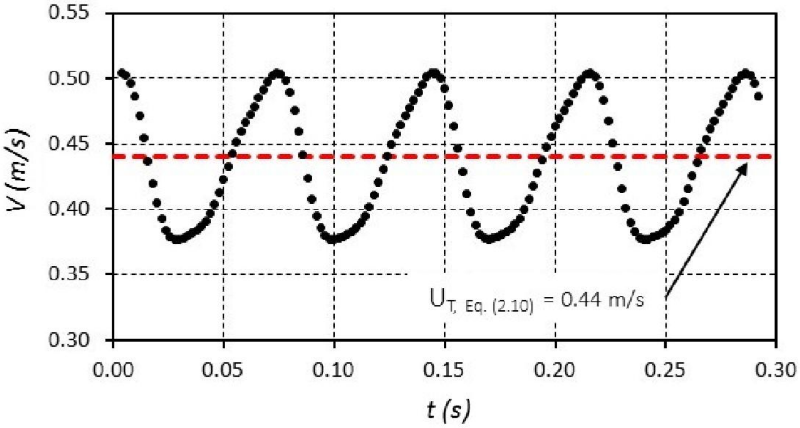

Figure 6.41 Plot of the velocity experienced by disk D1 during its free fall in mixture 65/35 at Re_P = 226.2.

In the plot of the drag force displayed in Figure 6.42 a similar sinusoidal configuration was obtained in the time-range t = 0.03 s – 0.26 s. The magnitude of the force fluctuated between F_D = 0.7 mN and F_D = 4.9 mN. The corresponding behaviour of the coefficient of resistance is illustrated in Figure 6.43 where regularities were also observed in the same interval of time. The range of C_D was 0.8 – 2.6, being the mean value equal to 1.7. In this case, the difference obtained with respect to Equation (2.24a) was 13 %. However, most of the experimental values of C_D were above the correlation result.

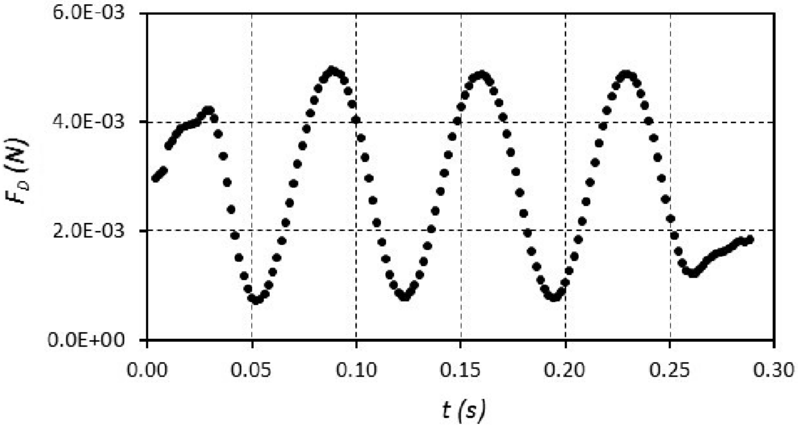

Figure 6.42 Drag force graph of disk D1 falling in mixture 65/35 at Re_P = 226.2.

As it can be noticed from the previous figures which belonged to the case of a tumbling disk, in this type of fall all the motion parameters are characterised for exhibiting a highly regular, alternating pattern. Furthermore, the settling path follows a straight but not vertical line. Tumbling did not appear again for the rest of Re_P studied here, but an oscillating mode of fall with increasing regularity was established, as illustrated in Figure 6.44 for disk D3 falling in liquids 50/50 and 0/100 with $Re_P = 384.4$ and 1362, respectively.

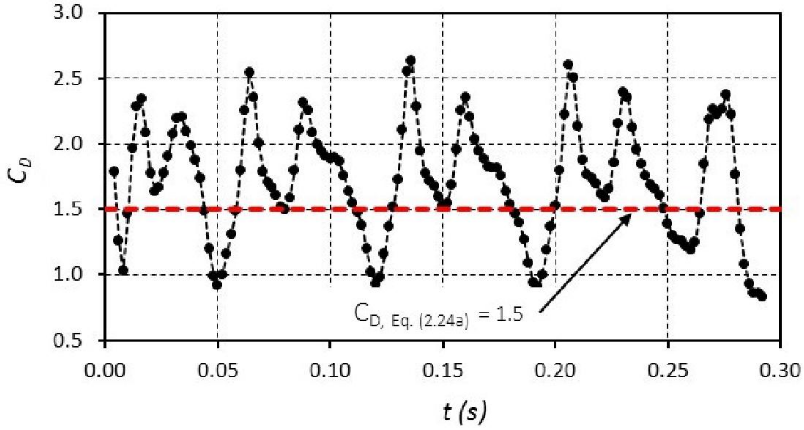

Figure 6.43 Plot of the coefficient of resistance determined for disk D1 when settling in mixture 65/35 at $Re_P = 226.2$.

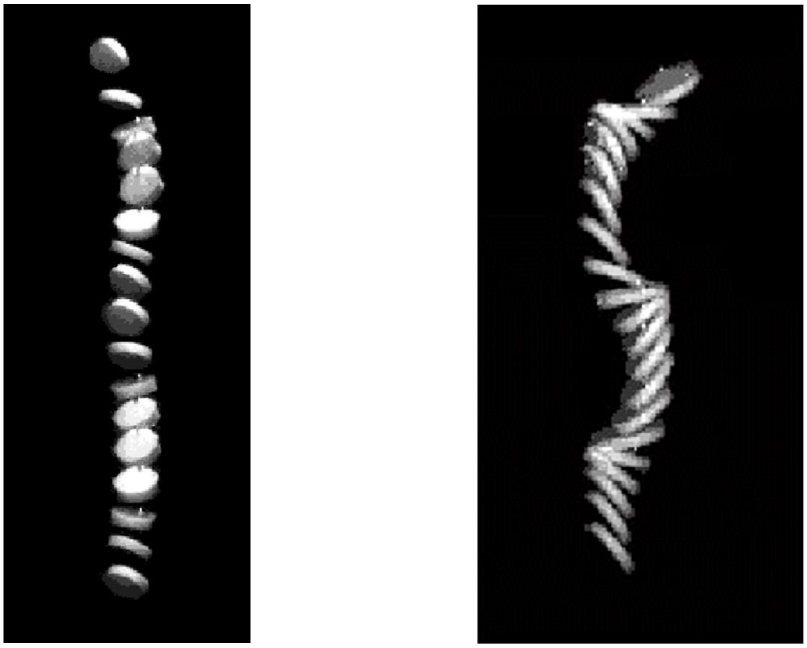

(a) (b)

Figure 6.44 2D visualization of the fall of disk D3 in mixtures 50/50 and 0/100 ($Re_P = 384.4$ and 1362, respectively).

Figure 6.44a shows that at $Re_P = 384.4$ the disk secondary motion was mainly composed by oscillation and gliding whilst Figure 6.44b depicts that at $Re_P = 1362$ it was formed by largely regular oscillations. In both cases, these secondary motions greatly deviated the 3D regenerated paths from straight trajectories, as displayed in Figure 6.45a, where the particle longest axis was not represented for clarity purposes. Only the disk centroids are still coloured with red points.

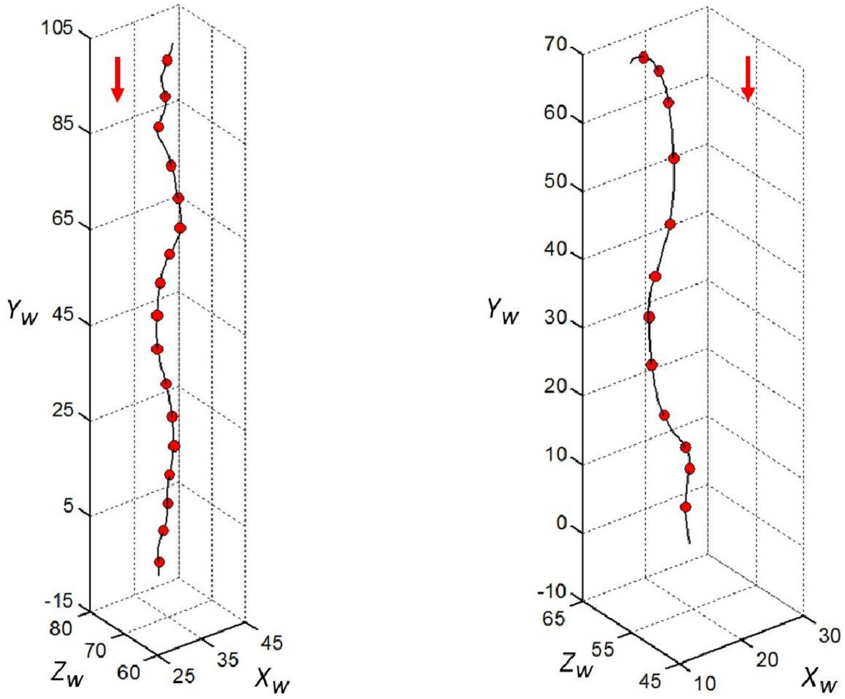

(a) (b)

Figure 6.45 3D reconstructed paths for the fall of disk D3 in mixtures 50/50 and 0/100 at *Re_P* = 384.4 and 1362, respectively. Dimensions in mm.

The characteristics of the flow downstream the disk at *Re_P* = 1362 can be appreciated from the Schlieren visualization portrayed in Figure 6.46. At this value of Reynolds number, the flow exhibited a high turbulence, which was increased even farther by every change in the orientation of the solid. In addition, the also turbulent trail left by the particle preserved the zig-zag shape until it was dissipated in the surrounding fluid. No symmetry was found in the visualized fluid.

In Figure 6.47 the behaviour of the angle of incidence is plotted in function of time for both settlings. As it can be seen, in the first case the combinations of gliding and oscillation avoid the formation of a uniform curve, like the one attained for the second case with approximately 55.8° of amplitude and 0.4 s of period. From both plots it can also be noticed that the alternations observed in the second fall were considerably larger in magnitude than those of the first one. This directly impacted on the values of the velocity, as illustrated in Figure 6.48.

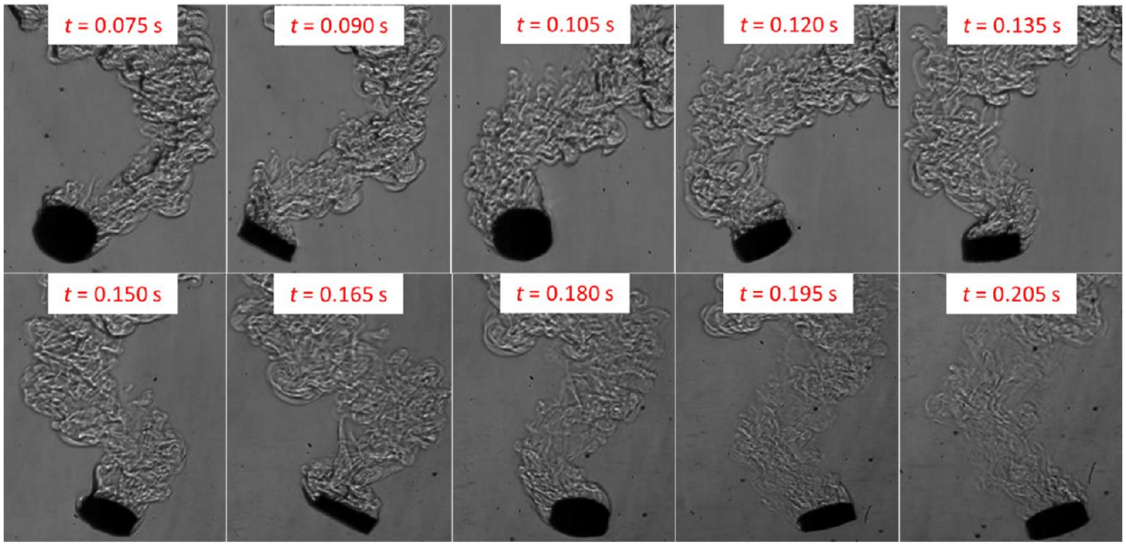

Figure 6.46 Schlieren visualization of disk D3 settling in mixture 0/100 at Re_P = 1362.

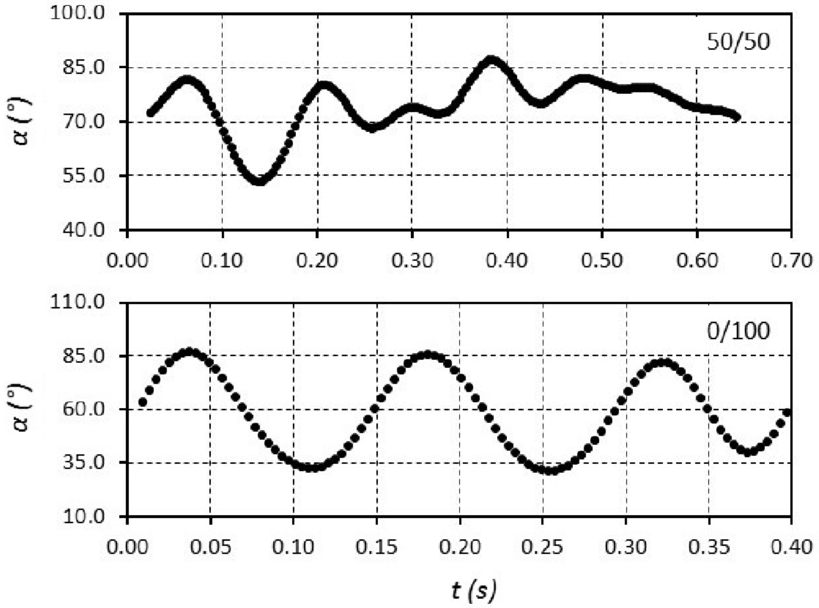

Figure 6.47 Variation of the angle of incidence for disk D3 settling in mixtures 50/50 and 0/100 at Re_P = 384.4 and 1362, respectively.

From the graphs of Figure 6.48 it was noticed that the values of the U_T computed with Equation (2.10) coincided in both cases with the maximum velocities registered for the settling of the disks, however they were 21 % and 33 % away from the averages U_T = 0.19 m/s and 0.18 m/s, respectively. It should also be noted that despite the fact that viscosity of the second liquid was lower, in it the disk fell with a smaller averaged-final velocity due to the larger alternations mentioned in the previous paragraph. Similar to the tumbling, the oscillatory and gliding motions did not have an explicit fixed value of the terminal velocity, thus averages needed to be calculated so that the comparison with the correlation could be done. Also, the corresponding Reynolds numbers were computed using these averages.

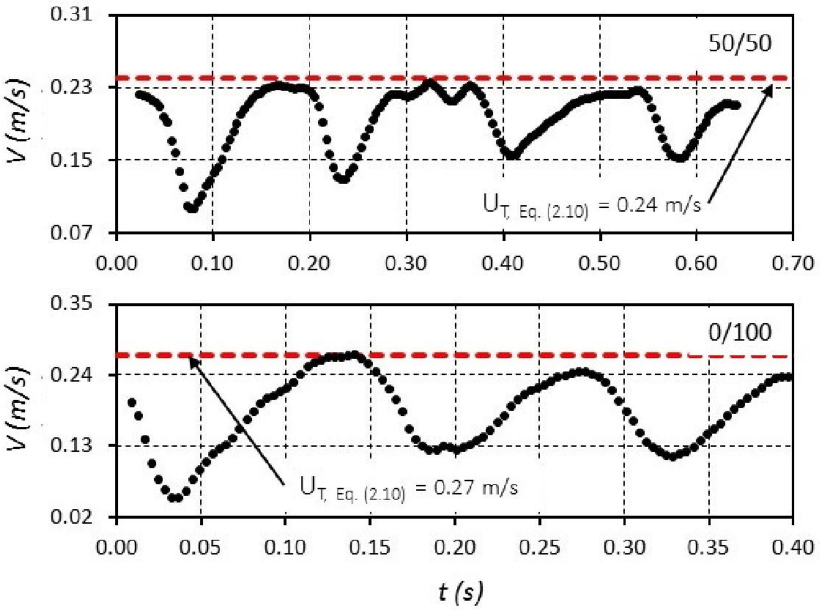

Figure 6.48 Plot of the velocity obtained for the settling of disk D3 in mixtures 50/50 and 0/100 at Re_P = 384.4 and 1362, respectively.

The plots of the drag force exerted on disk D3 while settling in these two mixtures are provided in Figure 6.49, where it can be perceived that alternated patterns were also acquired for both cases. The minimum and maximum magnitudes registered were $F_{D,min}$ = 0.3 mN and $F_{D,max}$ = 4.5 mN for the first mixture, and $F_{D,min}$ = 0.5 mN and $F_{D,max}$ = 4.2 mN for the other one. Here again, the influence of the larger oscillations can be perceived. The corresponding plots of the coefficient of drag are presented in Figure 6.50.

As displayed in Figure 6.50, during the whole time interval the coefficient of resistance does not exhibit a steady value in any of the cases, on the contrary, despite being most of the data relatively close to the values predicted by Equation (2.24a), C_D still presents considerably large fluctuations. Nevertheless, in order to perform a contrast with the correlation, the averaged values C_D = 1.8 and 2.5, respectively, were computed, showing that both were 29 % and 47 % bigger than the results of the equation. In the oscillation, gliding, and tumbling types of fall, the averaged-magnitudes were only simple representations for the purpose of comparison, because it is believed here that the large fluctuations which appeared in the plots cannot be fully summarised in just one number.

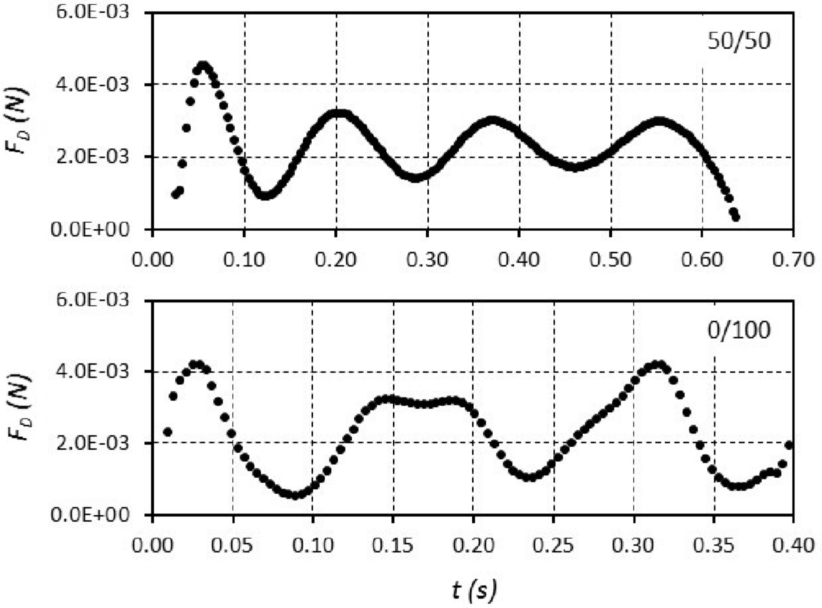

Figure 6.49 Drag force exerted on disk D3 during its fall in liquids 50/50 and 0/100 with *Re_P* = 384.4 and 1362, respectively.

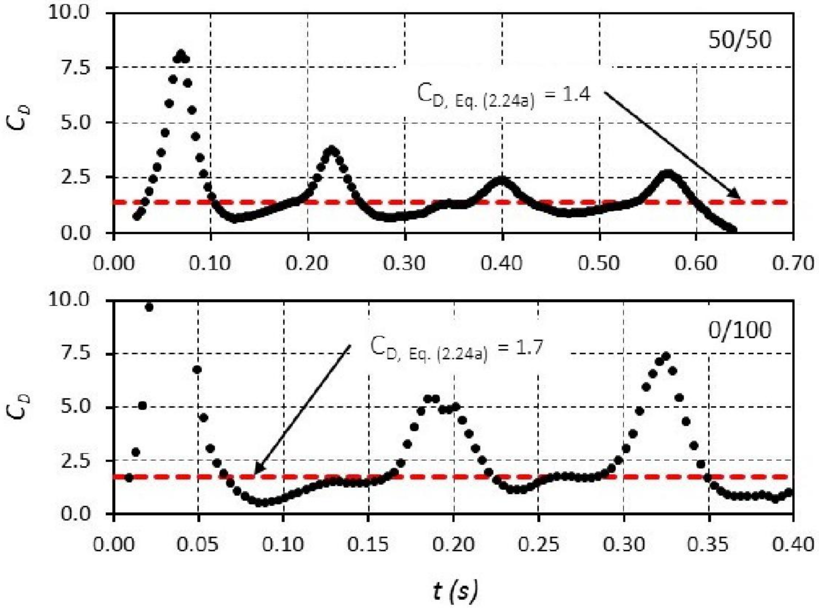

Figure 6.50 Variation of the coefficient of resistance for disk D3 settling in mixtures 50/50 and 0/100 at *Re_P* 384.4 and 1362, respectively.

By following the same procedure applied to the spheres and cylinders, in Figure 6.51 it is plotted the collection of all of the experimental values of U_T as a function of N, the number of Re_P investigated. The results given by Equation (2.10) are also included for comparison. The relation between N and Re_P is provided in Table 5.3. Each experimental U_T point corresponds to the arithmetic mean of all the tests done for every N. Moreover, it also has to be highlighted that because the situations where secondary motions were present lacked of a steady value of U_T, the average between $U_{T,max}$ and $U_{T,min}$ was taken for each individual case. From the figure, it was deduced that the largest discrepancies with respect to the correlation occurred at $Re_P < 20$ and $Re_P > 384$, with percentage equivalents situated in the range 16 % – 34 %. For the rest of Reynolds numbers, the differences fluctuated between 2 % and 6 %.

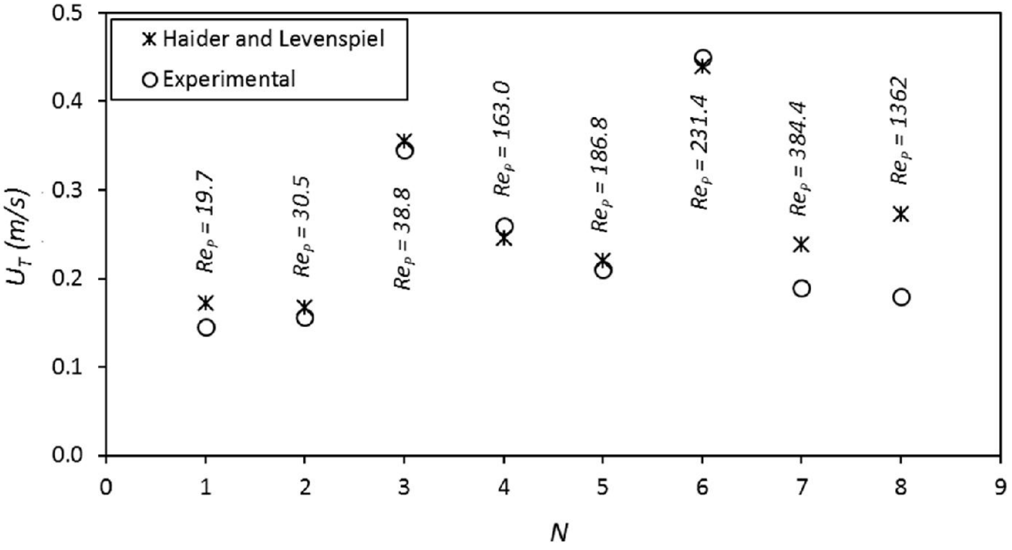

Figure 6.51 Comparison between the experimental and the predicted the terminal velocities obtained for the disks.

Table 5.3 Relation between N and Re_P of Figure 6.51.

N	Re_P	N	Re_P
1	19.7	5	186.8
2	30.5	6	231.4
3	38.8	7	384.4
4	163.0	8	1362.0

The summary of the drag coefficients obtained for the settling disks is also shown graphically in Figures 6.52. As it was done for U_T in the previous figure, every magnitude of C_D plotted corresponds to the average of all the tests done for that Re_P.

In addition, the theoretical results predicted by Equations (2.24a, 2.24c, 2.24d) are included in the plot for comparison. Furthermore, the theoretical magnitudes of the terminal velocity were not used here to estimate the particle Reynolds numbers used in the correlations, rather those obtained experimentally were employed.

Table 5.4 Relation between Re_P and C_D.

N	Re_P	C_D	$\emptyset$	N	Re_P	C_D	$\emptyset$
1	19.7	2.9	0.8	5	186.8	1.2	0.7
2	30.5	1.9	0.7	6	231.4	1.7	0.7
3	38.8	1.6	0.7	7	384.4	1.8	0.7
4	163.0	1.0	0.8	8	1362.0	2.5	0.7

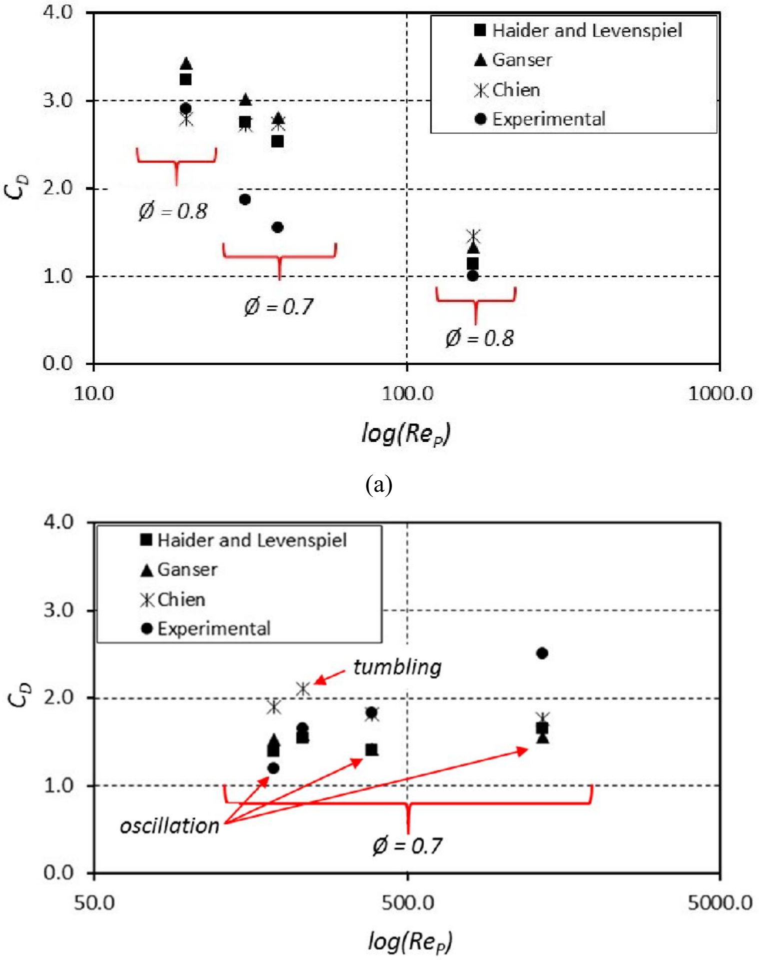

(a)

(b)

Figure 6.52 Comparison between the experimental and the correlation-predicted values of C_D found for the disks: (a) $10 < Re_P < 170$, (b) $180 < Re_P < 1500$.

For the cases plotted in Figure 6.52a there was an absence of secondary motions, thus a decreasing trend of C_D as Re_P augmented can be noticed. Moreover, for

$\emptyset = 0.8$ the disagreement between the experimental data and the literature correlations fluctuated between 4 % – 31 %, and for $\emptyset = 0.7$ the it was considerably larger, between 32 % – 45 %. This demonstrated the extent of the impact caused by a decrease in sphericity.

In Figure 6.52b, because of the presence of secondary motions, the trend of C_D was to increase with Re_P. This behaviour agreed with the tendency reported by Stringham et al. [26] in Figure 2.15 as $Re_P > 100$ roughly. The results from the three literature correlations included in Figure 6.52b failed to reflect such behaviour. Moreover, the differences between them and the experimental data fluctuated significantly, from about 1 % up to 60 %.

6.3 INFLUENCE OF THE ANGLE OF INCIDENCE ON THE COEFFICIENT OF DRAG FOR CYLINDERS AND DISKS

As it was seen in the previous sections, the magnitudes of C_D were considerably influenced by the presence of fully developed secondary motions because they modify the orientation of the particle with respect to the motion direction and alter the structure of the surrounding fluid. Provided that different researches have suggested that such an influence can be considered through mathematical correlations which express the dependency of C_D on α, in this section such dependency is investigated.

In Chapter 2 it was stated that particles behave different when they are allowed to travel freely than when they are held static and exposed to a moving fluid. Hence, correlations developed from fixed-particle works, such as the one published by Zastawny et al. [28], were discarded for the current study. Moreover, their correlation is valid for $Re_P < 300$. This contradicts the findings of Marchildon [25] and Chow and Adams [27], as well as the ones explicated in this thesis so far, where it has been remarked that the secondary motions, and subsequent angular orientation changes, begin when $Re_P > 300$, though they sometimes may appear before.

In spite of the fact that for most of the cases of oscillating cylinders exposed in Section 6.1, the angle of incidence did not vary in magnitudes large enough to produce outstanding fluctuations in the drag coefficient, plots of C_D in terms of α could still be generated, as illustrated in Figures 6.53, 6.55, and 6.56, where the results given by Equations (2.25) and (2.26), recommended by Rosendahl [11] and Mandø and Rosendahl [30], respectively, are added for comparison.

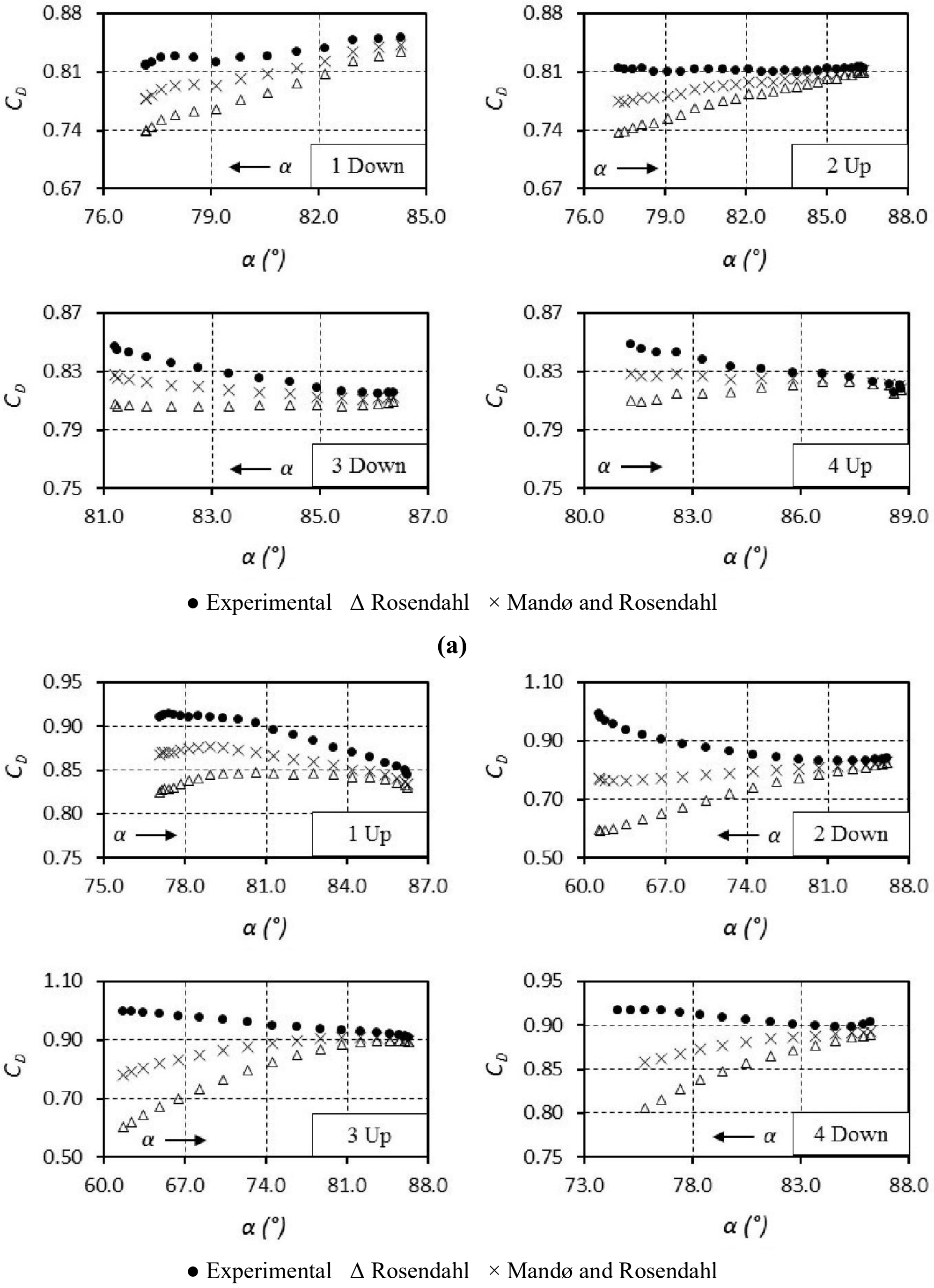

(a)

(b)

Figure 6.53 $C_D - \alpha$ plots for cylinder C2 falling in mixture 50/50 at Re_P = 413.0 (a) and 400.0 (b), respectively. The terms *down* and *up* refer to whether α was decreasing or increasing (see Figure 6.54).

The plots of Fig 6.53a were generated from the graphs shown in Figure 6.54, where the values of C_D were re-classified in agreement with the variations of α at conditions of terminal velocity only. In this way, the terms *down* and *up* refer to either a decreasing or increasing α, whilst the numbers *1*, *2*, *3*, *4* just express the order of the events. The plots of Figures 6.53b, 6.55, and 6.55 were created following the same procedure.

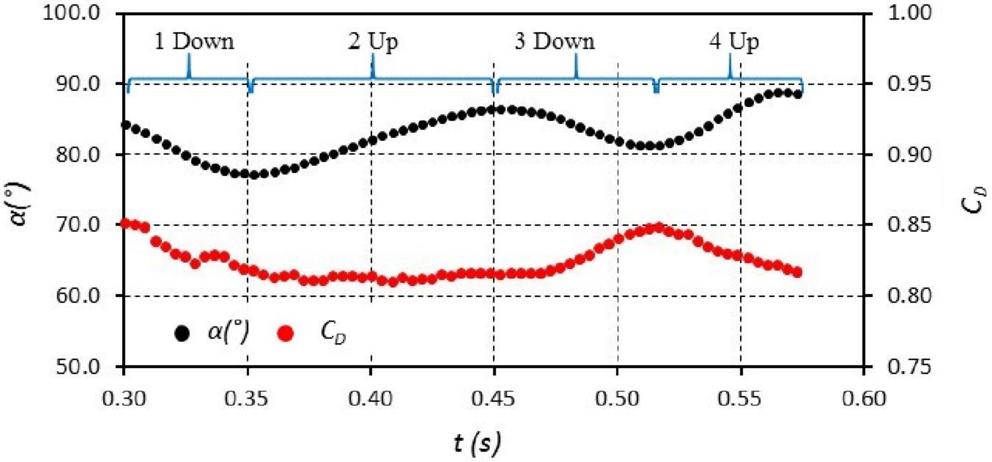

Figure 6.54 α and C_D time-variations at U_T conditions for cylinder C2 falling in mixture 50/50 at $Re_P = 413.0$. The terms *down* and *up* refer to a decreasing or increasing α.

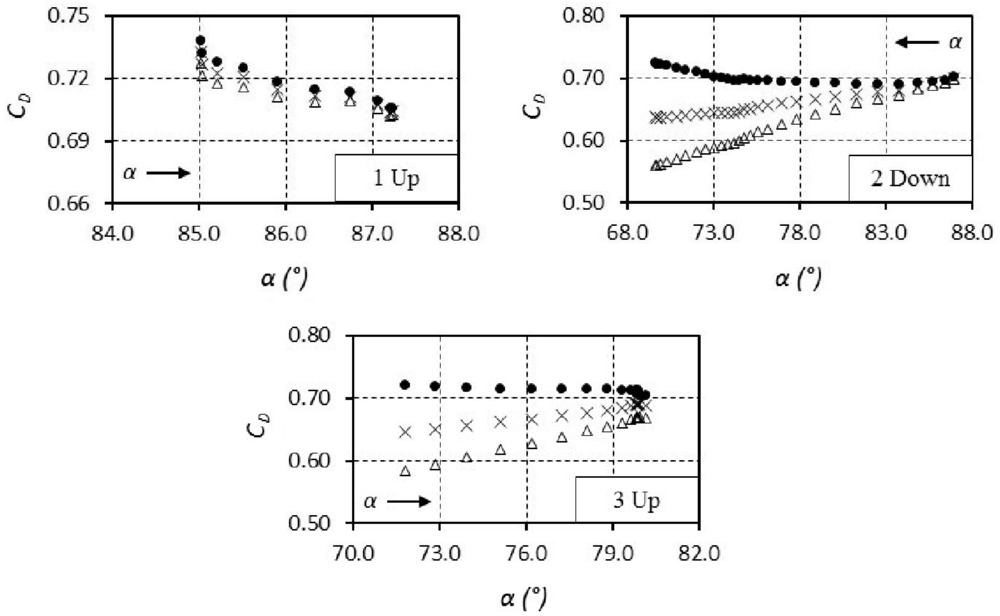

● Experimental   Δ Rosendahl   × Mandø and Rosendahl

Figure 6.55 $C_D - \alpha$ plots for cylinder C6 falling in mixture 50/50 at $Re_P = 614.6$.

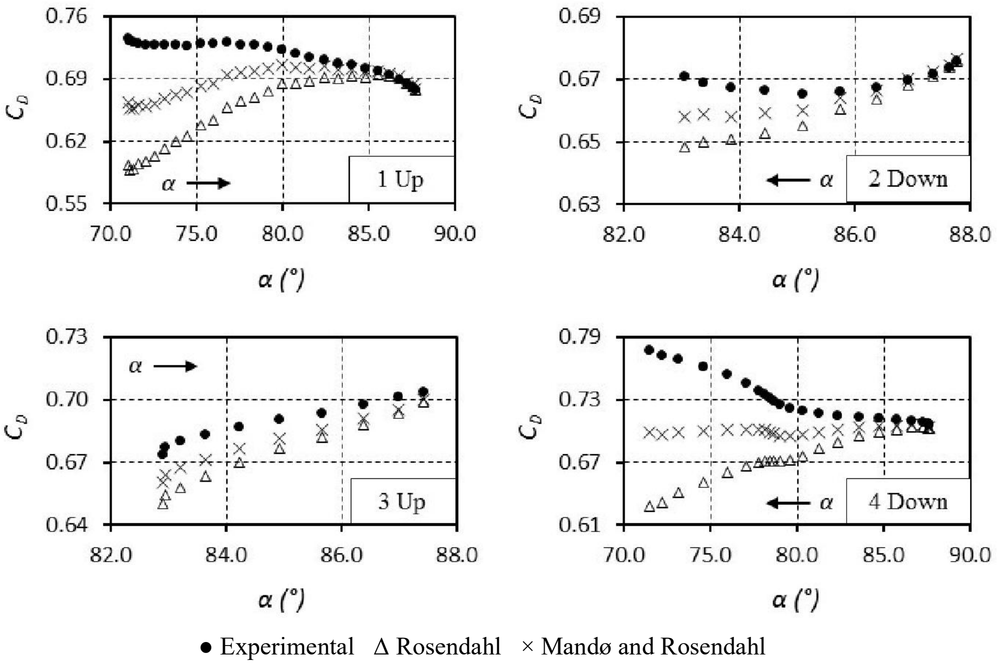

Figure 6.56 $\alpha - C_D$ plots for cylinder C4 settling in pure water at $Re_P = 1975$.

In Figures 6.53, 6.55, and 6.56 it can be observed that the approach recommended by Mandø and Rosendahl [30] performed better with respect to the experimental data than the one suggested by Rosendahl [11], nevertheless in some of the cases both approaches failed to reproduce the trend of the curve. This because in their models they assumed that any increment of α will always augment the magnitude of C_D, and sometimes this may not be true, as illustrated in Figures 6.53b and 6.56. Such an assumption is typical of configurations where the particle motion is restricted.

Hölzer and Sommerfeld [34] published a drag correlation which considers the influence of changes in orientation, nonetheless, as exemplified in Figure 6.57 for the fall of cylinder C4 in pure water at $Re_P = 1975$, it disagreed with the experimental results (by 35 % to 46 %) and the models of Rosendahl [11], and Mandø and Rosendahl [30]. Moreover, their correlation showed great similitude with those of Haider and Levenspier [16], Ganser [18], and Chien [53], which also over-estimated the magnitude of C_D by a similar amount.

In Figures 6.58 and 6.59, the variations of C_D with α for the case of two fully tumbling disks, of same dimensions and material, sinking in mixture 65/35 at $Re_P = 226.2$ and $Re_P = 236.5$, respectively, are displayed. The colours in Figures 6.58a and 6.59a represent the time intervals where the magnitude of α increased or decreased, whilst Figures 6.58b,c and 6.59b,c exhibit the behaviour of C_D as a function of α that was observed at those intervals.

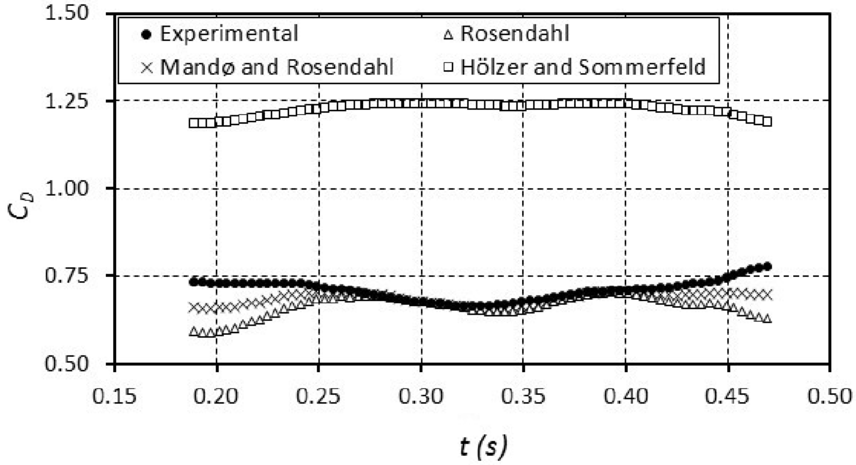

Figure 6.57 Comparison between the experimental and theoretical values of C_D obtained for the oscillating fall of cylinder C4 in pure water at $Re_P = 1975$.

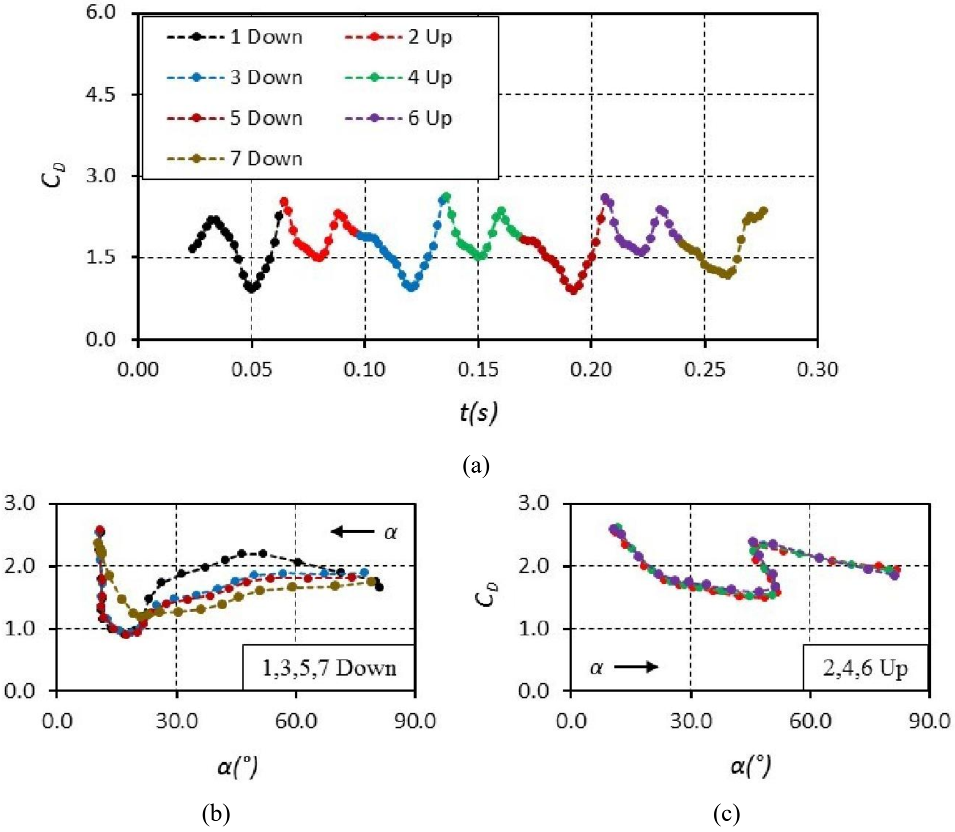

(a)

(b) (c)

Figure 6.58 Time variation of C_D for disk D1 falling in mixture 65/35 at $Re_P = 226.2$ (a). Each colour represents the interval where α increased (*up*) or decreased (*down*). Variation of C_D with α decreasing (b), and increasing (c).

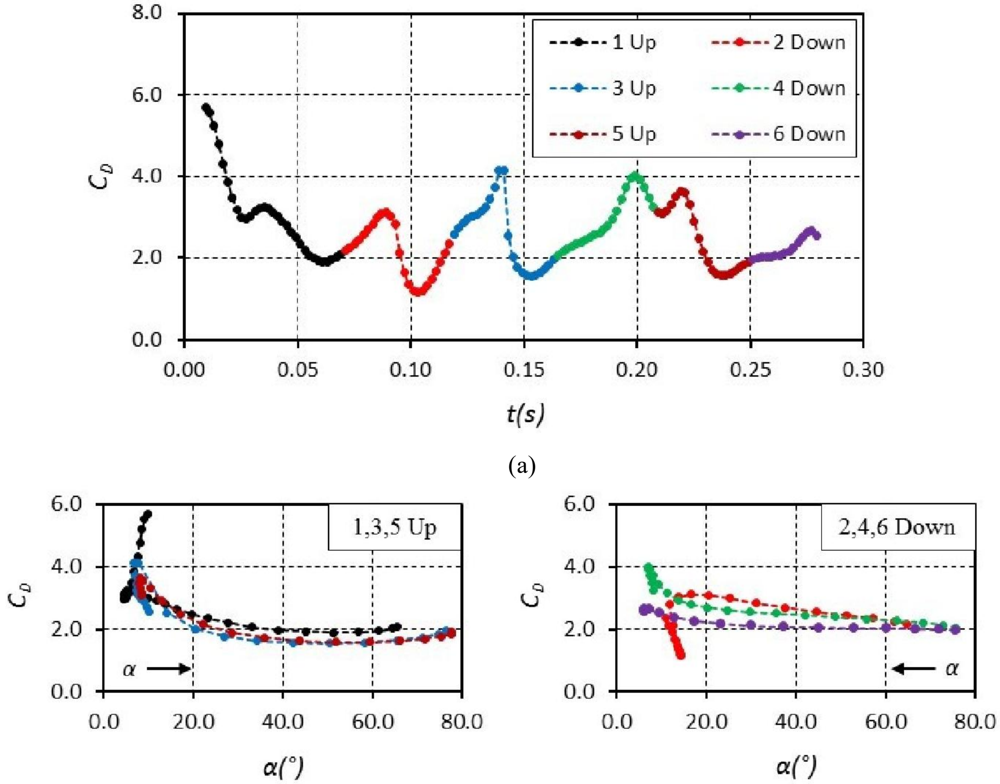

(a)

(b) (c)

Figure 6.59 Time variation of C_D for disk D1 falling in mixture 65/35 at $Re_P = 236.5$ (a). Each colour represents the interval where α increased (*up*) or decreased (*down*). Variation of C_D with α increasing (b), and decreasing (c).

In each of the $C_D - \alpha$ plots of Figures 6.58b,c and 6.59b,c it was distinguished that the curves followed a trend reasonably similar for every either augmenting or decreasing α, however no obvious resemblance was observed between the *up* and *down* curves. Furthermore, though some agreement can be noticed between Figures 6.58a and 6.59a, no similarity was detected between Figures 6.58b and 6.59b, and 6.58c and 6.59c, respectively.

It is believed that the reason for such behaviour lied on the fact that the development of the secondary motion and angular change did not follow the same history, even for the same particle tested at equal conditions. An identical deduction can also be achieved by analysing the $C_D - \alpha$ plots of Figures 6.60, which correspond to three different drops of disk D3 in mixture 50/50 at $Re_P = 390.5$ (a,b), 384.4 (c,d), and 380.2 (e,f), respectively. The secondary motions registered in these cases were random combinations of oscillation and gliding.

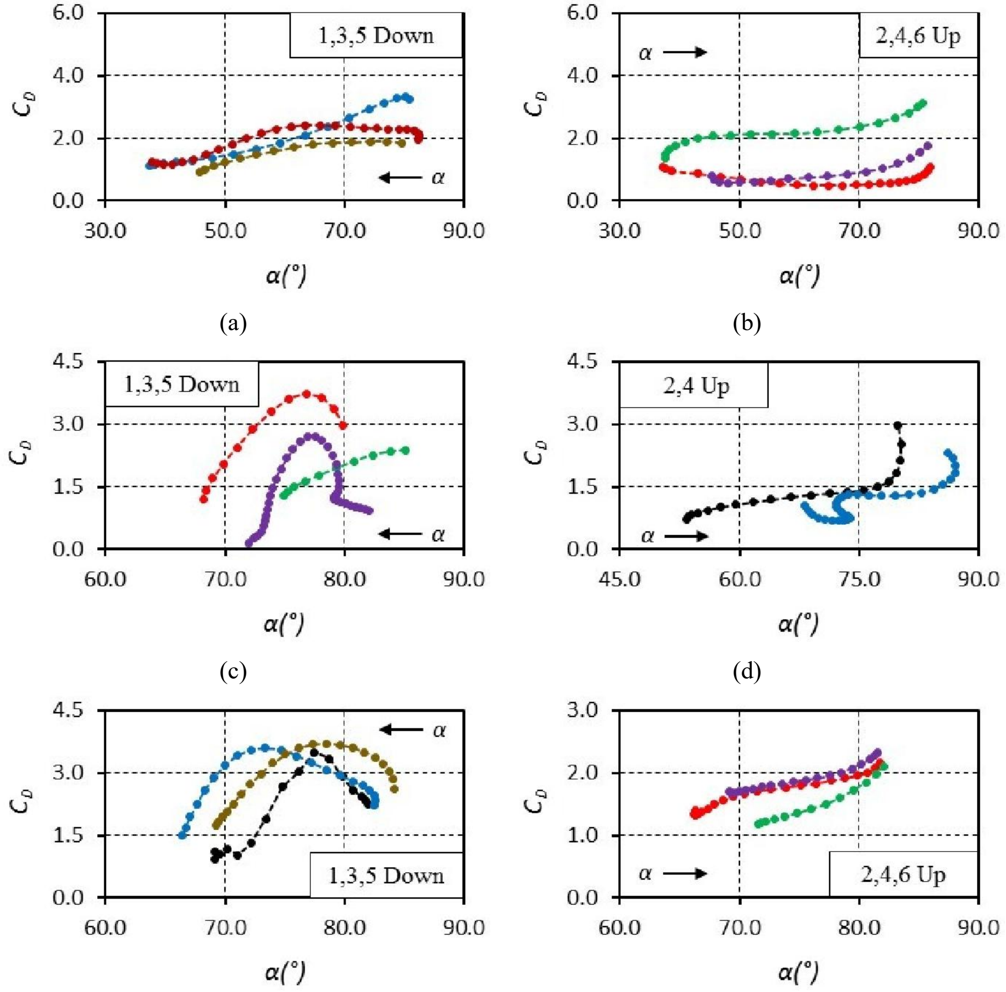

(a) (b)

(c) (d)

(e) (f)

Figure 6.60 $C_D - \alpha$ variation for three drops of disk D3 in mixture 50/50 at $Re_P = 390.5$ (a,b), 384.4 (c,d), and 380.2 (e,f), respectively. The terms *up* and *down* refer to an increasing or decreasing α.

By following the same colour-plotting principle, the behaviour of C_D with α for the case of a fully oscillating disk D3 settling in water at $Re_P = 1362$ is presented in Figure 6.61. It can be highlighted that in this case C_D changed to some extent in the same direction as α. Moreover, during the angular increase or decrease, the plots of C_D versus α exhibited a close resemblance, though the changes were considerably more abrupt for the situations when the angle of incidence augmented than when it diminished.

From the comparison of the values of the drag coefficient in Figures 6.58 to 6.61, it can be affirmed that a disk which settles under fully developed oscillatory motion conditions experience more resistance than a tumbling or oscillating/gliding disk. This because at pure oscillation the area projected by the solid is larger than at the other two secondary motions. Moreover, the structures of the surrounding fluid may play a role too.

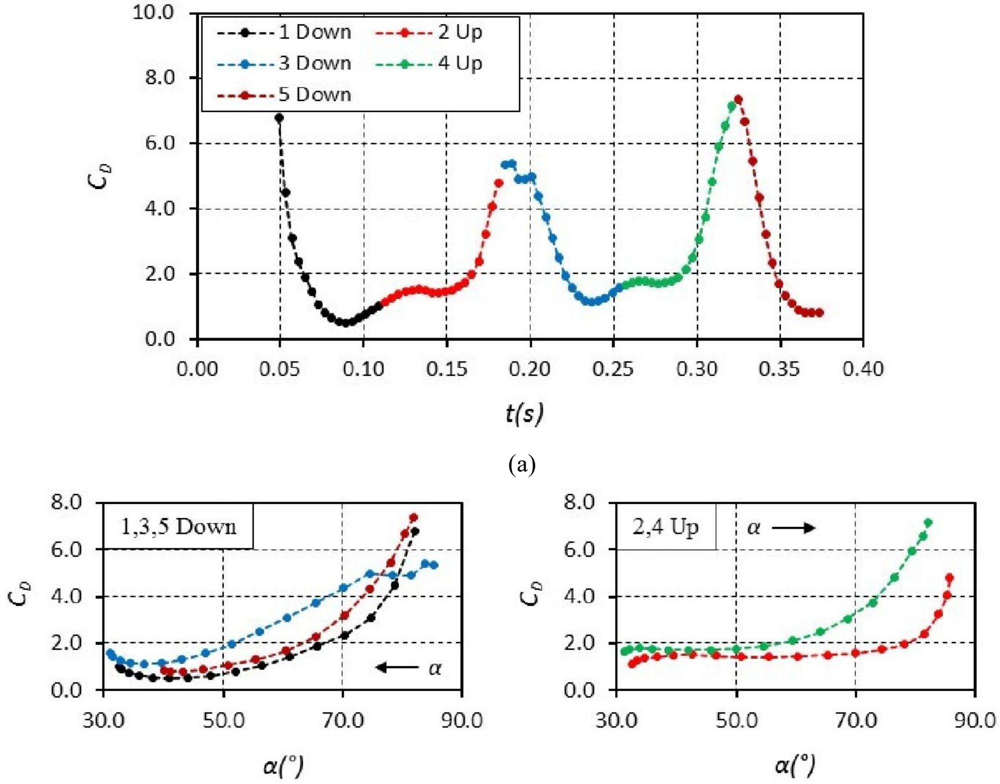

(a)

(b)

(c)

Figure 6.61 Time variation of C_D for disk D3 falling in pure water at $Re_P = 1362$ (a). Each colour represents the interval where α increased (*up*) or decreased (*down*). Variation of C_D with α increasing (b), and decreasing (c).

Based on the experimental results presented in Figures 6.53 to 6.61 it can be said that it was clearly demonstrated that at terminal velocity conditions, the presence of secondary motions continuously change the angular position of a non-spherical particle and that this has a direct effect on the magnitude of the coefficient of resistance, which may or may not be in the same direction as α. Additionally, it was also observed that since the evolution of the secondary motions may not be identical, even for the same particle and fluid, the trend of the C_D - α curves cannot be constant, however they should exhibit some resemblance.

Chapter 7

EXPLORATORY STUDY OF THE BEHAVIOUR OF IRREGULAR PARTICLES IMMERSED IN FLUIDS AT REST AND IN MOTION

Irregular particles do not exhibit clear patterns of fall such as the ones shown by the regular solids studied in the previous chapters due to their geometrical uneven characteristics. In fact, their behaviour can be remarkably different, thus making the prediction of any motion parameter more complicated. In this chapter, the behaviour of such irregular bodies both in free-fall and in an airflow is explored.

In Section 7.1, some PTFE particles resembling the shape of irregular wood chips were let to settle freely in pure water and in two mixtures of glycerine with water. Then, like in Chapters 5 and 6, the trajectories and other motion quantities were analytically investigated. The experimentally obtained values of C_D were also compared with the empirical Equation (2.24b) developed for irregular solids.

In Section 7.2 the case of wood chips immersed in a pipe-enclosed airflow is qualitatively examined. Alterations in the motion of the particles due to their geometrical irregularity and its interaction with the air current, as well as those caused by impacts against the pipe wall or by the proximity of another particle were identified and described.

This chapter does not aim for an in-depth study of the motion of irregular solids, but to highlight some of the complexities that can be found and the challenges they pose, and to show the advantages and limitations of the experimental image-based techniques applied in this thesis to address such phenomena. Other possible methods of analysis were also suggested.

7.1 IRREGULAR PARTICLES SETTLING IN LIQUIDS AT REST

The PTFE irregular particles used for the free settling experiments are displayed in Figure 7.1. All of them were made manually with the assistance in such a way that they could resemble the form of wood chips. In average the largest, intermediate, and shortest dimensions were 17.8 mm × 3.0 mm × 1.3 mm, respectively. A total of five particles were tested in each of the following glycerine-water mixtures: 80/20, 65/35, and 0/100 (pure water), according to Table 5.5.

Figure 7.1 Irregular PTFE particles.

In Figure 7.2 the two-dimensional visualisation of the free settling of two PTFE irregular particles in mixtures 80/20 and 65/35, respectively is illustrated. Their dimensions are 19.0 mm × 2.4 mm × 1.0 mm, and 18.8 mm × 2.0 mm × 1.6 mm, which corresponded to Re_P = 8.3 and 74.2, respectively. The three-dimensional paths can also be seen in Figure 7.3, where the longest axis has been marked with blue colour for some randomly chosen positions.

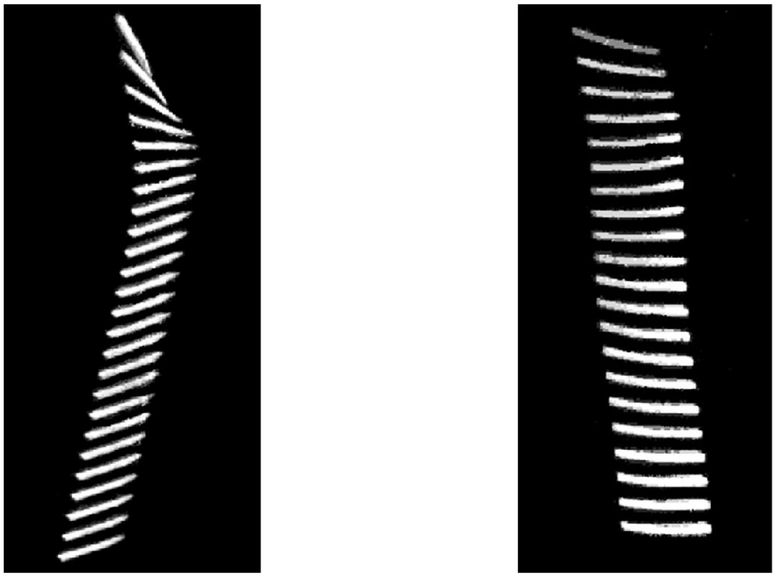

(a) (b)

Figure 7.2 2D visualisation of two PTFE chips falling freely in mixtures 80/20 and 65/35 at Re_P = 8.3 and 74.2, respectively.

From Figures 7.2a and 7.3a it can be observed that at this value of Re_P the irregular particle took a stable position with the heaviest part pointing downwards and exhibiting the maximum projected area to the direction of motion. The fall at the next higher Reynolds number also seemed to be considerably stable, with the largest area projected perpendicularly to the motion too. However, slight angular variations were also perceived.

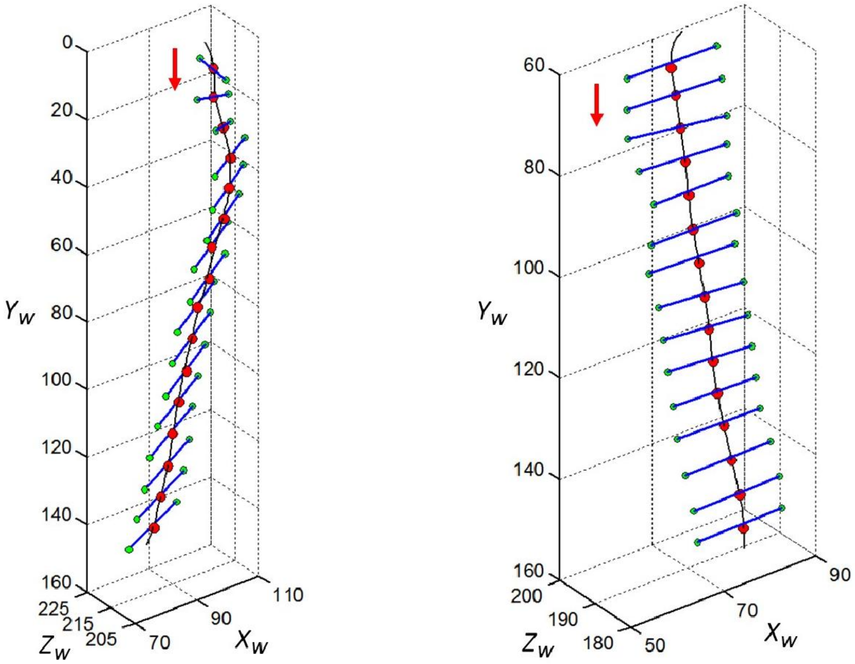

(a) (b)

Figure 7.3 3D paths of the two PTFE chips of Figure 7.1 settling in mixtures 80/20 and 65/35 at Re_P = 8.3 and 74.2, respectively.

The rest of irregular PTFE solids dropped in mixture 80/20 exhibited a similar behaviour to the one depicted in Figures 7.2a and 7.3a, nevertheless for mixture 65/35 it was found that although the particles normally kept their largest projected area perpendicular to the motion direction, some rotation around an axis normal to the camera axis also appeared for some cases, as shown in Figure 7.4. It is believed that the rotation happened as a result of the disturbances in the surrounding fluid imposed by the uneven geometry of the particles.

It can be argued from Figure 7.4 that the detection of the centroid in the zone enclosed by the red circle could still be achieved reasonably well, however the rotation makes it impossible to determine the correct particle longest axis, and the angular orientation in consequence. During the spin the particle hides most of its surface from the field of view. This phenomenon is named *occlusion*, and is a major disadvantage of the conventional two-camera stereo vision systems.

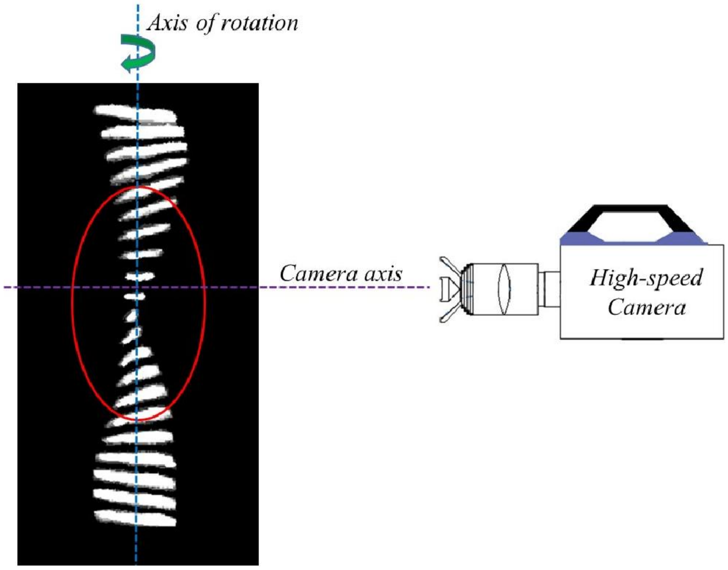

Figure 7.4 2D visualisation of a settling PTFE irregular particle with rotation.

Because occlusion cannot be overcome, it can be said that the technique used in this research is not suitable to track the full motion of a solid which experiences rotation around axes normal to the camera axis. An arrangement of two cameras at 90° from each could be a more suitable alternative since it provides two perpendicular views of the particle, which in turn could be used to quantify the angular velocities and torques expressed in Equations (2.34 – 2.36) provided that the moments of inertia can be determined.

In Figure 7.5 the angular change of the PTFE irregular chips of Figure 7.2 is displayed. It can be noticed that after $t = 1.3$ s, the first particle achieved a stable magnitude of α equal to 60.1° approximately, whilst the second one exhibited some variation between $\alpha = 76.7°$ and $\alpha = 87.0°$ once t exceeded 0.25 s. The corresponding values of the projected area, calculated as $A_P = ab\sin\alpha$, for the same times were $A_P = 30.0\ \mu m^2$, and $A_P = 35.0 – 37.0\ \mu m^2$, respectively.

From the velocity plots portrayed in Figure 7.6, it can be seen that conditions of terminal velocity were reached at $t = 0.40$ s and $t = 0.15$ s, approximately. The corresponding magnitudes were $U_T = 0.07$ m/s and $U_T = 0.13$ m/s. In this case, these results were not compared with Equation (2.10) because this one was developed for isometric particles only. The plots of the drag force experienced by the chips are illustrated in Figure 7.7, where practically the same steady value, F_D = 0.6mN, was determined for both solids. It is believed that the reason for such coincidence was the significant difference in shape between both irregular particles, as it can be seen in Figure 7.2. Whilst the first one resembles more a needle-like the second one is more similar to rectangular bar.

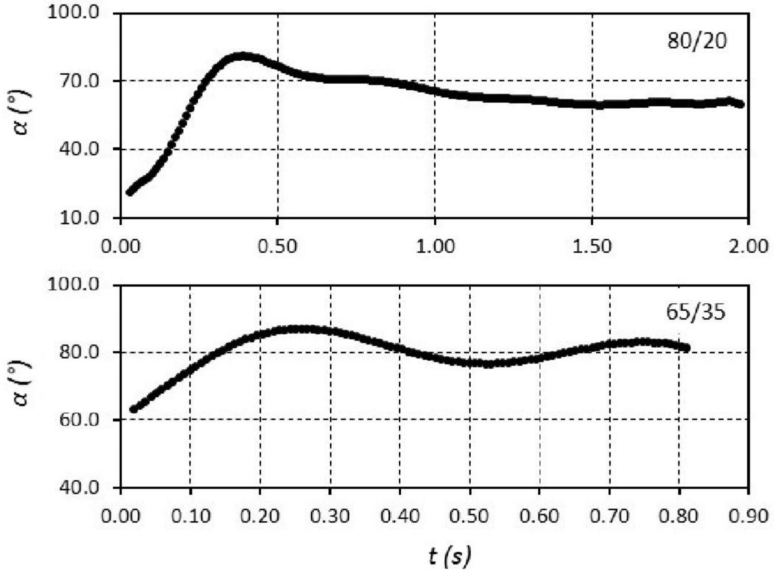

Figure 7.5 Variation of the orientation angle of the two PTFE chips of Figure 7.2 settling in mixtures 80/20 and 65/35 at Re_P = 8.3 and 74.2, respectively.

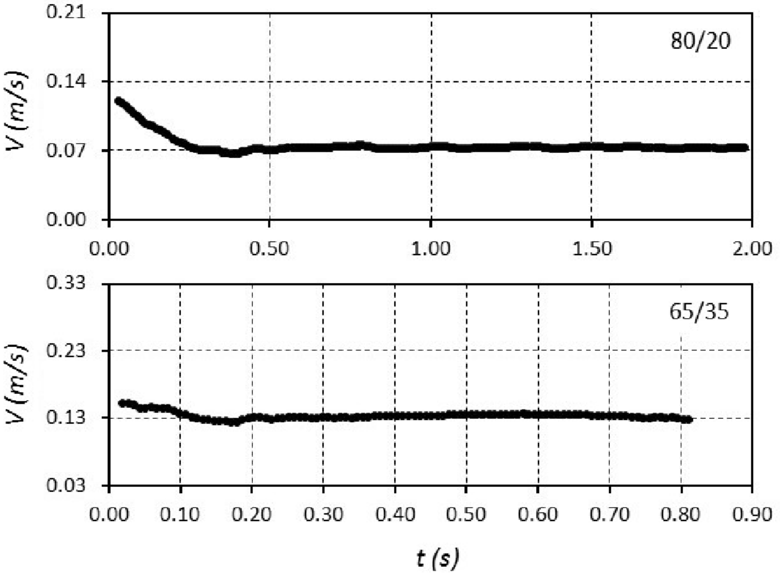

Figure 7.6 Velocity plots obtained for the two PTFE chips of Figure 7.2 falling in mixtures 80/20 and 65/35 at Re_P = 8.3 and 74.2, respectively.

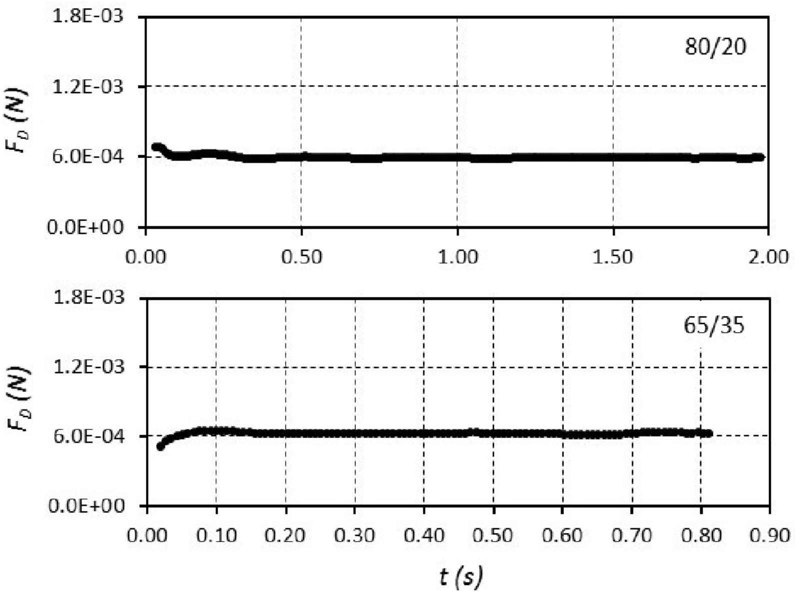

Figure 7.7 Plots of the drag force experienced by the two PTFE chips of Figure 7.2 whilst descending in mixtures 80/20 and 65/35 at $Re_P = 8.3$ and 74.2, respectively.

Considering the variation of the coefficient of resistance shown in Figure 7.8, it can be noticed that once the angle of incidence attained a fixed number, the first PTFE solid registered a C_D equal to 5.6, which was 33 % below the theoretical result predicted by Equation (2.24b), developed for crushed irregular particles. For the second chip, the experimental magnitude of C_D fluctuated between 1.6 and 1.7, which is nearly half of the estimation given by Equation (2.24b).

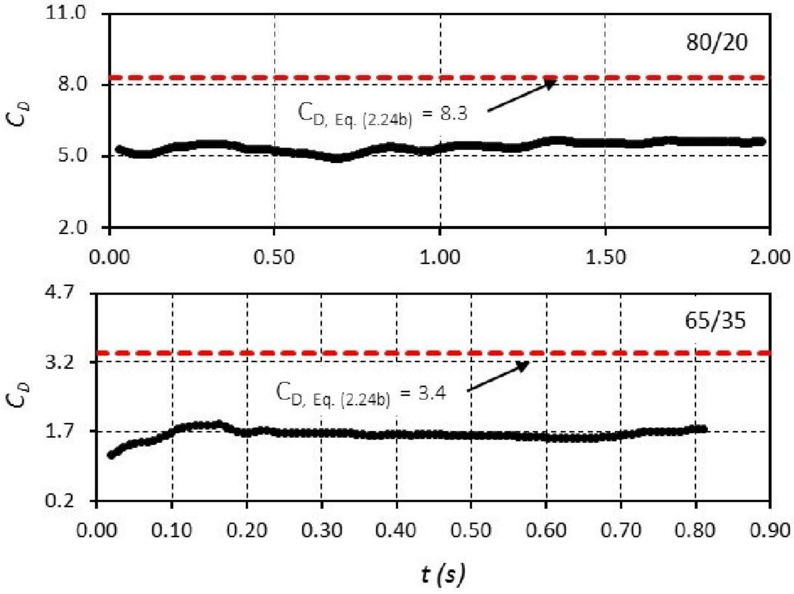

Figure 7.8 Variation of the coefficient of resistance for the two PTFE chips of Figure 7.2 falling in mixtures 80/20 and 65/35 at $Re_P = 8.3$ and 74.2, respectively.

At larger values of Re_P the fall of an irregular particle was no longer as steady as those shown in Figure 7.2, but more uneven as illustrated in Figure 7.9 for $Re_P = 689.2$, where the settling in pure water of a 19.5 mm × 2.3 mm × 1.4 mm PTFE chip is displayed. Moreover, at this Re_P regime, simultaneous rotations around 2 or 3 different axes was also found for other particles, such as the one portrayed in the series of pictures of Figure 7.10. Since the marked red point always corresponded to the same part of the solid, it was clear that the only possible way for that to happen was due to concurrent spins.

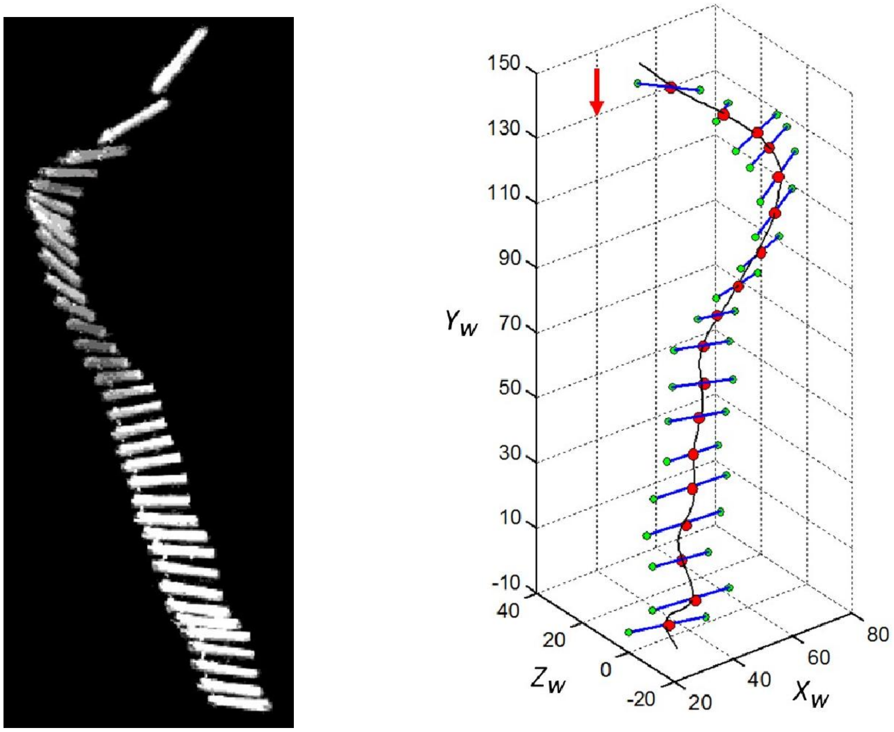

(a) (b)

Figure 7.9 2D (a) and 3D (b) visualisation of an irregular PTFE chip falling freely in pure water at $Re_P = 689.2$.

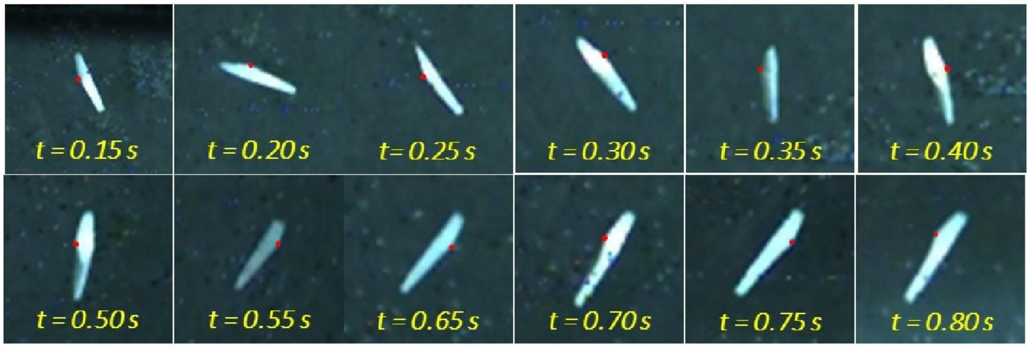

Figure 7.10 Settling of a 16.0 mm × 2.4 mm × 1.0 mm PTFE irregular chip in pure water, with simultaneous rotations around two or three different axes.

The turbulent structures of the flow adjacent to the PTFE irregular particles could also be revealed through Schlieren visualisation, such as the one portrayed in Figure 7.11, where for each particle orientation a different pattern can be observed. Furthermore, it was also noticed that because of the irregular geometry of the solid, with every rotation it did, the turbulence was enhanced.

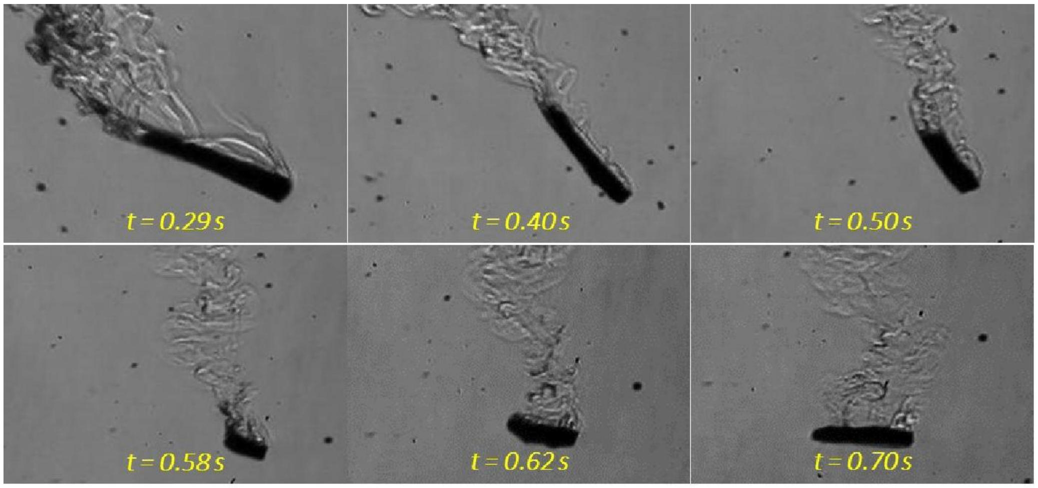

Figure 7.11 Schlieren visualisation of a PTFE irregular particle sinking in water.

The angular change of the PTFE irregular chip of Figure 7.9 is plotted in Figure 7.12, where two large fluctuations can be appreciated for $t < 0.45$ s. After that, the angle oscillated within the interval 83.9° < α < 87.3°. However, the fluctuation of the projected area for $t > 0.45$ s was practically negligible. The computed average value was $A_P = 37.8\ \mu\text{m}^2$. The plots of velocity, drag force, and coefficient of resistance for the same particle are exposed in Figures 7.13 to 7.15.

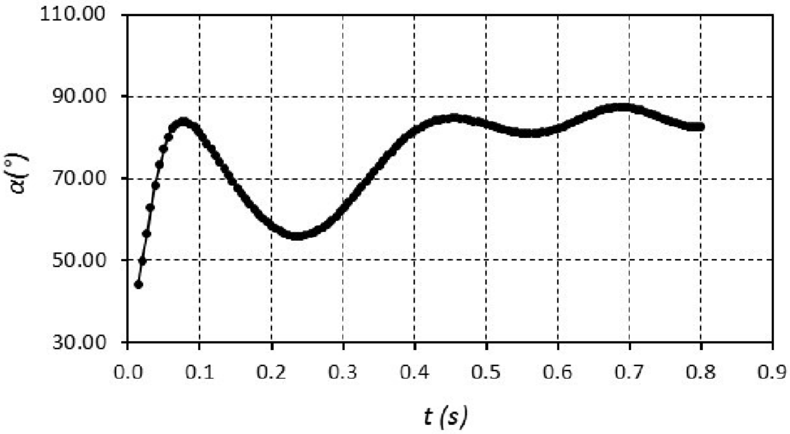

Figure 7.12 Angular variation of the irregular PTFE chip of Figure 7.9 settling in pure water at $Re_P = 689.2$.

From Figure 7.13 it can be inferred that a fixed terminal velocity magnitude was not obtained. Instead, after t = 0.45 s a moderately regular sinusoidal variation between 0.09 m/s and 0.18 m/s, with period of 0.8 s, was established. Nonetheless, to calculate the particle Reynolds number, the average was used: $U_{T,\, avg}$ = 0.14 m/s. From the drag plot of Figure 7.14, it can be seen that after the initial large fluctuations, the force stabilised around 0.6 mN for 0.2 s < t < 0.8 s.

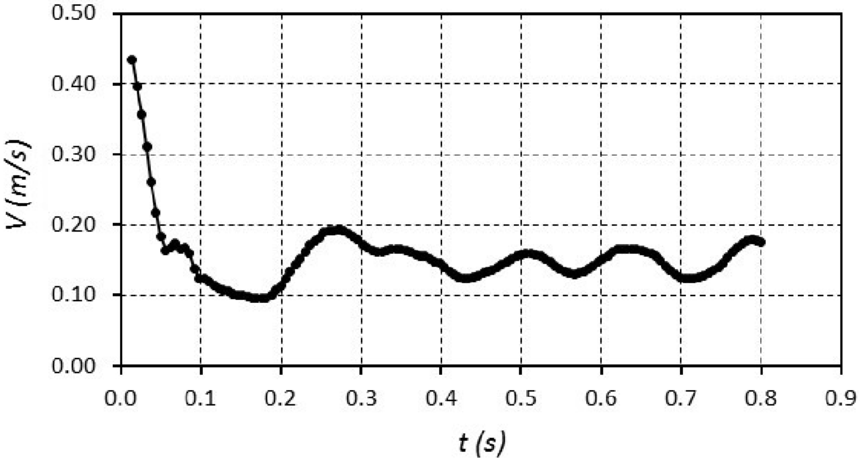

Figure 7.13 Plot of the velocity experience by the irregular PTFE chip of Figure 7.9 falling in pure water at Re_P = 689.2.

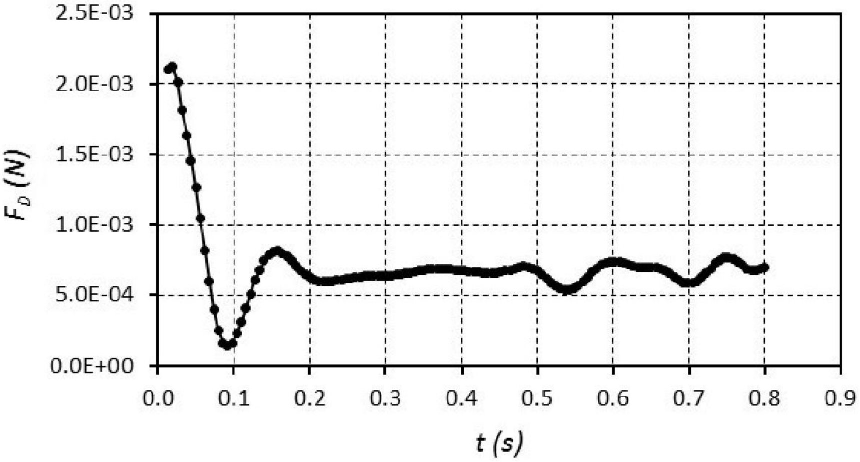

Figure 7.14 Drag force of the irregular PTFE chip of Figure 7.9 descending in pure water at Re_P = 689.2.

The coefficient of resistance plot of Figure 7.15 shows that after the instabilities found before t = 0.45 s, C_D exhibited a relatively even pattern until t = 0.8 s. In the interval 0.45 s < t < 0.8 s C_D varied between 1.2 to 2.0. In averaged, the discrepancy with respect Equation (2.24b) was approximately 60%. This occurred because Equation

(2.24b) was developed for irregular crushed particles, which are considerably different in shape to the irregular PTFE particles studied here.

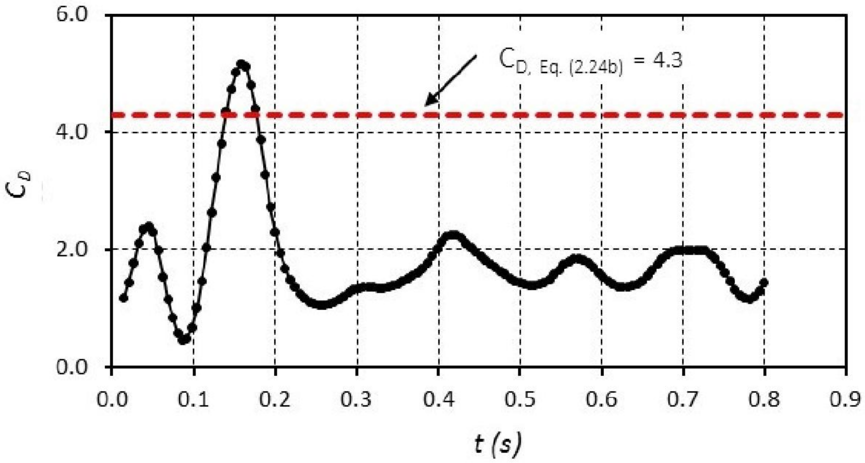

Figure 7.15 Coefficient of drag experimented by the irregular PTFE chip of Figure 7.9 settling in pure water at Re_P = 689.2.

Based on the plots of irregular chips falling into a liquid at rest shown in this Section, it was observed that at relatively low Reynolds numbers, all of the motion parameters analysed here still tend to a stable value despite the changes in the object orientation, nonetheless, for higher Reynolds numbers, relatively large fluctuations characterise their behaviour, even after terminal velocity conditions are achieved. This was confirmed too by the other irregular particles tested at $100 < Re_P < 1000$, whose results were not included in this section.

7.2 IRREGULAR PARTICLES MOVING IN A FLOW OF AIR

As part of this exploratory study, the motion of some of the irregular wood chips shown in Figure 7.16 was also investigated, though in a qualitative way. Each chip was manually inserted into a transparent acrylic pipe which was coupled to an axial fan through a connector on its lower end. The sketch of the experimental installation is displayed in Figure 7.17. A honeycomb-like flow straightener and a wire mesh to avoid the particles touch the fan were also employed. The system was mounted on a hollow plate which was fixed to another equipment and elevated from the ground.

Figure 7.16 Irregular wood chips.

The chips were fabricated from pine wood, with density ρ_P = 338 kg/m^3. In average, the largest, intermediate, and shortest dimensions were 17.3 mm × 2.5 mm × 1.5 mm, which were in agreement with the mean lengths published by Rosendahl et al. [8] in their physical characterisation of a 1.2 kg-sample of straw already prepared for pulverised fuel burning in a boiler. The chips were lying on top of the wire mesh before the fan was set on. After the flow was initiated, the motion of the chips was upwards, to the pipe top entrance. The pictures were taken at 2000 frames per second with the same stereo vision system used for the experiments of Chapters 5 and 6.

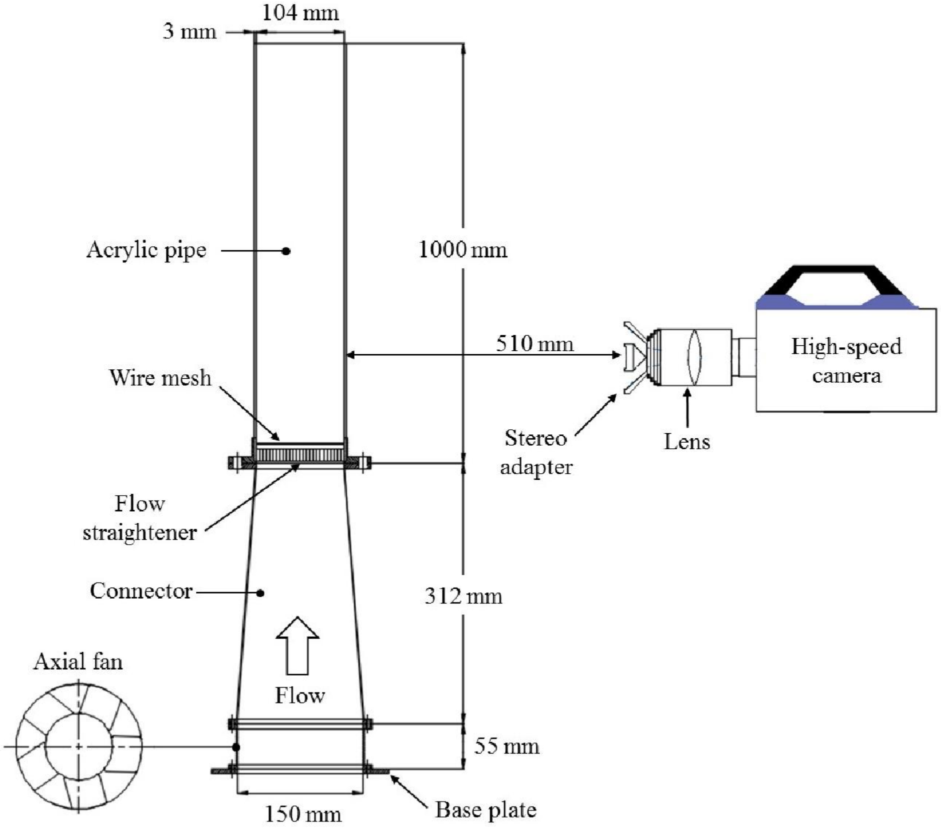

Figure 7.17 Experimental installation.

The axial fan, manufactured by EBM-PAPST and illustrated in Figure (7.18a), has a maximum flow rate of 380 m^3/h at 2700 rpm. The velocity of the air flow was measured at different points at the exit of pipe with the thermo-anemometer shown in Figure 7.18b, with resolution and accuracy of 0.01 m/s and $\pm$ 0.03 m/s, respectively. By using the punctual velocity measurements, the flow rate was estimated in order to find the mean velocity, which resulted in a pipe Reynolds number approximately equal to 3.5×10^4.

(a) (b)

Figure 7.18 (a) axial fan, (b) thermo-anemometer.

Because the air velocity was not excessively high, the particles were slowly dragged upwards. The ascension of a wood chip which moved from one place near the wall of the pipe to the opposite side is portrayed in Figures 7.19 and 7.20. From the first figure, the changes in the solid orientation become evident; nonetheless, from the second figure, it can be seen that the displacement was accompanied by constant rotation of the particle around its largest axis.

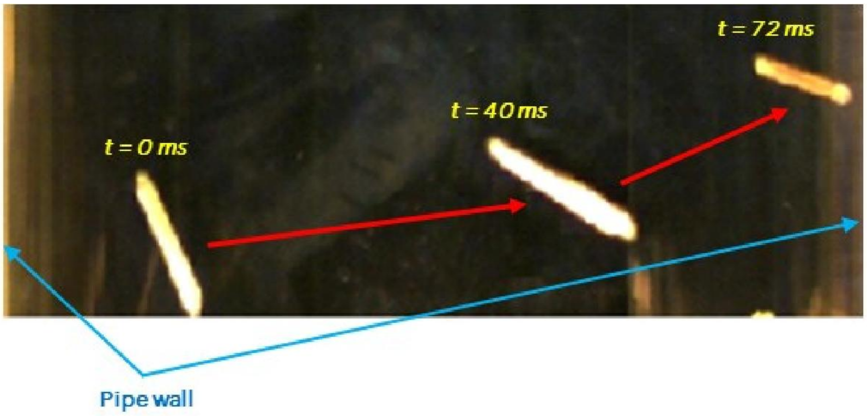

Figure 7.19 An irregular wood chip moving from one side of the pipe to the opposite while being dragged upwards by the air current.

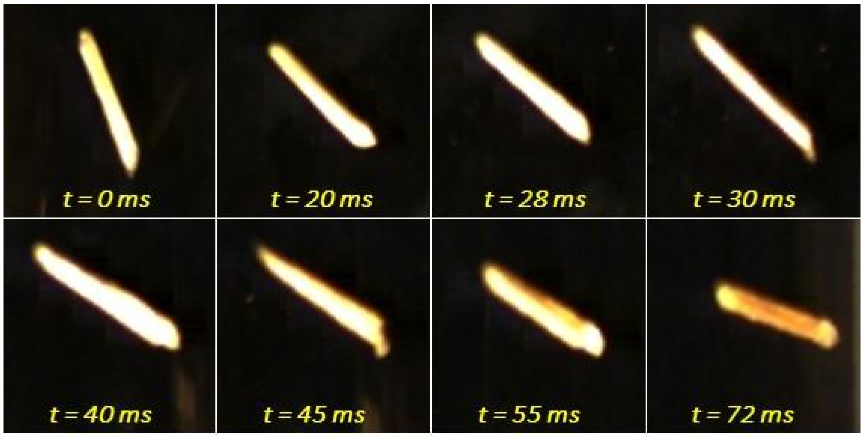

Figure 7.20 Series of pictures of the ascending irregular wood chip of Figure 7.19 exposing the constant rotation around its largest axis.

In Figure 7.21 the effects caused by the wall on the motion of the wood particle of Figure 7.19 are displayed. The wall is located at the right edge of the images. As the chip interacted with the wall, it experienced consecutive changes in its angular orientation as well as successive rotations. From the figure, it can be observed that at *t* = 72 ms the particle approached the wall with a highly horizontal position, whilst at *t* = 121 ms, it left the wall with a significantly vertical position.

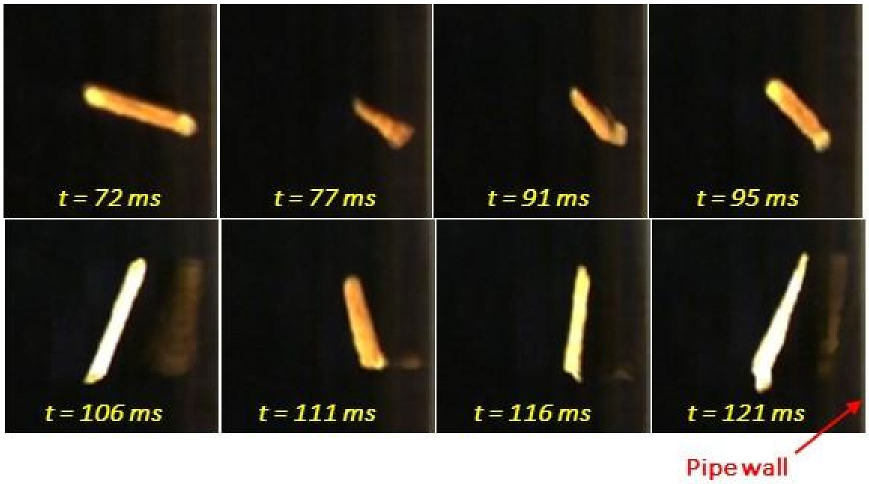

Figure 7.21 Series of pictures depicting the interaction between the irregular wood chip of Figure 7.19 and the pipe wall, situated at the right edge of the images.

In this study it was also found that the presence of another particle in the neighbourhood of the first one may produce alterations in the angular position and rotations on both solids, as illustrated in Figure 7.22, where the motion of two irregular wood chips is portrayed. It can be appreciated that as the lower particle moved slightly to the right, the orientation of the other one changed noticeably, however as both of them reached the pipe wall at t = 75 ms, the angular variation was reversed.

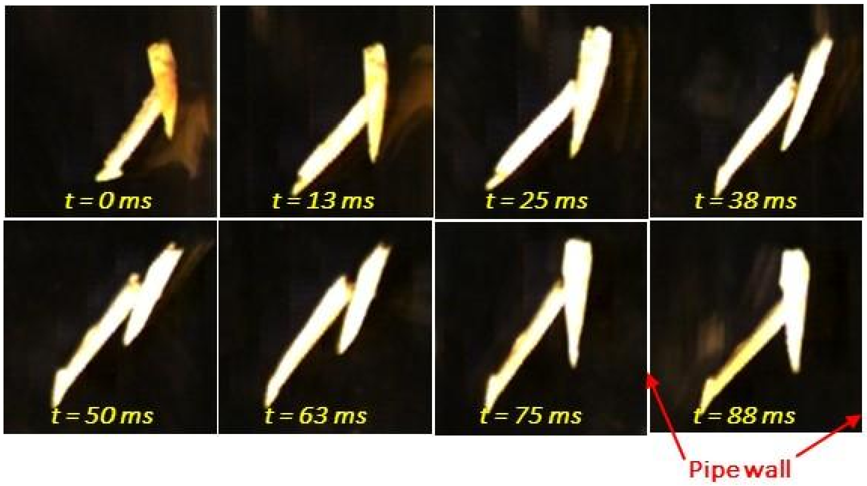

Figure 7.22 Series of pictures showing the interaction between two irregular wood chips as they moved up and to the right inside the pipe.

As observed from Figures 7.19 to 7.22 the motion of an irregular solid in a moving fluid is characterised by constant rotations and changes in its angular orientation as it displaces within the space. It is believed that such behaviour is caused by the irregular geometry of the particle as well as by external factors such as flow instabilities, the presence of another particle, or the closeness to a static wall. Therefore, it cannot be assumed that the particle will travel with a fixed position. This pose the necessity of tracking the rotation and angular orientation at each time instant in order to fully resolve the motion and obtain the true drag force exerted on the solid. Furthermore, to estimate the instantaneous coefficient of resistance, the projected area must also be approximated at each time step from the images.

The stereo technique employed in this research is able to determine the angular orientation provided that this one occurs in a plane normal to the camera axis, nonetheless since the rotation can also happen in other planes and given that either the particle itself or another neighbouring particle can produce occlusion, this technique cannot track all the rotations, thus obstructing the complete 3D motion resolution. To accomplish such a task through image-based methods, it is recommended to use three cameras to record the front, side, and top views of the particle, so that occlusion can be overcome and enough pixel data about the true particle location can be gathered.

Chapter 8

CONCLUSIONS AND FUTURE WORK RECOMMENDATIONS

8.1 CONCLUSIONS ON THE IMAGE-BASED TECHNIQUES

An original, non-intrusive methodology based on high-speed stereo vision, Schlieren photography, and digital image processing was developed in order to study quantitatively and qualitatively the settling motion of spherical and non-spherical particles in a fluid at different Reynolds numbers. The instantaneous 3D kinematics, angular orientation, and dynamics were determined, correspondingly, through particle tracking velocimetry, the computation of the angle between the particle longest axis 3D vector and the velocity vector, and the assistance of a Frenet reference frame which moves along the 3D centroid trajectory.

Within the context of image-based experiments, this is the first time that for a non-spherical particle, the angular orientation and drag force are calculated in these ways, that 3D centroid-displacement plots with the longest axis location highlighted are generated, and that Schlieren visualisations of the surrounding fluid at conditions of existing secondary flows are recorded. In addition, the drag coefficient calculations were based on the instantaneous, true projected area, and not on averaging approaches.

The techniques published by Zhang [99, 102] for camera calibration and 3D stereo reconstruction were applied. Nevertheless, instead of following the tradition of working in the left camera frame, the obtained 3D coordinates were projected back to the world reference frame $O_W X_W Y_W Z_W$ through an innovative approach where the analysis was then carried out. The accuracy of the procedure was tested by reconstructing the 256 corner coordinates of the squared calibration model at 34 positions within the interval -100 mm $\leq Z_W \leq$ 100 mm. It was found that the absolute error was dominated by the uncertainty in Z_W, nonetheless it was proved that a careful camera calibration can keep error under 1.0 mm.

In order to obtain the particle motion data needed by the 3D reconstruction algorithms from both the left and the right sides of each stereo picture, a novel procedure entirely based on digital image processing operations was designed and executed in Matlab 2014. It accomplished the main tasks of image enhancement and extraction of the pixel coordinates of the particle features to be 3D calculated: centroid and longest axis location. A large number of other programs were also written in the same software to accomplish the tasks of camera calibration, 3D stereo reconstruction and back projection, and for the computation of different particle motion parameters. Special emphasis was placed on performing the work in an as automated way as possible.

8.2 CONCLUSIONS ON THE PARTICLE MOTION

SPHERICAL PARTICLES

The settling motion of spheres in the range $0.3 \leq Re_P \leq 4939$ was investigated. All of the characteristics of the flow surrounding the spheres reported by Magarvey and Bishop [57] were corroborated: a highly symmetrical fluid recirculation zone at the rear of the sphere and a stable single trail for small Re_P; the change to a double and wavy trail in the interval $270 \leq Re_P \leq 290$; the formation and evolution of the hairpin structures of vortex shedding at larger Re_P; and a full turbulent wake for $Re_P > 1000$. Nevertheless, contrary to their affirmation that the hairpin structures end at $Re_P \sim 700$, it was observed that they can endure up to $Re_P \sim 900$.

It was observed that as the mentioned surrounding flow structures evolved with Re_P, the symmetry of the wake decreased until being null, deviating in consequence the 3D fall paths of the spheres from vertical straight lines. Nonetheless, in all of the cases steady values of U_T and C_D were achieved, though relatively small fluctuations were also registered. Moreover, it was noticed that at U_T conditions and for $Re_P > 270$ the magnitude of F_D can still vary considerably.

The obtained experimental values of U_T and C_D were contrasted with those predicted by the correlations of Haider and Levenspiel [16], Clift and Gauvin [15], Yow et al. [52], and Terfous et al. [35], resulting in a remarkable agreement throughout the whole Re_P interval. The maximum discrepancies registered were 13 % for U_T and 12 % for C_D. The only exception was that at $Re_P = 4939$ the experimental C_D was, in average, 38 % superior to all of the correlation-predicted values. By investigating nine droppings of one of the spheres under the same conditions, an approximate uncertainty of 1 % in the estimations of U_T and C_D was found.

The noteworthy similarity between the experimental results achieved here and those from the published correlations for spherical particles combined with the considerably low uncertainty achieved in the predictions of U_T and C_D suggested that the methodology developed in this research to study the 3D motion kinematics and dynamics of single particles can be considered valid.

CYLINDRICAL PARTICLES

The free fall of cylinders in the interval $0.7 < Re_P < 1975$ was studied. It was noticed that so long as $Re_P < 240$, the fall was steady and the cylinder maximum projected area was perpendicular to the direction of motion. Nevertheless, this behaviour did not guarantee a vertical, straight fall path. For $Re_P > 240$, the regular oscillating pattern described by Marchildon et al. [25] characterised the fall and further altered the trajectory. The structure of the flow surrounding the oscillating cylinders was visualised for the first time using Schlieren photography, and a complete turbulent, non-symmetric wake was found.

The angular variation caused by the secondary motions remained limited to the interval $70° < \alpha < 90°$ approximately. In consequence, only minor fluctuations in the velocity and drag coefficient plots were noticed at terminal conditions, and for most of the cases it could be said that despite the presence of such motions, consistent values of U_T and C_D were observed.

The achieved values of U_T and C_D were compared against those estimated with the correlations of Haider and Levenspiel [16], Ganser [18], Chien [53], and Chow and Adams [27]. With respect to the correlation of Haider and Levenspiel [16] it was noted that before $Re_P = 30$ U_T was over-predicted, then in the interval $30 < Re_P < 240$ a remarkable agreement occurred, and at $Re_P > 240$ it was under-estimated. Nevertheless, in the whole investigated range $0.7 < Re_P < 1975$ the differences between varied from 2 % to 17 %.

In the case of C_D, the discrepancies in the interval $0.7 < Re_P < 100$ fluctuated between 3 % to 20 %, however as Re_P increased and the secondary motions appeared, the difference between the experimental values of C_D and those from the correlations of Haider and Levenspiel [16], Ganser [18], Chien [53] increased up to 32 % for cylinders with $L < 10.5$ mm, and 55 % for those with $L > 20.0$ mm. On the other hand, with regard to the equation of Chow and Adams [27], which considers the effects of the oscillatory motion, the disagreement did not exceed 11 %, demonstrating then the importance of maintaining the particle-fluid interaction undisturbed, so that the influence of the secondary motions on the drag coefficient can be included. Nevertheless, it was evidenced here that their assumption that the oscillatory motion will always appear as long as $\sqrt{\frac{\rho_P/\rho_f}{\sigma}} > 0.5$ is correct only if $Re_P > 240$.

DISK-SHAPED PARTICLES

The free settling of disks in the interval $19.7 < Re_P < 1362$ was examined. It was seen that for $Re_P < 163$ the fall was totally flat with the largest area projected in the direction of motion. Moreover, consistent values of U_T, F_D, and C_D were noticed. However, as Re_P increased, the secondary motions reported by Stringham et al. [26] were witnessed, though at different values of Re_P. A fully tumbling pattern was detected at $Re_P = 226$. A highly regular oscillating disk was perceived at $Re_P = 1362$. The combinations of oscillation and gliding were found for the other cases. The structure of the neighbouring fluid during one of these motions, pure oscillation, was captured through Schlieren photography for the first time, revealing a complete turbulent behaviour.

From the 3D reconstructed centroid trajectories, it was discovered that the occurrence of secondary motions greatly deviated the paths from being vertical lines. In addition, their presence was also reflected in the velocity and drag force plots in the form of significantly regular sinusoid-like variations, mainly for pure tumbling and oscillation. For the combinations of oscillation and gliding, the regularity decreased, yet a similar trend was followed in some of the cases. In the plots of C_D, fluctuations were also found, nonetheless a clear pattern of change was not detected.

Unlike the cylinders, during the existence of the secondary phenomena, none of the calculated motion parameters reached fixed values at conditions of terminal velocity because the fluctuations were characterised by the relatively large amplitudes. Nevertheless, average magnitudes of the particle velocity and coefficient of resistance were computed in order to compare with the correlations given by Haider and Levenspiel [16], Ganser [18], Chien.

In the interval $30 < Re_P < 384$ the discrepancies in U_T were considerably low, fluctuating between 2 % and 6 %. However, for the other Re_P numbers, they were significantly higher with the experimental values being smaller than the predicted ones. For the averages of C_D, a remarkably different outcome was obtained. In the range $150 < Re_P < 230$ the disagreements did not surpass 20 %, yet for $Re_P < 100$ and $Re_P > 100$ huge dissimilarities of 40 % and 60 % were noticed. This suggests that in the presence of secondary particle motions, the approach of averaging V_P and C_D of disks for future analyses may lead to false results.

INFLUENCE OF α ON C_D

The influence that the angular variation has on C_D was analysed for the first time using experimental data in the form of $C_D - \alpha$ plots, as it has been proposed in some numerical works. For cylinders, Rosendahl [11], Hölzer and Sommerfeld [34], Mandø and Rosendahl [30], and Zastawny et al. [28] have suggested that for every increment of α a corresponding increment of C_D exists, yet in this study it was found that C_D can either increase or decrease with the augmentation of α. It is believed that the cause of this dissimilarity is the fact that in their models they set a fixed value of α and then solved the equations subjected to this assumption, thus interrupting the free interaction between the solid and the fluid which happens in reality.

The plots of $C_D - \alpha$ obtained for the tumbling, gliding, and oscillating disks further confirmed the fact that the angular orientation has an impact on the drag, since in these cases considerably larger fluctuations of C_D occurred due to changes in α. Furthermore, it was also seen that even for particles of the same material and dimensions settling at equal conditions, the shape of the curve $C_D - \alpha$ may not be the same, suggesting therefore that the evolutions of the secondary motions and the subsequent angular change are not constant. Moreover, it was noticed that for every increment of α, C_D can also either decrease or increase. A direct relation between both was not perceived.

IRREGULAR PARTICLES

The motion of irregular PTFE chip-like particles descending freely in a stagnant fluid and of woodchips immersed in an enclosed flow of air was explored. For the first case, it was found that despite the irregularity of their geometry, as long as $Re_P < 74$ the settling was steady, and in general with an unfluctuating angular orientation. Additionally, fixed values of U_T, F_D, and C_D were achieved.

As Re_P increased, the solids experienced oscillation, gliding, and rotation around different axes of reference. Provided that the rotation did not occur on an axis perpendicular to the line of vision of the camera, quantitative information could be acquired, just to reveal that none of the variables reached stable magnitudes even at conditions of terminal velocity.

Within the investigated interval, $8 < Re_P < 689$, all of the 3D reconstructed fall paths were neither vertical nor straight. In addition, from the comparison of the values of C_D obtained experimentally and those determined with the correlation of Swamee and Ojha [17], developed for crushed irregular particles, an evident disagreement was noticed, with the correlation estimations being significantly higher (30 % or more) than the experimental results.

For the first time high-speed Schlieren pictures of sinking irregular particles were taken. It was seen that the behaviour of the surrounding fluid was highly turbulent, and that the geometrical unevenness and the rotations of the solids further magnified the turbulence, which in consequence gave rise to irregular motion trajectories.

From the observation of the motion of woodchips inside a pipe-enclosed flow of air at $Re_P = 3.5 \times 10^4$, it was realised that their translational motion was always accompanied by continuous rotations around their longest axis, and sometimes around other perpendicular axes too. Thus giving chance to consecutive changes in orientation, which were further accentuated by interactions with the wall or with other neighbouring particles.

Because of the constantly rotating nature of the irregular particles as they travel in the fluid, occlusion effects may arise continuously, thus incapacitating the conventional two-camera stereo technique employed in this thesis to fully resolve their motion. To accomplish such a task through image-based methods, it is recommended to use at least three cameras so that the front, side, and top views of the particle can be tracked simultaneously and occlusion overcome.

8.3 RECOMMENDATIONS FOR FUTURE WORK

Considering the advantages and limitations of the methodology and techniques employed in this thesis, as well as the as the areas of particle motion that were not investigated here but are significantly relevant, the following recommendations for future works in this field can be announced:

i. With the current two-camera stereo technique the free settling motion of cylinders, disks, and other regular non-spherical solids with a wide range of dimensions should be investigated, especially at $Re_P > 150$, so that the secondary motions can be further analysed, and the influence of L and α on C_D can be more evident. Perhaps, empirical correlations to predict C_D in terms of α could be written.

ii. To develop the new methodology required to solve the particle rotational motion at free settling conditions only, and to implement it through an imaging system composed of two or three cameras, perpendicular to each other, so that the effects of occlusion can be overcome and the influence that the rotational motion has on C_D can be investigated for both regular and irregular solids.

iii. To extend the methodology suggested in the previous step to study the motion of regular and irregular solids that are dragged by a moving fluid, as it occurs in pneumatic transportation installations. The case of a single particle should be analysed first, then the move to multi-particle environments can be attempted.

iv. By means of improving the Schlieren configuration used here or by developing an alternative fluid visualisation technique, the structures of the wake and trail of non-spherical particles at low, medium, and high Re_P must be further investigated, since not only are they important for fluid mechanics but also for heat and mass transfer. Moreover, they can also be significantly relevant for areas related to the combustion of solid particles.

APPENDICES

A. HOMOGRAPHY CALCULATION

As mentioned in Section 3.2 the task of homography calculation becomes the minimization of some algebraic, geometric or statistical error due to the negative effects caused by image noise during the corner coordinates extraction. Assuming independent Gaussian noise on the image coordinates with mean zero and uniform standard deviation the maximum likelihood criterion (Appendix E) reduces the homography estimation problem to the minimization of the Mahalanobis distance

$$min_H \sum_{\boldsymbol{i}} \|\boldsymbol{m_i} - \boldsymbol{m'_i}\|^2 \tag{A1}$$

where

$$\boldsymbol{m'_i} = \frac{1}{\boldsymbol{h_3}^T \boldsymbol{M_{W,i}}} \begin{bmatrix} \boldsymbol{h_1}^T \boldsymbol{M_{W,i}} \\ \boldsymbol{h_2}^T \boldsymbol{M_{W,i}} \end{bmatrix} \tag{A2}$$

being $i=1,2,..,n$ the number of corner points and $\boldsymbol{h}_{j=1,2,3}$ the row vectors of H. The nonlinear minimization of Equation (A1) was solved through the Levenberg-Marquardt method, where the initial guess was obtained from the solution of the next system of $2n$ equations

$$\begin{bmatrix} \boldsymbol{M_{W,1}}^T & \boldsymbol{0}^T & -u_1 \boldsymbol{M_{W,1}}^T \\ \boldsymbol{0}^T & \boldsymbol{M_{W,1}}^T & -v_1 \boldsymbol{M_{W,1}}^T \\ \vdots & \vdots & \vdots \end{bmatrix} \begin{bmatrix} \boldsymbol{h_1}^T \\ \boldsymbol{h_2}^T \\ \boldsymbol{h_3}^T \end{bmatrix} = L\boldsymbol{X} = 0 \tag{A3}$$

The solution is the right eigenvector of L associated with its smallest eigenvalue [99]. Notice that $\boldsymbol{M}_{W,i}$ is expressed in homogeneous coordinates with $Z_{W,i} = 0$, therefore $\boldsymbol{M_{W,i}} = [X_i \quad Y_i \quad 1]^T$.

B. CAMERA CALIBRATION OPERATIONS [99]

After the homographies required by the calibration technique have been estimated the next step is to calculate the intrinsic and extrinsic parameters of the camera. For one orientation of the calibration model, from Equation (3.19) in Section 3.2.2 the following two equations can be derived provided that vectors $\boldsymbol{r_1}$ and $\boldsymbol{r_2}$ are orthonormal

$$\boldsymbol{h_1}^T A^{-T} A^{-1} \boldsymbol{h_2} = 0 \tag{B1}$$

$$\boldsymbol{h_1}^T A^{-T} A^{-1} \boldsymbol{h_1} = \boldsymbol{h_2}^T A^{-T} A^{-1} \boldsymbol{h_2} \tag{B2}$$

where $\boldsymbol{h}_{j=1,2,3}$ are the column vectors of H. The development of the matrix multiplication $A^{-T}A^{-1}$ defines a 3×3 symmetric matrix B

$$A^{-T}A^{-1} = \begin{bmatrix} \frac{1}{{\alpha_u}^2} & -\frac{\gamma}{{\alpha_u}^2\alpha_v} & \frac{v_0\gamma - u_0\alpha_v}{{\alpha_u}^2\alpha_v} \\ -\frac{\gamma}{{\alpha_u}^2\alpha_v} & \frac{\gamma}{{\alpha_u}^2{\alpha_v}^2} + \frac{1}{{\alpha_v}^2} & -\frac{\gamma(v_0\gamma - u_0\alpha_v)}{{\alpha_u}^2{\alpha_v}^2} - \frac{v_0}{{\alpha_v}^2} \\ \frac{v_0\gamma - u_0\alpha_v}{{\alpha_u}^2\alpha_v} & -\frac{\gamma(v_0\gamma - u_0\alpha_v)}{{\alpha_u}^2{\alpha_v}^2} - \frac{v_0}{{\alpha_v}^2} & \frac{(v_0\gamma - u_0\alpha_v)^2}{{\alpha_u}^2{\alpha_v}^2} + \frac{{v_0}^2}{{\alpha_v}^2} + 1 \end{bmatrix}$$
$$= \begin{bmatrix} B_{11} & B_{12} & B_{13} \\ B_{21} & B_{22} & B_{23} \\ B_{31} & B_{32} & B_{33} \end{bmatrix} \equiv B \tag{B3}$$

which can be substituted in Equation (B1) to give

$$[h_{11}h_{21} \quad h_{12}h_{21} + h_{11}h_{22} \quad h_{12}h_{22} \quad h_{13}h_{21} + h_{11}h_{23} \quad h_{13}h_{22} + h_{12}h_{23} \quad h_{13}h_{23}] \begin{bmatrix} B_{11} \\ B_{12} \\ B_{22} \\ B_{13} \\ B_{23} \\ B_{33} \end{bmatrix}$$

or

$${V_{12}}^T\boldsymbol{b} = 0 \tag{B4}$$

where $\boldsymbol{b} = [B_{11} \quad B_{12} \quad B_{22} \quad B_{13} \quad B_{23} \quad B_{33}]^T$. Similarly, the substitution of B in Equation (B2) produces

$$\{[h_{11}h_{11} \quad h_{12}h_{11} + h_{11}h_{12} \quad h_{12}h_{12} \quad h_{13}h_{11} + h_{11}h_{13} \quad h_{13}h_{12} + h_{12}h_{13} \quad h_{13}h_{13}] \\ - [h_{21}h_{21} \quad h_{22}h_{21} + h_{21}h_{22} \quad h_{22}h_{22} \quad h_{23}h_{21} + h_{21}h_{23} \quad h_{23}h_{22} + h_{22}h_{23} \quad h_{23}h_{23}]\}\boldsymbol{b} \\ = 0$$

or

$$\left\{{V_{11}}^T - {V_{22}}^T\right\}\boldsymbol{b} = 0 \tag{B5}$$

Equations (B4) and (B5) can be stacked to form

$$\begin{bmatrix} {V_{12}}^T \\ {V_{11}}^T - {V_{22}}^T \end{bmatrix}\boldsymbol{b} = 0 \tag{B6}$$

Equation (B6) represents a system of 2 equations for one single homography. For n homographies, a system of $2n$ equations results

$$V\boldsymbol{b} = 0 \tag{B7}$$

where matrix V has size $n \times 6$. The solution of Equation (B7) corresponds to the right eigenvector of matrix V associated with its smallest eigenvalue. Once vector $\boldsymbol{b}$ is known, the camera intrinsic parameters can be computed using the next equations

$$v_0 = \frac{B_{12}B_{13} - B_{11}B_{23}}{B_{11}B_{22} - {B_{12}}^2} \tag{B8a}$$

$$\lambda = B_{33} - \left[{B_{13}}^2 + v_0(B_{12}B_{13} - B_{11}B_{23})\right]/B_{11} \tag{B8b}$$

$$\alpha = \sqrt{\frac{\lambda}{B_{11}}} \tag{B8c}$$

$$\beta = \sqrt{\lambda B_{11}/\left(B_{11}B_{22} - {B_{12}}^2\right)} \tag{B8d}$$

$$\gamma = \frac{-B_{12}\alpha^2\beta}{\lambda} \tag{B8e}$$

$$u_0 = \frac{\gamma v_0}{\beta} - \frac{B_{13}\alpha^2}{\lambda} \tag{B8f}$$

Once the intrinsic parameters are known, for each of the *n* homographies the extrinsic parameters are obtained with the following relations

$$\boldsymbol{r_1} = \omega A^{-1}\boldsymbol{h_1} \tag{B9a}$$

$$\boldsymbol{r_2} = \omega A^{-1}\boldsymbol{h_2} \tag{B9b}$$

$$\boldsymbol{t} = \omega A^{-1}\boldsymbol{h_3} \tag{B9c}$$

$$\boldsymbol{r_3} = \boldsymbol{r_1} \times \boldsymbol{r_2} \tag{B9d}$$

where $\omega = \|A^{-1}\boldsymbol{h_1}\|^{-1}$. The computed matrix $Q = [\boldsymbol{r_1} \quad \boldsymbol{r_2} \quad \boldsymbol{r_3}]$ is still an approximate matrix which does not meet all the requirements of a rotation matrix. In order to find the best rotation matrix *R*, singular value decomposition is first applied $Q = USV^T$, then *R* is calculated as follows

$$R = UV^T \tag{B10}$$

C. RADIAL DISTORTION COEFFICIENTS ESTIMATION

Up to now the analysis has not considered the influence of lens aberration, which causes straight lines of the real world scenes to appear slightly curved in the image plane. In Figure B1 its effect on both tangential and radial directions, respectively, is illustrated. Tangential distortion arises from incorrect lens centring whilst the radial one is a consequence of improper lens shape and constitutes the most common distortion type, therefore it is the one included in this work.

Radial distortion is symmetric about the optical axis and can be classified as positive (pincushion visual effect, Figure B2a) or negative (barrel visual effect, Figure B2b) in agreement with the direction of the radial displacement of a given point in the image from its ideal position. Although being rare, a combination of both types may occur. It is known as *moustache* distortion.

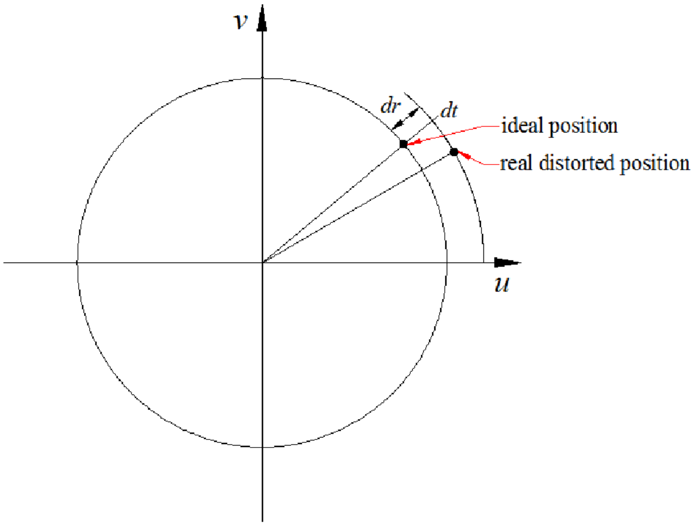

Figure B1 Tangential (*dt*) and radial (*dr*) distortions on one image point [111].

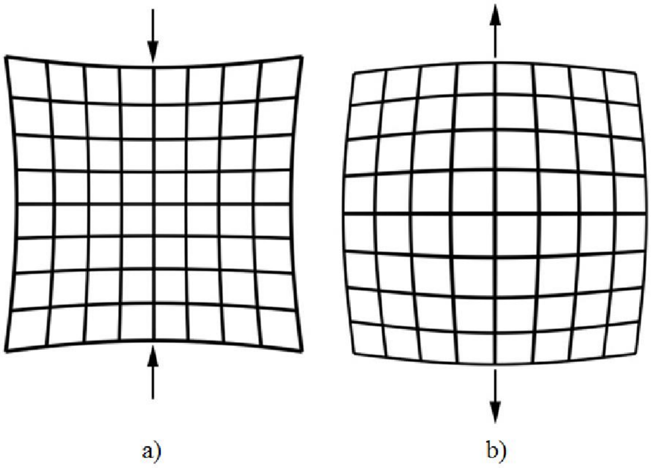

Figure B2 a) Pincushion radial distortion, b) barrel radial distortion.

The process of radial distortion correction relies on the application of a polynomial distortion model before completing the calibration of the camera. For a perfectly centered lens with the principal point at the center of distortion, the distorted radial distance (Figure B1) $r_d = r + dr$ can be modeled as follows

$$r_d = rf(r) = r(1 + c_1 r^2 + c_2 r^4 + c_3 r^6 + \cdots) \tag{C1}$$

where c_1, c_2, c_3,… are the distortion coefficients [112]. Since the first term of the polynomial is the most dominant one and to avoid numerical instability during the calculations, only the first two coefficients are preserved [111-114]. Consequently, Equation (C1) takes the form

$$r_d = rf(r) = r(1 + c_1 r^2 + c_2 r^4) \tag{C2}$$

The relation between the ideal, distortion-free pixel coordinates (u, v) and the real, distorted coordinates (u_d, v_d), respectively, of one image point is given by the following system of equations

$$u_d = u_0 + (u - u_0)f(r) = u_0 + (u - u_0)[c_1 r^2 + c_2 r^4] \tag{C3a}$$

$$v_d = v_0 + (v - v_0)f(r) = v_0 + (v - v_0)[c_1 r^2 + c_2 r^4] \tag{C3b}$$

where $r^2 = \hat{x}^2 + \hat{y}^2$, being $\hat{x}$, $\hat{y}$ the ideal normalized image coordinates, computed after the calculation of the intrinsic and extrinsic parameters of the camera. In matrix form and for n points Equation (C3) can be rewritten as

$$\begin{bmatrix} (u_1 - u_0)\left(\widehat{x_1}^2 + \widehat{y_1}^2\right) & (u_1 - u_0)\left(\widehat{x_1}^2 + \widehat{y_1}^2\right)^2 \\ (v_1 - v_0)\left(\widehat{x_1}^2 + \widehat{y_1}^2\right) & (v_1 - v_0)\left(\widehat{x_1}^2 + \widehat{y_1}^2\right)^2 \\ \vdots & \vdots \end{bmatrix} \begin{bmatrix} c_1 \\ c_2 \end{bmatrix} = \begin{bmatrix} u_{d,1} - u_0 \\ v_{d,1} - v_0 \end{bmatrix} \tag{C4}$$

or

$$D\boldsymbol{c} = \boldsymbol{d} \tag{C5}$$

where D is a $2n \times 2$ matrix. According to Zhang [99], the solution of Equation (C5) is

$$\boldsymbol{c} = (D^T D)^{-1} D^T \boldsymbol{d} \tag{C6}$$

The radial distortion coefficients which have just been estimated are used during the task of stereo reconstruction to correct the distorted 2D coordinates of the matching points before the geometry of the stereo system is computed and the reconstruction executed.

D. EPIPOLAR GEOMETRY COMPUTATION

The epipolar geometry can be entirely described by any of the essential or fundamental matrices, yet in the present work the procedure recommended by Zhang [102] which starts with the computation of the fundamental matrix was preferred since it allows an intermediate optimization process (which will be discussed later) during the calculations. Once $\mathcal{F}$ is obtained, then ε and the Euclidean motion parameters R and $\boldsymbol{t}$ can be estimated.

The methodology selected for the calculation of $\mathcal{F}$ is provided by the so-called *eight-point* algorithm [103], [96] which starts replacing $\mathcal{F}$ with an approximate 3 × 3 matrix F and expressing Equation (3.23) as a linear function in its elements $F_{ij=1,2,3}$

$$[u_1u_2 \quad v_1u_2 \quad u_2 \quad u_1v_2 \quad v_1v_2 \quad v_2 \quad u_1 \quad v_1 \quad 1]\begin{bmatrix} F_{11} \\ F_{12} \\ F_{13} \\ F_{21} \\ F_{22} \\ F_{23} \\ F_{31} \\ F_{32} \\ F_{33} \end{bmatrix} = q^T\boldsymbol{f} \ = 0 \qquad \text{(D1)}$$

where $\boldsymbol{m_1}(u_1, v_1)$ and $\boldsymbol{m_2}(u_2, v_2)$. For n matching pairs (m_1, m_2) becomes

$$Q\boldsymbol{f} \ = 0 \qquad \text{(D2)}$$

where $Q = [{q_1}^T \quad \ldots \quad {q_n}^T]^T$. The solution of Equation (C2), named as F_1, is the right eigenvector of Q associated with its smallest eigenvalue. Since F_1 does not meet the singularity condition of the fundamental matrix, the straightest forward way to apply it is by forcing its smallest eigenvalue to be equal to zero. This can be accomplished by making zero the third element of the diagonal matrix S product of the singular value decomposition of $F_1 = USV^T$. The result is

$$F_2 = U\hat{S}V^T \qquad \text{(D3)}$$

where $\hat{S}$ corresponds to the modified S. In agreement with Hartley [115], to avoid numerical instabilities and decrease the computational time, the coordinates of the n matching pairs (m_1, m_2) which constitute matrix Q in Equation (C2) should be normalized. The normalization process for each coordinate point m (u, v) is

$$\begin{bmatrix} u_{nor} \\ v_{nor} \\ 1 \end{bmatrix} = \begin{bmatrix} s_C & 0 & s_C T_X \\ 0 & s_C & s_C T_Y \\ 0 & 0 & 1 \end{bmatrix} \begin{bmatrix} u \\ v \\ 1 \end{bmatrix} \tag{D4}$$

or

$$\boldsymbol{m_{nor}} = T\boldsymbol{m} \tag{D5}$$

where T_X and T_Y represent the translation required for the centroid of the normalized coordinates to coincide with the origin of coordinates, and s_C is the scale which makes the *RMS* distance of the points from the origin equal to $\sqrt{2}$. The relations to compute them are

$$T_X = -\left(\sum_{i=1}^{n} u_i\right)\Big/ n \tag{D6a}$$

$$T_Y = -\left(\sum_{i=1}^{n} v_i\right)\Big/ n \tag{D6b}$$

$$s_C = \sqrt{2}n \Big/ \sum_{i=1}^{n} \sqrt{(u_i + T_X)^2 + (v_i + T_Y)^2} \tag{D6c}$$

Consequently, for the points corresponding to the left image the normalization process is expressed as $\boldsymbol{m_{1,nor}} = T_1\boldsymbol{m_1}$ whilst for those of the right it is $\boldsymbol{m_{2,nor}} = T_2\boldsymbol{m_2}$. If normalization is done, the matrix computed with Equation (C3) has to be de-normalized through the following relation

$$F_3 = {T_2}^T F_2 T_1 \tag{D7}$$

Instead of considering F_3 as the first guess of the fundamental matrix and moving into the essential matrix computation, the already mentioned intermediate optimization process can be introduced. It involves decomposing F_3 into seven independent parameters (provided that a fundamental matrix has rank-2 and is defined up to a scale factor), hence

$$F_3 = \begin{bmatrix} a & b & -ax_1 - by_1 \\ c & d & -cx_1 - dy_1 \\ -ax_2 - cy_2 & -bx_2 - dy_2 & (ax_1 + by_1)x_2 + (cx_1 + dy_1)y_2 \end{bmatrix} \tag{D8}$$

where (x_1, y_1) and (x_2, y_2) correspond to the coordinates of the epipoles e_1 and e_2, respectively, and *a, b, c, d* dictate the relation between the orientation of the two pencils of the epipolar lines [102]. Among the last four parameters one is not independent. Because the epipolar geometry constraint (Figure 3.11, Section 3.3) requests point m_2 to lie on line L_2, and m_1 on L_1 the optimization task consists on the minimization of the sum of the squared gap distances existing between those points and lines

$$min_d \sum_{i} \{[d(\boldsymbol{m_{2i}}, \mathcal{F}\boldsymbol{m_{1i}})]^2 + [d(\boldsymbol{m_{1i}}, \mathcal{F}^T\boldsymbol{m_{2i}})]^2\} \tag{D9}$$

The minimization can be done using the Levenberg-Marquardt algorithm with F_3 as initial guess [116]. Once completed a refined matrix F_4 is obtained from the optimized seven parameters. Then, after imposing the singularity constraint again the final estimated fundamental matrix is obtained, which in turn can be used to compute the ε using Equation (3.22) followed by singular value decomposition to impose the condition of having two non-zero singular values.

The Euclidean motion parameters can now be computed from the essential matrix. Following Zhang's methodology [102], provided that $\varepsilon^T \boldsymbol{t} = 0$, the translation vector is the solution of

$$min_{\boldsymbol{t}} \|\varepsilon^T \boldsymbol{t}\|^2 \text{ subject to } \|\boldsymbol{t}\| = 1 \tag{D10}$$

which turns to be the left eigenvector of ε associated to its smallest eigenvalue. If the condition $([\mathbf{t}_\times]\widehat{\boldsymbol{m_2}}) \cdot (\varepsilon\widehat{\boldsymbol{m_1}}) < 0$ is not accomplished, then the sign of $\boldsymbol{t}$ has to be inverted to agree with the sign of ε. The rotation matrix is found by solving

$$min_{\boldsymbol{R}} \sum_{k=1}^{3} \|R\boldsymbol{\varepsilon_k} - \boldsymbol{\tau_k}\|^2 \text{ subject to } R^T R = I \text{ and } det(R) = 1 \tag{D11}$$

where $\boldsymbol{\varepsilon_k}$ and $\boldsymbol{\tau_k}$ are the *kth* row vectors of ε and $[\mathbf{t}_\times]$. On the assumption that R can be represented by the unit quaternion $\boldsymbol{q}$ [117], then

$$R\boldsymbol{\varepsilon_k} = \boldsymbol{q}\boldsymbol{\varepsilon_k}\boldsymbol{q_C}$$

where $\boldsymbol{q_C}$ is the conjugate quaternion of $\boldsymbol{q}$. Therefore, Equation (C11) can be re-stated as follows

$$min_{\boldsymbol{R}} \sum_{k=1}^{3} \|\boldsymbol{q}\boldsymbol{\varepsilon_k}\boldsymbol{q_C} - \boldsymbol{\tau_k}\|^2 \text{ subject to } \|\boldsymbol{q}\| = 1 \tag{D12}$$

which in turn can be simplified to

$$min_{\boldsymbol{R}} \sum_{k=1}^{3} \|\boldsymbol{q}\boldsymbol{\varepsilon_k} - \boldsymbol{\tau_k}\boldsymbol{q}\|^2 = min_{\boldsymbol{R}} \sum_{k=1}^{3} \boldsymbol{q}^T {G_k}^T G_k \boldsymbol{q} \tag{D13}$$

where the elements of the 4 × 4 matrix $N = {G_k}^T G_k$ are calculated with the following set of equations [116]

$$\begin{gathered}
N_{11} = (\varepsilon_{k1} - \tau_{k1})^2 + (\varepsilon_{k2} - \tau_{k2})^2 + (\varepsilon_{k3} - \tau_{k3})^2 \\
N_{12} = -(\varepsilon_{k2} - \tau_{k2})(\varepsilon_{k3} + \tau_{k3}) + (\varepsilon_{k3} - \tau_{k3})(\varepsilon_{k2} + \tau_{k2}) \\
N_{13} = (\varepsilon_{k1} - \tau_{k1})(\varepsilon_{k3} + \tau_{k3}) - (\varepsilon_{k3} - \tau_{k3})(\varepsilon_{k1} + \tau_{k1}) \\
N_{14} = -(\varepsilon_{k1} - \tau_{k1})(\varepsilon_{k2} + \tau_{k2}) + (\varepsilon_{k2} - \tau_{k2})(\varepsilon_{k1} + \tau_{k1}) \\
N_{21} = N_{12} \\
N_{22} = (\varepsilon_{k1} - \tau_{k1})^2 + (\varepsilon_{k2} + \tau_{k2})^2 + (\varepsilon_{k3} + \tau_{k3})^2 \\
N_{23} = (\varepsilon_{k1} - \tau_{k1})(\varepsilon_{k2} - \tau_{k2}) - (\varepsilon_{k2} + \tau_{k2})(\varepsilon_{k1} + \tau_{k1}) \\
N_{24} = (\varepsilon_{k1} - \tau_{k1})(\varepsilon_{k3} - \tau_{k3}) - (\varepsilon_{k1} + \tau_{k1})(\varepsilon_{k3} + \tau_{k3}) \\
N_{31} = N_{13} \\
N_{32} = N_{23} \\
N_{33} = (\varepsilon_{k1} + \tau_{k1})^2 + (\varepsilon_{k2} - \tau_{k2})^2 + (\varepsilon_{k3} + \tau_{k3})^2 \\
N_{34} = (\varepsilon_{k2} - \tau_{k2})(\varepsilon_{k3} - \tau_{k3}) - (\varepsilon_{k3} + \tau_{k3})(\varepsilon_{k2} + \tau_{k2}) \\
N_{41} = N_{14} \\
N_{42} = N_{24} \\
N_{43} = N_{34} \\
N_{44} = (\varepsilon_{k1} + \tau_{k1})^2 + (\varepsilon_{k2} + \tau_{k2})^2 + (\varepsilon_{k3} - \tau_{k3})^2
\end{gathered} \tag{D14}$$

The solution of this problem is the unit quaternion corresponding to the smallest eigenvalue of

$$min_{\boldsymbol{q}} \sum_{k=1}^{3} N_k \tag{D15}$$

Before attempting the 3D reconstruction through linear triangulation, a second optimization based also on Equation (C9) has to be done to refine the motion parameters. First, the backwards calculation of ε and $\mathcal{F}$ to be used as input is completed. Then, the minimization employing the Levenberg-Marquardt algorithm and the forward calculation of $\mathcal{F}$, ε, R and $\boldsymbol{t}$ take place.

E. MAXIMUM LIKELIHOOD ESTIMATION

Either for homography estimation, camera calibration, or three-dimensional stereo reconstruction, the maximum likelihood estimation (MLE) criterion is used to seek the optimum results providing the real image points are subject to noise (i.e. measurement error). If such error is modelled statistically, the MLE comprises the search of the probability distribution that makes the given real data most likely [118].

For the already mentioned tasks it is commonly assumed that the noise obeys a *Gaussian* error model as long as the images are free of *outliers* and the image coordinates are extracted independently with the same technique. Thus, the MLE probability distribution, with mean zero and uniform standard deviation σ, is

$$P(\mathbb{x}) = \left(\frac{1}{2\pi\sigma^2}\right) exp\left(\frac{-d(\mathbb{x},\overline{\mathbb{x}})^2}{2\sigma^2}\right) \tag{E1}$$

where $\mathbb{x}$ corresponds to the real data point, $\overline{\mathbb{x}}$ to the equivalent non-distorted point, and $d(\mathbb{x},\overline{\mathbb{x}})$ to the distance between both [96]. The application of the MLE criterion (Equation 1) for camera calibration is equivalent to the nonlinear minimization of

$$\sum_{i=1}^{m}\sum_{j=1}^{n}\left\|\boldsymbol{m_{ij}} - \boldsymbol{\widehat{m}}\left(A, c_1, c_2, R_j, \boldsymbol{t_j}, M_{W,i}\right)\right\|^2 \tag{E2}$$

where m is the number of calibration pictures and n the number of corner points. $\boldsymbol{\widehat{m}}\left(A, c_1, c_2, R_j, \boldsymbol{t_j}, M_{W,i}\right)$ is the projection of $M_{W,i}$ in image j followed by distortion with Equations (C3). The rotation matrix is parameterized into a 3-element vector $\boldsymbol{r}$, whose magnitude equals the value of the rotation angle, and with the same direction as the rotation axis [99]. The first estimation of the intrinsic and extrinsic parameters as well as the radial distortion coefficients are used as input data. For 3D stereo reconstruction, the MLE criterion reduces to find the solution of

$$\hat{\theta} = arg\ min_{\boldsymbol{a}} \sum_{j=1}^{n} \left\{ min_{M_{W,j}} \left[\left\| \boldsymbol{m}_{1,j} - \boldsymbol{h_1}\left(\boldsymbol{a}, M_{W,j}\right) \right\|^2 + \left\| \boldsymbol{m}_{2,j} - \boldsymbol{h_2}\left(\boldsymbol{a}, M_{W,j}\right) \right\|^2 \right] \right\} \tag{E3}$$

where $\widehat{\boldsymbol{\theta}} = \left[\boldsymbol{a}^T, \boldsymbol{M_1}^T, \dots, \boldsymbol{M_2}^T, \dots, \boldsymbol{M_j}^T\right]^T$ is the refined motion and structure (5+3n)-element vector, and $\boldsymbol{h_1}\left(\boldsymbol{a}, M_{W,j}\right)$ and $\boldsymbol{h_2}\left(\boldsymbol{a}, M_{W,j}\right)$ are the projection of M_W on the left and right image planes, respectively. $\boldsymbol{a} = [\boldsymbol{r}^T, \emptyset^T]^T$ is the 5-element vector conformed by the rotation vector $\boldsymbol{r}$ and the 2-element parameterized translation vector $\emptyset$ [102]. In this case both $\boldsymbol{r}$ and $\emptyset$ correspond to the motion between cameras.

F. FINITE DIFFERENCE EQUATIONS

In Section 4.3 finite difference equations were employed to estimate the 1st, 2nd, and 3rd time derivatives of X_W, Y_W, and Z_W, respectively, needed to find the parameters which describe the Frenet reference frame. The operations were done in a Matlab program written for this purpose only, and the forward, backward, and centred schemes were used. For the forward approach, the finite difference equations to calculate the derivatives are:

$$\frac{df}{dt} \approx \frac{f(x_{i+1}) - f(x_i)}{\Delta t} \tag{F1}$$

$$\frac{d^2f}{dt^2} \approx \frac{f(x_{i+2}) - 2f(x_{i+1}) - f(x_i)}{\Delta t^2} \tag{F2}$$

$$\frac{d^3f}{dt^3} \approx \frac{f(x_{i+3}) - 3f(x_{i+2}) + 3f(x_{i+1}) - f(x_i)}{\Delta t^3} \tag{F3}$$

whilst for the backward scheme they are:

$$\frac{df}{dt} \approx \frac{f(x_i) - f(x_{i-1})}{\Delta t} \tag{F4}$$

$$\frac{d^2f}{dt^2} \approx \frac{f(x_i) - 2f(x_{i-1}) + f(x_{i-2})}{\Delta t^2} \tag{F5}$$

$$\frac{d^3f}{dt^3} \approx \frac{f(x_i) - 3f(x_{i-1}) + 3f(x_{i-2}) - f(x_{i-3})}{\Delta t^3} \tag{F6}$$

and for the centred approach the equations are:

$$\frac{df}{dt} \approx \frac{f(x_{i+1}) - f(x_{i-1})}{2\Delta t} \tag{F7}$$

$$\frac{d^2f}{dt^2} \approx \frac{f(x_{i+1}) - 2f(x_i) + f(x_{i-1})}{\Delta t^2} \tag{F8}$$

$$\frac{d^3f}{dt^3} \approx \frac{f(x_{i+2}) - 2f(x_{i+1}) + 2f(x_{i-1}) - f(x_{i-2})}{2\Delta t^3} \tag{F9}$$

G. PROGRAMS WRITTEN IN MATLAB

The programs written to execute the task of calibrating each virtual camera are:

calibration.m

It starts the calibration of the camera. It calls the next user-defined functions (UDF):

- LoadBoardImage.m
  It executes the first step of Figure 3.11 by loading the five recorded stereo pictures of the calibration model, converting them from RGB to grey-scale, and splitting them into left and right images through the UDF *separateimage.m*.
- CornersFCalibrationBoard.m
  It extracts the pixel coordinates of the black squares of the calibration model through Canny edge detection and Hough transform (step 2 of Figure 3.11). It calls the UDF's *hough.m, houghpeaks.m, CornersFSquares.m, cornerfinder.m*. Other UDF's called by some of these functions are: *getlines.m, orderrc.m, houghline.m, houghpixels.m, linesNumCorrect.m*.
- Calibrationfortviews.m
  It performs steps 3 to 6 of Figure 3.11 through the following UDF's:
  - InputImageCoordinates.m
  - InputModelCoordinates.m
  - ModelHomoImage.m: it solves step 3 of Figure 3.11 as explained in Appendix A. It calls the UDF *InitializeHomography.m* to find an initial homography guess by solving Equation (A3), and computes the homography through the nonlinear minimization of the Mahalanobis

distance (Equations A1 and A2) with the assistance of the UDF's *DistfProjPnts2ImgCoor.m, TDHomoTrans.m, CoorHomo.m*.

  - Closed_Form_Solution.m: it finds the intrinsic parameters (step 4 of Figure 3.11) by solving Equations (B7) and (B8) using the UDF's *VfromHomo.m, IntMatfV.m, IntriMatfIntPara.m*. It then computes the extrinsic parameters (step 5 of Figure 3.11) with Equations (B9) and (B10) and the UDF's *RTfIntMat.m, Rotation2Quaternion.m, TRtoFiveDVect.m*.
  - RadDistortEstimate.m: it determines the radial distortion coefficients (step 6 of Figure 3.11) as illustrated in Appendix C, using the UDF's: *IntriMatfIntPara.m, Homofa.m, FiveDVectoTR.m, quaternion2R.m, TDHomoTrans.m, CoorHomo.m*.

  It then completes the calibration by doing step 7 of Figure 3.11 through the UDF's: *IntparaAss.m, DistfProjPnts2ImgCoor_Com.m, IntriMatfIntPara.m, Homofa.m, TDHomoTrans.m, CoorHomo.m*.

The programs done to calculate the geometry of the stereo systems and do the 3D reconstruction of the corner points of the calibration model are:

MotionParameterEstimation2.m

It does steps 1 and 2 of Figure 3.13 using the UDF's *InputImageCoordinatesL.m, InputImageCoordinatesR.m, CorrectRadialDist.m, TDHomoTrans.m, CoorHomo.m*. It then calls the following UDF's to continue the next steps of the methodology:

- ThreeDReconstructMain2.m

  Starting at step 3, it completes the methodology of Figure 3.13. It calls the next UDF's:
  - normalization.m: it normalizes the distortion-corrected pixel coordinates with Equations (C4) – (C6) to be used by the eight-point algorithm. It calls the UDF's *TDHomoTrans.m, CoorHomo.m*.
  - Eightpoint.m: it computes the first estimation of the fundamental matrix by solving Equation (C2).
  - Rank2Mat.m: it improves the estimation of the fundamental matrix by imposing the required singularity condition (Equation C3), thus completing step 3 of Figure 3.13.

- Mat27Para.m: it re-expresses the fundamental matrix into seven independent parameters (step 4 of Figure 3.13) as seen in Equation (C8) through the UDF's *EpifromFund.m, FindScaleFac.m*.
- SevenParaRefine.m: it optimizes the seven parameters (step 5 of Figure 3.13) applying the criteria of Equation (C9). It calls the UDF's *Dist2EpiFuncofSeven.m, SevenParatoMatrix.m, restore_abcd.m*.
- SevenParatoMatrix.m: it begins step 6 of Figure 3.13 by re-computing the fundamental matrix from the optimized seven parameters and denormalizing it with Equation (C7). It also uses the UDF *restore_abcd.m*.
- EssentialtoTR.m: it calculates the essential matrix given the fundamental matrix and the motion parameters R and $\boldsymbol{t}$ with Equations (C10) and (C15), thus finishing step 6 of Figure 3.13. It calls the UDF's *Fmat2Emat.m, vec2matrix.m, quaternion.m, quaternion2R.m*.
- MotionParaRefine.m: it optimizes R and $\boldsymbol{t}$ (step 7 of Figure 3.13) with the same criteria of Equation (C9). It calls the UDF's *Dist2EpiFuncofMotion.m, FiveDVectoTR.m, TRtoEssential.m, Emat2Fmat.m*.
- PointsReconstructLinear.m: it obtains the 3D coordinates of the stereo matching points using the method of linear triangulation (step 8 of Figure 3.13). It calls the UDF's *FiveDVectoTR.m, ReconstructLinear.m*.
- PointsReconstructNonLinear2.m: it optimizes R, $\boldsymbol{t}$, and the obtained 3D points (step 8 of Figure 3.13) using the maximum likelihood criterion explicated in Appendix E. It calls the UDF's *MotNStruRefineOuter2.m, MotNStruRefineInner2.m, FiveDVectoTR.m*.

BackProj.m

It projects the 3D reconstructed coordinates of the corner points of the black squares of the calibration model from the left camera frame to the world reference frame and exports to an Excel spreadsheet, so that subsequent analysis on the accuracy of the reconstruction can be done.

The programs written for the analyses of particle motion are:

ParticleImgProcess4.m

It performs all the digital image processing operations listed in Figure 4.12 to the stereo pictures of the moving particles. It calls the UDF functions: *CtoGS.m, ImgEnhance2.m, Centroid.m, SeparateImage.m, Orientation4.m*. Then they export the results to an Excel spreadsheet.

ParticleCent3D.m, ParticleP1P23D.m

They compute the 3D coordinates of the centroid and points P_1 and P_2 in the left camera frame. The UDF's called are: *CorrectRadialDist.m, ReconstructLinear.m*. Then they export the results to an Excel spreadsheet.

ParticleCentBackProj.m, ParticleP1BackProj.m, ParticleP2BackProj.m

They project the 3D coordinates of the centroid and points P_1 and P_2 from the left camera frame to the world reference frame as indicated in Equation (3.32).

Particle3DMotion.m

It solves the kinematics of the moving particle in the context of the Frenet reference frame and exports the results to an Excel spreadsheet. The derivatives are found through the finite difference equations listed in Appendix F using the UDF *FinDiff.m*.

Particle3D_Dynamics2.m

It calculates the tangential, normal, and binormal forces within the Frenet reference frame, and computes the drag force experience by the particle. Then it exports the results to an Excel spreadsheet.

Plot3DPath.m

It reads the data from the corresponding Excel spreadsheet and generates 3D plots of the particle trajectories.

PUBLICATIONS

1. F. Carranza, Y. Zhang, “Single particle motion studies using stereo-vision and digital image processing,” presented and published in: Proceedings of the 12th International Conference on Heat Transfer, Fluid Mechanics and Thermodynamics, pp. 1484-1489, Malaga, Spain, July 2016.

   The Outstanding Paper Award in Multiphase Flow was received for this paper.

REFERENCES

[1] A. Demirbaş, "Sustainable cofiring of biomass with coal," *Energy Conversion and Management,* vol. 44, pp. 1465-1479, 2003.

[2] M. Sami, K. Annamalai, and M. Wooldridge, "Co-firing of coal and biomass fuel blends," *Progress in Energy and Combustion Science,* vol. 27, pp. 171-214, 2001.

[3] S. v. Loo, J. Koppejan, *The handbook of biomass combustion and co-firing*. London: Earthscan, 2008. pp. 203-247.

[4] J. P. Wolf, "Biomass combustion for power generation: an introduction," in *Biomass combustion science, technology and engineering*, L. Rosendahl, Ed., ed Cambridge: Woodhead Publishing, 2013, pp. 3-8.

[5] D. A. Tillman, "Biomass cofiring: the technology, the experience, the combustion consequences," *Biomass and Bioenergy,* vol. 19, pp. 365-384, 2000.

[6] K. R. G. Hein and J. M. Bemtgen, "EU clean coal technology—co-combustion of coal and biomass," *Fuel Processing Technology,* vol. 54, pp. 159-169, 1998.

[7] D. Osborne, *The Coal Handbook: Towards Cleaner Production: Coal Production*. Elsevier, 2013.

[8] L. A. Rosendahl, C. Yin, S. K. Kær, K. Friborg, and P. Overgaard, "Physical characterization of biomass fuels prepared for suspension firing in utility boilers for CFD modelling," *Biomass and Bioenergy,* vol. 31, pp. 318-325, 2007.

[9] C. Yin, "Biomass co-firing," in *Biomass combustion science, technology and engineering*, L. Rosendahl, Ed., ed Cambridge: Woodhead Publishing, 2013, pp. 84-105.

[10] L. Baxter, "Biomass-coal co-combustion: opportunity for affordable renewable energy," *Fuel,* vol. 84, pp. 1295-1302, 2005.

[11] L. Rosendahl, "Using a multi-parameter particle shape description to predict the motion of non-spherical particle shapes in swirling flow," *Applied Mathematical Modelling,* vol. 24, pp. 11-25, 2000.

[12] C. Yin, L. Rosendahl, S. Knudsen Kær, and H. Sørensen, "Modelling the motion of cylindrical particles in a nonuniform flow," *Chemical Engineering Science,* vol. 58, pp. 3489-3498, 2003.

[13] D. Gera, M. P. Mathur, M. C. Freeman, and A. Robinson, "Effect of Large Aspect Ratio of Biomass Particles on Carbon Burnout in a Utility Boiler," *Energy & Fuels,* vol. 16, pp. 1523-1532, 2002.

[14] D. Mills, *Pneumatic conveying design guide*, 2nd ed.: Oxford: Butterworth-Heinemann, 2004.

[15] R. Clift and W. H. Gauvin, "Motion of entrained particles in gas streams," *The Canadian Journal of Chemical Engineering,* vol. 49, pp. 439-448, 1971.

[16] A. Haider and O. Levenspiel, "Drag coefficient and terminal velocity of spherical and nonspherical particles," *Powder Technology,* vol. 58, pp. 63-70, 1989.

[17] P. Swamee and C. Ojha, "Drag Coefficient and Fall Velocity of nonspherical particles," *Journal of Hydraulic Engineering,* vol. 117, pp. 660-667, 1991.

[18] G. H. Ganser, "A rational approach to drag prediction of spherical and nonspherical particles," *Powder Technology,* vol. 77, pp. 143-152, 1993.

[19] G. V. Madhav and R. P. Chhabra, "Drag on non-spherical particles in viscous fluids," *International Journal of Mineral Processing,* vol. 43, pp. 15-29, 1995.

[20] R. P. Chhabra, L. Agarwal, and N. K. Sinha, "Drag on non-spherical particles: an evaluation of available methods," *Powder Technology,* vol. 101, pp. 288-295, 1999.

[21] E. Loth, "Drag of non-spherical solid particles of regular and irregular shape," *Powder Technology,* vol. 182, pp. 342-353, 2008.

[22] J. Gabitto and C. Tsouris, "Drag coefficient and settling velocity for particles of cylindrical shape," *Powder Technology,* vol. 183, pp. 314-322, 2008.

[23] F. Dioguardi and D. Mele, "A new shape dependent drag correlation formula for non-spherical rough particles. Experiments and results," *Powder Technology,* vol. 277, pp. 222-230, 2015.

[24] G. Bagheri and C. Bonadonna, "On the drag of freely falling non-spherical particles," *Powder Technology,* vol. 301, pp. 526-544, 2016.

[25] E. K. Marchildon, A. Clamen, and W. H. Gauvin, "Drag and oscillatory motion of freely falling cylindrical particles," *The Canadian Journal of Chemical Engineering,* vol. 42, pp. 178-182, 1964.

[26] G. E. Stringham, D. B. Simons, and H. P. Guy, "The behaviour of large particles falling in quiescent liquids," U.S. Department of the Interior. Washington D.C.: 1969, pp. 4-43.

[27] A. Chow and E. Adams, "Prediction of Drag Coefficient and Secondary Motion of Free-Falling Rigid Cylindrical Particles with and without Curvature at Moderate Reynolds Number," *Journal of Hydraulic Engineering,* vol. 137, pp. 1406-1414, 2011.

[28] M. Zastawny, G. Mallouppas, F. Zhao, and B. van Wachem, "Derivation of drag and lift force and torque coefficients for non-spherical particles in flows," *International Journal of Multiphase Flow,* vol. 39, pp. 227-239, 2012.

[29] S. Blaser, "Forces on the surface of small ellipsoidal particles immersed in a linear flow field," *Chemical Engineering Science,* vol. 57, pp. 515-526, 2002.

[30] M. Mandø and L. Rosendahl, "On the motion of non-spherical particles at high Reynolds number," *Powder Technology,* vol. 202, pp. 1-13, 2010.

[31] N. Kishore and S. Gu, "Momentum and heat transfer phenomena of spheroid particles at moderate Reynolds and Prandtl numbers," *International Journal of Heat and Mass Transfer,* vol. 54, pp. 2595-2601, 2011.

[32] A. Richter and P. A. Nikrityuk, "Drag forces and heat transfer coefficients for spherical, cuboidal and ellipsoidal particles in cross flow at sub-critical Reynolds numbers," *International Journal of Heat and Mass Transfer,* vol. 55, pp. 1343-1354, 2012.

[33] A. Richter and P. A. Nikrityuk, "New correlations for heat and fluid flow past ellipsoidal and cubic particles at different angles of attack," *Powder Technology,* vol. 249, pp. 463-474, 2013.

[34] A. Hölzer and M. Sommerfeld, "New simple correlation formula for the drag coefficient of non-spherical particles," *Powder Technology,* vol. 184, pp. 361-365, 2008.

[35] A. Terfous, A. Hazzab, and A. Ghenaim, "Predicting the drag coefficient and settling velocity of spherical particles," *Powder Technology,* vol. 239, pp. 12-20, 2013.

[36] M. Mando, Y. Chungen, H. Sorensen, and L. Rosendahl, "On the modelling of motion of non-spherical particles in two-phase flow," presented at the 6th International Conference on Multiphase Flow, Leipzig, Germany, 2007.

[37] A. E. Hawkins, "Characterizing the single particle," in *Principles of powder technology*, M. J. Rhodes, Ed., ed Chichester: John Wiley & Sons, 1995, pp. 9-27.

[38] T. Allen, *Particle size measurement*, 5 ed. vol. 1. London: Chapman & Hall, 1997.

[39] H. Wadell, "The coefficient of resistance as a function of Reynolds number for solids of various shapes," *Journal of the Franklin Institute,* vol. 217, pp. 459-490, 1934.

[40] H. Lu, E. Ip, J. Scott, P. Foster, M. Vickers, and L. L. Baxter, "Effects of particle shape and size on devolatilization of biomass particle," *Fuel,* vol. 89, pp. 1156-1168, 2010.

[41] G. H. Bagheri, C. Bonadonna, I. Manzella, and P. Vonlanthen, "On the characterization of size and shape of irregular particles," *Powder Technology,* vol. 270, Part A, pp. 141-153, 2015.

[42] R. M. Carter Y. Yan, "Measurement of particle shape using digital imaging techniques," *Journal of Physics: Conference Series,* vol. 15, p. 177, 2005.

[43] P. D. Komar and C. E. Reimers, "Grain Shape Effects on Settling Rates," *The Journal of Geology,* vol. 86, pp. 193-209, 1978.

[44] P. Dellino, D. Mele, R. Bonasia, G. Braia, L. La Volpe, and R. Sulpizio, "The analysis of the influence of pumice shape on its terminal velocity," *Geophysical Research Letters,* vol. 32, pp. n/a-n/a, 2005.

[45] D. Besnard and F. H. Harlow, "Nonspherical particles in two-phase flow," *International Journal of Multiphase Flow,* vol. 12, pp. 891-912, 1986.

[46] B. S. Klein, M. Gibert, A. Bérut, and E. Bodenschatz, "Simultaneous 3D measurement of the translation and rotation of finite-size particles and the flow field in a fully developed turbulent water flow," *Measurement Science and Technology,* vol. 24, p. 024006, 2013.

[47] M. Rhodes, *Introduction to particle technology*, 2 ed. Chichester: John Wiley & Sons, 2008.

[48] H. Schlichting and K. Gersten, *Boundary-layer theory*, 8 ed. Germany: Springer-Verlag, 2000.

[49] M. R. Maxey and J. J. Riley, "Equation of motion for a small rigid sphere in a nonuniform flow," *Physics of Fluids,* vol. 26, pp. 883-889, 1983.

[50] B. J. Lázaro, and J. C. Lasheras, "Particle dispersion in a turbulent, plane, free shear layer," *Physics of Fluids A: Fluid Dynamics,* pp. 1035-1044, 1989.

[51] E. B. Christiansen and D. H. Barker, "The effect of shape and density on the free settling of particles at high Reynolds numbers," *AIChE Journal,* vol. 11, pp. 145-151, 1965.

[52] H. N. Yow, M. J. Pitt, and A. D. Salman, "Drag correlations for particles of regular shape," *Advanced Powder Technology,* vol. 16, pp. 363-372, 2005.

[53] S.-F. Chien, "Settling Velocity of Irregularly Shaped Particles." SPE Drilling & Completion, vol. 9, pp. 281-289, 1994.

[54] S. F. Hoerner, *Fluid-dynamic drag*, 2nd ed. United States, 1965.

[55] C. Garrison, "Comments on Cross-Flow Principle and Morison's Equation," *Journal of Waterway, Port, Coastal, and Ocean Engineering,* vol. 111, pp. 1075-1079, 1985.

[56] B. Krueger, S. Wirtz, and V. Scherer, "Measurement of drag coefficients of non-spherical particles with a camera-based method," *Powder Technology,* vol. 278, pp. 157-170, 2015.

[57] R. H. Magarvey and R. L. Bishop, "Transition ranges for three-dimensional wakes," *Canadian Journal of Physics,* vol. 39, pp. 1418-1422, 1961.

[58] R. H. Magarvey and C. S. MacLatchy, "Vortices in sphere wakes," *Canadian Journal of Physics,* vol. 43, pp. 1649-1656, 1965.

[59] T. A. Johnson and V. C. Patel, "Flow past a sphere up to a Reynolds number of 300," *Journal of Fluid Mechanics,* vol. 378, pp. 19-70, 1999.

[60] N. Moradian, D. S. K. Ting, and S. Cheng, "The effects of freestream turbulence on the drag coefficient of a sphere," *Experimental Thermal and Fluid Science,* vol. 33, pp. 460-471, 2009.

[61] MIT Open CourseWare. (2006). *Flow past a sphere II: Stokes' law, the Bernoulli equation, turbulence, boundary layers, flow separation* [Online]. Available: http://ocw.mit.edu/courses/earth-atmospheric-and-planetary-sciences/12-090-special-topics-an-introduction-to-fluid-motions-sediment-transport-and-current-generated-sedimentary-structures-fall-2006/lecture-notes/ch3.pdf

[62] Y. Yong, "Mass flow measurement of bulk solids in pneumatic pipelines," *Measurement Science and Technology,* vol. 7, p. 1687, 1996.

[63] R. M. Carter and Y. Yong, "An instrumentation system using combined sensing strategies for online mass flow rate measurement and particle sizing," *Instrumentation and Measurement, IEEE Transactions on,* vol. 54, pp. 1433-1437, 2005.

[64] R. M. Carter, Y. Yan, and S. D. Cameron, "On-line measurement of particle size distribution and mass flow rate of particles in a pneumatic suspension using combined imaging and electrostatic sensors," *Flow Measurement and Instrumentation,* vol. 16, pp. 309-314, 2005.

[65] O. Melander and A. Rasmuson, "PIV measurements of velocities and concentrations of wood fibres in pneumatic transport," *Experiments in fluids,* vol. 37, pp. 293-300, 2004.

[66] Y. Zheng and Q. Liu, "Review of techniques for the mass flow rate measurement of pneumatically conveyed solids," *Measurement,* vol. 44, pp. 589-604, 2011.

[67] Y. Lu, D. H. Glass, and W. J. Easson, "An investigation of particle behavior in gas–solid horizontal pipe flow by an extended LDA technique," *Fuel,* vol. 88, pp. 2520-2531, 2009.

[68] C. Veldhuis, A. Biesheuvel, L. van Wijngaarden, and D. Lohse, "Motion and wake structure of spherical particles," *Nonlinearity,* vol. 18, p. C1, 2005.

[69] C. H. J. Veldhuis and A. Biesheuvel, "An experimental study of the regimes of motion of spheres falling or ascending freely in a Newtonian fluid," *International Journal of Multiphase Flow,* vol. 33, pp. 1074-1087, 2007.

[70] C. H. J. Veldhuis, A. Biesheuvel, and D. Lohse, "Freely rising light solid spheres," *International Journal of Multiphase Flow,* vol. 35, pp. 312-322, 2009.

[71] R. Wang, X. Li, and Y. Zhang, "Analysis and optimization of the stereo-system with a four-mirror adapter," *Journal of the European Optical Society - Rapid publications; Vol 3,* 2008.

[72] G. Xu, X. Li, J. Su, H. Pan, and L. Geng, "Integrative evaluation of the optimal configuration for the measurement of the line segments using stereo vision," *Optik - International Journal for Light and Electron Optics,* vol. 124, pp. 1015-1018, 2013.

[73] T. Xue, L. Qu, Z. Cao, and T. Zhang, "Three-dimensional feature parameters measurement of bubbles in gas–liquid two-phase flow based on virtual stereo vision," *Flow Measurement and Instrumentation,* vol. 27, pp. 29-36, 2012.

[74] T. K. Nishino, H. Kato, and K. Torii, "Stereo imaging for simultaneous measurement of size and velocity of particles in dispersed two-phase flow," *Measurement Science and Technology,* vol. 11, p. 633, 2000.

[75] K. Cheung, W. B. Ng, and Y. Zhang, "Three dimensional tracking of particles and their local orientations," *Flow Measurement and Instrumentation,* vol. 16, pp. 295-302, 2005.

[76] W. B. Ng and Y. Zhang, "Stereoscopic imaging and reconstruction of the 3D geometry of flame surfaces," *Experiments in Fluids,* vol. 34, pp. 484-493, 2003.

[77] K. Y. Cheung, "3D diagnostics based on optical and digital image processing," PhD thesis, Department of Mechanical, Aerospace and Civil Engineering, University of Manchester, Manchester, 2006.

[78] K. Cheung and Y. Zhang, "Stereo imaging and analysis of combustion process in a gas turbine combustor," *Measurement Science and Technology,* vol. 17, p. 3221, 2006.

[79] Q. Wang and Y. Zhang, "High speed stereoscopic shadowgraph imaging and its digital 3D reconstruction," *Measurement Science and Technology,* vol. 22, p. 065302, 2011.

[80] G. H. Bagheri, C. Bonadonna, I. Manzella, P. Pontelandolfo, and P. Haas, "Dedicated vertical wind tunnel for the study of sedimentation of non-spherical particles," *Review of Scientific Instruments,* vol. 84, p. 054501, 2013.

[81] R. C. Gonzalez, R. E. Woods, and S. L. Eddins, *Digital Image Processing Using Matlab*, 2nd edition ed. New Delhi: McGraw-Hill, 2010.

[82] R. M. Carter and Y. Yan, "On-line particle sizing of pulverized and granular fuels using digital imaging techniques," *Measurement Science and Technology,* vol. 14, p. 1099, 2003.

[83] Z. Zhang, J. Yang, L. Ding, and Y. Zhao, "Estimation of coal particle size distribution by image segmentation," *International Journal of Mining Science and Technology,* vol. 22, pp. 739-744, 2012.

[84] N. Tuyen and N.-S. Cheng, "A single-camera technique for simultaneous measurement of large solid particles transported in rapid shallow channel flows," *Experiments in Fluids,* vol. 53, pp. 1269-1287, 2012.

[85] A. Montenegro Ríos, D. Sarocchi, Y. Nahmad-Molinari, and L. Borselli, "Form From Projected Shadow (FFPS): An algorithm for 3D shape analysis of sedimentary particles," *Computers & Geosciences,* vol. 60, pp. 98-108, 2013.

[86] L. Gao, Y. Yan, G. Lu, and R. M. Carter, "On-line measurement of particle size and shape distributions of pneumatically conveyed particles through multi-wavelength based digital imaging," *Flow Measurement and Instrumentation,* vol. 27, pp. 20-28, 2012.

[87] Y. D. Song, L. Peng, G. Lu, S. Yang, and Y. Yong, "Digital image processing based mass flow rate measurement of gas/solid two-phase flow," *Journal of Physics: Conference Series,* vol. 147, p. 012048, 2009.

[88] W. Merzkirch and Y. Egami, "Density-Based Techniques," in *Springer Handbook of Experimental Fluid Mechanics*, C. Tropea, A. L. Yarin, and J. F. Foss, Eds., Berlin: Springer-Verlag, 2007, pp. 473-486.

[89] S. Shahi and E. Kuru, "An experimental investigation of settling velocity of natural sands in water using Particle Image Shadowgraph," *Powder Technology,* vol. 281, pp. 184-192, 2015.

[90] S. Shahi and E. Kuru, "Experimental investigation of the settling velocity of spherical particles in Power-law fluids using particle image shadowgraph technique," *International Journal of Mineral Processing,* vol. 153, pp. 60-65, 2016.

[91] H. Fiedler, K. Nottmeyer, P. P. Wegener, and S. Raghu, "Schlieren photography of water flow," *Experiments in Fluids,* vol. 3, pp. 145-151, 1985.

[92] G. Tanda, M. Fossa, and M. Misale, "Heat transfer measurements in water using a schlieren technique," *International Journal of Heat and Mass Transfer,* vol. 71, pp. 451-458, 2014.

[93] S. T. Barnard and M. A. Fischler, "Computational stereo," SRI International, Menlo Park, California, 1982.

[94] O. Faugeras, *Three dimensional computer vision: a geometric viewpoint*. Cambridge, MA: MIT Press, 1993.

[95] M. Inaba, T. Hara, and H. Inoue, "A stereo viewer based on a single camera with view-control mechanisms," *Intelligent Robots and Systems '93, IROS '93. Proceedings of the 1993 IEEE/RSJ International Conference on,* vol. 3, pp. 1857-1865 vol.3, 1993.

[96] R. Hartley and A. Zisserman, *Multiple view geomerty in computer vision*, 2nd ed. New York: Cambridge University Press, 2003.

[97] D. A. Forsyth and J. Ponce, *Computer vision: a modern approach*, 2nd ed. USA: Pearson, 2012.

[98] M. Sonca, V. Hlavac, and R. Boyle, *Image processing, analysis, and machine vision*. USA: Thomson, 2008.

[99] Z. Zhengyou, "A flexible new technique for camera calibration," *Pattern Analysis and Machine Intelligence, IEEE Transactions on,* vol. 22, pp. 1330-1334, 2000.

[100] J. Canny, "A Computational Approach to Edge Detection," *Pattern Analysis and Machine Intelligence, IEEE Transactions on,* vol. PAMI-8, pp. 679-698, 1986.

[101] P. V. C. Hough, "Method and means for recognizing complex patterns," U.S. Patent 3 069 654, December 18, 1962.

[102] Z. Zhang, "A new multistage approach to motion and structure estimation: from essential parameters to euclidean motion via fundamental matrix," INRIA Sophia-Antipolis, Cedex1996.

[103] H. C. Longuet-Higgins, "A computer algorithm for reconstructing a scene from two projections," *Nature,* vol. 293, pp. 133-135, September, 1981.

[104] R. Hartley, R. Gupta, and T. Chang, "Stereo from uncalibrated cameras," G.E. - Corporate Research and Development Schenectady, New York, 1992.

[105] R. Hartley and P. Sturm, "Triangulation," in *Computer Analysis of Images and Patterns*, V. Hlavac and R. Sara, Eds., ed Berlin: pringer-Verlag, 1995, pp. 190-197.

[106] Z. Zhang, "Determining the Epipolar Geometry and its Uncertainty: A Review," *International Journal of Computer Vision,* vol. 27, pp. 161-195, 1998.

[107] N. Otsu, "A threshold selection method from gray-level histograms " *IEEE Transactions on Systems, Man, and Cybernetics* vol. SMC-9, pp. 62-66, 1979.

[108] G. Mougin and J. Magnaudet, "The generalized Kirchhoff equations and their application to the interaction between a rigid body and an arbitrary time-dependent viscous flow," *International Journal of Multiphase Flow,* vol. 28, pp. 1837-1851, 2002.

[109] *Physical properties of glycerine and its solutions*: Glycerine Producers Association, 1963.

[110] J. R. Taylor, *An introduction to error analysis. The study of uncertainties in physical measurements.*, 2nd edition ed. United States of America: University Science Books, 1997.

[111] J. Weng, P. Cohen, and M. Herniou, "Camera calibration with distortion models and accuracy evaluation," *Pattern Analysis and Machine Intelligence, IEEE Transactions on,* vol. 14, pp. 965-980, 1992.

[112] T. A. Clarke and J. G. Fryer, "The Development of Camera Calibration Methods and Models," *The Photogrammetric Record,* vol. 16, pp. 51-66, 1998.

[113] W. Guo-Qing and M. Song De, "Implicit and explicit camera calibration: theory and experiments," *Pattern Analysis and Machine Intelligence, IEEE Transactions on,* vol. 16, pp. 469-480, 1994.

[114] L. Ma, Y. Chen, and K. L. Moore, "Rational radial distortion models of camera lenses with analytical solution for distortion correction," *International Journal of Information Acquisition,* vol. 01, pp. 135-147, 2004.

[115] R. I. Hartley, "In defense of the eight-point algorithm," *Pattern Analysis and Machine Intelligence, IEEE Transactions on,* vol. 19, pp. 580-593, 1997.

[116] Z. Zhang and O. D. Faugeras, *3D Dynamic Scene Analysis: A Stereo Based Approach*. Berlin, Heidelberg: Springer, 1992.

[117] B. K. P. Horn, "Closed-form solution of absolute orientation using unit quaternions," *Journal of the Optical Society of America A,* vol. 4, pp. 629-642, 1987.

[118] I. J. Myung, "Tutorial on maximum likelihood estimation," *Journal of Mathematical Psychology,* vol. 47, pp. 90-100, 2003.